Master's Thesis

Development of Multirate Model and Analysis of Applicability to Wind Turbine Digital Fluid Power Transmissions

MCE4-1026

Peter Junker
Tom-Erik Lindberg
Kasper B. Nielsen
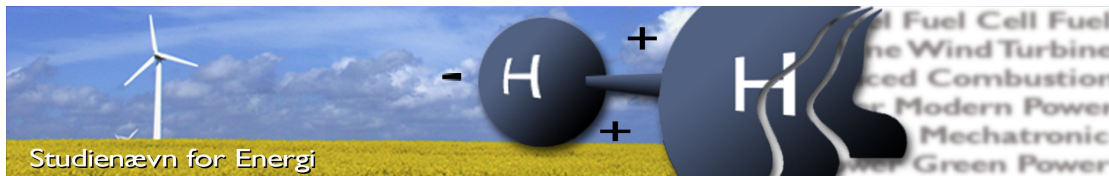
Title:	Development of Multirate Model and Analysis of Applicability to Wind Turbine Digital Fluid Power Transmissions
Semester:	4th, Spring Semester 2017
Semester theme:	Master Thesis
Project period:	01.02.17 to 01.6.17
ECTS:	30
Supervisor:	Niels-Henrik Pedersen
	Torben Ole Andersen
Project group:	MCE4-1026

Peter Junker

Tom-Erik Lindberg

Kasper B. Nielsen

Copies:	3
Pages, total:	221
Appendices:	A, B, C, D
Supplements:	None

SYNOPSIS:

Digital fluid power transmissions (DFPTs) are a promising alternative to drivetrains based on gearboxes and power electronics. One application is offshore wind turbines where the characteristics of high reliability and robustness of hydraulic systems are highly desirable.

A DFPT consists of a digital displacement pump and motor connected to shared pressure lines, thereby forming the transmission. The decision to update the displacement of such machines occurs at a number of fixed shaft positions, why for variable-speed operation, the control rates of the machines are both asynchronous and non-uniform creating a multirate control problem.

To obtain a linear control model, all dynamics are transformed to the spatial-domain. A new multirate modelling technique is hereafter derived by combining two existing multirate methods. From this multirate technique, the DFPT is linearly modelled and applicability of conventional control and analysis tools are evaluated.

Based on this thesis' results, it is concluded that multirate modelling and control of a DFPT is possible both in the time-domain and spatial-domain, but that the time-domain implementation of a spatial-domain control law is not straight forward.

By signing this document, each member of the group confirms that all participated in the project work and thereby all members are collectively liable for the content of the report. Furthermore, all group members confirm that the report does not include plagiarism.

Resumé

Dette kandidatspeciale undersøger mulighederne for at udlede en lineær model af en digital hydraulisk transmission til vindmølleapplikationer. Formålet med dette er at kunne foretage analyse samt regulatordesign ved brug af konventionelle lineære kontrolteori-værktøjer. Denne opgave er af en teknisk krævende natur i form af at systemet består af dynamiske elementer beskrevet i kontinuert tid som er aktueret af dynamiske elementer beskrevet i diskret tid. Disse diskrete tidselementer opererer ved uens samt uensartede rater, hvilket gør det nødvendigt at finde en modelbeskrivelse der kan håndtere op til flere rater i systemet.

For at håndtere udfordringerne i denne problemstilling individuelt er problemet blevet opdelt i tre mindre underproblemer. De to første underproblemer håndterer henholdsvis modellering af disse diskrete dynamiske elementer samt transformation af en uensartet rate til en ensartet rate. Med disse to løsninger bliver det muligt at undersøge problemet vedrørende modellering af et system med flere ensartede men uens rater, hvorefter det til sidst er muligt at sammensætte de tre løsninger for at diskutere det endelige resultat.

Med henblik på modellering af et system med flere rater introduceres et masse-fjeder-dæmper (MSD) system, hvortil de korrekte systemdynamikker let og intuitivt kan visualiseres, hvilket tillader en accelereret evaluering af modelleringsteknikkernes potentiale. Dette gøres da en vindmølletransmission med nominel effekt målt i MW er et højst avanceret system, hvorfor det er uegnet som udviklingsværktøj. I forbindelse med denne problemstilling undersøges to mulige modellingsteknikker. Der findes dog både ulemper og fordele ved begge metoder, men da disse ikke overlapper hinanden, vurderes det at ved at kombinere de to metoder, vil det være muligt at opstille en modelleringsteknik der muliggør løsning af problemstillingen.

Denne modelleringsteknik præsenteres som UNMR metoden, hvor det anses som essentielt for at modellen kan anvendes med konventionelle lineære kontrolteori-værktøjer at den matematisk både er lineær og tidsinvariant (LTI). For at opfylde det tidsinvariante krav, grupperes inputsene over en længere fælles periode kaldet BTPen. Set fra BTP til BTP er et system med flere rater tidsinvariant. Ved yderligere at beskrive systemet som en kombination af lineære systemdynamikker kan en LTI model opnås.

UNMR metoden anvendes på MSD systemet og findes generelt brugbar til at beskrive et multirate system i tidsdomænet, og metoden vælges derfor til anvendelse på den hydrauliske transmission. For at håndtere de uensartede rater i transmissionen, transformeres alle ligninger til et spatialt vinkeldomæne, hvor raterne er ensartede, omend stadig uens. Ydermere introduceres en fiktiv transmission med nominel effekt målt i kW med det formål at emulere udfordringerne ved en digital transmission designet til en vindmølle samtidig med at accelereret evaluering kan foretages. Herefter anvendes UNMR metoden, og simuleringsresultater fra den resulterende model sammenlignes med resultater fra en

ulineær simuleringsmodel. På baggrund af dette konkluderes det at modelleringsteknik-ken har potentiale for at kunne være brugbar, og videre arbejde forsættes med henblik på muligheder for systemanalyse og regulatordesign.

Ved analyse af UNMR-modellen af MSD-systemet findes det at grupperingsteknikken producerer ikke-kausale input-output-kombinationer, hvilket vanskeliggør analyse med traditionelle værktøjer, da disse ikke er udledt med henblik på at håndtere sådanne kombinationer. Ved analyse af resultater samt undersøgelse af systemets input-output-kombinationer findes det dog stadig muligt at anvende de konventionelle værkstøjer, dog med nogle begrænsninger vedrørende tolkning af resultaterne. Dertil bestemmes også at design af stabile tilstandsregulatorer er muligt, hvorfor det vurderes at metoden kan anvendes til analyse og regulatordesign til den digitale transmission.

Til den digitale transmission findes det at en vinkeldomæne-model også kan undersøges i frekvensdomænet, dog med en skaleret frekvensakse, og at modellen viser en realistisk respons. Regulatordesign og analyse kan derfor, efter den forudliggende afklaring vedrø-rende grupperingsmodeller, relativt trivielt overføres til transmissionen. Den anvendte vinkeltransformation medfører at alle kontrolsignaler styres af pumpeskaftvinklen, hvil-ket giver anledning til en vanskelig implementering af tilstandsregulatorens kontrollov ved varierende pumpehastighed. Forfatterne anbefaler derfor at den anvendte vinkel-transformation videre undersøges.

Det konkluderes dog at UNMR metoden er anvendelig til at beskrive et multirate-system med kontinuerte og diskrete elementer, som opererer ved flere forskellige rater såsom en digital transmission til en vindmølle. Metoden muliggør analyse samt regulatordesign til et system med flere rater, et emne som til trods for sin relative hyppighed i virkelige systemer sjældent håndteres i lærebøger.

Preface

This Master's thesis is written by group MCE4-1026 at the Department of Energy Technology at Aalborg University in the spring of 2017, and it is the result of a 4th semester Master of Science project. The purpose of this project is to develop a linear model, which is able to describe the multiple sampling rates occurring in a digital fluid power transmission, and then subsequently evaluate the applicability of the developed model for analysis and controller design.

In the project the following software has been used:

- **MATLAB/Simulink** - for model development and data analysis.
- **Maple** - for algebraic manipulation of equations.
- **Adobe Illustrator** - for illustrations.

Reader's Guide: On page ix a nomenclature which lists the variables and accompanying units used in the report is presented.

The list of literature utilised in the report can be found prior to the report appendices. The references will be presented using the following format (where applicable):

> [**Main Author's Surname Year**]
> [All Authors][(Year)][*Title*][Publisher][Edition]["Paper Title"][*Journal*]
> [Volume.Number][Pages][ISBN][ISSN][DOI][url]

The bibliography is alphabetically sorted by the surname of the author, and in the report the citations are given by: (Author's surname Year).

For referencing figures, tables and equations in the report, they are numbered in the following manner: (x,y), where x indicates the chapter, and y indicates the equation/figure/table number. In addition relevant captions for figures and tables can be found directly beneath the figure/table.

For matrix and vector notation, boldface capital and boldface lowercase notation is used, respectively.

A number of appendices are included with the report, and they can be found after the bibliography.

Nomenclature

Acronyms

Symbol	Description	Unit
BDC	Bottom dead center	
BTP	Basic Time Period	
CDE	Continuous Dynamic Element	
DD	Digital Displacement	
DDE	Discrete Dynamic Element	
DDM	Digital Displacement Machine	
DFPT	Digital Fluid Power Transmission	
DSM	$\Delta\Sigma$ Modulator	
FPT	Fluid power transmission	
GCD	Greatest Common Divisor	
HPL	High pressure line	
HPV	High pressure valve	
ICE	Internal Combustion Engine	
LCM	Least Common Multiple	
LPL	Low pressure line	
LPV	Low pressure valve	
MIMO	Multiple-input multiple-output	
MR	Multirate	
MSD	Mass Spring Damper	
multi-MW	Multi-megawatt	
NREL	National Renewable Energy Laboratory	
ODE	Ordinary differential equation	
RGA	Relative gain array	
SHE	Sample-and-Hold Element	
SISO	Single-input single-output	
SM	Synchronous generator	
STP	Short Time Period	
SVD	Singular value decomposition	
TDC	Top dead center	
UNMR	Unified Non-Minimal Realisation	
WT	Wind turbine	
ZOH	Zero-order Hold	

Latin Variables

Symbol	Description	Unit
$\mathbf{0}$	Zero matrix	
A	Area	m^2
$\boldsymbol{A}$	Continuous state-space $\boldsymbol{A}$-matrix	
$\boldsymbol{B}$	Continuous state-space $\boldsymbol{B}$-matrix	

b	Damping coeffcient	N/(m s)
$\boldsymbol{C}$	Continuous state-space $\boldsymbol{C}$-matrix	
C_{q}	WT torque coefficient	
$\boldsymbol{D}$	Continuous state-space $\boldsymbol{D}$-matrix	
$\boldsymbol{D}$	DDE transition matrix	
$\boldsymbol{d}$	DDE input transition matrix	
F	Force	N
$\boldsymbol{G}$	Discrete state-space equivalent of $\boldsymbol{A}$-matrix	
$\boldsymbol{H}$	Discrete state-space equivalent of $\boldsymbol{B}$-matrix	
$\boldsymbol{I}$	Identity matrix	
i	Iteration counter	
i	Row counter	
J_{rp}	Combined rotor pump inertia	$\mathrm{kg\,m}^2$
J	Cost function	
J	Inertia	$\mathrm{kg\,m}^2$
j	Column counter	
j	Iteration counter	
$\boldsymbol{K}$	Controller gain matrix	
k	Sample number	
k	Spring constant	N/m
l_i	Number of STP per T_i	
l	Iteration counter	
m	Mass	kg
N_{cr}	Number of cam rings	
N_{ec}	Number of eccentric cams	
N_{l}	Number of pump lobes	
N_{mn}	Number of motor pressure chambers	
N_i	Number of T_i per BTP	
$\bar{N}$	Sum of N_i	
$\boldsymbol{N}$	LQR input/state cross weighting matrix	
N	Quantity	
n	Sum of CDE, DDE and SHE states	
$\boldsymbol{P}$	Infinite horizon Riccati equation solution	
p	Number of inputs or outputs	
$\boldsymbol{Q}$	LQR state/output weighting matrix	
$\boldsymbol{R}_{\mathrm{c}}$	Controllability matrix	
$\boldsymbol{R}$	LQR input weighting matrix	
r	radius	m
$\boldsymbol{S}$	SHE transition matrix	
$\boldsymbol{S}$	SHE input transition matrix	
s	Laplace operator	
T_0	STP Period	s
T_{i}	i'th time period	s
t_{s}	Valve opening/closing time	s
T	BTP Period	s

t	Time	s
$\boldsymbol{U}$	Output selection matrix	
$\boldsymbol{u}$	State-space input vector	
V_{m0}	Motor pressure chamber minimum volume	m^3
V_{p0}	Pump pressure chamber minimum volume	m^3
$\boldsymbol{v}$	Combined input transition matrix, Kalman and Bertam equivalent to $\boldsymbol{B}$	
v	Iteration counter	
v	Wind speed	m/s
$\boldsymbol{x_{\mathrm{comb}}}$	Combined vector of CDE, DDE and SHE states	
$\boldsymbol{x}$	Expanded state vector	
$\boldsymbol{x}_{\mathrm{c}}$	CDE / continuous state vector	
$\boldsymbol{x}_{\mathrm{d}}$	DDE / discrete state vecotr	
$\boldsymbol{x}_{\mathrm{s}}$	SHE / sample-and-hold state vector	
$x_{\mathrm{m,stroke}}$	Motor piston stroke length	m
$x_{\mathrm{p,stroke}}$	Pump piston stroke length	m
x	Coordinate	m
$\boldsymbol{y}$	State-space output vector	
y	Coordinate	m
z	Discrete Laplace operator	
d_{r}	Damping coefficient	$\mathrm{Nm\,s/rad}$
k_{f}	Valve flow coefficient	$\sqrt{Pa}\,\mathrm{s/m}^2$
k_{l}	Leakage coefficient	$\mathrm{m}^3/(\mathrm{s\,Pa})$
p	Pressure	Pa
Q	Flow	m^3/s
R	Radius	m
V	Volume	m^3

Greek Letters

Symbol	Description	Unit
α	Displacement input	
β	Bulk modulus	Pa
β	Pitch angle	rad
$\boldsymbol{\kappa}$	Vector denoting periodically varying sampling operations	
$\boldsymbol{\Phi}$	CDE transition matrix	
$\boldsymbol{\Psi}$	Combined transition matrix, Kalman and Bertam equivalent to $\boldsymbol{A}$	
δ	Number of DDE states	
$\Delta\square$	Difference of $\square$	
ϵ	Volumetric ratio of free air	
ϵ_{A0}	Volumetric ratio of air at atmospheric pressure	
η	Efficiency	
γ	Number of CDE states	

λ	Integration variable	
$\Lambda(\square)$	RGA of $\square$	
μ	Iteration counter	
ω	Rotational speed	rad/s
ω_{n}	Natural frequency	rad/s
ϕ	Angle for torque calculation	rad
ρ	Density	kg/m^3
σ	Number of SHE states	
σ	Singular value	
τ	Time constant	s
τ	Time function variable	s
τ	Torque	Nm
θ	Shaft angle	rad
θ_{HPV}	HPV opening / closing angle	rad
θ_{LPV}	LPV closing angle	rad
ζ	Damping ratio	
$lambda$	RGA element	

Superscripts and Subscripts

Symbol	Description	Unit
$\bar{\square}$	Normalised value of $\square$	
$\square'$	Spatial derivative of $\square$	
$\square^{+}$	Time instant after discrete calculation	
$\square^{\mathsf{T}}$	Tranpose of $\square$	
$\square^{\mathrm{D}}$	Variable or coefficient related to Araki and Yamamoto's method	
$\square^{\Psi}$	Variable or coefficient related to A New Unified Non-minimal Realisation Method	
$\square_{\Delta\Sigma}$	Variable or coefficient related to $\Delta\Sigma$ modulator	
$\square_{\mathrm{A}}$	Variable or coefficient related to air	
$\square_{\mathrm{c}}$	Coefficient or variable related to CDE/continuous states	
$\square_{\mathrm{d}}$	Coefficient or variable related to DDE/discrete states	
$\square_{\mathrm{H}}$	Variable or coefficient related to high pressure line	
$\square_{\mathrm{in}}$	Model input variable or coefficient related $\square$	
$\square_{\mathrm{L}}$	Variable or coefficient related to low pressure line	
$\square_{\mathrm{mc}}$	Variable or coefficient to motor chamber	
$\square_{\mathrm{mH}}$	Variable or coefficient related to motorHPV	
$\square_{\mathrm{mL}}$	Variable or coefficient related to motor LPV	
$\square_{\mathrm{mp}}$	Variable or coefficient related to motor piston	
$\square_{\mathrm{m}}$	Motor related variable or coefficient	
$\square_{\mathrm{pc}}$	Variable or coefficient to pump chamber	
$\square_{\mathrm{pH}}$	Variable or coefficient related to pump HPV	
$\square_{\mathrm{pL}}$	Variable or coefficient related to pump LPV	

$\square_{\mathrm{pp}}$	Variable or coefficient related to pump piston
$\square_{\mathrm{p}}$	Pump related variable or coefficient
$\square_{\mathrm{r}}$	WT rotor related variable or coefficient
$\square_{\mathrm{s}}$	Coefficient or variable related to SHE/sample-and-hold states
$\square_{\mathrm{x}}$	x-coordinate of $\square$
$\square_{\mathrm{y}}$	y-coordinate of $\square$
$\square_e$	Error signal
$\check{\square}$	Minimum value of $\square$
$\dot{\square}$	Time derivative of $\square$
$\hat{\square}$	Maximum value of $\square$
$\square^*$	Reference value for $\square$

Contents

Introduction

This master thesis concerns the topic of modelling and control of a digital fluid power transmission for use in a wind turbine drivetrain. This chapter serves as an introduction, which purpose is to present the preliminary studies conducted in the process of choosing a thesis topic. This chapter hereby aims to answer why control of a digital fluid power transmission is an interesting topic of study seen from an academic and commercial point of view.

The primary objective of this thesis is to present the work conducted when studying the topic of model based control for a wind turbine's digital fluid power transmission. Prior to the choosing of this topic studies within the areas of wind turbines, fluid power transmission and control strategies for such systems have been carried out. It is the result of these studies that have shaped the content of this thesis, why this chapter is dedicated to summarising the important results and conclusions of these preliminary studies.
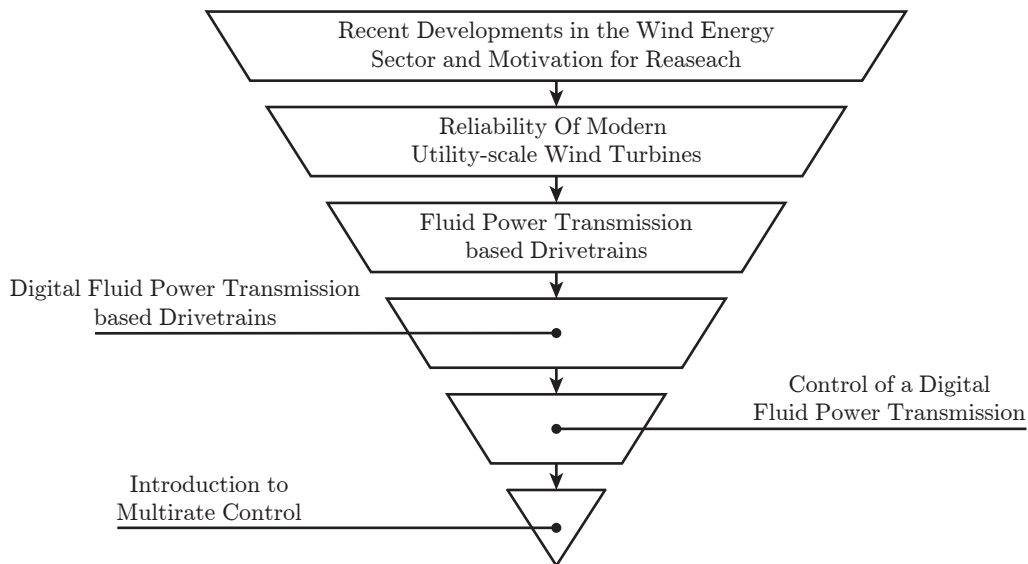
Fig. 1.1: Flowchart presenting the various areas of research studied in the process of determining a suitable master thesis topic.

The chapter is comprised of six individual sections, each section with a different focus area. The sections are presented in the chronological order in which they have been studied according to the flowchart in figure 1.1. This means that the first section presented in this chapter concerns the recent developments within the wind energy sector followed by sections which becomes increasingly more specific towards fluid power transmissions and the control thereof. As a result the chapter ends with a theoretical discussion of the general concepts of multirate control, which is the control approach of interest for this master's thesis.

For readers familiar with the recent development within the area of wind turbine reliability, fluid power transmission or digital displacement machines one or several of this chapter's sections might be redundant and can be omitted without loss of this chapter's essential conclusions.

With the objective of creating a common base of knowledge between the authors and readers of this thesis the first sections of this chapter aims to elaborate upon why fluid power transmission based drivetrains is an emerging technology within the wind industry sector.

1.1 Motivation

During the last four decades there has been an increasing interest in renewable energy sources as a result of an increasing demand for energy and rising oil prices. Globally and nationally this has lead to several political initiatives, wherein the main objective has been to reduce greenhouse gas emissions by utilising renewable energy sources. Examples of this include the Kyoto protocol (1997), the European Union "Renewable Energy Road Map" (2007) and the Danish "Energy Agreement" (2012) (Danish Ministry of Climate, Energy and Building 2012; Perez et al. 2013). Common for all of these initiatives is that they all proposes the need for harvesting wind energy as one of the primary sources for producing renewable energy.

The wind industry have made several advances, since the first electricity-generating horizontal axis wind turbine (WT) emerged in the mid-1900s, in order to adapt to the increasing demand for renewable energy. This is especially evident in the more recent years where the world wide wind energy capacity has more than doubled every three years (Global Wind Energy Council 2015).

To illustrate the rapid development in the last 17 years within the global wind industry market figure 1.2 has been made. It presents the increase in installed wind power capacity (blue bars) on a world wide scale from 2000 to 2016. Studying the significant increase in wind power capacity during the most recent years it becomes evident that currently a large economical potential in the wind industry exists. Furthermore, if the forecast of future expected wind power capacity (seen as the red bars in figure 1.2) is taken into account, it provides the necessary motivation for future advances in the wind industry.

A large part of the development within the wind industry has been focused on reducing the cost of WTs and to improve the overall efficiency. To reduce the cost of generating electricity using WTs and to supply the increasing energy demand, the state of the art trend within the wind industry is to upscale the WT's power rating to the multi-megawatt (multi-MW) scale. Currently the worlds largest commercial WT is the MHI Vestas V164 offshore WT, which has a power rating of 8 MW with a rotor diameter of 164 m (wind-turbine-models.com 2016d). As an alternative to upscaling, manufacturers have put effort into utilising commercially available components in their WT designs in the aim of reducing costs. To improve the efficiency, design changes have been made on all levels in the WT.
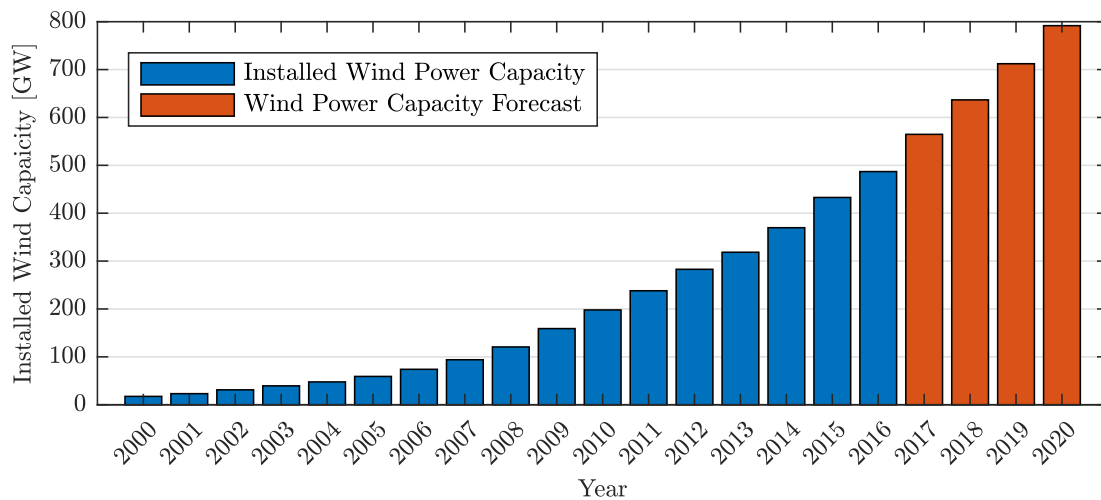
Fig. 1.2: Globally installed wind power capacity (blue) and forecast (red). Data from Global Wind Energy Council (2015, 2016).

Many different design topologies have emerged over the years, such as vertical and horizontal axis designs, upwind and downwind rotor placement, variable- or fixed-speed operation, multiple numbers of blades and different drivetrain constructions. The majority of the available WTs today are based on the same design principle. This includes a horizontal axis, three blades with pitch control, variable-speed operation and either a direct-drive drivetrain or a drivetrain utilising a gearbox. Even though the development seen in the wind industry sector has resulted in more efficient WTs, which has made harvesting wind energy more attractive, some future issues such as reliability must still be addressed. (Echavarria et al. 2008)

The continued expansion of the wind industry has raised the interest for studying the reliability of WTs installed world wide. A reason for why this has become a hot topic is because a significant part of the WTs installed world wide have reached an age where wear-out issues start to appear and due to more focus on the maintenance cost related to operating a WT. This creates an interesting topic of study, specifically which parts of the WT are more prone to failure and how the reliability might be improved. This will be the topic of the next section.

1.2 Reliability of Modern Wind Turbines

In order to study WT reliability and identifying which WT components are prone to failure, it is beneficial to have a basic understanding of WT topologies and the general components used to construct a modern utility-scale WT. Thus the general design of a modern utility-scale WT will first be considered before the related reliability studies will be presented.

1.2.1 Wind Turbine Structure

The parts used to comprise a WT varies depending on the design topology, although many design configurations often remain the same independently of choice of topology. Figure 1.3 presents the parts used to comprise one of today's common horizontal axis utility WT designs.
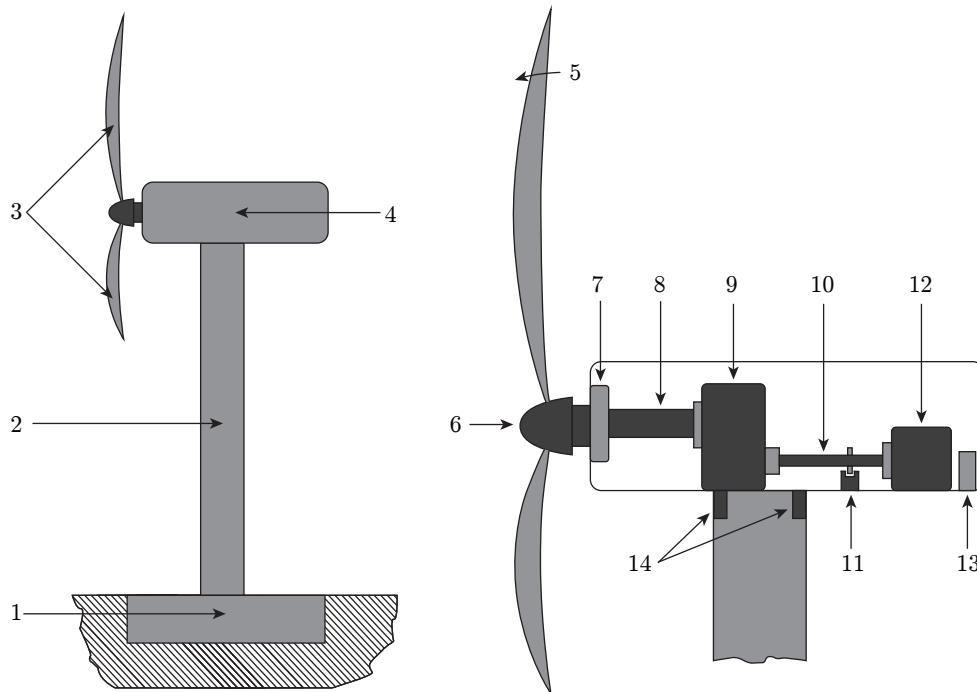
Fig. 1.3: General design of common horizontal axis WT with pitch regulated blades. Elaboration of numbers can seen in text. (Perez et al. 2013)

.

The tower (2) of an onshore WT is mounted on a foundation (1). The nacelle (4) is mounted on the top of the tower and may be rotated by the yaw system (14) to align the turbine blades (3) with the wind direction. The blades of the WT are mounted to the WT's hub (6). During operation the blades can be rotated by the pitch system (5) in order to adjust the amount of power going to the WT. Furthermore, the pitch system may be used as an aerodynamic brake, in the scenario where rotation of the blades must come to a stop.

The hub and gearbox (9) are connected by the main (low speed) shaft (8), which rotates at the speed of the blades, and is supported by the main bearing (7). The gear box transfers the energy from the main shaft to the high speed shaft (10). The high speed shaft drives the WT's generator (12), which then transfers the rotational energy of the high speed shaft to the grid. On the high speed shaft a mechanical brake (11) is installed, which can also be used to bring the WT to a stop.

Depending on drivetrain topology some of the presented components might not be pre-

sent, just as additional components sometimes are utilised. For instance a converter (13) can be used to connect the generator to the grid. A classification of today's most common WT drivetrains can be found in appendix A.1.

The topology of the drivetrain is generally defined by the type of generator utilised in the turbine nacelle. The design choices for external components, i.e. the rotor, hub, tower and so on, will generally remain the same independently of the choice of WT drivetrain. Given a basic understanding of the structure of today's modern utility-scale WT, the next section will proceed with investigating the reliability of these WTs.

1.2.2 Wind Turbine Reliability

Multiple studies have been made in the aim of determining which critical parts are more prone to failure in a modern utility-scale WT. In order to generate reliable results in these studies a large amount of data must be collected. However, there are not many databases which contain the necessary data for studying the reliability of WTs (Echavarria et al. 2008). Therefore data is often voluntarily supplied by wind farms and WT manufacturers. These data sets can, however, often be considered as biased and caution must thus be taken when studying such data. Furthermore, when studying reliability of data collected from different organisations there exists the challenge of comparing data from various WT topologies, at varying operational ages, which information is collected at different geographical locations using diverse procedures. As a result the information available for studying which WT components are more prone to failure is somewhat limited.

Two studies which are considered to present reliable information with regard to reliability, failure rate and downtime are the Reliawind study by Gayo (2011) and the research thesis by Kaidis (2013). Common for both studies is that their findings are based on the same database, which includes data from Gayo (2011) and Hahn et al. (2006). The data initially collected by Hahn et al. (2006) consists of information with regards to failure rate and average downtime for different subparts of 1500 WTs. These data have been used to create figure 1.4, which aims to identify which subparts of a WT are most prone to failure and which subparts contribute the most to downtime.

The top bar plot (blue bars) in figure 1.4, shows the contribution to the overall failure rate of different subparts of the WT. The numbers displayed above each bar represents the actual failure rate [failure/WT/year] for the corresponding subpart. The top bar plot suggest that the *Power Module* which include the generator and converter among other components, are more likely to fail, specifically 0.62 time per year. Subparts such as *Electrical Control*, *Rotor Module* and *Other* also have a significant failure rate which gives incentive for improvements.

When the financial incentive for improvements must be considered it is not sufficient only to investigate the failure rates, but the downtime and cost of each failure should also be taken into account. The lower bar plot (red bars) shows the contribution to overall downtime. The number above each bar displays the average downtime [days/failure] for the corresponding subpart. It is interesting to see that the subparts which contributes to the most downtime, do not necessarily have the largest failure rate. For instance
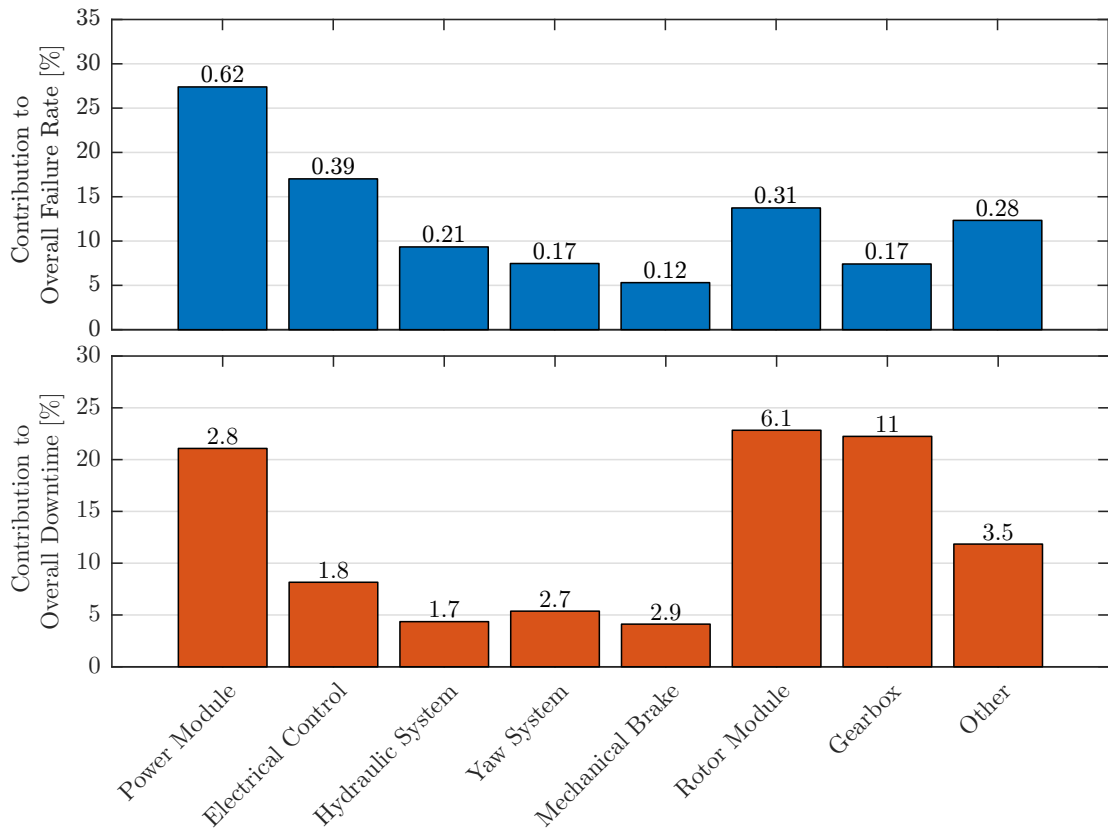
Fig. 1.4: Subparts contribution of overall failure rate (blue bars) and overall downtime (red bars) in WTs. The numbers displayed above each bar represent the failure rate [failure/WT/year] for upper bar plot and downtime [days/failure] for lower bar plot. Data from Hahn et al. (2006).

the *Rotor Module* and *Gearbox* have failure rates that are half and less than half of the maximum failure rate of 0.62 [failure/WT/year]. However, these two subparts account for more than 40 % of the total downtime. Considering that these two subparts furthermore represents above 40 % of the costs in a common WT design, there exists a strong financial incentive to improve the reliability of both the *Rotor Module* and the *Gearbox* (Perez et al. 2013). It is therefore chosen to investigate how the drivetrain of a modern utility-scale WT, which is comprised of both the *Power Module* and *Gearbox* and others subparts, can be improved with regards to reliability.

In recent years focus has been increased on developing alternative drivetrain designs for WTs in the aim of improving the reliability. To investigate some of these it is deemed necessary to further study the current drivetrain topologies. This is considered necessary for the purpose of determining the efficiency of currently produced WTs, and to clarify the performance requirements for potential alternative drivetrain solutions. A study of currently installed drivetrain topologies and their efficiencies have been carried out and can be found in appendices A.1 and A.2 respectively. The study shows an overall efficiency of ~95 % close to rated power, and rarely efficiency at partial load below ~80 %.

In the following section one of WT drivetrain alternatives, namely the concept of fluid power transmission (FPT) based drivetrains will be studied.

1.3 Fluid Power Transmission

One alternative to the conventional drivetrains now present in the industry is the FPT based drivetrain. FPT is not a new concept, and has been utilised for several decades to drive heavy machinery, where a need for converting high speed to low speed rotation is required. Today's usage include on- and off-road vehicles, rock crushers, paper mills amongst others (Rampen 2006).

1.3.1 Fluid Power Transmission for Wind Turbines

Even in the wind power industry utilising FPT as a gearless transmission is not an entirely new concept. One of the first WTs with a variable FPT was developed by British engineer Sir Henry Lawson-Tancred in the 1980s, unfortunately the developed design was never successfully built and only serves as a proof of concept. In recent year several different attempts have been made, some with more success than others. Common for all of them is, however, that they are based on the same general FPT design principle, which is depicted in figure 1.5.
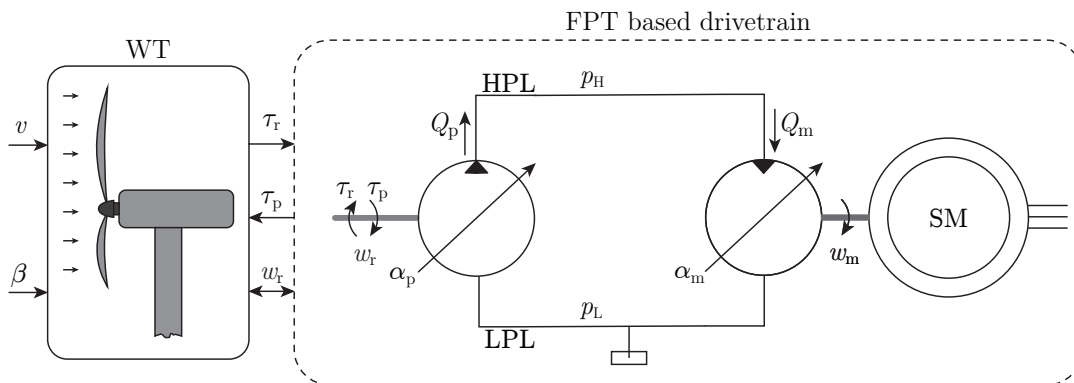
Fig. 1.5: General principle of a FPT based drivetrain for a WT.

In accordance with figure 1.5, the WT has the wind speed, v, as an exogenous input and the pitch angle of the rotor blades, β, as an input. The pitch angle is determined by a wind power extraction control strategy, which depends on the wind speed. The general WT control strategy is elaborated upon in appendix B.

The hydraulic pump depicted in figure 1.5 is of the low speed high displacement type and has the WT as the prime mover. The turbine torque, τ_r, drives the low speed shaft, and together with the reactive pump torque, τ_p, determines the rotational WT speed, ω_r. The pump outputs a pressurised fluid flow, Q_p, from the low pressure line (LPL) into the high pressure line (HPL), which in turn is used to drive the hydraulic motor.

The motor seen in figure 1.5 is of a high speed low displacement type. The motor shares

a high speed shaft with a synchronous generator (SM), which is connected directly to the grid. As such, the rotational speed of both motor and generator is fixed by the synchronous frequency of the generator i.e. the grid frequency.

The pump and motor are in figure 1.5 depicted to be of the variable displacement type, creating two control inputs to the drivetrain. These are the displacement α_p and α_m of the pump and motor respectively. Alternatively the pump or motor could have been replaced by a fixed displacement type, and hereby reducing the complexity of controlling the transmission.

When a FPT must be realised additional components such as pressure relief valves, accumulators, boost circuits, filters and drains must furthermore be included, however these have not been depicted in figure 1.5 since these are not essential for understanding the working principle of a FPT.

1.3.2 Advantages of Fluid Power Transmissions in Wind Turbines

Evidently, the FPT concept under consideration omits both gearboxes and power converters, which were in section 1.2 found to be a large source of unreliability in conventional WTs, and thus FPT based drivetrains are a potential topology for reliability improvements. In general a number of advantages can be achieved by the use of FPT based drivetrains compared to today's commercially available solutions. These advantages include:

- Mechanical decoupling between WT blades and generator. As a result the loading on the nacelle structure can be reduced when wind gusts and turbulence are occurring (Carroll et al. 2014).

- The conventional fluid power systems is considered to have great robustness due to high reliability.

- Fluid power systems have a high power to weight ratio, suggesting that the weight of the transmission can be reduced compared to a mechanical gearbox (Rampen 2006). Furthermore, FPTs offer the possibility of placing the motor and generator at ground level, reducing the weight of the nacelle even further (Carroll et al. 2014). This, however, comes at the cost of a diminished efficiency.

- Including an accumulator in the FPT can reduce pressure fluctuations and furthermore work as a energy storage capacity superior in power and energy density compared to capacitor based energy storage (R. H. Hansen 2013). This is beneficial when wind turbulence or grid loss are occurring (Rampen 2006).

- Using a variable displacement motor, the high-speed shaft speed can be maintained constant and a synchronous generator can be utilised. Theoretically, this omits the need for a frequency converter and transformer. (Roemer 2014)

To benefit from the presented advantages multiple attempts to successfully design a FPT based drivetrain have in the recent years been conducted. The company ChapDrive AS has developed a FPT based drivetrain for a 900kW WT. It consisted of a Hägglunds

fixed displacements pump and two Bosch Rexroth variable displacement motors. The motors were located at the tower base together with a synchronous generator. The WT was fully operational for a three year period before the company closed down, and no data with respect to reliability or efficiency has been presented. (Chapple et al. 2012)

Another recent attempt is described by Schmitz et al. (2013). It concerns a research project from *Institut fur angewandtes Stoffstrommanagement*, where a FPT based drivetrain is designed for a 1 MW WT. The design of the FPT drivetrain seen in figure A.6 employs two low speed fixed displacement pumps connected in parallel and four hydraulic displacement motors. For details see appendix A.3.

1.3.3 Disadvantages of Fluid Power Transmissions in Wind Turbines

A general issue with conventional fluid power machines is that they only exhibit high efficiencies at full load, since the mechanical losses in conventional fluid power pumps and motors do not scale down with reduced power output. This is a concern in FPT based drivetrains for WTs, which are often operated at partial load. The efficiency of FPT based drivetrains have been studied in appendix A.4 and the findings show an overall efficiency spanning between 50 % and 80 % when the majority of the operating range in considered, the phenomena illustrated by figure 1.6. Such low efficiencies is insufficient compared to the efficiencies of conventional WT drivetrains, which are typically above 90 % in the majority of its operating range (for elaboration see appendix A.2). Thus it must be concluded that the relatively poor efficiency at partial load makes conventional FPT based drivetrains a poor alternative for many application including WTs.
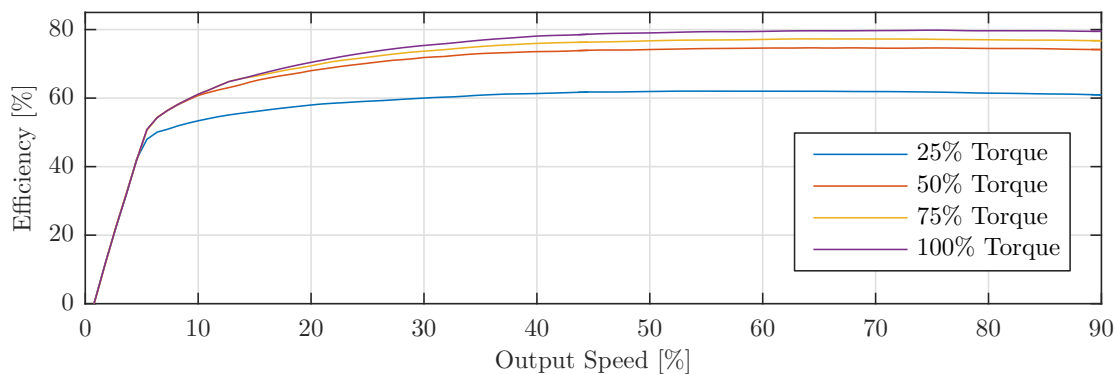
Fig. 1.6: Overall efficiency as a function of output speed and torque for a typical commercial available FPT. (Rampen 2006)

In order to make FPTs more competitive, the recent years research have been concerning the utilisation of hydraulic digital displacement machines (DDMs), which have shown to exhibit attractive efficiencies. The next section thus concerns the study of digital fluid power transmission (DFPT), and aims to determine if this technology can give FPT the competitive edge needed to emerge into the wind industry market.

1.4 Digital Fluid Power Transmission

The difference between conventional variable displacement machines and digital displacement machines is that DDMs utilises independently manipulated valves to control each pressure chamber. A digital hydraulic machine is characterised by its use of on/off valves in contrast to conventional servo valves, swashplates or vanes. DDMs often consist of several pressure chambers, which can be individually controlled to either execute a pumping, idling or motoring operation. During partial load of a DDM, selected pressure chambers can be controlled to idle causing the chamber not to be pressurised, which leads to improved efficiency during partial load operations compared to conventional variable displacement machines. This is the primary reason why DDMs exhibits a superior efficiency over conventional variable displacement machines. A study of the typical efficiency of DDMs can be found in appendix A.4, whereas this section will continue with a description of the DDM's general design, operating principle and usage.

1.4.1 General Digital Displacement Machine Design

A pressure chamber in a DDM is operated by the use of two independently controlled on/off (digital) valves. Depending on how these valves are controlled three distinct operation modes, defined as idling, pumping and motoring, can be achieved. The pressure chamber in a DDM can be depicted as seen in figure 1.7.
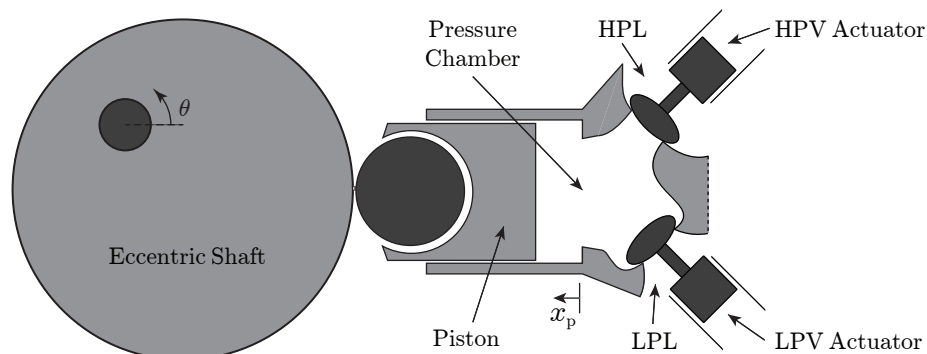
Fig. 1.7: The pressure chamber in a DDM including eccentric shaft and valve configuration. The depicted seat valves are controlled actively by the use of electromagnetic actuators and passively by pressure differentials.

As figure 1.7 depicts, the stroke of the piston is a direct result of the rotation of the eccentric shaft. The figure furthermore shoes two leakage-free seat valves connected to the LPL and HPL respectively. The acronyms LPV and HPV defines the low pressure and high pressure valves, respectively. By controlling the operation of the valves in accordance to the piston stroke, opening and closing of the valve against high pressure forces can be avoided (Rampen et al. 1995). As a result each valve can be directly controlled by what can be considered as a relative weak electromagnetic actuator. These types of digital valves, which exhibit no leakage and low power consumption are a fundamental component in digital displacement technology, and a core element in achieving high

efficiencies. (Rampen et al. 1995; Roemer 2014)

Different types of DDM designs exist, where figure 1.8 displays the sectional view of two commonly used DDM designs utilised in WT DFPT based drivetrains proposed by recent state of the art literature (Carroll et al. 2014; Kameda et al. 2014; Rampen 2006; Sasaki et al. 2014). The left side of figure 1.8 depicts a cam ring type design, which is ideal for the design of the digital displacement (DD) pump in a DFPT, since it offers high displacement at low rotational speed due to its many pressure chamber activations per revolution. The right side of figure 1.8 depicts a Calzoni type design, with tilting cylinders. This design only offers high displacement at high rotational speed due to relative small amount of chamber activations per revolution, which is why this design often is proposed as the DD motor in a DFPT. Common for both designs is that the pressure chambers are radially distributed at the circumference around the rotational shaft. This allows for external positioning of the valve actuators and high and low pressure manifolds.

Cam Ring Type DD Machine   Calzoni Type DD Machine
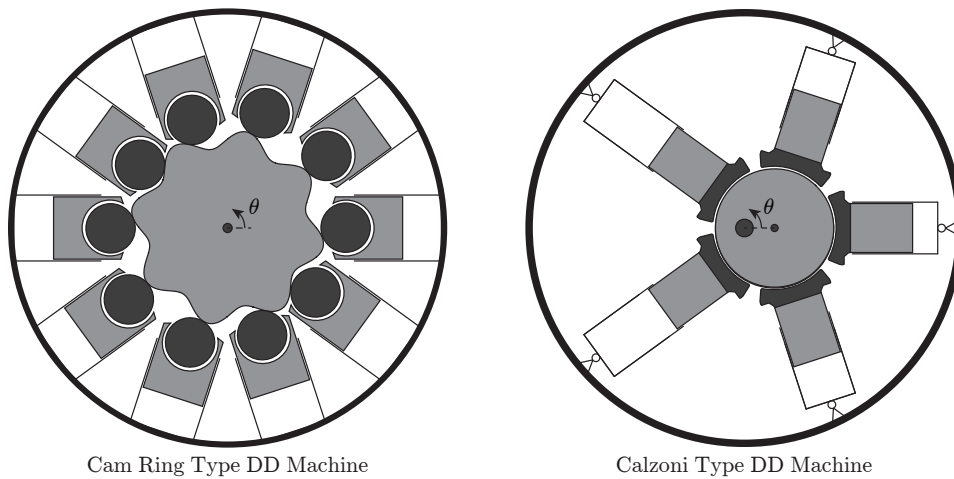
Fig. 1.8: Sectional view of two possible DDM designs. To the left a cam ring type design and to the right a Calzoni type design. For simplicity the valves and pressure lines have been omitted. Designs inspired by Johansen (2014) and Kameda et al. (2014).

The design of a DDM is often constructed from several modules, where the sectional view in figure 1.8 could represents one module. The power rating of DD machines thus depends on the number of modules, number of chambers per module and the size of each pressure chamber. A more detailed description of the cam ring and Calzoni type design is presented in appendix C, where the sizing of this report's DFPT based drivetrainss is also presented.

1.4.2   Operating Principle of Digital Displacement Machines

A variable DDM is defined by how its pressure chambers are operated, and generally speaking two distinct operation schemes exist, namely partial and full stroke operation. In full stroke operation, a change in operation mode to pumping, motoring or idling, can only occur at specific piston positions, whereas in partial stroke, the operation can be

changed independently of the piston position. The full stroke operation is considered the simplest, but it has the drawback that the DDM only can obtain a discrete displacement resolution, corresponding to the size of its pressure chambers. In this report only full stroke operation is considered.

It is essential to understand the three distinctive operation modes of a DDM if an algorithm for controlling a DFPT based drivetrain must be developed. Thus the full stroke operation modes idling, pumping and motoring mode must be known and understood. To aid the description of each operation mode the characteristics of a DDM's pressure chamber is visualised by figure 1.9.
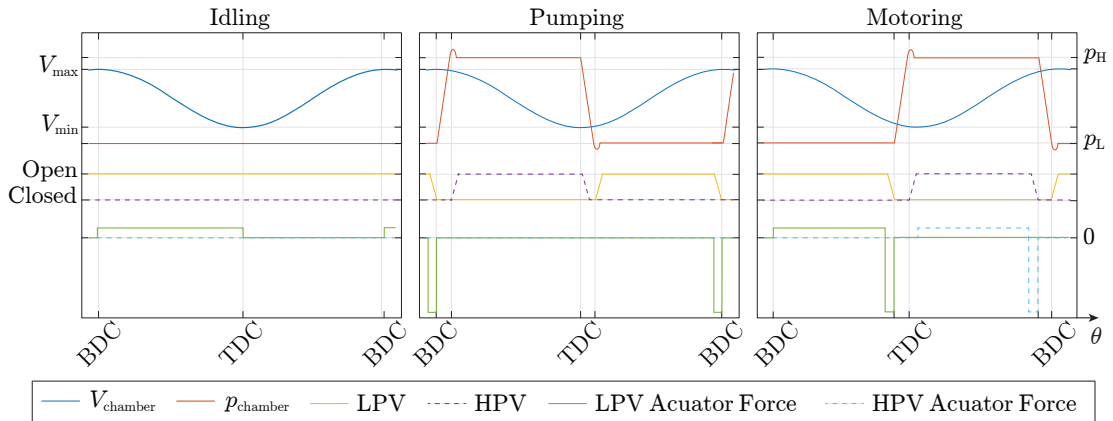
Fig. 1.9: The characteristics of a DDM's pressure chamber during the operation modes of idling, pumping and motoring. The illustration is based on a full stroke operation, where one operation mode is maintained for one cycle.

Idling: The idling mode operation is the simplest of the three different modes. It is achieved by having the LPV open during an entire cycle. During the piston movement from bottom dead center (BDC) to the top dead center (TDC) a small actuator force is required to maintain the LPV open due to opposing flow forces. From TDC to BDC the flow from the LPL and into the chamber ensures that no actuator force is required to maintain the LPV open. During the entire cycle no fluid is pressurised and no effective fluid displacement occurs.

Pumping: The characteristics of the pumping operation mode is shown in the middle of figure 1.9. At the instant where the piston is at the BDC both valves are closed. As the piston moves from the BDC and towards the TDC, the fluid in the chamber is pressurised. While the increasing pressure forces will maintain the LPV closed, the HPV will passively open as the chamber pressure exceeds the pressure in the HPL, p_H. In turn fluid will be displaced from the chamber and into the HPL.

When the piston reaches the TDC the HPV is closed, which can be done both actively or passively (as depicted in figure 1.9) depending on machine topology (Roemer 2014). Following a positive change in chamber volume as the piston moves towards BDC the fluid in the chamber is depressurised until the LPV will passively open. Fluid is then withdrawn from the LPL until the LPV is actively

closed near the BDC and the cycle is repeated.

Motoring: The motoring operation mode is the only mode that requires active closing of both the HPV and LPV. In motoring mode fluid is displaced from the HPL and into the chamber as the piston moves from TDC to BDC. During this time period a small actuator force is required to maintain the HPV open due to the flow forces acting on the valve.

As the piston approaches the BDC the HPV is actively closed. This results in the chamber fluid being depressurised which in turn passively opens the LPV. As the LPV is open during the piston movement from BDC towards TDC, the chamber fluid is displaced into the LPL. In this time period a small actuator force is required to maintain the LPV open as it is the case for the idling mode.

Near the TDC the LPV is actively closed, which causes the chamber pressure to increase (assuming sufficient kinetic energy is stored in the eccentric shaft) and in turn passively opens the HPV, which ends the motoring cycle. It should be noted that if the HPV is passively opened, the motoring operation mode is not available at zero rotational velocity of the eccentric shaft. This could be avoided by choosing a valve design, which includes the option of actively opening the valve.

The construction of a DDM includes multiple pressure chambers. Individually choosing the operation mode of each chamber enables high displacement control bandwidth, assuming a high displacement frequency. The result is a DDM which can approximate a continuous variable displacement.

Some considerations can be made with regards to efficiency and the distinctive operation modes of a DDM. These are listed below:

- Choosing a radial piston based design of the DDM gives the option of placing the valves at the outer circumference (similar to what is depicted in figure 1.7), which leads to physical space for relatively large valve opening areas. This would result in small flow losses in all operation modes. (Rampen et al. 1995)

- By timing the opening and closing of the valves in accordance with the movements of the piston, the electromagnetic actuators of the valves do not have to overcome any large pressure forces. Hence small and compact actuators with little power consumption may be utilised in the valve design. (Roemer 2014)

- The presented operations modes utilise passive openings of the valves, which means the pressure in the chamber and manifold (HPL or LPL) are equal, why throttling loses due to pressure equalisation can be avoided. (Roemer 2014)

- In order to achieve energy efficient operation modes, the timing of the valve movements are essential. The following should thus be true:

  - In pumping mode, the LPV should be fully closed at exactly BDC. If the valve is closed early the fluid in the chamber is depressurised to unwanted levels and cavitation might occur. Furthermore the required pressurisation needed to passively open the HPV will require more time. Alternatively if

the valve is closed later, fluid displacement into the LPL will occur and the effective displacement to the HPL will be reduced.

– In motoring mode the closing of the LPV should be timed so that the HPV (passively opened) is fully open at exactly TDC. If the LPV is closed early, fluid is displaced into the HPL. Alternatively a late closing will eliminate the option of passively opening the HPV (since depressurisation starts directly after the piston reaches TDC).

- Closing forces and opening holding forces are required for both valves' actuator systems (see figure 1.9). To improve efficiency, holding forces may be achieved by passive components such as springs or permanent magnets. Furthermore, utilisation of passive components might lead to a simpler and cheaper valve design.

- Providing a passive opening holding force in the LPV would result in no power consumption in the actuator system during the idling operation mode. (Roemer 2014)

- Passively opening the valves by pressurising or depressurising the chamber (as seen in figure 1.9) leads to a diminished effective fluid displacement in comparison to the ideal displacement. This is especially evident in pressure chambers with large dead volumes.

Having acquired an understanding of the benefits and general operating principles of DDMs, the focus changes to investigate how such machines can be utilised to create a DFPT based drivetrain.

1.4.3   Utilisation of Digital Displacement Machines

One example of a DFPT for a WT is developed by the company Mitsubishi Heavy Industries (MHI) and Artemis Intelligent Power (AIP). They have together developed a DPFT prototype for a 7 MW offshore WT. The FPT design consists of a 7 MW variable displacement DD pump and two 3.5 MW variable displacement DD motors. Each motor is connected to a synchronous generator with a rated output of 4.2 MW. A picture of the prototype is shown in figure 1.10. The prototype drivetrain has been installed in an offshore WT named SeaAngel. No operational data of the WT has been available, why it is difficult to evaluate the true potential of the DFPT based drivetrain designed by MHI and AIP. (Roemer 2014; Sasaki et al. 2014)

Currently there does not exist any DFPT commercially available for utilisation in WTs. MHI and AIP are considered to be the pioneers with regards to developing the first commercial available DFPT, but no deadline seem to reflect when this will be realised.

The study and developments of DFPT based drivetrains for WTs is not only limited to the big companies within the wind industry, but during most recent years several research projects have been conducted by universities world wide (see Carroll et al. (2014), Rampen (2006), and Roemer (2014)). One of these research projects is the danish HyDrive project, which concerns FPT based drivetrains for renewable energy applications (Aalborg University 2016). This project studies many different aspects of

Variable DD Pump of 7 MW

4.2 MW
Synchronous Generator

3.5 MW Variable DD Motor
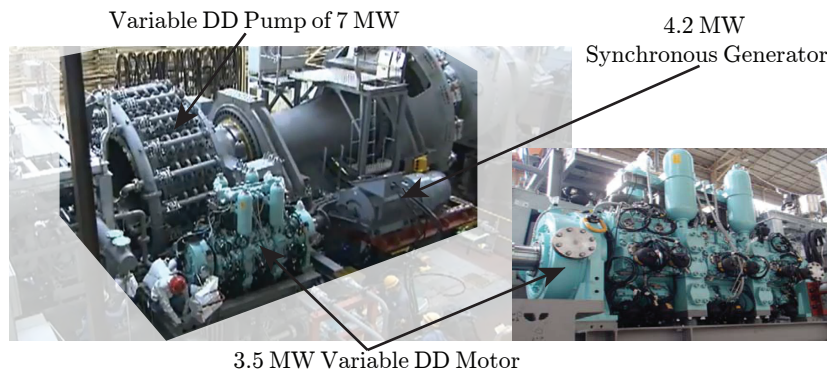
Fig. 1.10: DFPT based drivetrain for a 7 MW WT designed by MHI and AIP. (Roemer 2014; Sasaki et al. 2014)

DFPTs such as dynamic modeling, design optimisation at component level, efficiency improvements, failure diagnostics and development of control algorithms. All of these studies could have an important impact on the design and development of future DFPT based drivetrains.

A big part of implementing DFPT in WTs is dimensioning of the components used to comprise the DFPT based drivetrain and the development of applicable control strategies. This task of dimensioning the drivetrain greatly depends on the size of the WT, whether it is onshore or offshore and sometimes on the specific geographical location. Whereas the development of applicable control strategies for DFPT based drivetrains in WTs could be considered as a more uniform task, which to some extent is independent on the size and location of the WT. The development of applicable control strategies is an important task, which has to be solved before DFPT based drivetrains can gain success within the wind industry. The next section will consider the challenges which have to be considered when applicable control strategies for a DFPT based drivetrain must be developed and tries to summarise the research done within this area.

1.5   Control of a Digital Fluid Power Transmission

The challenge of developing a applicable control approach for a DFPT can be addressed in various ways. If a DFPT system had been available as a physical test stand, a practical approach might be utilised, however, it often comes with the cost of stability uncertainties. To overcome this issue, a theoretical approach, where the stability of the system can be evaluated, is deemed a more suitable choice. The challenge of developing an applicable control approach for the DFPT is thus viewed as a theoretical model based control problem.

Literature describing a model based control approauch for DFPT in a WT is close to non-existing. The company MHI have applied multiple control strategies during the development of the DFPT based drivetrain presented in Sasaki et al. (2014) and Tsutsumi et al. (2012). However, no test results for these strategies have been published. Expan-

ding the scope to investigate what methods have been utilised to control DDMs, several studies can be found (see Armstrong and Qinghui (2006), Ehsan et al. (1997), Heikkila (2013), and Sniegucki et al. (2013)). These studies propose how torque, pressure, flow and speed control approaches of a DDM can be developed using e.g. open loop control or precalculated activation sequences. Common for all of them is that the DDMs were operated under fixed speed or simplified load conditions. As a result, the proposed strategies are not directly applicable for DFPTs in WTs. Furthermore, none of these presented studies employ model based feedback controller design.

Two papers which studies the topic of model based feedback control for DFPT based drivetrains in WTs have been found, which include Pedersen et al. (2016a,b). These papers takes their starting point in a variable speed and variable pitch 5 MW WT from the National Renewable Energy Laboratory (NREL) where the conventional drivetrain has been replaced with a DFPT based drivetrain. The papers present a dynamic model of the entire drivetrain, which consists of a fixed DD pump, a variable DD motor (operated at fixed speed) and a synchronous generator connected directly to the grid.

A reason for the limited literature available within the area of DFPT based drivetrains, is partly because it is a relatively new topic of study and due to its challenging nature. Control of a conventional FPT has been well established throughout literature (Lennevi 1993; Rajabhandharaks 2014), which indicates that the challenging nature of the DFPT is the result of utilisation of DDMs. The next sections will thus present the challenges arising from including DDMs in a FPT.

Input and Output of a WT's DFPT:
Prior to model based control can be developed, the DFPT based drivetrain's input and output relations must be mathematically described (viewed as the control model in figure 1.11). Depending on the type of control desired to be utilised, linear or non-linear, the mathematical system representation must be made accordingly. In this thesis the study will concern the application of linear control theory. However, before a linear representation of the system can be developed, the DFPT based drivetrain's input and output must be considered.
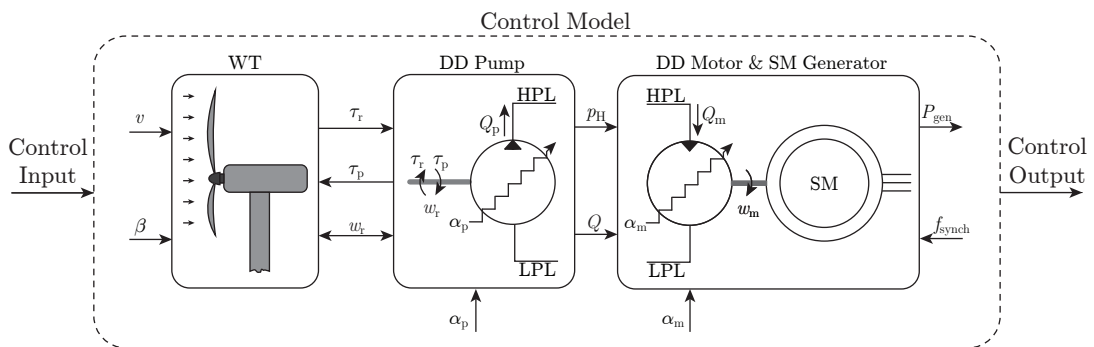
Fig. 1.11: The DFPT based drivetrain (Control Model) when represented as part of a model based control problem.

To determine an appropriate output of the DFPT based drivetrain (labeled *Control Model* in figure 1.11) the overall control objective for a modern utility-scale WT must be studied. Studies regarding this, which are elaborated upon in appendix B, determines the overall control objective to be maximum power production of the WT. Depending on the wind speed, maximum power production is achieved by either solely controlling the reactive torque acting on the turbine rotor shaft or in combination with controlling the WT's blade pitch angle. Considering control of the WT's blade pitch angle as a separate control problem, the desired control output of the DFPT based drivetrain is the reactive pump torque, τ_p, corresponding to controlling the torque acting on the rotor shaft.

The input to the DFPT based drivetrain depends on the DDMs used to comprise the DFPT. Choosing a combination of one fixed and one variable DDM, e.g. fixed DD pump and variable DD motor, will yield one control input being the motor displacement, α_m. This will result in a single-input single-output (SISO) control model as illustrated in the left part of figure 1.12. Alternatively, the DFPT based drivetrain could be comprised of two variable DDMs as depicted in figure 1.11. This will yield two control inputs being the displacement of both the pump and motor, α_p and α_m, respectively. This furthermore allows for a secondary control output. For instance choosing the pressure difference between the HPL and LPL, Δp, as the secondary control output could maximise the efficiency of the DDMs in accordance with appendix A.4. The utilisation of two variable DDMs results in a multiple-input multiple-output (MIMO) control model as illustrated in the right part of figure 1.12.
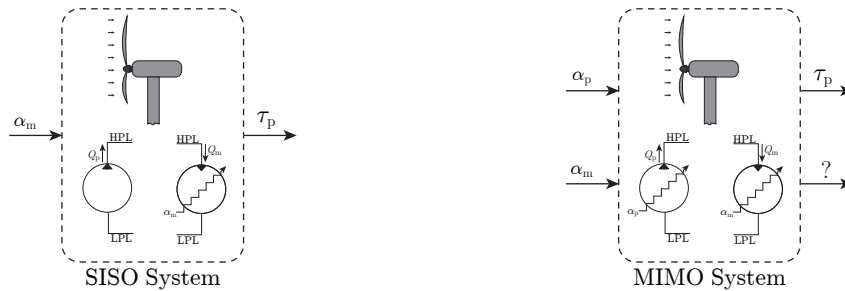
Fig. 1.12: To the left a SISO representation of the DFPT based drivetrain utilising a fixed DD pump and a variable DD motor. Input being the motor displacement, α_m, and output being the reactive pump torque, τ_p. To the right a MIMO representation of the DFPT based drivetrain utilising a variable DD pump and DD motor. Inputs being the pump and motor displacements, α_p and α_m. Outputs being the reactive pump torque, τ_p, and an additional output freely chosen depending on secondary control objective.

When a model based control approach is to be developed for a DFPT based drivetrain, the system can be seen as both a SISO control problem or MIMO control problem depending on the DDMs utilised in the drivetrain. Other combinations of DDMs, than the two examples in figure 1.12, could also be used to comprise a DFPT based drivetrain. However, in the next section these two examples suffices to illustrate how the control challenges differs depending on viewing the DFPT as a SISO or MIMO control problem.

1.5.1 Control Challenges and State of the Art Control Approaches

The control challenges discussed in this section could essentially be viewed as one large challenge, namely how to develop a control model appropriate for utilisation of model based controller design and stability analysis. The subchallenges related to this are far from trivial, and extensive knowledge on how a DDM is operated must be attained in order understand the fundamental issues behind these challenges and how to potentially solve them. As all later chapters in this thesis evolve around these challenges it is fundamental for the reader to have good understanding of what these challenges contains. This section aims to provide that by dividing the overall challenge of developing a control model, into three subchallenges.

As the three challenges described next all originates from the discrete activations of a DD machine's pressure chamber, an explanatory figure 1.13 have been made to aid the understanding of the three challenges. The figure depicts the activation sequence of a DDM operated at fixed speed and variable speed respectively. The sequence is not only shown in the spatial-domain (angle-domain), but also in the time-domain since mathematical models often are derived here.
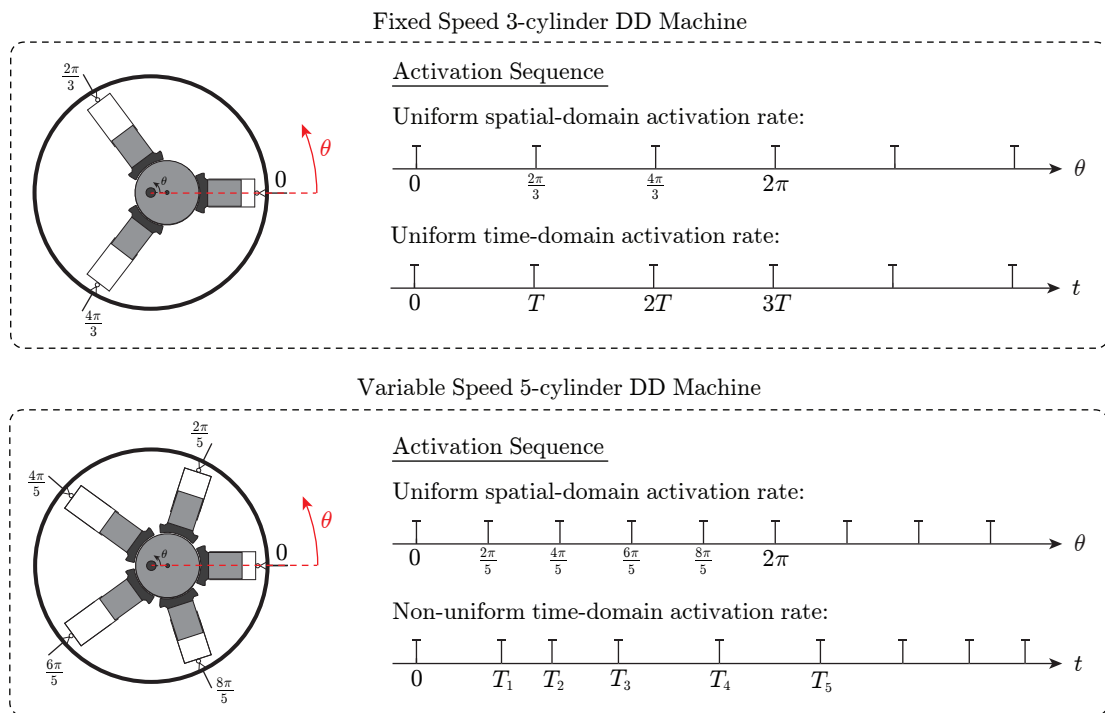
Fig. 1.13: Explanatory figure depicting the activation sequence of a fixed speed and a variable speed DDM. The top part depicts a 3-cylinder DDM operated at fixed speed and is intended to represent the motor in a DFPT. The bottom part depicts a 5-cylinder DDM with variable speed, which resembles the characteristics of the pump in a DFPT. The activation sequences for pump and motor are presented in both the spatial- (angle-) and time-domain.

Challenge I - DD Machine Modelling:

When applying a model based control approach, the first challenge arises in mathematically representing the true dynamics of the DDMs used to comprise the DFPT. This is further complicated as the model, which must be developed, has to be linear to utilise linear control theory. To develop such a model it is vital to understand the operating principles of full stroke operation of the DDMs. In essence, how the pressure chamber activations (initiation of pumping, motoring or idling) in the DDM can only be initiated at discrete instants, corresponding to specific piston positions (the full stroke operating principle is described in section 1.4). This is illustrated in figure 1.13.

The control challenges of the SISO system presented in figure 1.12 can be considered under the assumption, that the DD motor, connected to a synchronous generator, is operated at a fixed speed corresponding to the grid frequency. In this case, the time between chamber activations will be constant (as depicted in the top part of figure 1.13), which allows for a discrete control with constant sampling period in the time-domain. The challenge thus remains, how to develop a linear model of a DDM with a constant pressure chamber activation rate.

Control Approach Addressing Challenge I:

To overcome control challenge I, Pedersen et al. (2016a) proposes a discrete state space model representation of a SISO controlled DFPT. The state space model includes the dynamics of a fixed displacement pump, a variable DD motor, pressure lines and turbine dynamics, where the sampling period is chosen to be the time between successive chamber activations in the fixed speed DD motor.

A discrete representation of the DD motor dynamics is based upon a convolution sum model of shifted impulse responses of the motor flow, which initially was proposed by Johansen et al. (2016). To give the reader a general idea how a sum of shifted impulse responses can be used to describe the flow of a variable DDM figure 1.14 has been made.
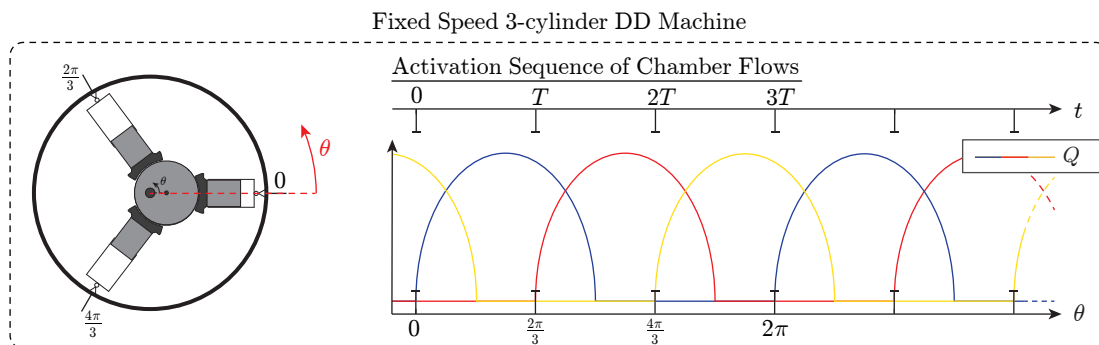
Fig. 1.14: Activation sequence of chamber flows for a variable DD machine. Chamber flows being continuous and activation sequence being discrete.

The figure depicts the flow of each successive pressure chamber in a 3-cylinder DDM. At time zero the first pressure chamber is activated, resulting in a continuous displacement

of fluid seen as the blue graph. In the next 3 time periods (or 2π) the flow from this pressure chamber cannot be changed, and thus activating a pressure chamber can be represented as an impulse response. As a DDM consists of several pressure chambers, activated at different positions, the accumulated chamber flows (the sum of the blue, red and yellow graphs) can be represented as a sum of shifted impulse responses. A more detailed explanation of the concept is presented in section 5.2.2 or in Johansen et al. (2016).

Combining the convolution sum model of shifted impulse responses with a discrete approximation of the continuous dynamics of the pressure lines, DD pump and turbine, a control model can be formed, which can used for controller design and stability analysis.

Challenge II - Non-uniform Activation Sequence:
The utilisation of variable DD pump in a WT's DFPT arises a second challenge. The DD pump is attached directly to the rotor shaft, and thus has a varying speed, why a non-uniform activation sequence of the pump's pressure chamber exist. The scenario is depicted in the bottom part of figure 1.13.

Without a constant activation rate a static linear model representation of the DD machine is not possible. Furthermore, a non-uniform activation sequence does not allow for the use of convolution sum model representation of the DD pump. However, if the activation of pressure chambers are described in the spatial-domain, a uniform activation rate can be achieved (scenario depicted in figure 1.13), hereby allowing for the utilisation of the convolution sum model. The challenge thus remaining, is how to develop a mathematical representation of the DFPT's dynamics in the spatial-domain contrary to the time-domain.

Control Approach Addressing Challenge II:
To the authors' knowledge no published literature exists, which studies the MIMO control approach of a DFPT, and thus the scenario of making a control model including a DDM with varying speed. Partly due to this, a 3rd-semester M.Sc. project (see Junker et al. (2016)) dealing with this topic was conducted prior to this master's thesis by the authors. This 3rd-semester project originated from the work done by Johansen et al. (2016) and Pedersen et al. (2016a), and sought to extend the discrete model approximation of a DDM made by Pedersen et al. (2016a) to accommodate varying rotational speeds. Hereby making the discrete model approximation applicable for describing the dynamics of a variable DD pump in a DFPT.

To overcome the issue of a non-uniform sampling period, Junker et al. (2016) continued the work done by Pedersen et al. (2016a). This included utilising event driven control theory, initially proposed by Heemels et al. (1999), to transform the mathematical expression relating to the dynamics of the DD pump from the time-domain to the spatial-domain. In the spatial-domain a discrete model approximation of the DD pump can be derived with a constant sampling rate, corresponding to the rotational angle between activation of subsequent pressure chambers. Combining this modelling approach with linear control has shown to be sufficient for rotational speeds varying within a relative limited operating range, as it is the case for WT's rotor.

The theory of event-driven control is not elaborated upon in this section, but is in section 5.2.3 applied to transform time-domain equations into the spatial-domain. Additional literature of event-driven control includes Heemels et al. (1999) and Junker et al. (2016).

Challenge III - Multirate Activation Sequences:
The approaches for solving challenge I and II generates challenge III, which is how to combine the discrete models of two DDMs. The approauch presented for addressing challenge I was to develop a discrete model of the DD motor in a DFPT using a constant sampling time corresponding to the time between subsequent chamber activations. Challenge II was addressed by transforming the mathematical equations used to describe the DD pump to the spatial-domain by use of event driven control theory. The new challenge arises when the discrete models of the motor and pump must be combined.

To allow for a combined model, the fist step is to transform the model of the DD motor to the spatial-domain, which does not pose additional challenges since the activation sequence will remain uniform as depicted in figure 1.13. However, inspecting the activation sequences in the spatial-domain for the DD pump and motor depicted in figure 1.13 it becomes evident that the machines have different activation rates. Hereby creating the need for a multirate control model if the convolution sum model of the DD motor and pump must be combined, as it is the case if the DFPT must be seen as a MIMO system. Thus the essence of challenge III, is how to develop a linear MIMO representation of the DFPT's dynamics which accommodates the different activation rates of the DD pump and motor.

Control Approach Addressing Challenge III:
To the authors' knowledge there has not been presented any literature excluding Junker et al. (2016), which directly deals with the MIMO control of a DFPT, and thus no approaches for developing a multirate model of a DFPT have been found.

Even though the 3rd-semester M.Sc. project, Junker et al. (2016), developed a MIMO control approach of a DFPT, it did not present a method for making a combined linear model of the entire DFPT based drivetrain. Instead a decentralised control approach was proposed, allowing for two separate models of the DD pump and motor. The result was a control strategy where the DD pump was controlled in the spatial-domain and the DD motor in the time-domain. Hereby neglecting their mutual cross couplings and thus also limiting the ability for stability analysis. Nonetheless the presented control strategy shows stable control performance. Herewith supporting the choice a utilising event driven control in combination with discrete model approximations of the DDMs as a method for controlling a DFPT.

Ending Remarks on Control of DFPT's:
This concludes the description of DFPT control challenges and the state of the art control approaches to address these. However, none of the presented approaches have established a MIMO model based control approach, which allows for the use of conventional linear analysis and control tools. What the presented control approaches have failed to address, is a method for a combined control model of both DD pump and motor, which accom-

modates multiple activation rates of the DD machines' pressure chambers. Based on the knowledge presented it is assessed that additional control theory must be introduced to solve the challenges related to multiple activation rates. An area of control theory which is considered most likely to hold the key to solving these challenges is multirate control, which thus has become a topic of interest for the remainder of this thesis.

1.6 Introduction to Multirate Control

This section presents the multirate control problem, while also offering a historical perspective on the need for multirate techniques. The multirate problem is generally defined by considering the sampling operations as time propagates with the aim of forming a common basis for discussion.

1.6.1 Computer Controlled Systems

Modern control systems often implement various control functionalities, such as reference commands or sensor feedback, by use of computers or embedded micro-controllers. Many reasons for the rise of digitally controlled systems exist and amongst others the possibilities for implementing various control laws and high accuracy, repeatability and reliability of digital controllers are highly desirable characteristics. Suffice to say, the reasons for using digital control are numerous and well covered in literature (Amit 1980; Åström and Wittenmark 1984; Franklin and Powell 1981; Ogata 1987) and their high applicability is proven by their near unanimous implementation in modern control systems.

The use of digital controllers necessitates quantization of continuous-time signals by sampling them for computer processing of control commands, and subsequent signal holding (by a zero-order hold (ZOH)[1]) until a new command is computed. The process of digital control applied to an analog plant is illustrated in figure 1.15.
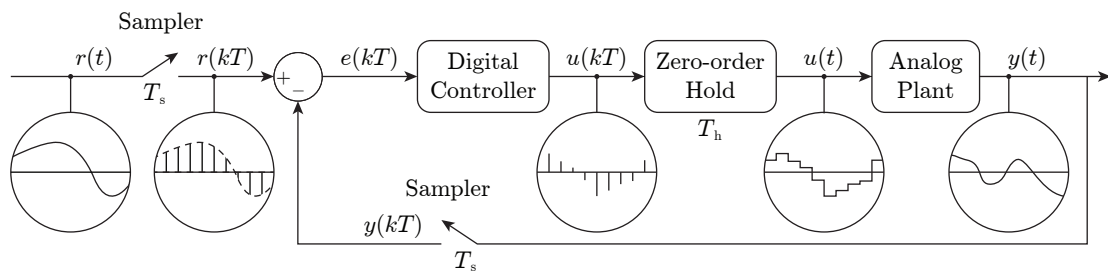
Fig. 1.15: Closed loop computer controlled analog plant. Signals at various points in the control process are illustrated.

Conventional computer controlled systems typically perform the Analog to Digital (A/D) and Digital to Analog (D/A) operations synchronously at a single uniform rate ($T_s = T_h$ = constant). Techniques for analysis and controller design for such systems have been

---

[1]Higher orders of hold are also possible, but the work presented here is limited to the commonly used zero-order hold.

mature and well developed since the 1980s and many textbooks regarding the topic have been published (Åström and Wittenmark 1984; Franklin and Powell 1981; Ogata 1987).

Single rate analysis and design adequately describe many systems, but for some systems, such as those with both fast and slow modes, or with multiple transducers with different bandwidths, the conventional techniques may not be applicable. This is where systems incorporating multiple sampling and control rates start to become an interesting topic.

1.6.2 Historical Perspective on Multirate Systems

Historically, multirate analysis was developed in the 1950s as a to analyse the intersample behaviour of signals and states of conventional single rate systems. These frequency domain (transfer function based) methods were developed by introducing a fictive "phantom sampler" operating at some integer multiple of the single rate system. A more in-depth review of these frequency domain methods is available in Amit (1980) and Glasson (1983).

Following the early development of the frequency domain methods, Kalman and Bertram (1959) started the development of time-domain (state-space representations) methods for multirate systems. While the frequency domain methods were further developed to describe a number of different situations (e.g. slow input sampling with fast output sampling, vice versa and nested loops), the time-domain approach of Kalman and Bertram was left practically untouched until the 1970s, when the aerospace industry found use for Kalman and Bertram's previously unused method. (Amit 1980; Glasson 1983)

Motivated by practical implementation concerns, development of multirate methods was propelled by the aerospace industry. High-performance aircrafts are an example of systems, which include slow and fast modes, i.e. those associated with rigid body motion and structural vibration of the airframe, respectively, all of which must be controlled to maintain controlled flight. Limited by the computational power of period processors, meant that when transitioning from analog to digital flight computers, the flight control algorithms associated with slower modes had to be implemented with slower update rates to conserve limited computer memory. Specific examples of aircraft implementing multirate control systems include the McDonnell Douglas/Boeing Northrop F-18 and the former American space shuttle. (Amit 1980; Glasson 1983; Stengel and Berry 1977)

It may be argued that with the ever increasing processing power of even cheap microcontrollers, the need for multirate techniques is rapidly diminishing, as the sampling and control rates may simply be increased to a single common fast rate. However, such supersampling of the system signals and states can only alleviate the multirate problem when computational resources are plentiful and transducer bandwidth is not the limitation.

A hitherto undescribed situation that may benefit from multirate sampling are continuous (or discrete) systems with periodic and discrete actuation. The defining characteristic of such a system, is the fact that actuators can only be activated at specific (and periodic) time instants, and an example of such a system are the DDMs utilised in the DFPT. When combining multiple of such machines, a system with multiple different actuation rates is obtained. Thus the DFPT drivetrain with its discretely activated digital machines

represents a different class of systems, which may not simply be handled by single rate techniques (super-sampled or not).

The motivation for applying multirate techniques to this system is not, as previously, limited computational power. The motivation is now the need for a combined model structure, which can be utilised for system analysis using conventional linear control theory tools, such as the Relative Gain Array (RGA) and Singular Value Decomposition (SVD), and for controller design. To the best of the author's knowledge, no such combined model description, which is also suitable for system analysis and controller design, regarding this type of system has previously been developed.

1.6.3 Multirate Systems

To form a common basis for discussion of the multirate control problem, the definition of the multirate system according to Kalman and Bertram (1959) is presented. Subsequently an example is presented and commented upon.

Definition: A multirate system is a sampled-data system which includes no less than two quantization and hold elements. The multiple analog to digital and digital to analog operations occur with fixed intervals, but at least two have unequal intervals.

The definition of the multirate system differs from the conventional single rate sampled-data systems, where all sampling operations are performed synchronously and with a fixed period between successive samples.

A system which satisfies this definition is the multiple-input multiple-output system of figure 1.16. The analog plant contains both quickly and slowly varying signals. To accommodate the different time-scales of the system, multiple samplers operating at different, but fixed, rates are utilised. To generalise the problem, it is noted that the rate of the controller output and signal holding does not necessarily need to correspond with the sampling rates.
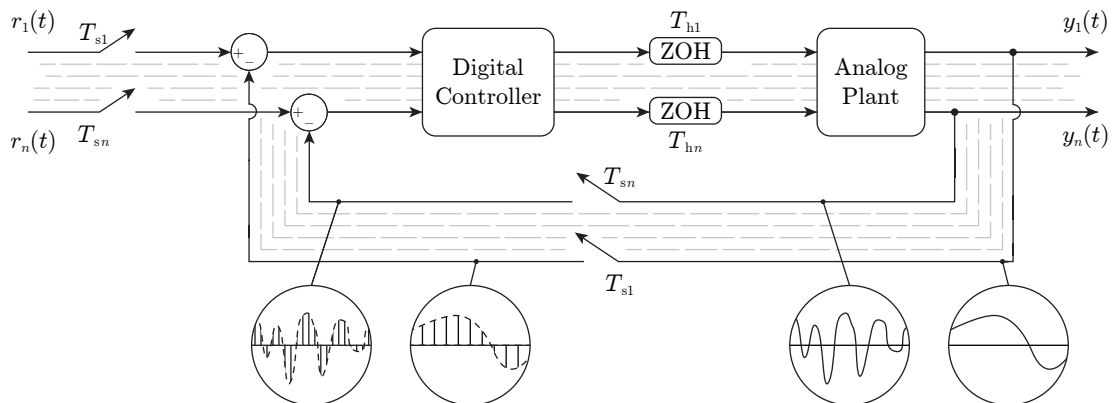
Fig. 1.16: Multirate control applied to system with different time-scales, inspired by Amit (1980).

Based on the example provided by Amit (1980), figure 1.17 illustrates a generalised multirate sampling scheme, which could have been used in conjunction with a system such as the one in figure 1.16. The sampling scheme contains three samplers all operating at fixed rates of $1/T_1$, $1/T_2$ and $1/T_3$, where T_i is some time unit. The second sampler is out of synchronisation by τ_2.
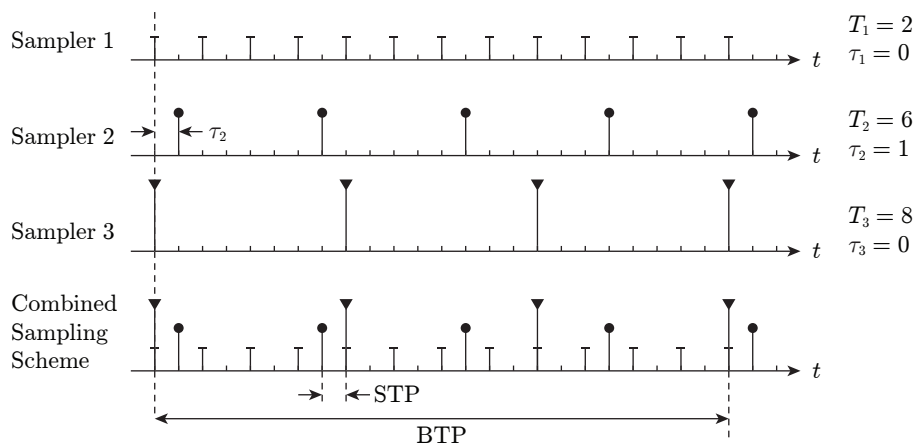
Fig. 1.17: Example of multirate sampling scheme, inspired by Amit (1980).

Some comments on the multirate system and the sampling operations which occur in it:

Remark 1.6.A: All sample and hold operations do not need to occur at different rates. The multirate definition is still satisfied when some, but not all, operations occur at the same rate.

Remark 1.6.B: The sampling operations do not need to be synchronised, such that a time instant exists where signals are sampled simultaneously. Desynchronised sampling are in many systems caused by delays. These delays are, however, often small enough to be neglible (Amit 1980). For the DFPT, delays in the sampling scheme can be avoided by appropriate choice of initial conditions, such that the actuation rates of the DDMs are synchronised.

Remark 1.6.C: With fixed sampling rates, the combined sampling scheme will always be periodic. This is readily observed by examining the bottom axis of figure 1.17, where the periodicity of the sampling scheme is given by the Basic Time Period (BTP). The BTP is the least common multiple of the different sampling periods, also denoted as T, and is defined as:

$$\text{BTP} = T \equiv \text{LCM}(T_1, T_2, T_3, \ldots, T_n, \tau_1, \tau_2, \tau_3, \ldots, \tau_n) \tag{1.1}$$

The basic time period can become unpractically large if the ratio of sampling periods is irrational (or practically so) (Kalman and Bertram 1959).

Remark 1.6.D: All sampling periods and delays in the sampling scheme can be expressed as integer multiples of the Short Time Period (STP). The STP is the greatest common divisor of the different sampling periods, also denoted as T_0, and is defined as:

$$\text{STP} = T_0 \equiv \text{GCD}(T_1, T_2, T_3, \ldots, T_n, \tau_1, \tau_2, \tau_3, \ldots, \tau_n) \qquad (1.2)$$

The short time period, similarly to the BTP, may become unpractically small if the ratio of sampling periods is irrational.

Remark 1.6.E: The analog plant can be linear or non-linear, although the common control theory tools for analysis are based on linear model representations, and a linear description would thus be preferable.

This concludes the introduction to the multirate control problem. Chapter 4 continues the investigation of the problem and how it may be handled, such that multirate modeling tools can be develop for the DFPT.

The next chapter in this report will clearly define the problem under investigation together with the chosen approach for attempting to derive a solution. Furthermore the general limitations of the work in this report are also presented.

Problem Statement

The Digital Fluid Power Transmission (DFPT) represents a class of systems, which are generally characterised by having continuous-time dynamics, and are actuated by multiple discrete-time actuators operating with different update rates.

In DFPT operation, control challenges arise from the digital displacement pump and motor. The displacement of such Digital Displacement machines (DDMs) can only be changed at specific shaft positions in full stroke operation. Modelling and control of a single fixed-speed DD machine, which exhibits uniform time steps between possible displacement changes, was in literature addressed by considering the linear impulse response of the machine. Similarly, variable-speed operation of a single DDM, which has a non-uniform time step between possible displacement changes, has been addressed by transforming the previously developed time-domain equations to the spatial-domain, where the angle between possible displacement updates is uniform. However, the challenge of operating multiple DDMs in a variable-speed and non-uniform setting still remains, and thus the problem which this thesis seeks to answer can be formulated as:

How can a multirate method be used to develop a linear time-invariant model of a utility-scale Wind Turbine Digital Fluid Power Transmission, such that conventional linear multiple-input multiple-output control and analysis tools can be applied?

The main underlying hypothesis of this statement is: given a linear time-invariant model on a conventional form (transfer function or state-space), then it is possible to apply the conventional well known and well documented tools linear control theory has to offer.

The motivation for answering the presented problem is that obtaining a linear multiple-input multiple-output DFPT model will allow the control engineer to evaluate stability and dynamic couplings of a DFPT such that appropriate control algorithms can be used.

2.1 Problem Solving Approach

A utility-scale Wind Turbine (WT) DFPT is considered a highly complex system, due to the discrete activation of a high number of pressure chambers which is a consequence of its multi-MW power rating. This high complexity of such a system makes it unsuitable for development of advanced multirate methods, why this thesis will make use of three dynamic systems to answer the above presented problem statement.

A linear double Mass Spring Damper (MSD) system, with well known dynamics, is introduced as a tool for developing a multirate method and investigating the applicability of conventional analysis and control design tools. Each mass in the system is defined to be discretely actuated at different rates and together with its coupled dynamics this resembles the main challenges with regard to modelling and control of a DFPT. Contrary to a DFPT, a MSD model does not have to address the difficult challenge of modelling

a DDM, why such a system is considered ideal for an accelerated evaluation of the properties of potential multirate methods.

In addition to the MSD system, two DFPTs are considered in this thesis, a 5.4 MW and a 10 kW DFPT. The 5.4 MW DFPT, shown in figure 2.1, represents a drivetrain for a utility-scale WT and its operation and parameters are based on the 5.4 MW drivetrain of the NREL reference WT. The transmission consists of two digital displacement machines acting as pump and motor, respectively. The pump is a low-speed high-displacement cam ring type machine and the motor is a high-speed low-displacement Calzoni type machine. By connecting them to shared high and low pressure lines, the transmission is formed. The functional principle of the digital fluid power transmission is exactly the same as described in section 1.3.1, and will therefore not be repeated here.
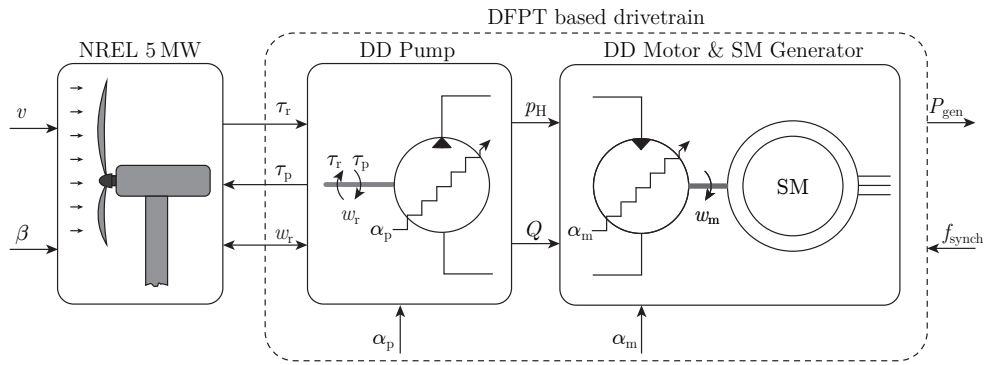
Fig. 2.1: Simplified diagram of this thesis' 5.4 MW DFPT including its inputs and subsystems.

As discussed in section 1.5, the inputs are defined as being the variable displacement of the two machines, α_p and α_m. Both of these inputs are in fact discrete binary sequences, which determines whether the displacement is increased or decreased in the DDM. To have non-binary inputs to the system, a $\Delta\Sigma$-modulator is placed at the input of each DDM (not illustrated in figure 2.1). Limiting the project to considering square systems, two outputs can be chosen where one of these should be the reactive pump torque, τ_p, as previously described. The second output is chosen as the pressure difference between the shared pressure lines, Δp, as the highest efficiency of the DDMs is obtained when operated at their rated pressure.

The high power rating of the 5.4 MW DFPT necessitates a large number of pressure chambers in the transmission (100 for the pump and 42 for the motor). Although all the chambers are identical, and thus modelling more than one chamber is relatively trivial, describing the timing of the chambers relative to each other is complex and quite cumbersome. For this reason, it has been decided to introduce a downscaled and purely fictional version of the 5.4 MW DFPT, where the power rating and number of pressure chambers is reduced to 10 kW with 1 and 3 pressure chambers for the pump and motor, respectively. The same governing equations describe both transmissions, and thus downscaling is only a question of changing a number of constants.

The purpose of 10 kW DFPT is to serve as a qualified platform for efficient evaluation of

the derived multirate methods applicability towards DFPT systems. Here the underlying hypothesis is, that a multirate model successfully applied to the downscaled DFPT, also can be expanded to the full rating 5.4 MW DFPT. It is therefore considered sufficient to apply conventional analysis and control design tools on a multirate model derived for the 10 kW DFPT in order to answer this thesis' problem statement.

The 5.4 MW DFPT will serve as a reference system throughout this thesis and all decisions, whether it be in regard to multirate modelling, controller design or other topics, will be made with the applicability on the 5.4 MW DFPT in mind. As a result this DFPT will be a key point in discussions and conclusions made throughout this thesis.

2.2   Methodology

The topic of multirate modelling and control of a DFPT is to the authors' knowledge a hitherto unconsidered topic, and the work presented in thesis is therefore on a research stage. As such, the following chapters are not limited to presenting the answers to the problem statement, but also seeks to elaborate upon the experience gained within the research process. An outline of the methodical approach to the research process is presented in figure 2.2.

The methodical procedure is elaborated upon in the following:

Chp. 1 - Introduction: Initial background research regarding DFPTs in wind turbines and the control thereof. Control challenges and state of the art for overcoming these challenges are defined. The purpose of this chapter is to introduce the reader to the control problem, and form a common basis for the work presented in later chapters.

Chp. 2 - Problem Statement: The system and associated challenges under consideration is clearly defined together with the overall limitations of the presented work.

Chp. 3 - System Modeling: The governing equations for the Digital Fluid Power Transmission are derived, and models for both the downscaled 10 kW DFPT and full 5.4 MW DFPT are implemented in Simulink.

Chp. 4 - Multirate Methods for Model Synthesis: A literature study is conducted to find viable methods for describing a system containing multiple sampling rates. A describing theory is presented and possibly modified, and its applicability is tested by applying it to the mass spring damper system. The red arrow denotes this as an iterative process, which continues until a satisfactory result is reached.

Chp. 5 - Multirate DFPT Modelling: The chosen method from the previous chapter, is here applied to the 10 kW DFPT to obtain a multirate model. To do this, linear models describing the individual components in the DFPT are derived. All the individual solutions to the subchallenges posed by the DFPT, as defined in section 1.5.1, are here combined to derive a multirate model of a DFPT, and the suitability of the individual solutions are discussed in relation to multirate DFPT modelling. Furthermore, the hypothesis regarding expanding the multirate method to the 5.4 MW DFPT is also discussed.
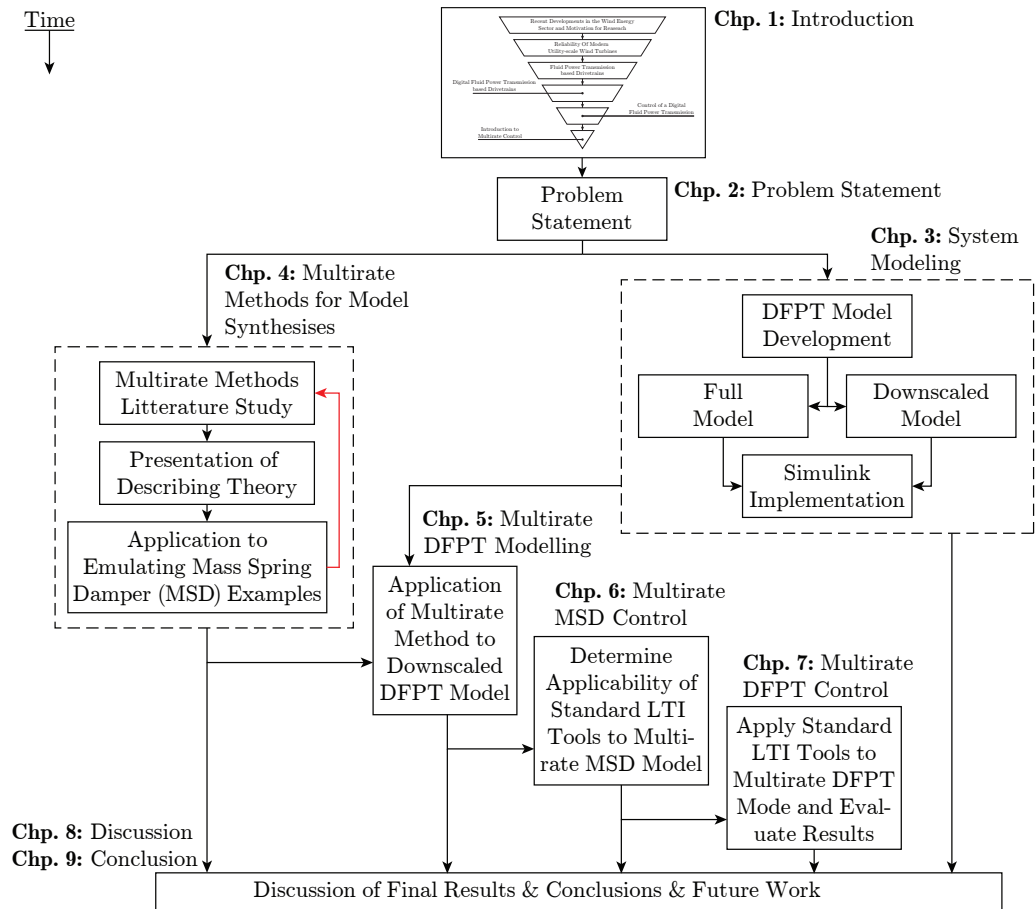
Fig. 2.2: Outline of the methodical approach to the research process posed by of multirate model-
ling and control of a Digital Fluid Power Transmission.

Chp. 6 - Multirate MSD Control: Having developed the multirate MSD model, the
task it now to determine the applicability of conventional LTI control theory tools
for MIMO systems, such as the RGA and SVD. Finally the possibilities for using
the model for controller design are considered.

Chp. 7 - Multirate DFPT Control: Based on the results from the previous chapter,
conventional control theory tools are here applied to the $10\,\mathrm{kW}$ DFPT where they
are found applicable. Furthermore, possibilities for applying the multirate method
and associated controller structure to the full power $5.4\,\mathrm{MW}$ DFPT are discussed.

Discussion, Conlcusion and Future Work: The final results of the thesis are dis-
cussed along with the methodical approach utilised to solve the multirate DFPT
control problem. Furthermore, conclusions regarding the work presented in the
thesis are drawn, and suggestions toward future work are made.

As indicated in the figure, many of these steps are conducted in parallel and furthermore
they overlap. With the presented methodical approach, extensive studies have to be

conducted to determine the multirate method's applicability. These studies include the derivation of multirate models for a MSD system along with the downscaled DFPT, followed by an investigation of the applicability of standard LTI MIMO control theory tools to the derived multirate models. Due to the extensiveness of these studies, it is unlikely that multiple multirate methods can be tested within the time frame of this thesis, why there is no guarantee that a multirate method which solves the problem statement will be found.

2.3 Overall Limitations

To limit the scope of the project, the overall limitations of the work presented in this thesis are defined here:

Quantitative or Qualitative Performance Analysis: The performance of the Digital Fluid Power Transmission is not evaluated quantitatively or qualitatively. This is not done, since the purpose of this thesis is to derive a multirate modelling method, which can be applied to DFPTss.

Linear Control Theory: The work presented here is limited to the application of linear control theory.

Deterministic Control: Furthermore, any developed control algorithms are limited to only considering deterministic control, and thereby noise and disturbance terms are generally omitted.

Theoretical Project: No test stand is available for the system under consideration, and thus the project work presented is purely theoretical.

In general the thesis presented here deals with a highly complex system with a large number of subelements. For this reason many simplifications are made throughout the work, but wherever possible they are listed and commented upon, such that the reader is familiar with the limitations of the presented work.

System Modelling

This chapter presents the governing equations used to form non-linear models of the DFPTs considered in this project. Firstly, the purpose of the mathematical model is established which leads to a description of the main assumptions made for simplifying the modelling task. This is followed by a presentation of the main governing equations describing the DFPT dynamics which includes modelling of the digital displacement pump and motor.

The DFPTs considered in this thesis can be divided into several elements which can be modelled individually and then combined by using the output from one element as the input to other elements. Figure 3.1 presents the elements used to comprise the DFPTs on a block diagram form.
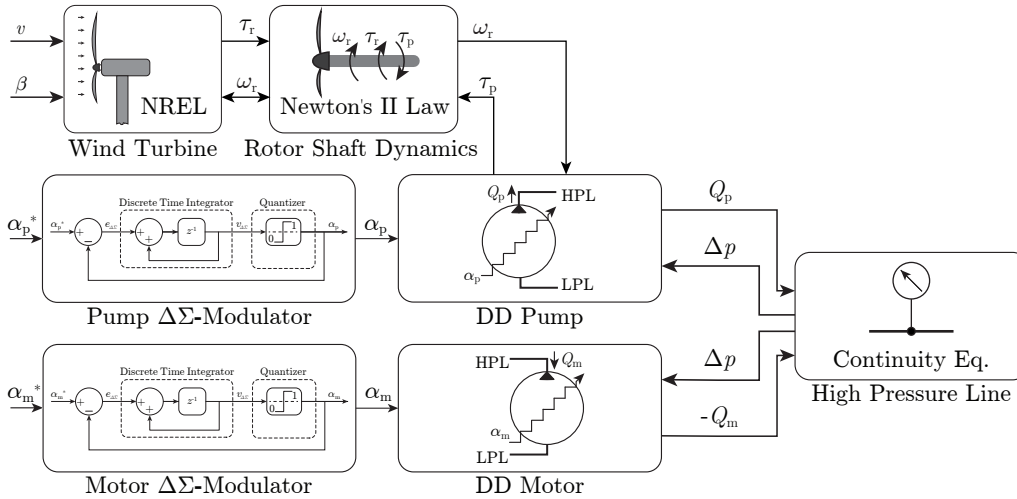
Fig. 3.1: Elements, comprising the DFPTs, which are to be modelled, including inputs and outputs which connects the elements.

The inputs to the model consists of the exogenous wind speed input, v, and the user set inputs of the blade pitch angle, β, and the non-binary displacement references for the pump and motor, $\alpha_\mathrm{p}{}^*$ and $\alpha_\mathrm{m}{}^*$, respectively. The displacement references are used for determining the amount of cylinders pumping/motoring or idling. The $\Delta\Sigma$-modulators then transforms the non-binary displacement references to binary ones, α_p and α_m, which can be used as input to the DDMs.

The main focus of this thesis is the DFPT why a highly simplified wind turbine model, representing the NREL reference wind turbine, is utilised. An elaboration of the wind turbine model is presented in appendix B. The rest of the elements including their inputs and outputs are explained throughout this chapter. Before the governing equations describing each element are presented, the purpose of the model is established.

3.1 Purpose of System Modelling

This thesis deals with the development of a multirate model which can be used to design control for a DFPT in a wind turbine. As described in chapter 2, two DFPTs with different power ratings are considered, a utility-scale 5.4 MW DFPT and a downscaled 10 kW DFPT. Before models of the DFPTs are developed, the purpose of these should be established such that the model comprehensiveness, with regard to which contributions should be neglected or included, resembles the intended use. The level of comprehensiveness of the models is determined from an engineering assessment since no test data is available for model verification.

The 5.4 MW DFPT is, due to its high number of pressure chambers (142 in total), in itself a highly complex system why applying advanced multirate methods is considered a challenging task. In order to ease this task, the downscaled 10 kW DFPT (4 pressure chambers in total), is introduced as a tool on which the applicability of the developed multirate methods and conventional control algorithms can be evaluated prior to applying it to the 5.4 MW DFPT. This evaluation will, however, not be of qualitative or quantitative nature since the 10 kW DFPT is a fictive system. Based on this, the purpose of the 10 kW DFPT model is established. It is important to note that this thesis does not seek to design control for the 5.4 MW DFPT why a simulation model is not necessary. This chapter, however, takes its basis in modelling of both the 5.4 MW and 10 kW DFPT. This is done since operation and consequently modelling of the 5.4 MW is more intuitive than the 10 kW DFPT. Furthermore, presenting the modelling of the 5.4 MW DFPT should allow for easier continuation of the work presented in this thesis.

Based on the established modelling purposes it is desired that the two models have the same level of comprehensiveness with regard to dynamic contributions such that the multirate methods and algorithms developed for the 10 kW DFPT can, to some extent, be directly applied to the 5.4 MW DFPT. Thus, it is decided that the two models should include the same dynamic contributions. This means that the only difference between the two models will be the number of pressure chambers in each of the DDMs. Furthermore, the multirate methods and control algorithms will not be developed with the scope of being directly applicable in a physical WT but serves as a proof of concept. It is therefore deemed redundant to develop highly detailed and complex models as this would primarily complicate the modelling task and furthermore increase the simulation time.

The engineering assessment of which contributions should be included in the models is made based on a desire of obtaining models which includes the control challenges of a DFPT, i.e. the digital nature, coupled dynamics and unequal sampling of the two DDMs. Furthermore, the assessment is made based on a trade off between the gain in model accuracy versus the modelling complexity. However, some contributions might be complex to include but are vital for describing the dynamics of the DFPT and thus they are included in the model. Based on this engineering assessment of which contributions should be included or not, certain assumptions have been made in order to simplify modelling. These assumptions apply to both the 10 kW and 5.4 MW model. The assumptions which are presented here, are those which are generally applicable to the

entire DFPT. The more specific assumptions regarding individual components in the DFPT are presented throughout the chapter, where the relevant element is modelled.

Simplified hydraulic circuit without pressure smoothing accumulators, pressure boost circuits or filters, which would change system dynamics and require redesign. These components are all common in physical implementations of hydraulic systems, however, with the modelling purpose in mind, they only complicate the modelling task. The omission of accumulators increases pressure ripples, which in turn also increases speed, torque and power ripple. Thus it may be considered, that if satisfactory control performance is achievable without accumulators, then performance may be further increased by the addition of these to the system. The omission of modelling a pressure boost circuit for the LPL means that the pressure is assumed constant at p_L.

Structural dynamics of the wind turbine and transmission are not included and is thus considered completely rigid. As such excessive wear on WT components due to torque pulsations cannot be evaluated.

Grid Connection Requirements: These have not been considered since the choice of a suitable generator is beyond the scope of this project. Potential requirements are assumed fulfilled by choice of suitable generator and overall WT operation strategy.

The presented main assumption all have the purpose of simplifying the modelling task of the DFPT. The assumption are, however, made with the modelling purpose in mind and should not remove the main control challenges of a DFPT. Thus, the model is considered to be qualified for evaluating and validating the multirate methods and control algorithms which are to be applied, despite these simplifications. Further modelling simplifications are presented throughout this chapter and all fulfill the same requirement of not removing the main control challenges of a DFPT.

3.2 Main Dynamic System Elements

This section presents the main governing equations describing the DFPT based drivetrain. These equations consist of a mathematical description of the dynamics of motion of the DD pump and the pressure dynamics in the HPL which connects the DD pump and motor. The equations are valid for modelling both the 5.4 MW and the 10 kW DFPT.

DD Pump Motion Dynamics:
The dynamics of motion of the DD pump depends on the torque acting on the pump shaft. This can be described by the rotational analogue to Newton's second law of motion:

$$\dot{\omega}_r = \frac{1}{J_{rp}}\left(\tau_r - d_r\,\omega_r - \frac{\tau_p}{\eta_p}\right) \tag{3.1}$$

where $\dot{\omega}_r$ is the angular acceleration of the pump shaft, J_{rp} is the total inertia of the turbine rotor and the DD pump, d_r is the viscous damping coefficient and η_p is the mechanical efficiency of the pump. τ_p is the reactive pump torque generated by the cylinder force acting on the pump cam shaft. An expression for this will be presented

in the following. τ_r is the WT rotor torque generated by the wind acting on the turbine blades which drives the pump. The rotor torque depends on the rotor dimensions and the wind speed, v, and is modelled statically by:

$$\tau_r = \frac{1}{2} R_r \, A_r \, \rho_A \, C_q \, v^2 \tag{3.2}$$

where ρ_A is the air density, A_r is the rotor swept area, R_r is the rotor radius and C_q is the WT torque coefficient. An elaboration of the turbine model is presented in appendix B.

Remark 3.2.A: Friction is included in the DD pump model by a viscous friction term and a mechanical efficiency. The omission of Couloumb friction is considered reasonable, since a WT never changes direction of rotation, whereby the Coulomb friction is merely a constant offset. Thereby omitting any concerns with regard to start-up, which are generally not considered in this thesis.

Alternatively, friction could be modelled for each chamber which would require applying Newton's second law of motion to each chamber. This would also greatly increase the simulation time which is undesired. As the purpose of the simulation model is not to obtain a highly accurate DFPT model these assumptions are considered reasonable. Furthermore, they do not compromise the model's ability to simulate the main control challenges of a DFPT. The simplified friction model may affect the efficiency of the DDMs, however, this is not a concern in this thesis.

HPL Pressure Dynamics:
The pressure, p_L, in the LPL is assumed to be controlled by an external boost pump and is thus, for simplicity, considered constant. The pressure in the HPL is modelled as function of the pump and motor flow, Q_p and Q_m, and is described by applying the continuity equation to the control volume in the HPL assuming constant volume due to rigid pipes in the HPL (Andersen 2003):

$$\Delta\dot{p} = \frac{\beta_H}{V_H} \left(Q_p - Q_m - k_l \, \Delta p \right) \tag{3.3}$$

where $\Delta p = p_H - p_L$ and k_l is the combined motor and pump leakage coefficient. Assuming $\dot{p}_L = 0$ means $\Delta\dot{p} = \dot{p}_H$.

Remark 3.2.B: The volumetric efficiency of the machines is included by a pressure dependent leakage term from the HPL to LPL. The volumetric efficiency is also included inherently in how the DDMs are operated since passive opening of the valves requires pressure build up which reduces the volumetric efficiency.

Remark 3.2.C: The bulk modulus, β_H is assumed constant in the HPL. This is considered a reasonable assumption since the pressure dependency in the bulk modulus is relatively small for pressures above $\sim$40 bar. It is expected that the HPL pressure will be controlled such that it is above 300 bar during operation.

Remark 3.2.D: The volume of the HPL is assumed constant due to the assumption of rigid pipes in the DFPT. This simplifies modelling significantly and does not remove the model's ability to include the main control challenges of a DFPT.

Table 3.1 presents the parameters used to model the HPL pressure dynamics.

Description	Parameter	Value
HPL Bulk modulus	β_{H}	$16\,000\,\mathrm{bar}$
HPL control volume	V_{H}	$0.816\,\mathrm{m}^3$

Tab. 3.1: Parameters used for modelling the HPL pressure dynamics.

Having obtained the main governing equations describing the DFPT drivetrain, the next section presents the modelling of the DD pump and motor.

3.3 Digital Displacement Machine Modelling

This section presents the modelling of the DD machines utilised in the DFPT based drivetrain. The DD pump and motor in both the 5.4 MW and 10 kW DFPTs are, as previously described, comprised of one or multiple pressure chambers. Thus, the approach of modelling the DDMs is to model a single pressure chamber and utilise this single chamber model in all DDMs. The chambers will, however, have different dimensions and actuations due to the different geometry and ratings of the machines. As such, it is important to note that the equations presented for modelling both the DD pump and motor in the following sections will be valid for both the 5.4 MW and the 10 kW DFPT.

3.3.1 DD Pump Modelling

The DD pump utilised in both the 10 kW and 5.4 MW DD pump is a cam ring type with a multi lobe geometry in order to obtain multiple chamber activations during one revolution. A section view of both pumps can be seen in figure 3.2.
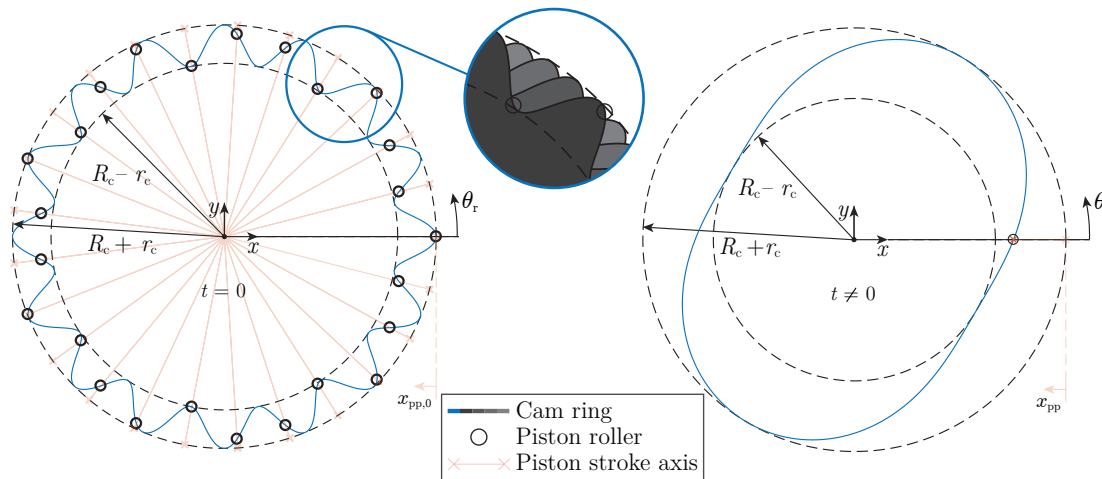
Fig. 3.2: To the left, section view of the cam ring in the 5.4 MW DD pump including the piston rollers for the first module and a zoomed view showing the multiple radially distributed modules. To the right, the 10 kW DD pump including the location of the single piston roller.

The 5.4 MW DD pump consist of four stacked cam rings, referred to as modules, attached to the same shaft which is also evident from figure 3.2. This geometry ensures relatively high displacement at low angular speed. As presented in section 2.1, the 10 kW DD pump is introduced as a development tool why its geometry is highly simplified compared to the 5.4 MW DD pump. The result of this is a 10 kW DD pump which only consist of a single module. The 10 kW DD pump is further simplified by only having 2 lobes and only containing 1 cylinder. This design results in 2 cylinder activations per pump shaft revolution. The 10 kW pump geometry can be seen in figure 3.2.

Based on figure 3.2 the equations describing the 5.4 MW and 10 kW DD pump kinematics are presented next.

Pump Kinematics:
The angular location of the individual pump cylinders may be described by:

$$\theta_{\mathrm{pc},j} = \frac{2\,\pi\,j}{N_{\mathrm{pc}}} \qquad\qquad j = \{0,\,1,\,\ldots,\,N_{\mathrm{pc}}-1\} \qquad\qquad (3.4)$$

where N_{pc} is the number of cylinders attached to a single cam ring, N_{l} is the number of lobes on a single cam and θ_{r} is the pump shaft angle. The piston roller bearings always lie on the cam ring, and thus the location of the cylinder's roller bearing in the Cartesian coordinate system may be described by:

$$\boldsymbol{x}_{\mathrm{pc}}(t) = \begin{bmatrix} x_{\mathrm{pc}}(t) \\ y_{\mathrm{pc}}(t) \end{bmatrix} = \begin{bmatrix} \overbrace{(R_{\mathrm{c}} + r_{\mathrm{c}}\,\cos(N_{\mathrm{l}}\,(\theta_{\mathrm{pc}} - \theta_{\mathrm{r}}(t))))}^{\text{Time translation of cylinder piston}} \overbrace{\cos(\theta_{\mathrm{pc}})}^{\text{Cylinder location}} \\ (R_{\mathrm{c}} + r_{\mathrm{c}}\,\cos(N_{\mathrm{l}}\,(\theta_{\mathrm{pc}} - \theta_{\mathrm{r}}(t))))\,\sin(\theta_{\mathrm{pc}}) \end{bmatrix} \qquad (3.5)$$

where the second term determines the location of the cylinder, and the first term describes the stroke of the cylinder with regard to the global coordinate system as illustrated in figure 3.2. As the 10 kW DD pump only contains one cylinder, $\theta_{\mathrm{pc}} = 0$ rad.

The pump piston stroke may be related to the location of the roller bearings, described by equation 3.5, by the following mapping:

$$x_{\mathrm{pp}}(t) = R_{\mathrm{c}} + r_{\mathrm{c}} - |\boldsymbol{x}_{\mathrm{pc}}(t)| = r_{\mathrm{c}}\,(1 - \cos\,(N_{\mathrm{l}}\,(\theta_{\mathrm{pc}} - \theta_{\mathrm{r}}(t)))) \qquad (3.6)$$

x_{pp} is then defined, so that at $x_{\mathrm{pp}} = 0$ the piston is placed at the minimum stroke referred to as TDC. For the only cylinder in the 10 kW pump, at $t = 0$, $x_{\mathrm{pp}} = 0$. The expression describing the pump piston stroke will in the following be utilised for describing the pressure chamber dynamics.

Pressure Chamber:
All pressure chambers in the DD pump are assumed identical why this section describes the dynamics for a single cylinder only. The various variables in the following derivations are shown without dependencies, e.g. time dependencies such as $x(t)$, for simplicity. Figure 3.3 shows a simplified hydraulic diagram of a single pressure chamber attached to a lobed cam shaft and the associated High Pressure Valve (HPV) and Low Pressure Valve (LPV). It is important to note that the number of lobes is not drawn to scale but only to illustrate how the piston is actuated.
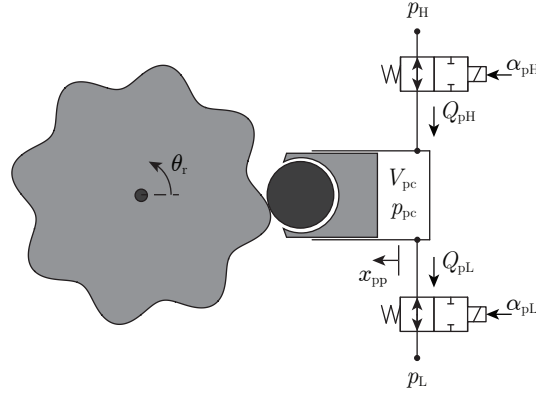
Fig. 3.3: Pump pressure chamber diagram for deriving the governing equations. Variables and directions of flows and coordinates are as defined in the diagram. Drawing not to scale.

The pressure dynamics can be described by applying the continuity equation to the defined control volume seen in figure 3.3 and solving for the chamber pressure gradient, $\dot{p}_{pc}$ yields (Andersen 2003):

$$\dot{p}_{pc} = \frac{\beta}{V_{pc}} \left(Q_{pH} - Q_{pL} - \dot{V}_{pc} \right) \tag{3.7}$$

where V_{pc} is the pressure chamber volume and Q_{pH} and Q_{pL} are the flows through the HPV and LPV, respectively. These flows are modelled using the orifice equation given by (Andersen 2003):

$$Q_{pL} = \frac{\bar{x}_{pL}}{k_f} \sqrt{|p_{pc} - p_L|} \operatorname{sign}(p_{pc} - p_L) \tag{3.8}$$

$$Q_{pH} = \frac{\bar{x}_{pH}}{k_f} \sqrt{|p_H - p_{pc}|} \operatorname{sign}(p_H - p_{pc}) \tag{3.9}$$

where $\bar{x}_{pL}$ and $\bar{x}_{pH}$ are the normalised valve plunger position of the LPV and HPV, respectively. k_f is the valve flow coefficient.

The total pump flow, Q_p, is defined as the sum of the flow through all HPVs given as:

$$Q_p = -\sum_{j=1}^{N_{pc}} Q_{pH,j} \tag{3.10}$$

where the negative sign is due to the definition of direction of the valve flow. Utilising equation 3.10 for the 10 kW DD pump does not require the sum as it only contains one cylinder. However, the sum is included as it also applies for the 5.4 MW DD pump which contains multiple cylinders.

The volume, V_{pc}, in equation 3.7, is defined as:

$$V_{pc} = x_{pp} A_{pp} + V_{p0} \tag{3.11}$$

where V_{p0} is the minimum chamber volume and A_{pp} is the piston area. Substituting the expression in equation 3.6 which describes the piston position as function of the pump shaft's angular position results in the expression describing the chamber volume as function of θ_r:

$$V_{pc} = \frac{V_{pp}}{2} \left(1 - \cos\left(N_l\left(\theta_{pc} - \theta_r\right)\right)\right) + V_{p0} \tag{3.12}$$

where $V_{pp} = 2\,r_c\,A_{pp}$. The chamber volume gradient used in equation 3.7 is given as the derivative of equation 3.12 with respect to time:

$$\dot{V}_{pc} = -\frac{V_{pp}\,\dot{\theta}_r\,N_l}{2}\,\sin\left(\theta_{pc} - \theta_r\right) \tag{3.13}$$

β in equation 3.7, is the effective bulk modulus of the oil which describes the stiffness of the oil given by (Andersen 2003):

$$\beta = \frac{1}{\dfrac{1}{\beta_F} + \dfrac{\epsilon_A}{\beta_A}} \tag{3.14}$$

where ϵ_A is the volumetric ratio of free air in the oil, β_F is the bulk modulus of the pure oil and β_A is the bulk modulus of the free air. Assuming the bulk modulus to be pressure dependent only, ϵ_A can be described as (Andersen 2003):

$$\epsilon_A = \frac{1}{\left(\dfrac{1 - \epsilon_{A0}}{\epsilon_{A0}}\right)\left(\dfrac{p_{atm}}{p_{pc}}\right)^{\frac{-1}{c_{ad}}} + 1} \tag{3.15}$$

where ϵ_{A0} is the volumetric ratio of free air in the fluid at atmospheric pressure, p_{atm}, and c_{ad} is the adiabatic air constant. β_A from equation 3.14 is given by (Andersen 2003):

$$\beta_A = c_{ad}\,p_{pc} \tag{3.16}$$

where p_c is the absolute pressure of the fluid. The parameters used to model the oil bulk modulus can be seen in table 3.2:

Description	Parameter	Value
Pure oil bulk modulus	β_F	16 000 bar
Adiabatic air constant	c_{ad}	1.4
Reference volumetric ratio of free air	ϵ_{A0}	0.01
Atmospheric pressure	p_{atm}	1 bar

Tab. 3.2: Main parameters used for modelling the bulk modulus.

The effective bulk modulus as function of pressure can be seen in figure 3.4 with the parameters seen in table 3.2.
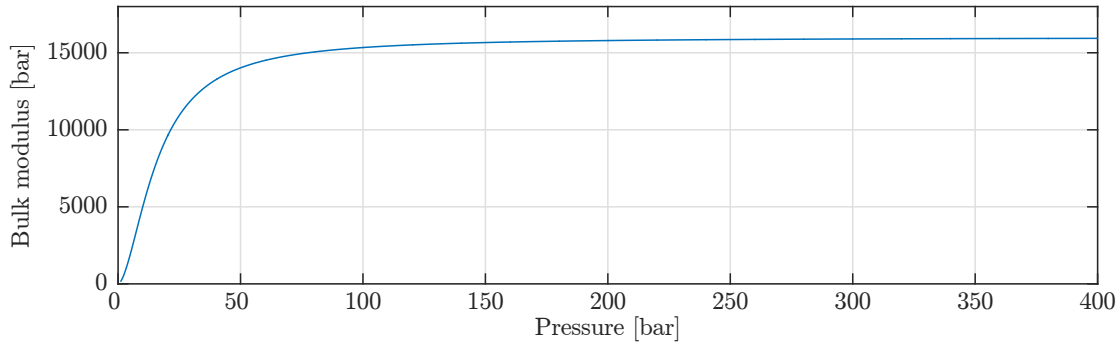
Fig. 3.4: Bulk modulus as function of pressure with the parameters used in the model.

Remark 3.3.A: The bulk modulus of the oil in each cylinder chamber is modelled dynamically as function of the chamber pressure only. The temperature and density dependency in the bulk modulus model describing the oil stiffness in the cylinder chambers is neglected since this dependency is considered negligible compared to the pressure dependency (Andersen 2003). This assumption simplifies modelling and does not remove the model's ability to include the DFPT control challenges.

The bulk modulus is included in the simulation model by tabulating the effective bulk modulus as function of the chamber pressure as seen in figure 3.4 and implemented as a lookup table in order to reduce simulation time.

Valve Dynamics and $\Delta\Sigma$-Modulator:

The flow through the HPV and LPV is proportional to the normalised plunger position, $\bar{x}_{\mathrm{pL}}$ and $\bar{x}_{\mathrm{pH}}$, seen in equations 3.8 and 3.9. As a simplification, the motion of the valve plunger is modelled by assuming piecewise constant acceleration. This also constitutes a reduction in simulation time compared to modelling the plunger motion by considering the forces acting on the plunger using Newton's second law. Furthermore, a generic model of the plunger motion is obtained where the geometry of the plunger is not taken into account. Figure 3.5 shows the valve plunger response as implemented in the model during opening of the valve, including the corresponding constant acceleration and velocity.
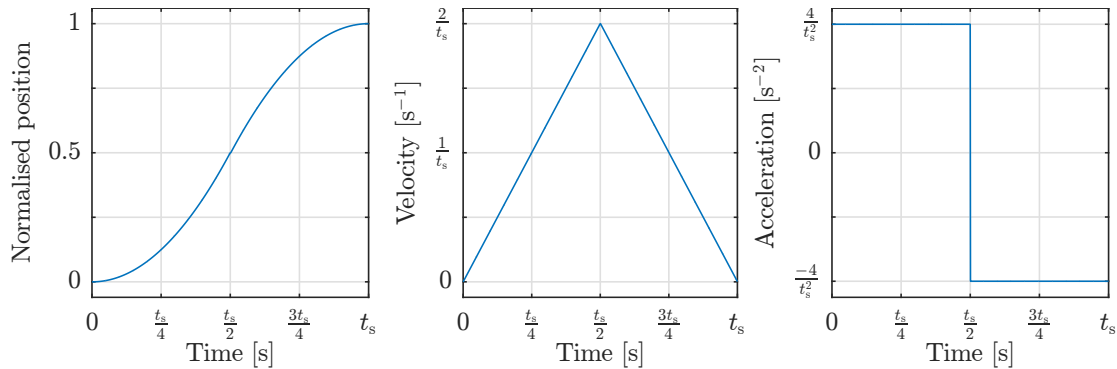
Fig. 3.5: Plunger position response as implemented in model including corresponding velocity and acceleration response.

As seen from the figure, the acceleration is constant positive for $0 \leq t < t_\mathrm{s}/2$ and constant negative with identical magnitude for $t_\mathrm{s}/2 \leq t \leq t_\mathrm{s}$, where t_s is the valve opening and closing time. The closing of the valves is modelled to have the same response, except the acceleration is initially negative in order to close it. The valve position response is tabulated as function of time and implemented as a lookup table in the model.

Initiating a valve opening or closing is done by changing the valve input to 1 or 0, respectively. As an example, a closed HPV is opened by setting $\alpha_\mathrm{pH} = 1$. Similarly, can the HPV be closed again by setting $\alpha_\mathrm{pH} = 0$. The same applies for the LPV. Triggering of the HPVs and LPVs in the DD pump is modelled by the following conditions assuming the appropriate initial conditions in the model are set:

$$\alpha_\mathrm{pH} = \begin{cases} 1, & \text{if} \quad p_\mathrm{pc} \geq p_\mathrm{H} \wedge \bar{x}_\mathrm{pH} = 0 \\ 0, & \text{if} \quad \theta_\mathrm{r} = \theta_\mathrm{HPV} \wedge \bar{x}_\mathrm{pH} = 1 \end{cases} \tag{3.17}$$

$$\alpha_\mathrm{pL} = \begin{cases} 1, & \text{if} \quad p_\mathrm{pc} \leq p_\mathrm{H} \wedge \bar{x}_\mathrm{pL} = 0 \\ 0, & \text{if} \quad \theta_\mathrm{r} = \theta_\mathrm{LPV} \wedge \bar{x}_\mathrm{pL} = 1 \wedge \alpha_\mathrm{p} = 1 \end{cases} \tag{3.18}$$

It should be noted that opening of the valves are initiated when the stated pressure conditions are satisfied. This condition is utilised for obtaining passive opening since the generic plunger motion model is used in contrary to modelling the forces acting on the plunger. The value of the valve inputs α_pH and α_pL are held in the model until a new set of conditions is satisfied which changes the value of these inputs. α_p is the user-set input which is used for modelling a pumping stroke ($\alpha_\mathrm{p} = 1$) or a idling stroke ($\alpha_\mathrm{p} = 0$). As seen, the LPV can only be closed, initiating a pumping stroke, when the pump angle is equal to the LPV closing angle, θ_LPV and $\alpha_\mathrm{p} = 1$. Individual closing angles for the HPV and LPV, θ_HPV and θ_LPV respectively, are set for each cylinder connected to the pump shaft.

α_p, which is used for determining the operation mode (pumping or idling) of each of the pressure chambers in the DD pump, is a binary variable. In order to utilise a conventional control structure which will output a non-binary displacement reference, α_p^*, a first-order $\Delta\Sigma$-modulator is used to transform this non-binary displacement reference to a binary one. A block diagram of the first-order $\Delta\Sigma$-modulator is shown in figure 3.6.
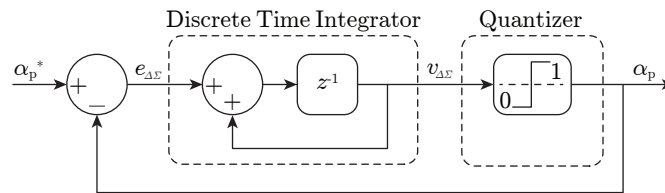
Fig. 3.6: First order $\Delta\Sigma$-modulator utilised for transforming a non-binary displacement reference to a binary one.

The $\Delta\Sigma$-modulator consists of a discrete time integrator and a quantizer. The discrete time integrator can be described by the difference equation:

$$v_{\Delta\Sigma}(k) = \alpha_\mathrm{p}{}^*(k-1) - \alpha_\mathrm{p}(k-1) + v_{\Delta\Sigma}(k-1)$$
$$= e_{\Delta\Sigma}(k-1) + v_{\Delta\Sigma}(k-1) \tag{3.19}$$

The quantizer is the element which transforms the non-binary $v_{\Delta\Sigma}$ to a binary displacement reference, α_p. The output of the quantizer can be described by equation 3.20:

$$\alpha_\mathrm{p}(k) = \begin{cases} 0 & \text{for} \quad v_{\Delta\Sigma}(k) < 0.5 \\ 1 & \text{for} \quad v_{\Delta\Sigma}(k) \geq 0.5 \end{cases} \tag{3.20}$$

Remark 3.3.B: Utilising a generic model of the valve plunger motion constitutes relatively low simulation times compared to modelling the plunger motion using Newton's second law of motion. This assumption is considered reasonable as the purpose of the model is not to obtain a highly accurate model but a model which contains the main control challenges of a DFPT. This assumption mainly affects the efficiency of the DFPT which is not a concern in this thesis.

Pump Reactive Torque:

The pump reactive torque is the result of the pressure force which is generated by the pressure in each cylinder chamber. Figure 3.7 shows the variables which are used for deriving an expression describing the pump reactive torque. The figure is shown for a single module in the 5.4 MW DD pump but the equations also applies for describing the reactive torque for the 10 kW DD pump.
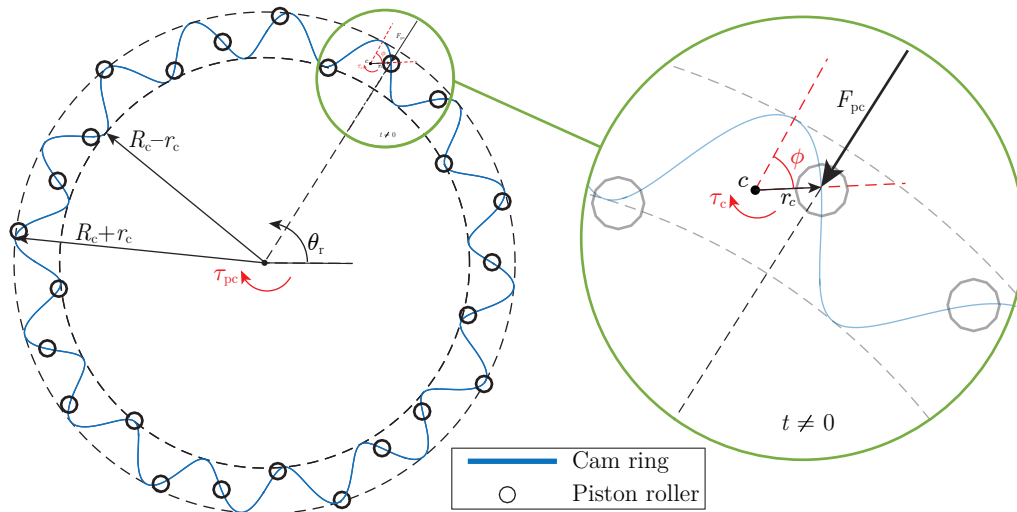
Fig. 3.7: 5.4 MW DD pump shaft with variables used for deriving reactive pump torque expression.

The torque acting on the point c from a single cylinder can be expressed as:

$$\tau_{\mathrm{c}} = r_{\mathrm{c}} \sin(\phi) \, F_{\mathrm{c}} \tag{3.21}$$

where $\phi = N_{\mathrm{l}} \, (\theta_{\mathrm{pc}} - \theta_{\mathrm{r}})$. Equation 3.21 can be rewritten to obtain an expression for the torque acting around the center of the pump shaft, by multiplying N_{l}. This is done since the angular velocity of the piston stroke is N_{l} times faster than the angular velocity of the pump shaft. Furthermore, the expression describing the pressure force from a single cylinder, $F_{\mathrm{pc}} = A_{\mathrm{pp}} \, p_{\mathrm{pc}}$, is inserted. This yields the following torque expression:

$$\tau_{\mathrm{pc}} = N_{\mathrm{l}} \frac{V_{\mathrm{pp}}}{2} \, \sin(N_{\mathrm{l}}(\theta_{\mathrm{pc}} - \theta_{\mathrm{r}})) \, p_{\mathrm{pc}} \tag{3.22}$$

For the 10 kW DD pump, equation 3.22 describes the total reactive pump torque since it only contains a single cylinder. For the 5.4 MW DD pump, the total reactive pump torque is given as the sum of the torque contribution from each cylinder:

$$\tau_{\mathrm{p}} = N_{\mathrm{l}} \frac{V_{\mathrm{pp}}}{2} \sum_{j=1}^{N_{\mathrm{pc}}} \sin(N_{\mathrm{l}}(\theta_{\mathrm{pc},j} - \theta_{\mathrm{r}})) \, p_{\mathrm{pc},j} \tag{3.23}$$

Remark 3.3.C: In order to utilise equation 3.22 for describing the reactive pump torque it is assumed that the cam shaft surface can be described by a sine function. This is however not the case, as the cam shaft surface is stretched due to the lobes being radially distributed around a round cam shaft. It should, however, be noted that more lobes means a cam shaft surface closer to a sine wave. This also means that utilising this torque expression for the 10 kW DD pump which only has two lobes involves a less accurate torque expression compared to utilising it for the 5.4 MW DD pump.

Having presented the governing equations describing the dynamics for a single cylinder, these can be applied to each pump cylinder to obtain a mathematical model of the 10 kW and 5.4 MW DD pump. The operation of a single cylinder is verified with respect to the DDM operation presented in section 1.4 by simulating two full strokes, one pumping and one idling stroke. The simulation, which is illustrated in figure 3.8, is started at the LPV closing angle, θ_{LPV}, where the LPV closes, initialising a pumping stroke. After a full revolution, indicated by the dashed line, the LPV is kept open, yielding an idling stroke. The simulation is performed at a pump shaft speed of 10 rpm and $p_{\mathrm{H}} = 360$ bar.

It should be noted that the chamber volume, V_{pc}, is plotted such that when $V_{\mathrm{pc}} = 0$, the volume is equal to the dead volume, V_{p0}. As previously explained the decision to pump or idle is made when the pump shaft reaches the angle θ_{LPV}.

This concludes the derivation of the mathematical model for the DD pump dynamics.

DD Pump Specifications:
The specifications for the 10 kW and 5.4 MW DD pump models are given in table 3.3.
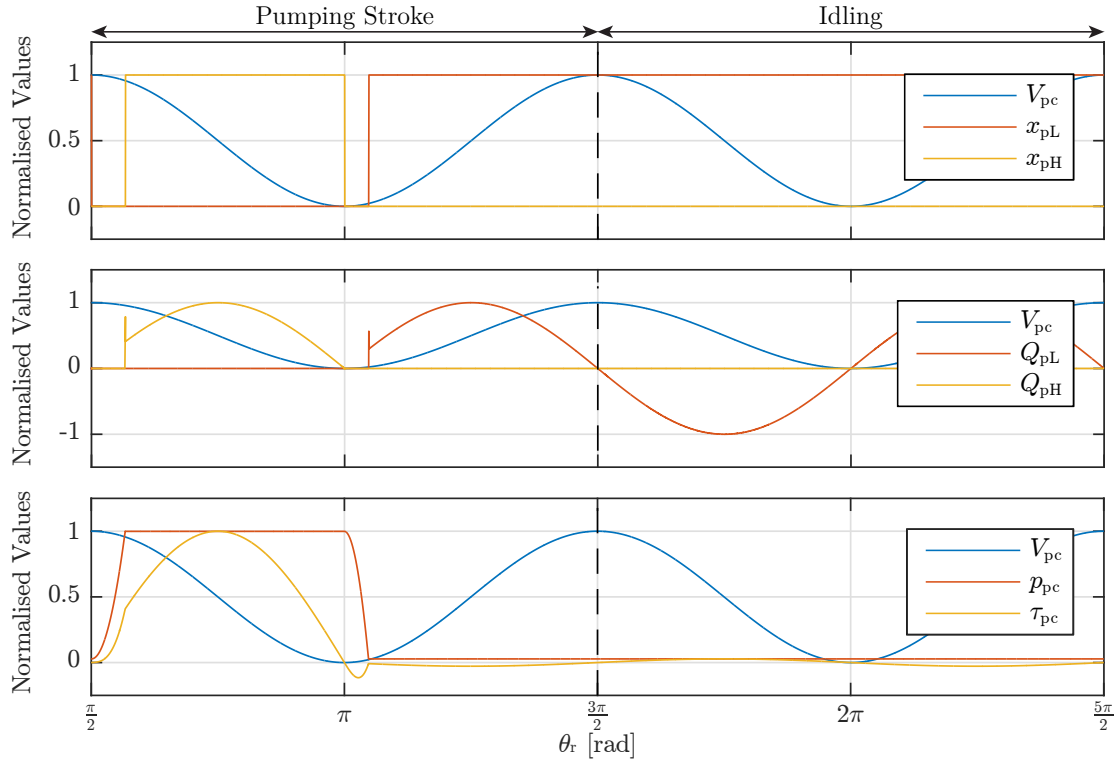
Fig. 3.8: Simulation results of single cylinder for 2 full strokes with all values shown as normalised. Initially full pumping stroke followed by a full idling stroke. Dashed black line indicates θ_{LPV} for the particular cylinder. The x-axis corresponds to the 10 kW DD pump.

Description	Parameter	10 kW	5.4 MW
Cam rings	N_{cr} [-]	1	4
Lobes per cam ring	N_{l} [-]	2	16
Cylinders per cam ring	N_{pc} [-]	1	25
Piston stroke length	$x_{\mathrm{p,stroke}}$ [m]	12.5×10^{-3}	54.1×10^{-3}
Pump piston area	A_{pp} [m^2]	48.9×10^{-5}	9.20×10^{-3}
Cylinder dead volume	V_{p0} [m^3]	61.0×10^{-5}	4.98×10^{-4}
Valve actuation time	t_{s} [s]	1×10^{-3}	1×10^{-3}
Valve flow coefficient	k_{f} [$\sqrt{\mathrm{Pa}}\,\mathrm{s}/\mathrm{m}^3$]	0.5×10^5	0.5×10^5
Pump & rotor inertia	J_{rp} [kg m^2]	133	7.76×10^7
Viscous damping coefficient	d_{r} [Nm s/rad]	17.2×10^{-2}	50×10^3
Pump mechanical efficiency	η_{p} [-]	0.95	0.95

Tab. 3.3: Main specifications of modelled 10 kW and 5.4 MW DD pump.

3.3.2 DD Motor Modelling

The 5.4 MW motor is a radial piston type motor, with multiple eccentric cams, referred to as modules, on a common shaft. Multiple cylinders are evenly distributed radially around the eccentric, and modules are then stacked one after another to increase the rating of the motor. The eccentric geometry reduce torque and pressure pulsations due to lumped activation of pressure chambers. The 10 kW motor is simplified by reducing the number of modules to one and reducing the number of cylinders such that it only contains three cylinders shifted by an angle of $\frac{2\pi}{3}$ rad between them. The eccentric shaft is maintained in the 10 kW such that each cylinder completes a full stroke during a single motor shaft revolution in contrary to the pump where each cylinder is activated multiple times per revolution due to the lobed geometry.

The stroke of the cylinder pistons is always perpendicular to the tangent of the cam at the interface between the two. As such, the pistons must be able to tilt, and the functional principle of the radial piston type motor is then very similar to how a crankshaft interacts with pistons and connection rods in an ICE.

Figure 3.9 shows a section view of the 5.4 MW DD motor to the left and the 10 kW DD motor to the right including the locations of the contact points between the cylinder pistons and the eccentric. The left part includes a zoomed view of the even radial distribution of the multiple modules in the 5.4 MW DD motor.
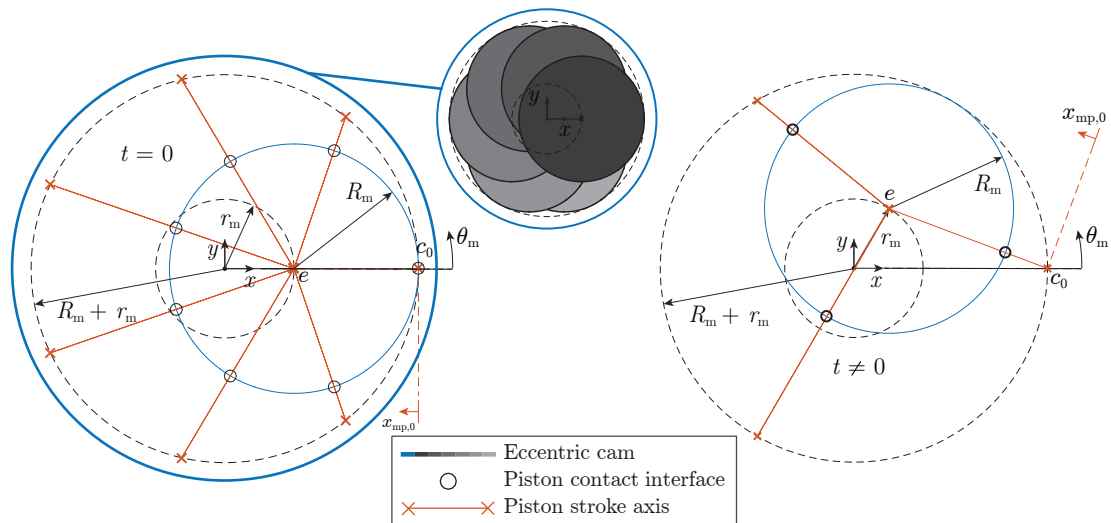
Fig. 3.9: Simple section view of the 5.4 MW DD motor to the left and the 10 kW DD motor to the right including the location of the contact points between the piston and cam shaft for the first module. The left part includes a zoomed view of the radial distribution of the multiple modules in the 5.4 MW motor.

To simplify the derivations presented in this section, only the first cylinder in the motor, denoted c_0 in figure 3.9, will be considered. The general equations will still be the same for all modules and cylinders, the only difference lies in angular shifts in the periodic

sine and cosine functions, since the initial positions at $t = 0$ will differ. Furthermore, the equations presented in the following sections applies for both the the 5.4 MW and the 10 kW DD motor as only the number of modules and cylinders differs.

Motor Kinematics:
The location of the individual cylinders may be described by:

$$\theta_{\mathrm{mc},j} = \frac{2\,\pi\,j}{N_{\mathrm{mc}}} \qquad\qquad j = \{0,\,1,\,\ldots,\,N_{\mathrm{mc}} - 1\} \qquad (3.24)$$

where N_{mc} is the number cylinders in a single module of the motor.

The piston contact interface always lies on the eccentric cam, and is furthermore always perpendicular to tangent of the cam, thus the motor piston stroke always lies along the red piston stroke axis in figure 3.9. For this to be possible the cylinders must be able to tilt. The motor piston stroke may be found by considering the vector between the cylinder location ($\boldsymbol{c}$) and cam center point location ($\boldsymbol{e}$):

$$\boldsymbol{c} = \begin{bmatrix} c_{\mathrm{x}} \\ c_{\mathrm{y}} \end{bmatrix} = \begin{bmatrix} (r_{\mathrm{m}} + R_{\mathrm{m}})\,\cos(\theta_{\mathrm{mc}}) \\ (r_{\mathrm{m}} + R_{\mathrm{m}})\,\sin(\theta_{\mathrm{mc}}) \end{bmatrix} \qquad \boldsymbol{e}(t) = \begin{bmatrix} e_{\mathrm{x}}(t) \\ e_{\mathrm{y}}(t) \end{bmatrix} = \begin{bmatrix} r_{\mathrm{m}}\,\cos(\theta_{\mathrm{m}}(t)) \\ r_{\mathrm{m}}\,\sin(\theta_{\mathrm{m}}(t)) \end{bmatrix} \qquad (3.25)$$

where r_{m} is the eccentric radius, R_{m} the radius of the cam and θ_{m} the motor shaft angle.

The magnitude of the cylinder stroke $\boldsymbol{x}_{\mathrm{mp}}$ may then be determined as:

$$|\boldsymbol{x}_{\mathrm{mp}}(t)| = |\boldsymbol{e}(t) - \boldsymbol{c}| - R_{\mathrm{m}} \qquad (3.26)$$

For the first cylinder of the motor equation 3.26 becomes:

$$|\boldsymbol{x}_{\mathrm{mp},0}(t)| = \sqrt{\left(r_{\mathrm{m}}\,(\cos(\theta_{\mathrm{m}}(t)) - 1) - R_{\mathrm{m}}\right)^2 + \left(r_{\mathrm{m}}\,\sin(\theta_{\mathrm{m}}(t))\right)^2} - R_{\mathrm{m}} \qquad (3.27)$$

x_{mp} is then defined just like x_{pp}, so that at $x_{\mathrm{mp}} = 0$ the piston is placed at the minimum stroke referred to as TDC. For the first cylinder at $t = 0$, then $x_{\mathrm{mp},0} = 0$. Shown in figure 3.9, is only one coordinate origin for the piston stroke, for the remaining pistons the coordinate origin will be distributed radially like the cylinders. This definition of the piston stroke, corresponds with x_{mp} reaching TDC at the same instant the cylinder pressure chamber attains its minimum volume. The equations presented in this section have been verified by animating figure 3.9.

Pressure Chamber:
The equations describing the pressure dynamics are similar to those presented for the DD pump, however, they are shown here for clarity. The presented equations will be applicable to all cylinders in the DD motor. Figure 3.10 shows a simplified hydraulic diagram of the motor cam shaft including the defined flows through the associated HPV and LPV. The figure is shown for the 10 kW DD motor.
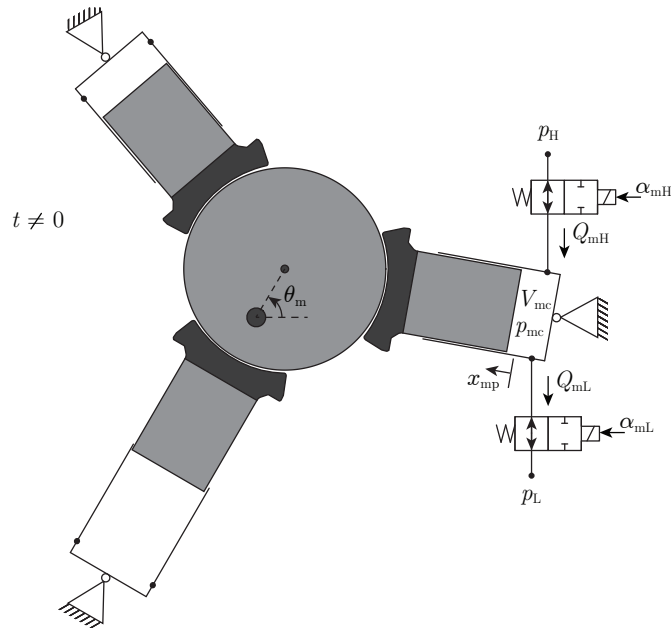
Fig. 3.10: Motor pressure chamber diagram for deriving the governing equations. Variables and directions of flows and coordinates are as defined in the diagram. Drawing not to scale.

Similarly to the DD pump, the continuity equation is applied to the control volume seen in figure 3.10 in order to obtain an expression for the pressure dynamics:

$$\dot{p}_{\mathrm{mc}} = \frac{\beta}{V_{\mathrm{mc}}} \left(Q_{\mathrm{mH}} - Q_{\mathrm{mL}} - \dot{V}_{\mathrm{mc}} \right) \tag{3.28}$$

The orifice equations used to model the flows through the LPV and HPV are given by:

$$Q_{\mathrm{mL}} = \frac{\bar{x}_{\mathrm{mL}}}{k_{\mathrm{f}}} \sqrt{|p_{\mathrm{mc}} - p_{\mathrm{L}}|}\, \mathrm{sign}(p_{\mathrm{mc}} - p_{\mathrm{L}}) \tag{3.29}$$

$$Q_{\mathrm{mH}} = \frac{\bar{x}_{\mathrm{mH}}}{k_{\mathrm{f}}} \sqrt{|p_{\mathrm{H}} - p_{\mathrm{mc}}|}\, \mathrm{sign}(p_{\mathrm{H}} - p_{\mathrm{mc}}) \tag{3.30}$$

The total motor flow, Q_{m} is given as the sum of the flow through all HPVs given as:

$$Q_{\mathrm{m}} = \sum_{j=1}^{N_{\mathrm{mc}}} Q_{\mathrm{mH},j} \tag{3.31}$$

The chamber volume, V_{mc} in equation 3.28, is defined as:

$$V_{\mathrm{mc}} = x_{\mathrm{mp}}\, A_{\mathrm{mp}} + V_{\mathrm{m0}} \tag{3.32}$$

where V_{m0} is the minimum chamber volume and A_{mp} is the piston area.

Substituting equation 3.27, describing $x_{\mathrm{mp}}(\theta_{\mathrm{m}})$, into equation 3.32 yields an expression describing $V_{\mathrm{mc}}(\theta_{\mathrm{m}})$ for the first cylinder.

Similar to the pump, the volume gradient, $\dot{V}_{\mathrm{mc}}$, used in equation 3.28, is found by differentiating the expression describing $V_{\mathrm{mc}}(\theta_{\mathrm{m}})$ with respect to time to obtain $\dot{V}_{\mathrm{mc}}(\theta_{\mathrm{m}})$. The volume equations are not shown here for simplicity.

Remark 3.3.D: An identical bulk modulus model is used to model the oil stiffness in the motor chambers as for the pump, including identical parameters. Similarly the bulk modulus is tabulated as function of oil pressure and included as a lookup table.

Valve Triggering and Dynamics:
The HPVs and LPVs used in the DD motor are assumed identical to those used in the DD pump. Thus, the dynamics and characteristics are identical and are therefore modelled in the same manner. The opening and closing characteristic can be seen in figure 3.5.

Similar to the pump, a set of conditions are utilised for triggering the opening and closing of the HPV and LPV. These conditions are given as:

$$\alpha_{\mathrm{mH}} = \begin{cases} 1, & \text{if} \quad p_{\mathrm{mc}} \geq p_{\mathrm{H}} \wedge \bar{x}_{\mathrm{mH}} = 0 \\ 0, & \text{if} \quad \theta_{\mathrm{m}} = \theta_{\mathrm{HPV}} \wedge \bar{x}_{\mathrm{mH}} = 1 \end{cases} \tag{3.33}$$

$$\alpha_{\mathrm{mL}} = \begin{cases} 1, & \text{if} \quad p_{\mathrm{mc}} \leq p_{\mathrm{H}} \wedge \bar{x}_{\mathrm{mL}} = 0 \\ 0, & \text{if} \quad \theta_{\mathrm{m}} = \theta_{\mathrm{LPV}} \wedge \bar{x}_{\mathrm{mL}} = 1 \wedge \alpha_{\mathrm{m}} = 1 \end{cases} \tag{3.34}$$

As seen, pressure conditions, similar to the pump, are utilised for modelling the passive opening of the valves.

A first order $\Delta\Sigma$-modulator, as the presented for the DD pump is utilised in the motor for transforming a non-binary displacement reference, α_{m}^*, to a binary reference, α_{m}.

Remark 3.3.E: The DD motor shaft speed is assumed constant. This effectively removes the need for a generator model and the torque summation around the shared generator and motor shaft. It also implies that it is not possible to model grid faults that will affect the generator speed. This is considered a reasonable assumption as the obtained model will include the main control challenges of a DFPT, i.e. the digital nature, different sampling rates and coupled dynamics of the two DDMs.

Remark 3.3.F: Friction is not included in the DD motor model. This is considered a reasonable simplification since the dynamics of motion for the motor are not modelled due to the assumption of fixed generator speed.

Combining the presented governing equations yields a mathematical model of a single DD motor chamber. The single chamber model is verified with respect to the DDM operation presented in section 1.4, by simulating two full strokes. One motoring stroke followed by an idling stroke. The simulation results can be seen in figure 3.11, with a simulation performed for the first cylinder at a constant motor speed of 1500 rpm and $p_{\mathrm{H}} = 360$ bar.
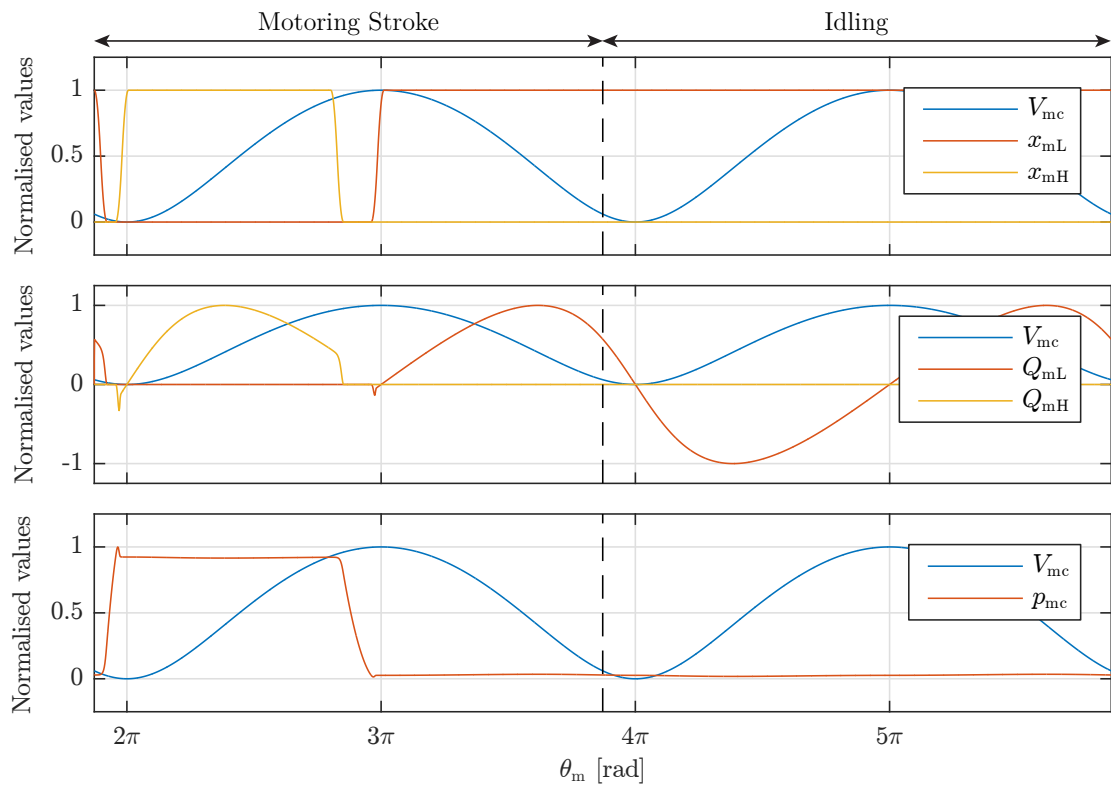
Fig. 3.11: Simulation results of single motor cylinder for 2 full strokes with all values shown as normalised. Initially full motoring stroke followed by a full idling stroke. Dashed black line indicates θ_{LPV} for the particular cylinder.

The simulation is initiated at the LPV closing angle, θ_{LPV}, and performs a full motoring stroke. It should be noted that the relatively small negative flow occurring when the HPV opens during the motor stroke is due to the chamber pressure increasing above p_{H} which results in a backflow into the HPL. The same is the case for the backflow seen for Q_{mL} when the LPV opens. Backflow is undesired as the volume of oil that flows back into the HPL does not contribute to driving the motor. The backflow could be reduced in several ways, e.g. by increasing the dead volume of each cylinder chamber. This project is however not concerned with the mechanical design and as the backflow is considered sufficiently small, no further effort is put into reducing it.

DD Motor Specifications:
The main specifications used for modelling the 10 kW and 5.4 MW DD motor are given in table 3.4.

Description	Parameter	10 kW	5.4 MW
Eccentric cams	N_{ec} [-]	1	6
Cylinders per eccentric cam	N_{mc} [-]	3	7
Radius of eccentric cam	R_{m} [m]	45×10^{-3}	45×10^{-3}
Eccentric cam radius	r_{m} [m]	7.61×10^{-3}	25.6×10^{-3}
Piston stroke length	$x_{\text{m,stroke}}$ [m]	15.2×10^{-3}	51.3×10^{-3}
Motor piston area	A_{mp} [m^2]	2.62×10^{-4}	29.8×10^{-4}
Cylinder dead volume	V_{m0} [m^3]	3.99×10^{-6}	1.53×10^{-4}
Valve actuation time	t_{s} [s]	1×10^{-3}	1×10^{-3}
Valve flow coefficient	k_{f} [$\sqrt{\text{Pa}}\,\text{s}/\text{m}^3$]	0.5×10^5	0.5×10^5

Tab. 3.4: Main specifications of the 10 kW and 5.4 MW DD motor.

The equations presented for modelling the 10 kW DD motor and pump are implemented in Simulink together with the equations describing the dynamics of the HPL and motion of the pump shaft to form a non-linear model of the 10 kW DFPT. The presented equations also applies for modelling the 5.4 MW DFPT. As such, part of the groundwork for continuing the work of this thesis is done since further work includes the design and implementation of a controller for the 5.4 MW DFPT. This concludes the modelling of the 10 kW and 5.4 MW DFPT. The next chapter seeks to develop a method which can be used for producing a multirate discrete-time model on state-space form.

CHAPTER 4

Multirate Methods for Model Synthesises

The purpose of this chapter is to develop a method which can be used for obtaining a multirate DFPT model. To do this, the essential challenges of DFPT multirate modelling will be presented together with the desirable characteristics of a solution. Furthermore, the strategy for obtaining a solution is presented. This is followed by a description of the considered methods and application to the DFPT emulating Mass Spring Damper (MSD) system with different sampling ratios. Utilising the MSD system for evaluating the methods means that the reader does not need to be familiar with a DFPT to understand the presented methods. The chapter ends with the selection of a multirate modelling approach, which is deemed suitable for describing the DFPT.

4.1 The DFPT Multirate Problem

For the DFPT the multirate problem was generally defined in sections 1.5 and 1.6. The problem of non-uniform sampling rates has, as described, already been solved, but the problem regarding multiple sampling rates has so far been untreated. Considering the DDMs of the DFPT in the spatial-domain, the challenge essentially remains how to establish a combined MIMO model of the DFPT, wherein the DDMs utilise different activation rates (pressure chamber activation decisions per revolution). An additional complication of a DFPT for a utility-scale WT is that the activation rates are vastly different for the pump and motor.

The approach for developing a method which can be used for obtaining a multirate DFPT MIMO model, and thus also the remainder of this chapter, is to progress as:

1. Present a method for describing a multirate system.
2. Apply the method to increasingly complex emulating examples:
   (a) Single rate sampled MSD system to introduce the reader to the method.
   (b) Multirate sampled MSD system with similar, but different sampling rates, corresponding to the sampling rates in the 10 kW DFPT, which will later be utilised for evaluating the developed method on a DFPT.
   (c) Multirate sampled MSD system with vastly different sampling rates corresponding to the sampling ratio in the utility-scale 5.4 MW DFPT.
3. Evaluate applicability of the presented method and if not satisfactory repeat from step 1.

The desirable characteristics of the multirate model description are defined as:

1. MIMO representation with transfer characteristics being well defined for all input

and output couplings, i.e. model separation techniques, such as two time-scale decompositions, are not desirable as these do not allow proper analysis of mutual system couplings.

2. Linear Time-Invariant (LTI) description, e.g. a static model description with constant matrices and gains, such that conventional control theory tools, i.e. RGA and SVD analysis, potentially can be utilised.

3. State-space description of the linear system, thereby remaining directly compatible with previously developed linear DDM models.

The three characteristics are seen as essential and necessary for the work in this thesis to succeed. Thus to proceed, the next section will present the simple linear double MSD system which is utilised as a tool for developing a multirate method.

4.1.1 Mass Spring Damper System

The system used for presenting, testing and developing the multirate methods in this chapter is the simple linear double mass spring damper (MSD) system presented in figure 4.1.
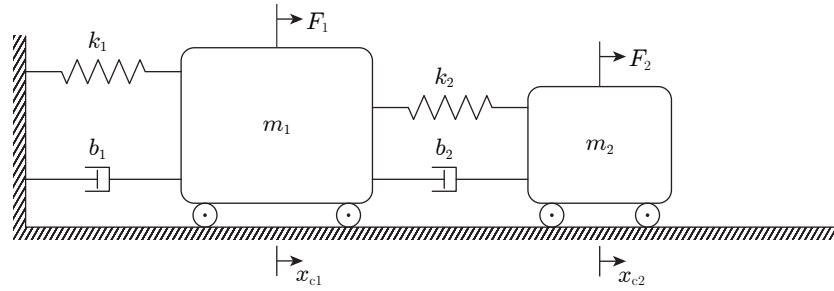
Fig. 4.1: Mass spring damper (MSD) system with multiple inputs and cross couplings.

No friction acts on the carts and the system is linear, why it is both simple to understand and easy to visualise the correct motion trajectories. In a state-space formulation, the system may be mathematically described by:

$$
\overbrace{\begin{bmatrix} \dot{x}_{c1} \\ \dot{x}_{c2} \\ \ddot{x}_{c1} \\ \ddot{x}_{c2} \end{bmatrix}}^{\dot{x}_c} = \overbrace{\begin{bmatrix} 0 & 0 & 1 & 0 \\ 0 & 0 & 0 & 1 \\ -\frac{k_1+k_2}{m_1} & \frac{k_2}{m_1} & -\frac{b_1+b_2}{m_1} & \frac{b_2}{m_1} \\ \frac{k_2}{m_2} & -\frac{k_2}{m_2} & \frac{b_2}{m_2} & -\frac{b_2}{m_2} \end{bmatrix}}^{A} \overbrace{\begin{bmatrix} x_{c1} \\ x_{c2} \\ \dot{x}_{c1} \\ \dot{x}_{c2} \end{bmatrix}}^{x_c} + \overbrace{\begin{bmatrix} 0 & 0 \\ 0 & 0 \\ \frac{1}{m_1} & 0 \\ 0 & \frac{1}{m_2} \end{bmatrix}}^{B} \overbrace{\begin{bmatrix} F_1 \\ F_2 \end{bmatrix}}^{u_c} \qquad (4.1a)
$$

$$
\underbrace{\begin{bmatrix} y_{c1} \\ y_{c2} \end{bmatrix}}_{y_c} = \underbrace{\begin{bmatrix} 1 & 0 & 0 & 0 \\ 0 & 1 & 0 & 0 \end{bmatrix}}_{C} x_c \qquad (4.1b)
$$

where the states are given as the positions and velocities of the carts, and the system inputs are the two forces F_1 and F_2, which act directly on the carts, and with the outputs being defined as the two positions. The values of the system constants are given in table 4.1:

	Mass 1	Mass 2	Unit
m	10	1	kg
k	1	10	N/m
b	1	0.1	N s/m

Tab. 4.1: Specifications of the mass spring damper system.

Some comments on the control related properties of the system:

1. Linear system, why linearisation techniques need not be considered.
2. Double complex conjugate poles at $s = -0.05 \pm j0.30$ and $s = -0.06 \pm j3.32$. The associated natural frequencies are $\omega_{n1} = 0.30\,\text{rad/s}$ and $\omega_{n2} = 3.32\,\text{rad/s}$ with damping ratios of $\zeta_1 = 0.15$ and $\zeta_2 = 0.02$, respectively. Similarly, the associated time constants are $\tau_1 = 1/(\zeta_1\,\omega_{n1}) = -1/\text{real}(s) = 22\,\text{s}$ and $\tau_2 = 16.7\,\text{s}$.
3. The fast mode is associated with the lighter mass, while the slow mode is associated with the large mass.
4. The natural frequencies are different by an order of magnitude, why the system could benefit from multirate sampling.
5. MIMO system, wherein the positions are considered the system outputs for later examples.

By use of this simple system, the challenges related to the DFPT, including multirate sampling and coupled dynamics, is emulated, such that the reader may develop an understanding of the multirate modelling approach without necessarily having extensive understanding of DDM operation.

4.2 Kalman and Bertram's Unified Approach

Kalman and Bertram (1959) presents their approach as a unified method for describing any sampled-data system. Thus, the method is generally able to describe conventional, multirate, random, non-synchronised and non-instantaneous sampling operations, why it seems like an ideal choice for describing the DFPT multirate problem.

The method takes it basis in already existing closed-loop systems and can be utilised for analysis of the sampled-data feedback system. However, for the purposes of this thesis, the method is adapted to handle open-loop configurations as well. Furthermore, the method is expanded from describing only SISO systems as presented by Kalman and Bertram (1959), to also describing MIMO systems by the authors of this thesis. The method derives a time-domain time-invariant discrete model in a state-space matrix-vector form. The time step of this model is equal to the Basic Time Period[1] (BTP) of the entire sampling scheme. Based on figures such as figures 1.15 and 1.16 Kalman and Bertram (1959) define three different types of system elements in a sampled-data system being the Continuous Dynamic (CDE), Discrete Dynamic (DDE) and Sample-and-Hold elements (SHE). Each element is associated with its own type of state, and Kalman and

---

[1]The periodicity of the entire sampling scheme as defined in section 1.6

Bertram combine them by defining the expanded state vector:

$$\boldsymbol{x} \equiv \left[\begin{array}{c|c|c} \boldsymbol{x_c}^{\mathsf{T}} & \boldsymbol{x_d}^{\mathsf{T}} & \boldsymbol{x_s}^{\mathsf{T}} \end{array}\right]^{\mathsf{T}} \qquad \begin{array}{l} [\boldsymbol{3} \times \boldsymbol{1}] \\ [n \times 1] \end{array} \qquad (4.2)$$

Equation 4.2 presents two dimensions in the right hand side. The bold font represents the dimension of the presented vector/matrix on block form (where applicable), while the non-bold font represents the combined dimension of all the block vectors/matrices or equivalently the absolute dimension of the presented vector/matrix. This notation is utilised throughout this chapter.

The Kalman and Bertram method then produces a model of the form:

$$\boldsymbol{x}((k+1)T) = \boldsymbol{\Psi}(\boldsymbol{\Phi}, \boldsymbol{S}, \boldsymbol{D})\boldsymbol{x}(kT) + \sum_{l=1}^{N} \boldsymbol{v}_l(\boldsymbol{\Phi}, \boldsymbol{S}, \boldsymbol{D}, \boldsymbol{s}, \boldsymbol{d})\,\boldsymbol{u}(kT + \kappa_l) \qquad (4.3\text{a})$$

$$\boldsymbol{y}(kT) = \boldsymbol{C}\boldsymbol{x}(kT) \qquad (4.3\text{b})$$

where $\boldsymbol{u}(kT + \kappa_l)$ are the external inputs acting on the system with κ_l being the entries of a vector denoting the periodically varying sampling operations in the system. $\boldsymbol{\Psi}(\boldsymbol{\Phi}, \boldsymbol{S}, \boldsymbol{D})$ and $\boldsymbol{v}_l(\boldsymbol{\Phi}, \boldsymbol{S}, \boldsymbol{D}, \boldsymbol{s}, \boldsymbol{d})$ are matrices containing the combined transition characteristic of all elements in the system, and are obtained as matrix products of the element transition matrices. $\boldsymbol{\Phi}$ being the CDE transition matrix, $\boldsymbol{D}$ the DDE transition matrix, and $\boldsymbol{S}$ the SHE transition matrix. $N = T/T_0$ is the number of STPs per BTP, which is also an upper bound for the number of times an input can be given per BTP.

Before applying the Kalman and Bertram method to the MSD system some general definitions necessary for applying the method will first be presented. The theory presented in the following section is generally complex and difficult to understand, and the direct application of the method will not be obvious from the presented matrices and equations. For this reason the theory is followed by a number of examples where the method is applied to the MSD system in order to demonstrate the application of the Kalman and Bertram method. First the governing equations associated with the elements and their states are defined.

Continuous Dynamic Elements (CDE):

Otherwise denoted as *Analog Plant* in various figures, these elements are described by linear ordinary differential equations, and with states denoted by $\boldsymbol{x_c}(t)$ with dimension $[\gamma \times 1]$. By using a matrix formulation, these may be described as in equation 4.1a. This only describes the state transition for an infinitesimal time change, so to calculate the state transition for a finite change in time, the time-domain solution is necessary (Ogata 1987, pp. 538-540):

$$\boldsymbol{x_c}(t) = e^{\boldsymbol{A}(t-t_0)}\,\boldsymbol{x_c}(t_0) + \int_{t_0}^{t} e^{\boldsymbol{A}(t-\tau)}\,\boldsymbol{B}\boldsymbol{u_c}(\tau)\,d\tau \qquad (4.4)$$

Assuming the plant input always to be connected to the output of a sample-and-hold element, such that $\boldsymbol{u_c} = \boldsymbol{x_s}$ (see section *Sample-and-Hold Elements (SHE)* on page 58

for definition of $\boldsymbol{x_s}$), then the plant input is always piecewise constant between successive sampling instances. However, no assumption regarding the uniformness, synchronisation or periodicity of the input rate is made. Thereby two transition matrices, related to the natural initial condition response[2] and the forced external input response, can be defined:

$$\boldsymbol{G_c}(\tau) \equiv e^{\boldsymbol{A}\tau} \quad [\gamma \times \gamma] \qquad\qquad \boldsymbol{H_c}(\tau) \equiv \int_0^\tau e^{\boldsymbol{A}\lambda}\boldsymbol{B}d\lambda \quad [\gamma \times \sigma] \qquad (4.5)$$

These matrices may be put into the context of the expanded state vector in equation 4.2, by writing the block transition matrix, which calculates the CDE state transitions for any finite time change:

$$\boldsymbol{\Phi}(\tau) \equiv \left[\begin{array}{c:c:c} \boldsymbol{G_c}(\tau) & \boldsymbol{0} & \boldsymbol{H_c}(\tau) \\ \hdashline \boldsymbol{0} & \boldsymbol{I} & \boldsymbol{0} \\ \hdashline \boldsymbol{0} & \boldsymbol{0} & \boldsymbol{I} \end{array}\right] \begin{array}{l} \} \; \gamma \text{ rows} \\ \} \; \delta \text{ rows} \\ \} \; \sigma \text{ rows} \end{array} \qquad \begin{array}{l} [\boldsymbol{3} \times \boldsymbol{3}] \\ {[n \times n]} \end{array} \qquad (4.6)$$

This matrix describes the CDE state transitions between two sampling instances and similar transition matrices will also be presented for the other system elements. Generally all transition matrices in the Kalman and Bertram method start as identity matrices, in which the appropriate rows corresponding to the states of interest are then subsequently modified to take the state transitions into account. Block partitioning is utilised to separate rows and columns according to the definition of the state vector in equation 4.2.

Deriving a model is then a case of appropriately multiplying transition matrices according to the sampling scheme, as will be illustrated by examples in section 4.2.1. The use of modified identity matrices means that states unaffected by the transition are not affected by the matrix product.

Discrete Dynamic Elements (DDE):

These elements are described by conventional linear difference equations, and have their states denoted by $\boldsymbol{x_d}(t)$ with dimension $[\delta \times 1]$. These elements are idealised representations of numerical computer calculations, thus the state transitions caused by these elements occur discontinuously and instantly in $t_k \to t_k^+$ (t_k being the discrete time instant where calculations are carried out), or more generally in the time needed to execute the programming instructions. Thus, the state transition of these elements are described by linear combinations of other states:

$$x_i(t_k^+) = \sum_{j=1}^{\gamma+\delta} D_{ij}\, x_j(t_k) + \sum_{l=1}^{\delta_{\text{in}}} d_{il}\, u_l(t_k) \qquad\qquad i = \{\gamma+1,\ldots,\gamma+\delta\} \qquad (4.7)$$

where D_{ij} and d_{il} are constants and u_l are external inputs acting on the DDE, of which there are δ_{in}. The first summation accounts for transitions occurring due to the continuous and discrete states of the model, while the second summation accounts for external inputs affecting the system through the DDE. Equation 4.7 may be put into context

---

[2]Kalman and Bertram denote $\boldsymbol{G_c}(\tau)$ as $\boldsymbol{\Phi^{cc}}(\tau)$

of the expanded state vector in equation 4.2, by writing the block transition matrices, which calculates the DDE state transitions at a single sampling instant:

$$
\boldsymbol{D}_{i(i+1)} \equiv \left[\begin{array}{ccc|ccc|c}
 & \boldsymbol{I} & & & \boldsymbol{0} & & \boldsymbol{0} \\ \hline
0 & \cdots & 0 & 1 & \cdots & 0 & \\
D_{i1} & \cdots & D_{i\gamma} & D_{i(\gamma+1)} & \cdots & D_{i(\gamma+\delta)} & \boldsymbol{0} \\
D_{(i+1)1} & \cdots & D_{(i+1)\gamma} & D_{(i+1)(\gamma+1)} & \cdots & D_{(i+1)(\gamma+\delta)} & \\
0 & \cdots & 0 & 0 & \cdots & 1 & \\ \hline
 & \boldsymbol{0} & & & \boldsymbol{0} & & \boldsymbol{I}
\end{array} \right]
\begin{array}{l} \\ \\ \leftarrow i^{\text{th}} \text{ row} \\ \leftarrow (i+1)^{\text{th}} \text{ row} \\ \\ \\ \end{array}
\begin{array}{l} [\boldsymbol{3} \times \boldsymbol{3}] \\ [n \times 1] \end{array} \quad (4.8)
$$

$$
\boldsymbol{d}_{i(i+1)} \equiv \left[\begin{array}{ccc}
 & \boldsymbol{0} & \\ \hline
0 & \cdots & 0 \\
d_{i1} & \cdots & d_{i\delta_{\text{in}}} \\
d_{(i+1)1} & \cdots & d_{(i+1)\delta_{\text{in}}} \\
0 & \cdots & 0 \\ \hline
 & \boldsymbol{0} &
\end{array} \right]
\begin{array}{l} \\ \\ \leftarrow i^{\text{th}} \text{ row} \\ \leftarrow (i+1)^{\text{th}} \text{ row} \\ \\ \end{array}
\begin{array}{l} [\boldsymbol{3} \times \boldsymbol{1}] \\ [n \times \delta_{\text{in}}] \end{array} \quad (4.9)
$$

$\boldsymbol{D}_{i(i+1)}$ and $\boldsymbol{d}_{i(i+1)}$ calculate the discrete state transitions of the ith and $(i+1)^{\text{th}}$ states at discrete time instants t_k. The shown matrices calculate two state transitions, but matrices calculating only a single state transition could just as easily have been presented. No assumptions regarding the uniformness of the time rate of t_k has been made while building the matrices.

Sample-and-Hold Elements (SHE):

These are, like the DDE, described by difference equations, and with states denoted by $\boldsymbol{x}_{\mathbf{s}}(t)$ with dimension $[\sigma \times 1]$. The sampling operations occur discontinuously and instantly in $t_k \rightarrow t_k^+$. Generally the input and output of the SHE are identical (at least ideally), although the input of a SHE can be a linear combination of multiple states, such that the SHE state transition is described by:

$$
x_i(t_k^+) = \sum_{j=1}^{\gamma+\delta} S_{ij}\, x_j(t_k) + \sum_{l=1}^{\sigma_{\text{in}}} s_{il}\, u_l(t_k) \qquad i = \{\gamma + \delta + 1, \ldots, n\} \tag{4.10}
$$

where S_{ij} and s_{il} are constants and u_l are external inputs acting through the SHE, of which there are σ_{in}. The first summation accounts for sampling of the continuous and discrete states of the model, while the second summation accounts for external inputs affecting the system through the SHE. Equation 4.10 may be put into context of the expanded state vector in equation 4.2, by writing the block transition matrices, which calculates the SHE state transitions at a single sampling instant:

$$
\boldsymbol{S}_i \equiv \left[\begin{array}{ccc|ccc|cc}
 & \boldsymbol{I} & & & \boldsymbol{0} & & & \boldsymbol{0} \\ \hline
 & \boldsymbol{0} & & & \boldsymbol{I} & & & \boldsymbol{0} \\ \hline
0 & \cdots & 0 & 0 & \cdots & 0 & 1 & \cdots 0 \\
S_{i1} & \cdots & S_{i\gamma} & S_{i(\gamma+1)} & \cdots & S_{i(\gamma+\delta)} & 0 & \cdots 0 \\
0 & \cdots & 0 & 0 & \cdots & 0 & 0 & \cdots 1
\end{array} \right]
\begin{array}{l} \\ \\ \\ \leftarrow i^{\text{th}} \text{ row} \\ \\ \end{array}
\begin{array}{l} [\boldsymbol{3} \times \boldsymbol{3}] \\ [n \times n] \end{array} \quad (4.11)
$$

$$\boldsymbol{s}_i \equiv \begin{bmatrix} \mathbf{0} \\ \mathbf{0} \\ 0 \cdots 0 \\ s_{il} \cdots s_{i\sigma_{\text{in}}} \\ 0 \cdots 0 \end{bmatrix} \leftarrow i^{\text{th}} \text{ row} \qquad\qquad \begin{matrix} [\mathbf{3} \times \mathbf{1}] \\ [n \times \sigma_{\text{in}}] \end{matrix} \qquad (4.12)$$

$\boldsymbol{S}_i$ and $\boldsymbol{s}_i$ calculate the discrete state transitions of the ith state at discrete sampling instants t_k. No assumptions regarding the uniformness of the time rate of t_k has been made while building the matrices.

Remark 4.2.A: The input matrix $\boldsymbol{s}_i$ is defined with σ_{in} columns, such that if the input is generated to be a vector containing σ_{in} inputs at all points, then matrix vector products may be utilised throughout all derivations. The same holds true for the $\boldsymbol{d}_i$ input matrix.

Remark 4.2.B: The SHE and associated states may also simply be considered as a Hold element, since no mathematical description is normally associated with the sampling/quantization process. Therefore it is typically combined with the signal holding process. More intuitively, the two operations should be kept separate, such that there would be total coherence between signal types for block diagram analysis. Exactly this has been done in various figures throughout the thesis, where the two processes are denoted as *Sampler* and *Zero-order Hold*, respectively.

For the same reason, Kalman and Bertram also consider all DDEs to contain input sampling operations, such that they may be directly connected to CDE outputs.

Remark 4.2.C: With the definitions of Kalman and Bertram, there is nearly no practical difference between a DDE and SHE. A more conventional definition of a SHE would only allow a single input, and not linear combinations of multiple inputs, which may be more logically attributed to the DDE.

Remark 4.2.D: The reason for associating the SHEs with a state is to allow for imperfect descriptions of the sampling operation, e.g. non-instantaneous sampling or imperfect signal holding. However, the work presented here is limited to considering the idealised sampling operation, why there is little difference between the SHE and DDE, as mentioned. Furthermore, the SHE states are superfluous and result in a non-minimal description, but they may be eliminated at a later stage.

Remark 4.2.E: Kalman and Bertram do not mention it, but it is the experience of the authors' that there can only be one $\boldsymbol{D}$ or $\boldsymbol{S}$ matrix per sampling rate. If separate matrices are made for each DDE or SHE then sometimes incorrect state transitions are obtained.

The three system elements described in this section can be used to construct any kind of system, as long as the signals are kept in coherence, e.g. the output of a DDE cannot be directly connected to a CDE, but must be connected through a SHE. How the mathematical descriptions of the system elements can be used to construct models is not obvious from the previous descriptions, and for this reason the next section will present a number of examples applying the presented method.

4.2.1 Various Examples

In the following, three different examples of increasing complexity will be presented along with remarks and interpretations of the utilised method.

Single Rate System:

Based on the MSD system presented in section 4.1.1, the open-loop sampled-data system of figure 4.2 is presented. To illustrate the application of the method, an example wherein all samplers and hold elements are synchronised and operated at a single rate of $T = 1/10\,\text{s}$ is first presented.
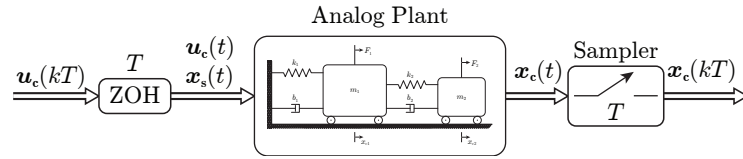
Fig. 4.2: Block diagram representation of the physical open-loop MSD system, with sampled outputs and zero-order held inputs operated at a single rate.

Kalman and Bertram (1959) defines a four step procedure for establishing a model of the sampled-data system:

1. Defining the state variables.
2. Calculating the various transition matrices as defined in the previous section.
3. Deriving transition equations for the sampling operations and sample-free time-intervals for a BTP.
4. Combining and simplifying transition equations to obtain a time-invariant model.

In the following, the four steps will be applied to the single rate sampled MSD system:

Step 1: For the system depicted in figure 4.2, there are $\gamma = 4$ CDE states, $\delta = 0$ DDE states and $\sigma = 2$ SHE states. From the figure, it can be seen that the SHE states are defined as being equal to the output of the *Hold* element. The expanded state vector is defined as:

$$\boldsymbol{x} = \left[\; \boldsymbol{x_c}^\mathsf{T} \;\middle|\; \boldsymbol{x_s}^\mathsf{T} \;\right]^\mathsf{T} = \left[\begin{array}{cccc|cc} x_{\text{c}1} & x_{\text{c}2} & \dot{x}_{\text{c}1} & \dot{x}_{\text{c}2} & x_{\text{s}1} & x_{\text{s}2} \end{array}\right]^\mathsf{T} \tag{4.13}$$

Step 2: For the CDE, the transition matrix is given by equation 4.14, with block matrix entries as defined in equation 4.5.

$$\boldsymbol{\Phi}(\tau) = \left[\begin{array}{c|c} \boldsymbol{G_c}(\tau) & \boldsymbol{H_c}(\tau) \\ \hline \boldsymbol{0} & \boldsymbol{I} \end{array}\right] \tag{4.14}$$

The transition matrix associated with the *hold* elements can now be defined. The inputs to the *hold* elements are simply the system inputs, and thus when defining the transition matrix, there will be no dependency on the internal model states, such that the

coefficients S_i in the ith row of $\boldsymbol{S}_{56}$ will all be zeros:

$$\boldsymbol{S}_{56} = \begin{bmatrix} \boldsymbol{I} & \vdots & \boldsymbol{0} \\ \hline 0 \ 0 \ 0 \ 0 & 0 \ 0 \\ 0 \ 0 \ 0 \ 0 & 0 \ 0 \end{bmatrix} \Big\} \ \gamma \ \text{rows} \tag{4.15}$$

The system inputs $\boldsymbol{u}(kT)$ may be accounted for by the input matrix $\boldsymbol{s}_{56}$:

$$\boldsymbol{s}_{56} = \begin{bmatrix} \boldsymbol{0} \\ \hline 1 \ 0 \\ 0 \ 1 \end{bmatrix} \Big\} \ \gamma \ \text{rows} \tag{4.16}$$

Step 3: To derive the transition equations, the state progression and sampling sequence must be known, thus the top part of figure 4.3 is presented. The figure illustrates the continuous progression of the CDE states and the discrete updates of the *hold* states. It may be seen that the sampling scheme is periodic with T, which is also equal to the BTP and STP.
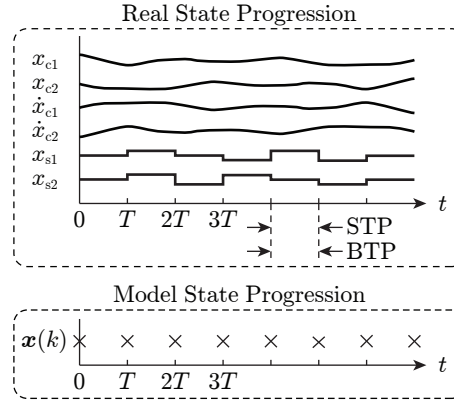
Fig. 4.3: In the top: the real state progression of continuous and piecewise constant *hold* states for a system with single rate sampling. In the bottom: the progression of the model states.

Then by examining the figure, it may be seen that within a single BTP (the successive open intervals $[kT \quad (k+1)T[$) the following two transitions occur. The first being related to the sample-and-hold operation and the second being related to the sample-free interval until the next BTP begins:

$$t = kT \to t = kT^+ \qquad \boldsymbol{x}\big(kT^+\big) = \boldsymbol{S}_{56}\,\boldsymbol{x}(kT) + \boldsymbol{s}_{56}\,\boldsymbol{u_c}(kT) \tag{4.17a}$$

$$kT < t < (k+1)T \qquad \boldsymbol{x}(kT+\tau) = \boldsymbol{\Phi}(\tau)\boldsymbol{x}\big(kT^+\big) \qquad\qquad 0 < \tau < T \tag{4.17b}$$

Step 4: Equations 4.17a and 4.17b may then be combined to obtain a time-invariant model with time step equal to the BTP:

$$\boldsymbol{x}((k+1)T) = \boldsymbol{\Phi}(T)\boldsymbol{S}_{56}\,\boldsymbol{x}(kT) + \boldsymbol{\Phi}(T)\boldsymbol{s}_{56}\,\boldsymbol{u_c}(kT) \tag{4.18a}$$

$$= \boldsymbol{\Psi}\boldsymbol{x}(kT) + \boldsymbol{v}\,\boldsymbol{u_c}(kT) \tag{4.18b}$$

Here $\mathbf{\Psi}$ and $\boldsymbol{v}$ represent time-invariant constant matrices for the state vector and input, respectively. The state progression of this model then corresponds to the bottom part of figure 4.3.

To test the applicability of the method, the block diagram of figure 4.2 has been implemented in MATLAB Simulink and simulated. Similarly the model represented by equation 4.18 has also been simulated using the same inputs and initial conditions. For both models, the inputs to the analog plant are updated at a rate of $T = 1/10\,\mathrm{s}$. The results of these two simulations are presented in figure 4.4, where the two position outputs are shown for each simulation.
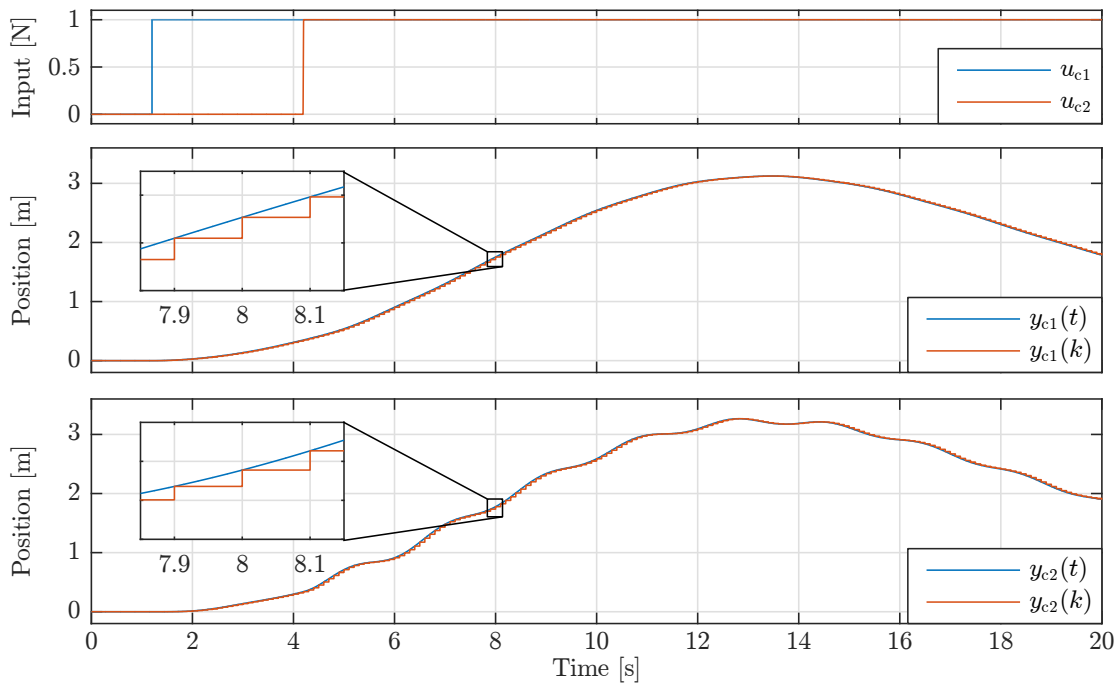
Fig. 4.4: Simulation results for a Matlab Simulink implementation of figure 4.2 and for the model represented by equation 4.18, both utilising a single update rate.

For the Kalman and Bertram model, the two outputs are plotted using zero-order hold line interpolation between subsequent data points, thereby leading to the stair-like appearance of the waveforms. Note that for simplicity only the two waveforms for the position outputs have been shown, and not the remaining six state waveforms. Based on the figure, it can generally be concluded that the model obtained by Kalman and Bertram's method is able to reproduce the results obtained using MATLAB Simulink.

This concludes the demonstration of how the method proposed by Kalman and Bertram may be applied to a single rate MIMO system. Based on the presented equations and their relation to each other, it should now be evident how the method may be used to describe any kind of sampled-data system. Before proceeding to the application of the method to a multirate system, a few remarks on the method in relation to the presented example are made:

Remark 4.2.F: The presented example does not include any discrete dynamical elements, why this subset block has been omitted in all matrices. For computer controlled continuous plants, these elements will typically occur with digital implementation of integral control action, and are generally present whenever a previous sample is used in calculations.

Remark 4.2.G: For single rate systems, the Kalman and Bertram method yields the same results as conventional zero-order hold equivalent discretisation, which may be found in e.g. Ogata (1987, pp. 538-540). Although the conventional method does not typically associate states with the hold elements.

Multirate System with Similar Sampling Rates:

The system under consideration in this example is again the MSD system from section 4.1.1. In contrast to the previous example, the system is now modified to utilise two different sampling rates. For this example, the first plant input is updated at a rate of $T_1 = T/2 = 0.15\,\text{s}$ and the second plant input is updated at a rate of $T_2 = T/3 = 0.1\,\text{s}$. The BTP of this sampling system is then $T = 0.3\,\text{s}$, and the STP is $T_0 = 0.05\,\text{s}$. The multirate system is illustrated in figure 4.5.
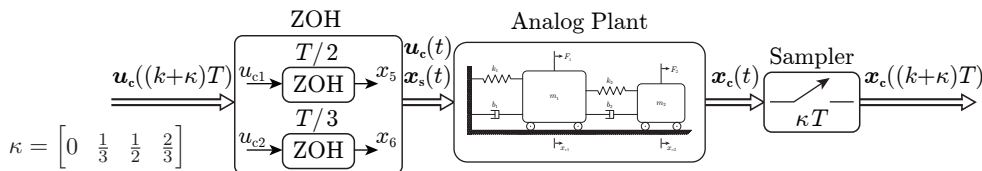
Fig. 4.5: Block diagram representation of the physical open-loopMSD system, with sampled outputs and zero-order held inputs operated at a multiple rates.

Step 1: The states are the same as in the previous example, why the reader is referred there.

Step 2: The CDE transition matrix $\boldsymbol{\Phi}(\tau)$ is the same as in the previous example, as it is only applied to the sample-free intervals between sampling operations. Thus this matrix is always the same no matter which sampling scheme is employed.

With regard to the two SHEs, they now operate at different rates, why it is now necessary to define separate matrices. Like before, the inputs to the *hold* elements are simply the system inputs, why coefficients in the associated row are all zero:

$$\boldsymbol{S}_5 = \begin{bmatrix} \boldsymbol{I} & \vdots & \boldsymbol{0} \\ 0\ 0\ 0\ 0 & 0\ 0 \\ 0\ 0\ 0\ 0 & 0\ 1 \end{bmatrix} \qquad \boldsymbol{S}_6 = \begin{bmatrix} \boldsymbol{I} & \vdots & \boldsymbol{0} \\ 0\ 0\ 0\ 0 & 1\ 0 \\ 0\ 0\ 0\ 0 & 0\ 0 \end{bmatrix} \qquad (4.19)$$

The system inputs $\boldsymbol{u}(kT)$ may be accounted for by the matrices $\boldsymbol{s}_5$ and $\boldsymbol{s}_6$:

$$\boldsymbol{s}_5 = \begin{bmatrix} \boldsymbol{0} \\ 1\ 0 \\ 0\ 0 \end{bmatrix} \qquad \boldsymbol{s}_6 = \begin{bmatrix} \boldsymbol{0} \\ 0\ 0 \\ 0\ 1 \end{bmatrix} \qquad (4.20)$$

63

Step 3: For this step, the top part of figure 4.6, which illustrates the multirate sampling scheme and state progression is presented.
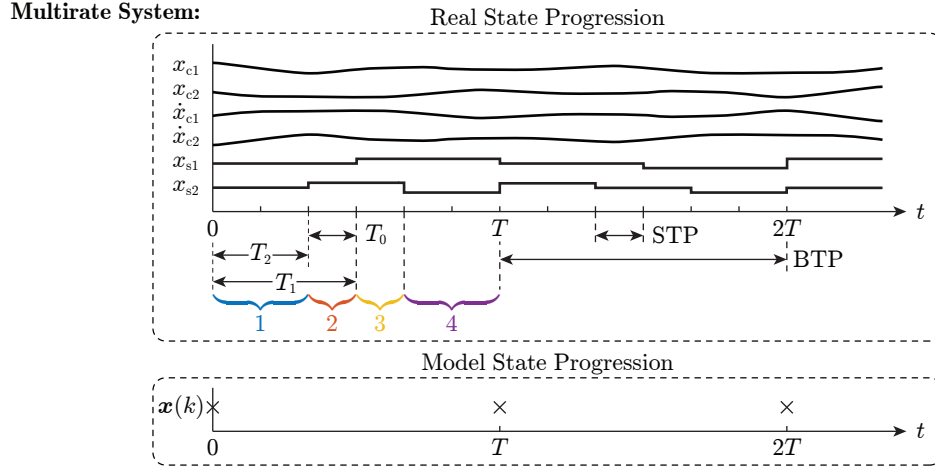
Fig. 4.6: In the top: the real state progression of continuous and piecewise constant *hold* states for a system with multirate sampling. In the bottom: the progression of the model states.

The sample-and-hold element associated with the $x_5 = x_{s1}$ state updates at a rate of $T_1 = T/2$, while the sample-and-hold element associated with the $x_6 = x_{s2}$ state updates at a rate of $T_2 = T/3$. As such, the number of sampling operations and sample-free intervals in the BTP is greatly increased, why careful bookkeeping is necessary while deriving the transition equations:

$$1 \begin{cases} t = kT \rightarrow t = kT^+ & \boldsymbol{x}\big(kT^+\big) = \boldsymbol{S}_6\boldsymbol{S}_5\boldsymbol{x}(kT) + (\boldsymbol{s}_6 + \boldsymbol{s}_5)\boldsymbol{u_c}(kT) & \text{(4.21a)} \\[2mm] kT < t < kT + T_2 & \boldsymbol{x}(kT+\tau) = \boldsymbol{\Phi}(\tau)\boldsymbol{x}\big(kT^+\big) & 0 < \tau < T_2 \quad \text{(4.21b)} \end{cases}$$

$$2 \begin{cases} t = kT + T_2 \rightarrow t = (kT + T_2)^+ & \boldsymbol{x}\big((kT + T_2)^+\big) = \boldsymbol{S}_6\boldsymbol{x}(kT + T_2) + \boldsymbol{s}_6\boldsymbol{u_c}(kT + T_2) & \text{(4.21c)} \\[2mm] kT + T_2 < t < kT + T_1 & \boldsymbol{x}(kT + T_2 + \tau) = \boldsymbol{\Phi}(\tau)\boldsymbol{x}\big((kT + T_2)^+\big) & 0 < \tau < T_0 \quad \text{(4.21d)} \end{cases}$$

$$3 \begin{cases} t = kT + T_1 \rightarrow t = (kT + T_1)^+ & \boldsymbol{x}\big((kT + T_1)^+\big) = \boldsymbol{S}_5\boldsymbol{x}(kT + T_1) + \boldsymbol{s}_5\boldsymbol{u_c}(kT + T_1) & \text{(4.21e)} \\[2mm] kT + T_1 < t < kT + 2T_2 & \boldsymbol{x}(kT + T_1 + \tau) = \boldsymbol{\Phi}(\tau)\boldsymbol{x}\big((kT + T_1)^+\big) & 0 < \tau < T_0 \quad \text{(4.21f)} \end{cases}$$

$$4 \begin{cases} t = kT + 2T_2 \rightarrow t = (kT + 2T_2)^+ & \boldsymbol{x}\big((kT + 2T_2)^+\big) = \boldsymbol{S}_6\boldsymbol{x}(kT + 2T_2) + \boldsymbol{s}_6\boldsymbol{u_c}(kT + 2T_2) & \text{(4.21g)} \\[2mm] kT + 2T_2 < t < kT + T & \boldsymbol{x}(kT + 2T_2 + \tau) = \boldsymbol{\Phi}(\tau)\boldsymbol{x}\big((kT + 2T_2)^+\big) & 0 < \tau < T_2 \quad \text{(4.21h)} \end{cases}$$

Step 4: Equation 4.21 may then be combined to obtain a time-invariant model with

time step equal to the BTP, as illustrated in the bottom part of figure 4.6:

$$\boldsymbol{x}((k+1)T) = \boldsymbol{\Psi}\boldsymbol{x}(kT) + \boldsymbol{v}_1\boldsymbol{u_c}(kT) + \boldsymbol{v}_2\boldsymbol{u_c}(kT+T_2) + \boldsymbol{v}_3\boldsymbol{u_c}(kT+T_1) + \boldsymbol{v}_4\boldsymbol{u_c}(kT+2T_2) \quad (4.22)$$

$$\boldsymbol{\Psi} = \underbrace{\boldsymbol{\Phi}(T_2)\boldsymbol{S}_6}_{4}\underbrace{\boldsymbol{\Phi}(T_0)\boldsymbol{S}_5}_{3}\underbrace{\boldsymbol{\Phi}(T_0)\boldsymbol{S}_6}_{2}\underbrace{\boldsymbol{\Phi}(T_2)\boldsymbol{S}_6\boldsymbol{S}_5}_{1}$$

$$\boldsymbol{v}_1 = \underbrace{\boldsymbol{\Phi}(T_2)\boldsymbol{S}_6}_{4}\underbrace{\boldsymbol{\Phi}(T_0)\boldsymbol{S}_5}_{3}\underbrace{\boldsymbol{\Phi}(T_0)\boldsymbol{S}_6}_{2}\underbrace{\boldsymbol{\Phi}(T_2)(\boldsymbol{s}_6 + \boldsymbol{s}_5)}_{1} \qquad \boldsymbol{v}_3 = \underbrace{\boldsymbol{\Phi}(T_2)\boldsymbol{S}_6}_{4}\underbrace{\boldsymbol{\Phi}(T_0)\boldsymbol{s}_5}_{3}$$

$$\boldsymbol{v}_2 = \underbrace{\boldsymbol{\Phi}(T_2)\boldsymbol{S}_6}_{4}\underbrace{\boldsymbol{\Phi}(T_0)\boldsymbol{S}_5}_{3}\underbrace{\boldsymbol{\Phi}(T_0)\boldsymbol{s}_6}_{2} \qquad\qquad\qquad \boldsymbol{v}_4 = \underbrace{\boldsymbol{\Phi}(T_2)\boldsymbol{s}_6}_{4}$$

Again the Kalman and Bertram derived model is simulated and compared to a MATLAB Simulink implementation and the results of this are shown in figure 4.7.
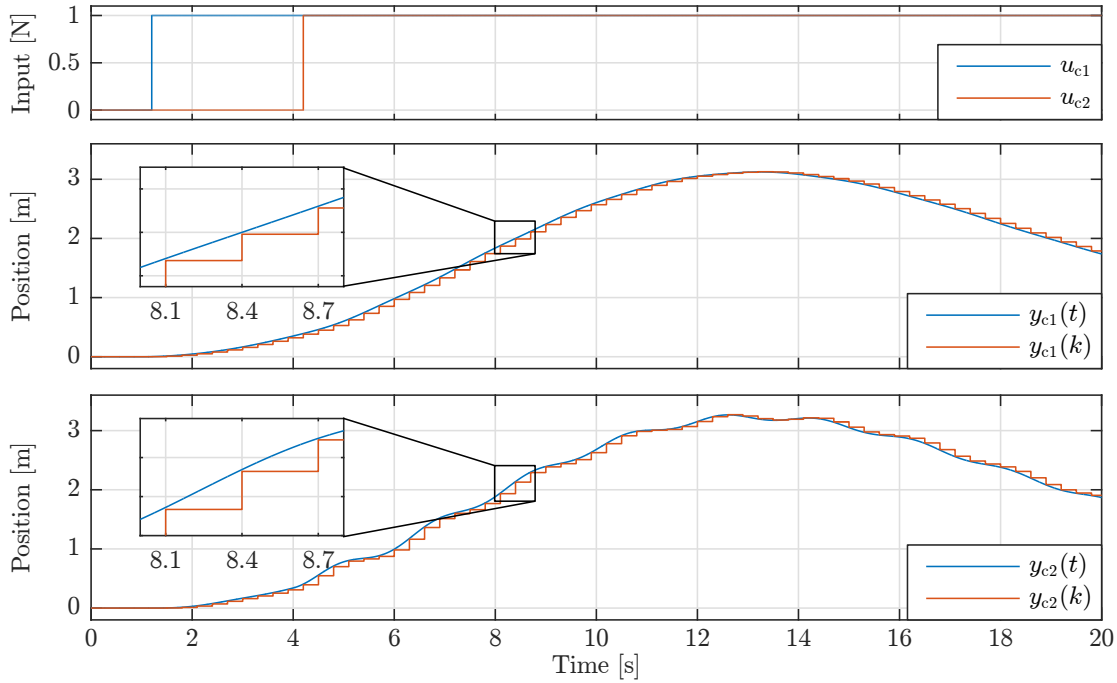
Fig. 4.7: Simulation results for a Matlab Simulink implementation of figure 4.2 and for the model represented by equation 4.22, both utilising similar but different update rates.

The first subplot illustrates the model inputs for both models. The second and third subplots illustrate the response of the cart positions to the step inputs. It can be seen that the outputs of the Kalman and Bertram model only update at a rate corresponding to the BTP, which for the example under consideration approximates the continuous response fairly well. It should, however, also be obvious that if the BTP becomes larger, performing meaningful simulations may become difficult.

This concludes the demonstration of how the method proposed by Kalman and Bertram may be applied to a multirate MIMO system. Again a few remarks on the method in

relation to the presented example are made:

Remark 4.2.H: While Kalman and Bertram's method is fairly simple, it does require careful bookkeeping while deriving the state transitions.

Remark 4.2.I: It may be seen that although the method can describe almost any type of sampled-data system, the periodicity of the sampling scheme is essential if a finite model representation is to be obtained.

Multirate System with Vastly Different Sampling Rates:

This example is the same as the previous multirate example, it does, however, differ in one important aspect, the rate at which the control inputs are updated. The rate of the first input is now $T_1 = 0.15$ s, which is sufficient for controlling the slow dynamics of the heavy cart. The rate of the second input is lower than the first by a factor of $7 \cdot 6/(25 \cdot 4 \cdot 16)$, corresponding to the ratio of DDM activation rates in the 5.4 MW DFPT. This results in $T_2 = 0.0039$ s, allowing for near continuous control of the second cart. With these activation rates the BTP is $T = 3.15$ s and the STP becomes $T_0 = 1.88 \times 10^{-4}$ s.

Step 1 & Step 2: The states and transition matrices are the same as in the previous example, why the reader is referred to those sections.

Step 3 & Step 4: The number of intervals and sampling operations which must be considered to derive the transition equations becomes very large, why this step has been automated by writing an algorithm in MATLAB. An upper bound on the number of intervals is given by $T/T_0 = 16800$, noting that multiple successive STPs may occur before a sampling operation takes places (as is the case in figure 4.6), why the actual number of intervals is less than the upper bound. Furthermore each interval is also preceded by a sampling operation, such that the number of steps which must be considered is upper bounded by $2T/T_0$. Thus setting up the transition equations by hand (as done in equation 4.21) becomes extremely cumbersome, when the ratio T/T_0 becomes large.

As done previously, models using these update rates have been constructed, and the results of the simulations are presented in figure 4.8.

It can now be seen that while the Simulink model produces useful waveforms, the Kalman and Bertram model, although not unstable, completely misses the fast dynamics of the light mass. This result was not unexpected, and the presented example is here used to highlight this problem.

This concludes the example of the method applied to a multirate system with vastly different rates. Again a few final and general remarks are made regarding the method:

Remark 4.2.J: While the presented method produces a model using a state-space formulation, the final model includes multiple input matrices, whereas a conventional state-space formulation contains only a single input matrix. Thus a concern arises when controller design must be considered: How can the multiple input matrices be taken into account? A possible solution could be to see the system as time-variant, and proceed along this path, but this violates the requirement of obtaining
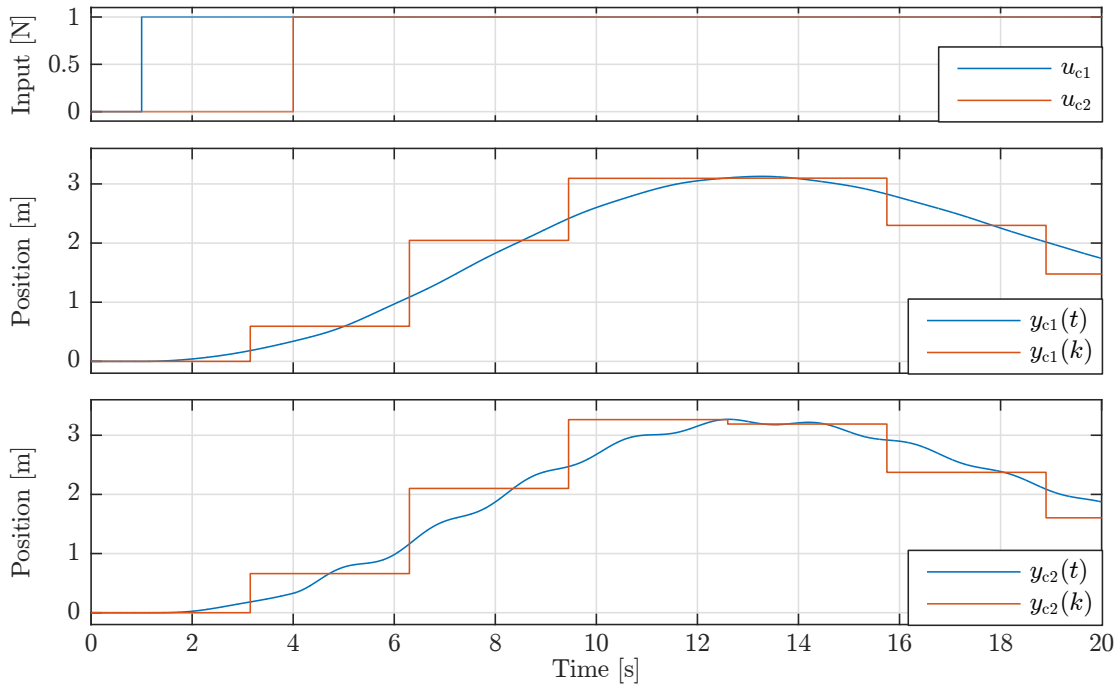
Fig. 4.8: Simulation results for a Matlab Simulink implementation of figure 4.2 and for Kalman and Bertram model, both utilising vastly different control update rates.

a time-invariant multirate model, as defined in section 4.1.

Remark 4.2.K: Furthermore, the method produces a discrete model with a time step equal to the BTP. If system time constants are equal or less than this, then the derived model does not hold much use as a simulation tool. However, all state transitions within the BTP are still contained in the model, and it might still hold potential as a tool for controller design and system analysis. A consequence of the BTP time step, is that control inputs can only be updated with a period corresponding to the BTP, since these transitions are the only thing the model provides analysis and design tools for. This appears rather wasteful, since technically the control inputs can be updated with a period as low as the STP. As for the multiple input matrices, this problem could potentially also be handled by considering a time-variant model of the system.

These concerns remain unsolved, why the Kalman and Bertram model is considered unsuitable. Thus it is decided to investigate a different method for deriving a multirate model, such that a model can be obtained which meets the desirable characteristics.

4.3 Araki and Yamamoto's Non-minimal Realisation

Araki and Yamamoto (1986) presents an approach for describing a multivariable multirate sampled-data system on a discrete-time state-space form. This is also achieved by utilising Kalman and Bertram's method as presented in the previous section, however,

the previously described method produces a model with a time step equal to the BTP without describing the inter-sample behaviour. This poses a problem in systems where the BTP is greater than or equal to the system's time constants. Ideally, a state space model should be formulated with a time step equal to the STP. This is, however, generally not possible without violating the requirement of obtaining a time-invariant state-space model due to the non-uniform multirate sampling and non-uniform behaviour between samplings. As the model formulated by Kalman and Bertram's method does not describe the system states at steps equal to the STP it is not optimal as a simulation tool or controller design tool.

The method presented by Araki and Yamamoto (1986), referred to as Araki and Yamamoto's method, is based on the method originally developed by Kalman and Bertram. Similarly to Kalman and Bertram, the resulting state-space model has a time step equal to the BTP, however, Araki and Yamamoto (1986) has modified Kalman and Bertram's method to describe the states with steps corresponding to the STP. As the time step of the state-space model is equal to the BTP, the model remains time-invariant while describing the states at steps of the STP. This method is also known as the lifting technique.

The method presented in Araki and Yamamoto (1986) only applies to forming a model of continuous dynamic elements and does not directly include an approach for including potential discrete dynamic elements. As Araki and Yamamoto's method is initially based on Kalman and Bertram's method it may be possible to modify Araki and Yamamoto's method, such that it is able to include discrete dynamic elements.

Araki and Yamamoto's method is applied to the MSD system presented in section 4.1.1. The method is initially presented on a general form prior to applying it to the MSD system such that it can be commented upon in a general manner.

Expanded Discrete-time Signals:
The theory which is presented in the following is in general complex why the direct application of the method might not be clear from the equations. Thus, the presentation of the general theory is followed by examples where the theory is applied to ease the understanding of the method.

Applying Araki and Yamamoto's method for describing a system yields a state-space model of the form:

$$\boldsymbol{x}(k+1) = \boldsymbol{G}^{\mathrm{D}}\,\boldsymbol{x}(k) + \boldsymbol{H}^{\mathrm{D}}\,\boldsymbol{u}(k) \tag{4.23a}$$

$$\boldsymbol{y}(k) = \boldsymbol{C}^{\mathrm{D}}\,(\boldsymbol{U_1}\,\boldsymbol{x}(k+1) + \boldsymbol{U_2}\,\boldsymbol{x}(k)) \tag{4.23b}$$

where the matrices $\boldsymbol{G}^{\mathrm{D}}$, $\boldsymbol{H}^{\mathrm{D}}$ and $\boldsymbol{C}^{\mathrm{D}}$ are the discrete equivalents to the $\boldsymbol{A}$, $\boldsymbol{B}$ and $\boldsymbol{C}$ matrices in a continuous state-space model. The block matrices $\boldsymbol{U_1}$ and $\boldsymbol{U_2}$, of equal dimensions, are used to obtain the desired outputs and are given by:

$$\boldsymbol{U_1} \equiv \begin{bmatrix} \boldsymbol{I} & \boldsymbol{0} \\ \boldsymbol{0} & \boldsymbol{0} \end{bmatrix} \qquad \boldsymbol{U_2} \equiv \begin{bmatrix} \boldsymbol{0} & \boldsymbol{0} \\ \boldsymbol{0} & \boldsymbol{I} \end{bmatrix} \begin{matrix} \} N\gamma - \gamma \text{ rows} \\ \} \gamma \text{ rows} \end{matrix} \qquad \begin{matrix} [\boldsymbol{2} \times \boldsymbol{2}] \\ [N\gamma \times N\gamma] \end{matrix} \tag{4.24}$$

where γ is the number of states used to continuously describe the given system and N defines STPs per BTP, i.e. $N = T/T_0$ where T_0 is equal to the STP.

Remark 4.3.A: The output vector $\boldsymbol{y}(k)$ depends on both $\boldsymbol{x}(k)$ and $\boldsymbol{x}(k+1)$. The dependence on $\boldsymbol{x}(k+1)$ is unconventional in discrete state-space models, however, this is a consequence of how the discrete states and outputs are defined.

Remark 4.3.B: The definition of the output equation makes sense when it is compared to the discrete-time signals in figure 4.9. However, it may be noted that it may be combined with the state equation to obtain a conventional output equation of the form $\boldsymbol{y}(k) = \boldsymbol{Cx}(k) + \boldsymbol{Du}(k)$.

Remark 4.3.C: When simulating a model represented by equation 4.23, the state transition equation is normally calculated before the output equation. Thereby $\boldsymbol{x}(k+1)$ is available when calculating the output, and thus there are no timing conflicts regarding availability of data.

Before the method is presented some definitions are established. The time step of the ith component is defined as:

$$T_i \equiv \frac{T}{N_i} \qquad\qquad i = \{1, \ldots, p\} \qquad\qquad (4.25)$$

where p describes the number of inputs or outputs in the continuous representation of the system. The constant $\bar{N}$ is introduced as the sum of N_i as $\bar{N} = N_1 + N_2 + ... + N_p$ and l_i defines STPs per time step for the ith component, i.e. $l_i = T_i/T_0$.

Figure 4.9 illustrates a sampling scheme, where Araki and Yamamoto's method is applied, for a system where $N_1 = 2$, $N_2 = 3$ and $N = 6$ and which can be continuously described with $\gamma = 4$ states and with $p = 2$ inputs and outputs. The figure shows the instants where the inputs are updated including the corresponding discrete states and outputs.
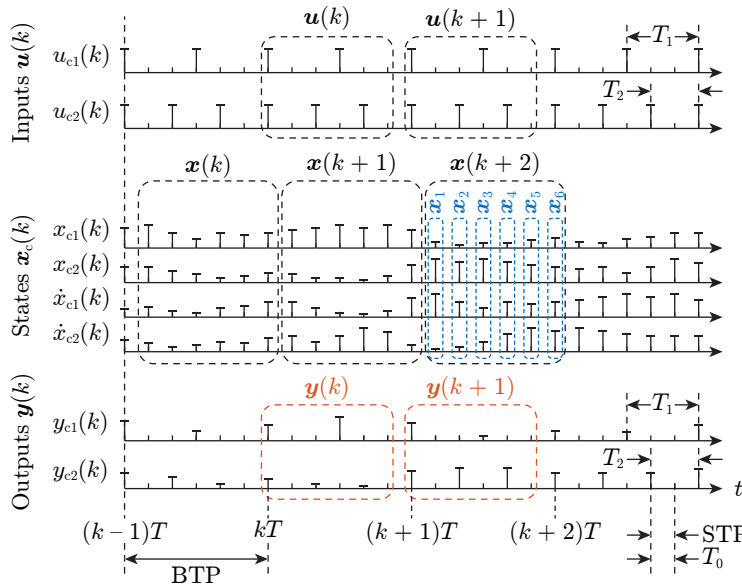
Fig. 4.9: Discrete-time signals including inputs, outputs and states for a system with $\gamma = 4$ continuous states and $p = 2$ inputs and outputs. Inspired by Araki and Yamamoto (1986).

From figure 4.9 it is evident how the discrete-time state vector $\boldsymbol{x}(k)$ contains information about each of the 4 continuous states with a time step equal to the STP. Figure 4.9 furthermore shows that the state vector $\boldsymbol{x}(k+1)$ is given from information from the input vector $\boldsymbol{u}(k)$ and the last subvector $\boldsymbol{x}_6(k)$ of $\boldsymbol{x}(k)$. In accordance with the sampling scheme shown in figure 4.9, equations describing the discrete states, inputs and outputs can be presented on a general form.

Araki and Yamamoto forms an expanded discrete-time state vector, $\boldsymbol{x}(k)$, describing the states of a sampled-data system, here shown as a block vector:

$$\boldsymbol{x}(k) \equiv \begin{bmatrix} \boldsymbol{x}_1(k) \\ \vdots \\ \boldsymbol{x}_{N-1}(k) \\ \boldsymbol{x}_N(k) \end{bmatrix} = \begin{bmatrix} \boldsymbol{x}_c((k-1)T + T_0) \\ \vdots \\ \boldsymbol{x}_c((k-1)T + (N-1)T_0) \\ \boldsymbol{x}_c(kT) \end{bmatrix} \qquad \begin{matrix} [\boldsymbol{N} \times \boldsymbol{1}] \\ [N\gamma \times 1] \end{matrix} \qquad (4.26)$$

It is clear that the discrete time state vector describes the set of states, $\boldsymbol{x_c}$, with a time step equal to the STP.

The expanded discrete-time output vector are given by the block vector:

$$\boldsymbol{y}(k) \equiv \begin{bmatrix} \boldsymbol{y}_1(k)^\mathsf{T} & \cdots & \boldsymbol{y}_p(k)^\mathsf{T} \end{bmatrix}^\mathsf{T} \qquad \begin{matrix} [\boldsymbol{p} \times \boldsymbol{1}] \\ [\bar{N} \times 1] \end{matrix} \qquad (4.27)$$

where each element, $\boldsymbol{y}_i$, is given by a N_i-dimensional vector:

$$\boldsymbol{y}_i(k) \equiv \begin{bmatrix} y_{i,0}(k) \\ y_{i,1}(k) \\ \vdots \\ y_{i,N_i-1}(k) \end{bmatrix} = \begin{bmatrix} y_i(kT) \\ y_i(kT + T_i) \\ \vdots \\ y_i(kT + (N_i-1)T_i) \end{bmatrix} \qquad [N_i \times 1] \qquad (4.28)$$

The input vector is not shown since it is equal to the output vector in terms of dimension and the time instants at which they are described. It is evident that the discrete-time input and output vectors describes the input and outputs at the T_i time steps.

Remark 4.3.D: As the state vector $\boldsymbol{x}(k+1)$ only depends on the input vector $\boldsymbol{u}(k)$ and the last subvector $\boldsymbol{x}_N(k)$ of $\boldsymbol{x}(k)$, the subvectors $\boldsymbol{x}_1(k)$ to $\boldsymbol{x}_{N-1}(k)$ could be omitted. Including these subvectors yields a non-minimal realisation which is desired in this case since all continuous states are then described uniformly with a time step of the STP.

Remark 4.3.E: As evident from equation 4.26, the number of states in the discrete-time state-space model is equal to $N\gamma$. A consequence of having vastly different sampling rates in a system may be that the N-parameter becomes relatively large which will thus result in a large number of discrete-time states. Thus, writing computer algorithms is necessary when forming the model since it may not be possible to apply the method by hand to a system with vastly different sampling rates. This is also the reason why the method will be applied to a system with similar but different sampling rates initially to ease the understanding of the method by being able to visualise the resulting discrete-time state space model.

Remark 4.3.F: Applying Araki and Yamamoto's method yields an input and output vector which is $\bar{N} \times 1$ dimensional. Thus, discretisation using this method means that the number of input and outputs are increased compared to the continuous state-space model of the system. It is, however, important to note that the number of inputs and outputs are equal in the discrete state-space model, which is considered an advantage when controller design is to be considered.

Remark 4.3.G: With reference to both figure 4.9 and equation 4.23, the relative position of the $\boldsymbol{x}(k)$, $\boldsymbol{u}(k)$ and $\boldsymbol{y}(k)$ blocks to one and another might at first seem unintuitive, but as will be illustrated, it is logical.

Consider first a single rate example, as later illustrated by an example and with figure 4.11. Then it may be seen that the blocks are all aligned, as is typically the case for discrete models. This corresponds well with the model formulation in equation 4.23, which states that both $\boldsymbol{x}(k)$ and $\boldsymbol{u}(k)$ must be available at the same time instance to calculate $\boldsymbol{x}(k+1)$.

Consider then again the multirate situation of figure 4.9, if $\boldsymbol{u}(k)$ is not shifted to be semi-aligned with $\boldsymbol{x}(k+1)$, then a number of new inputs would occur during $\boldsymbol{x}(k+1)$, which would not be used to calculate the transitions, and without these it would not be possible to arrive at the correct final value $\boldsymbol{x_6}(k+1)$. Thus the alignment of $\boldsymbol{u}(k)$, $\boldsymbol{x}(k)$ and $\boldsymbol{x}(k+1)$ could not be any other way. The first subvector in $\boldsymbol{u}(k)$ must be aligned with the last subvector in $\boldsymbol{x}(k)$ to be able to describe single rate systems, and $\boldsymbol{u}(k)$, must be semi-aligned with $\boldsymbol{x}(k+1)$ to correctly arrive at the final value.

Generally it may be stated that when the sampling rates diverge, the $\boldsymbol{u}(k)$ block will extend to the right, and the $\boldsymbol{x}(k)$ block to the left.

The alignment of the blocks in figure 4.9 is further considered in appendix D.1, where it is shown that if a state vector in the conventional form is to be obtained, i.e. $\boldsymbol{x}(k+1) = \boldsymbol{G}\boldsymbol{x}(k) + \boldsymbol{H}\boldsymbol{u}(k)$, then the only viable alignment is the one illustrated in figure 4.9.

Remark 4.3.H: The unconventional form, both with regard to the state vector and output equation, of the state-space model produced by applying Araki and Yamamoto's method is a consequence of the states being lifted. This form is, however, a necessity in order to obtain a linear time-invariant model which is a requirement in this thesis, cf. requirement 2 in section 4.1. Even though the model is linear time-invariant, controller design may not be straight forward due to this unconventional form. However, several studies, including Guo and Liao (2016), Lee (2006), and Tangirala et al. (2001), each referring to multiple other studies, considers controller design for a model constructed based on lifting theory. Due to the lifting method and subsequent controller design being well documented it is decided to move forward with this approach.

Having presented the input, output and state vector, the next section describes how the open-loop system matrices are formed.

Open-loop System Matrices:

This section presents how the open-loop system matrices $\boldsymbol{G}^{\mathrm{D}}$, $\boldsymbol{H}^{\mathrm{D}}$ and $\boldsymbol{C}^{\mathrm{D}}$ are calculated. As previously stated only the last subvector, $\boldsymbol{x}_N(k)$, of $\boldsymbol{x}(k)$ is used for describing the state vector $\boldsymbol{x}(k+1)$. Thus, the $\boldsymbol{G}^{\mathrm{D}}$-matrix becomes a block matrix given by:

$$
\boldsymbol{G}^{\mathrm{D}} \equiv
\begin{bmatrix}
\boldsymbol{0} & \cdots & \boldsymbol{0} & \boldsymbol{G_c}(T_0) \\
\vdots & \ddots & \vdots & \vdots \\
\boldsymbol{0} & \cdots & \boldsymbol{0} & \boldsymbol{G_c}(N\,T_0)
\end{bmatrix}
\qquad
\begin{array}{c}
[\boldsymbol{N} \times \boldsymbol{N}] \\
[N\gamma \times N\gamma]
\end{array}
\qquad (4.29)
$$

It is clear that the zero block matrices ensures that only the last subvector, $\boldsymbol{x}_N(k)$, of $\boldsymbol{x}(k)$ is used for describing the state vector $\boldsymbol{x}(k+1)$. The $\boldsymbol{G_c}(l\,T_0)$-matrices are calculated as shown for the Kalman and Bertram method in equation 4.5 where τ is replaced with $l\,T_0$ such that a time step equal to the STP is obtained in this case:

$$
\boldsymbol{G_c}(l\,T_0) = \boldsymbol{G}^{\mathrm{D}}_l = e^{\boldsymbol{A}\,l\,T_0} \qquad l = \{1, ..., N\} \qquad [\gamma \times \gamma] \qquad (4.30)
$$

$\boldsymbol{H}^{\mathrm{D}}$ in equation 4.23 is a block matrix defined as:

$$
\boldsymbol{H}^{\mathrm{D}} \equiv \begin{bmatrix} \boldsymbol{H}^{\mathrm{D}}_1 & \cdots & \boldsymbol{H}^{\mathrm{D}}_p \end{bmatrix}
\qquad
\begin{array}{c}
[\boldsymbol{1} \times \boldsymbol{p}] \\
[N\gamma \times N]
\end{array}
\qquad (4.31)
$$

Each block in the $\boldsymbol{H}^{\mathrm{D}}$-matrix are block matrices given by:

$$
\boldsymbol{H}^{\mathrm{D}}_i = \begin{bmatrix} \boldsymbol{h}^{\mathrm{D}}_{i,l\mu} \end{bmatrix}, \quad i = \{1, ..., p\}, l = \{1, ..., N\}, \mu = \{0, ..., N_i - 1\} \quad [N\gamma \times N_i] \quad (4.32)
$$

The subscript l defines the row number and $\mu + 1$ defines the column number. The variable λ_l is introduced to obtain a more compact expression and is defined as:

$$
\lambda_l = lT_0 - \tau \qquad l = \{1, ..., N\} \qquad (4.33)
$$

Each $\boldsymbol{h}^{\mathrm{D}}_{i,l\mu}$ element is then given by:

$$
\boldsymbol{h}^{\mathrm{D}}_{i,l\mu} =
\begin{cases}
\boldsymbol{0}, & \text{if } l \le \mu l_i \\[2mm]
\displaystyle\int_{\mu\, l_i\, T_0}^{l\,T_0} e^{\boldsymbol{A}\lambda_l} \boldsymbol{b}_{j=i}\, d\tau, & \text{if } \mu\, l_i < l \le (\mu+1)l_i \\[2mm]
\displaystyle\int_{\mu\, l_i\, T_0}^{(\mu+1)l_i\, T_0} e^{\boldsymbol{A}\lambda_l} \boldsymbol{b}_{j=i}\, d\tau, & \text{if } (\mu+1)\, l_i < l
\end{cases}
\qquad [\gamma \times 1] \qquad (4.34)
$$

$\boldsymbol{b}_j$ is the jth column of the $\boldsymbol{B}$-matrix from the continuous state-space representation. The three conditions presented in equation 4.34 are used to obtain elements in the $\boldsymbol{H}^{\mathrm{D}}$-matrix such that the elements in the input vector only affects the desired outputs. This will be more clear when the method is applied to various examples in the following sections. Comparing equation 4.34 with equation 4.5 it is seen that calculating the $\boldsymbol{H}$-matrix in the Kalman and Bertram method and $\boldsymbol{h}^{\mathrm{D}}_{i,l\mu}$ in Araki and Yamamoto's method is similar, but different in the limits over which the integrals are evaluated.

The $\boldsymbol{C}^{\mathrm{D}}$-matrix shown in equation 4.23 is a block matrix defined as:

$$\boldsymbol{C}^{\mathrm{D}} \equiv \begin{bmatrix} \boldsymbol{C}_1^{\mathrm{D}\intercal} & \cdots & \boldsymbol{C}_p^{\mathrm{D}\intercal} \end{bmatrix}^{\intercal} \qquad \begin{matrix} [\boldsymbol{p} \times \boldsymbol{1}] \\ [\bar{N} \times N\gamma] \end{matrix} \qquad (4.35)$$

Each block is given by $N_j \times N$ block matrices as:

$$\boldsymbol{C}_j^{\mathrm{D}} = \begin{bmatrix} \boldsymbol{c}_{j,vl}^{\mathrm{D}} \end{bmatrix} \quad j = \{1, ..., p\}, v = \{0, ..., N_j - 1\}, l = \{1, ..., N\} \quad [N_j \times N\gamma] \quad (4.36)$$

The row number of the block matrices in $\boldsymbol{C}_j^{\mathrm{D}}$ are described by $v + 1$ and the column number by l. The blocks matrices $\boldsymbol{c}_{j,vl}^{\mathrm{D}}$ are defined as:

$$\boldsymbol{c}_{j,vl}^{\mathrm{D}} = \begin{cases} \boldsymbol{c}_{i=j} & \text{if } v = 0 \wedge l = N \vee v\, l_j = l \\ \boldsymbol{0}, & \text{else} \end{cases} \qquad [1 \times \gamma] \qquad (4.37)$$

$\boldsymbol{c}_i$ is the ith row of the $\boldsymbol{C}$-matrix used for the continuous state space representation.

Remark 4.3.I: From the above presented open-loop equations it can be shown that applying Araki and Yamamoto's method to a single rate system corresponds to simply performing a conventional zero-order hold discretisation to a given system. This will be evident from the examples presented in the next section.

Remark 4.3.J: As previously stated, Araki and Yamamoto's method is only directly applicable for describing an open-loop system. This is, however, an advantage when the method is to be applied to the DFPT since it is desired to perform an open-loop system analysis with regards to potential system cross couplings. Furthermore, an open-loop description is advantageous for controller design.

Remark 4.3.K: Araki and Yamamoto's method does not directly present an approach for including discrete dynamic elements in the model. Further effort should therefore be put into this method before it is applied to the DFPT.

Remark 4.3.L: Applying Araki and Yamamoto's method yields multiple evaluations of the integrals presented in Equation 4.34 for calculating the $\boldsymbol{H}^{\mathrm{D}}$-matrix. This might not pose a problem when applied to a system with different but similar sampling rates as this limits the number of evaluations. However, when applied to a system with vastly different sampling rates, the number of evaluations might increase extensively why the relatively computational heavy operation of numerical integral evaluations may yield problems with time consumption of the state-space model formulation. Thus, applying Araki and Yamamoto's method to a system with vastly different sampling rates requires intelligent scripting to reduce the time consumption of the model formulation.

Having presented the tools and theory necessary for applying Araki and Yamamoto's method to the mass spring damper system, the next section presents various examples similar to the ones presented for Kalman and Bertram's method.

4.3.1 Various Examples

Three examples are presented in the following where the first examples applies Araki and Yamamoto's method to the single rate sampled MSD system.

Single Rate System:

A single sample rate of $T = 1/10$ s is utilised and all samplers are synchronised. Figure 4.10 shows the open loop system which are to be discretely described by applying Araki and Yamamoto's method.
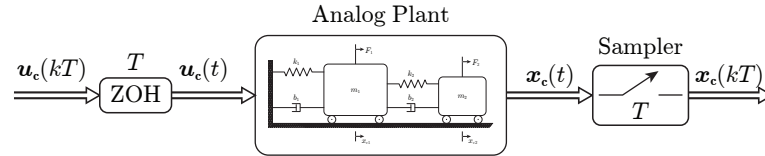
Fig. 4.10: Block diagram representation of the physical open-loop MSD system, with sampled outputs and zero-order held inputs operated at a single rate.

The input is seen to be the system input sampled with a time step equal to T whereas the output is seen to be the state vector $\boldsymbol{x_c}(kT)$. Alternatively to the state, the output $\boldsymbol{y_c}(kT)$ could have been illustrated since the only difference between the two vectors is the multiplication of the $\boldsymbol{C}_\mathrm{D}$ and $\boldsymbol{U_2}$ matrices. As previously presented, the system can be continuously described by $\gamma = 4$ states. Utilising the notation presented for Araki and Yamamoto's method, $T = T_0 = T_1 = T_2 = 1/10$ s, and $N = N_1 = N_2 = 1$. Utilising a single sample rate in the double MSD system yields a 4×1 state vector:

$$\boldsymbol{x}(k) = [\boldsymbol{x}_1(k)] = [\boldsymbol{x}_\mathrm{c}(kT)] = \begin{bmatrix} x_{\mathrm{c}1}(kT) & x_{\mathrm{c}2}(kT) & \dot{x}_{\mathrm{c}1}(kT) & \dot{x}_{\mathrm{c}2}(kT) \end{bmatrix}^\mathsf{T} \qquad (4.38)$$

The state vector simply contains the four continuous states sampled at the single sample rate of T. Similarly, the input and output vectors are given by:

$$\boldsymbol{u}(k) = \boldsymbol{u_c}(kT) = \begin{bmatrix} u_{\mathrm{c}1}(kT) & u_{\mathrm{c}2}(kT) \end{bmatrix}^\mathsf{T} \qquad (4.39)$$

$$\boldsymbol{y}(k) = \boldsymbol{y_c}(kT) = \begin{bmatrix} y_{\mathrm{c}1}(kT) & y_{\mathrm{c}2}(kT) \end{bmatrix}^\mathsf{T} \qquad (4.40)$$

Figure 4.11 depicts the sampling scheme when Araki and Yamamoto's method is applied. The top part shows the continuous state progression, i.e. the states in the physical system while the bottom part shows the instants at which the inputs, states and outputs are described in the discrete state-space model. The discrete state $\boldsymbol{x}(k)$ is seen to include the four states sampled with time steps equal to T as shown in equation 4.38.

Having determined the discrete-time states, inputs and outputs, the open-loop equations can be applied to form a state-space model.
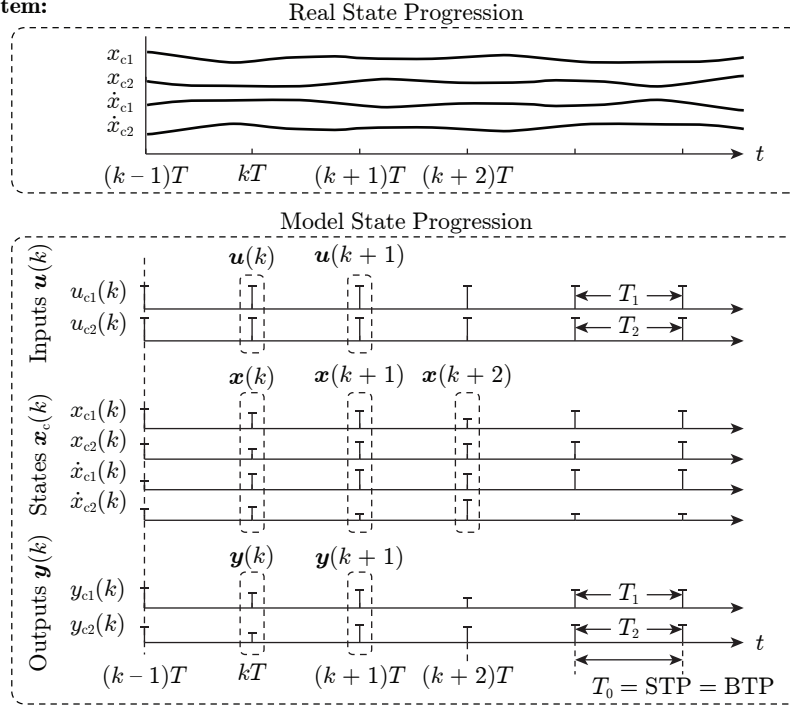
Fig. 4.11: Top part shows the continuous state progression, i.e. the states in the physical system. Bottom part shows the instants at which the inputs, states and outputs are described in the discrete model.

As $N = 1$, the $\boldsymbol{G}^{\mathrm{D}}$-matrix becomes a 1×1 block matrix where the block $\boldsymbol{G}_1^{\mathrm{D}}$ is a 4×4-dimensional matrix. Applying equation 4.30 yields the following $\boldsymbol{G}^{\mathrm{D}}$-matrix:

$$\boldsymbol{G}^{\mathrm{D}} = \begin{bmatrix} \boldsymbol{G}_1^{\mathrm{D}} \end{bmatrix} = \begin{bmatrix} e^{\boldsymbol{A}T} \end{bmatrix} \tag{4.41}$$

The $\boldsymbol{H}^{\mathrm{D}}$-matrix is in this example a 1×2 block vector where the vectors $\boldsymbol{h}_{1,10}^{\mathrm{D}}$ and $\boldsymbol{h}_{2,10}^{\mathrm{D}}$ are determined from equation 4.34:

$$\boldsymbol{H}^{\mathrm{D}} = \begin{bmatrix} \boldsymbol{H}_1^{\mathrm{D}} & \boldsymbol{H}_2^{\mathrm{D}} \end{bmatrix} = \begin{bmatrix} \boldsymbol{h}_{1,10}^{\mathrm{D}} & \boldsymbol{h}_{2,10}^{\mathrm{D}} \end{bmatrix} \tag{4.42}$$

$$= \begin{bmatrix} \int_0^T e^{\boldsymbol{A}\lambda_1} \boldsymbol{b}_{j=1} \, d\tau & \int_0^T e^{\boldsymbol{A}\lambda_1} \boldsymbol{b}_{j=2} \, d\tau \end{bmatrix}$$

where $\lambda_1 = T - \tau$. The $\boldsymbol{C}^{\mathrm{D}}$-matrix is for the single rate example equal to the $\boldsymbol{C}$-matrix utilised in the continuous state-space model.

The presented equations for the single rate system are inserted into equation 4.23 to yield

a model on state-space form:

$$
\overbrace{\begin{bmatrix} \boldsymbol{x}_1(k+1) \end{bmatrix}}^{\boldsymbol{x}(k+1)} = \overbrace{\begin{bmatrix} e^{\boldsymbol{A}T} \end{bmatrix}}^{\boldsymbol{G}^{\mathrm{D}}} \overbrace{\begin{bmatrix} \boldsymbol{x}_1(k) \end{bmatrix}}^{\boldsymbol{x}(k)} + \overbrace{\begin{bmatrix} \int\limits_0^T e^{\boldsymbol{A}\lambda_1}\boldsymbol{b}_{j=1}\ d\tau & \int\limits_0^T e^{\boldsymbol{A}\lambda_1}\boldsymbol{b}_{j=2}\ d\tau \end{bmatrix}}^{\boldsymbol{H}^{\mathrm{D}}} \overbrace{\begin{bmatrix} u_{\mathrm{c}1}(kT) \\ u_{\mathrm{c}2}(kT) \end{bmatrix}}^{\boldsymbol{u}(k)} \quad \text{(4.43a)}
$$

$$
\underbrace{\begin{bmatrix} y_{\mathrm{c}1}(kT) \\ y_{\mathrm{c}2}(kT) \end{bmatrix}}_{\boldsymbol{y}(k)} = \underbrace{\begin{bmatrix} \boldsymbol{c}_1 \\ \boldsymbol{c}_2 \end{bmatrix}}_{\boldsymbol{C}^{\mathrm{D}}} \underbrace{\begin{bmatrix} \boldsymbol{x}_1(k) \end{bmatrix}}_{\boldsymbol{x}(k)} \qquad\qquad\qquad\qquad\qquad\qquad\qquad\qquad \text{(4.43b)}
$$

The open-loop system presented in figure 4.10 is implemented in MATLAB Simulink and simulated in order to compare it to the discrete state-space model in equation 4.43. Both models are applied with the same inputs with an update rate of $T = 1/10$ s. Figure 4.12 shows the position of the two simulations where the first subplot illustrates the inputs given to the two models, the second subplot shows the position response from the Simulink model and the third subplot illustrates the response from the state-space model. For the state-space model, the two outputs are plotted using zero-order hold line interpolation between subsequent data points which leads to the stair-like appearance of the waveforms. This will also be the case in the following simulation plots.
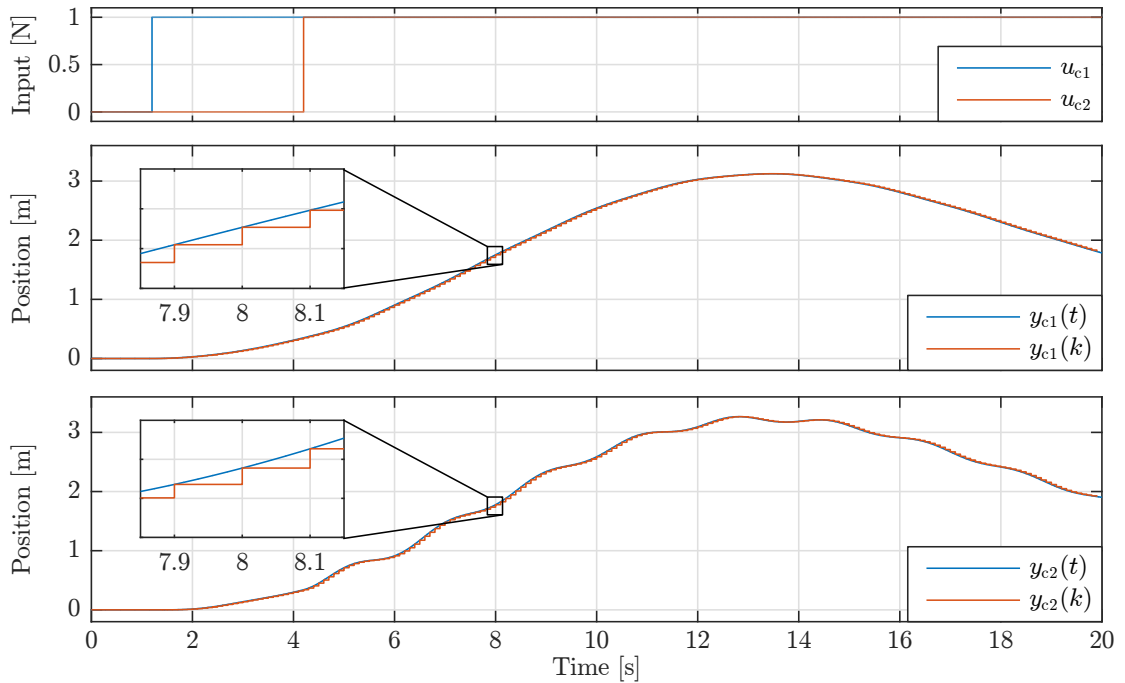
Fig. 4.12: Simulation results for a MATLAB Simulink implementation of figure 4.10 and for Araki and Yamamoto's state-space model, utilising equal sampling rates.

Based on the simulation shown in figure 4.12 it is clear that applying Araki and Yamamoto's method produces a state-space model with the same response as the model implemented in Simulink.

Remark 4.3.M: It is evident from equations 4.41 and 4.42 that applying Araki and Yamamoto's method to a single rate sampled system yields a discretisation which corresponds exactly to applying a conventional zero-order hold dicretisation to the system. This was also shown to be the case when applying Kalman and Bertram's methods to a single rate system.

Multirate System with Similar Sampling Rates:

Again, the MSD system is considered. As for Kalman and Bertram's method the system is now modified to utilise two different sampling rates, being $T_1 = T/2 = 0.15\,\text{s}$ and $T_2 = T/3 = 0.1\,\text{s}$ and a BTP of $T = 0.3\,\text{s}$. These sampling times yields a STP $= T_0 = 0.05\,\text{s}$. Thus, $N = 6$, $N_1 = 2$ and $N_2 = 3$. Figure 4.13 shows an open-loop block diagram of the system described using Araki and Yamamoto's method.
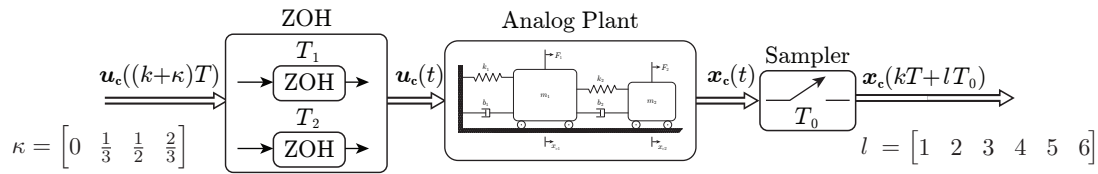
Fig. 4.13: Block diagram representation of the physical open-loop MSD system, with sampled outputs and zero-order held inputs operated at two different but similar rates.

Applying Araki and Yamamoto's method results in the following 24×1 state vector for the given sampling rates:

$$
\boldsymbol{x}(k) = \begin{bmatrix} \boldsymbol{x}_1(k) \\ \boldsymbol{x}_2(k) \\ \boldsymbol{x}_3(k) \\ \boldsymbol{x}_4(k) \\ \boldsymbol{x}_5(k) \\ \boldsymbol{x}_6(k) \end{bmatrix} = \begin{bmatrix} \boldsymbol{x}_\text{c}((k-1)T + T_0) \\ \boldsymbol{x}_\text{c}((k-1)T + 2\,T_0) \\ \boldsymbol{x}_\text{c}((k-1)T + 3\,T_0) \\ \boldsymbol{x}_\text{c}((k-1)T + 4\,T_0) \\ \boldsymbol{x}_\text{c}((k-1)T + 5\,T_0) \\ \boldsymbol{x}_\text{c}(kT) \end{bmatrix} \tag{4.44}
$$

It is clear that applying Araki and Yamamoto's method yields a state vector described with time steps equal to the STP. The input and output are given by the 5×1 vectors:

$$
\boldsymbol{u}(k) = \begin{bmatrix} u_\text{c1}(kT) \\ u_\text{c1}(kT + T_1) \\ u_\text{c2}(kT) \\ u_\text{c2}(kT + T_2) \\ u_\text{c2}(kT + 2\,T_2) \end{bmatrix} \qquad \boldsymbol{y}(k) = \begin{bmatrix} y_\text{c1}(kT) \\ y_\text{c1}(kT + T_1) \\ y_\text{c2}(kT) \\ y_\text{c2}(kT + T_2) \\ y_\text{c2}(kT + 2\,T_2) \end{bmatrix} \tag{4.45}
$$

77

Figure 4.14 shows the sampling scheme for the multirate MSD system.

Fig. 4.14: Top part shows example of the real state progression while the second part shows the instants at which the input, states and outputs are described in the discrete model.

The top part shows an example of the real state progression while the second part shows the instants at which the input, states and outputs are described in the discrete model. It is clear that the discrete inputs, states and outputs in figure 4.14 corresponds well with equations 4.44 and 4.45, e.g. the input vector $\boldsymbol{u}(k)$ has five samples, two for $u_{c1}(k)$ and three for $u_{c2}(k)$.

Next the open-loop system matrices are formed. Applying equation 4.30 yields the following 24×24 $\boldsymbol{G}^{\mathrm{D}}$-matrix for the system:

$$
\boldsymbol{G}^{\mathrm{D}} = \left[\begin{array}{c|c} & e^{\boldsymbol{A}\,T_0} \\ & e^{\boldsymbol{A}\,2\,T_0} \\ \boldsymbol{0} & e^{\boldsymbol{A}\,3\,T_0} \\ & e^{\boldsymbol{A}\,4\,T_0} \\ & e^{\boldsymbol{A}\,5\,T_0} \\ & e^{\boldsymbol{A}\,6\,T_0} \end{array}\right] \tag{4.46}
$$

The $\boldsymbol{H}^{\mathrm{D}}$-matrix is given by the following matrix where each element yields a 4×1 vector:

$$
\boldsymbol{H}^{\mathrm{D}} = \left[\begin{array}{c|c|c|c|c}
\int\limits_{0}^{T_0} e^{\boldsymbol{A}\lambda_1}\boldsymbol{b}_1 d\tau & \boldsymbol{0} & \int\limits_{0}^{T_0} e^{\boldsymbol{A}\lambda_1}\boldsymbol{b}_2 d\tau & \boldsymbol{0} & \boldsymbol{0} \\ \hline
\int\limits_{0}^{2T_0} e^{\boldsymbol{A}\lambda_2}\boldsymbol{b}_1 d\tau & \boldsymbol{0} & \int\limits_{0}^{2T_0} e^{\boldsymbol{A}\lambda_2}\boldsymbol{b}_2 d\tau & \boldsymbol{0} & \boldsymbol{0} \\ \hline
\int\limits_{0}^{3T_0} e^{\boldsymbol{A}\lambda_3}\boldsymbol{b}_1 d\tau & \boldsymbol{0} & \int\limits_{0}^{2T_0} e^{\boldsymbol{A}\lambda_3}\boldsymbol{b}_2 d\tau & \int\limits_{2T_0}^{3T_0} e^{\boldsymbol{A}\lambda_3}\boldsymbol{b}_2 d\tau & \boldsymbol{0} \\ \hline
\int\limits_{0}^{3T_0} e^{\boldsymbol{A}\lambda_4}\boldsymbol{b}_1 d\tau & \int\limits_{3T_0}^{4T_0} e^{\boldsymbol{A}\lambda_4}\boldsymbol{b}_1 d\tau & \int\limits_{0}^{2T_0} e^{\boldsymbol{A}\lambda_4}\boldsymbol{b}_2 d\tau & \int\limits_{2T_0}^{4T_0} e^{\boldsymbol{A}\lambda_4}\boldsymbol{b}_2 d\tau & \boldsymbol{0} \\ \hline
\int\limits_{0}^{3T_0} e^{\boldsymbol{A}\lambda_5}\boldsymbol{b}_1 d\tau & \int\limits_{3T_0}^{5T_0} e^{\boldsymbol{A}\lambda_5}\boldsymbol{b}_1 d\tau & \int\limits_{0}^{2T_0} e^{\boldsymbol{A}\lambda_5}\boldsymbol{b}_2 d\tau & \int\limits_{2T_0}^{4T_0} e^{\boldsymbol{A}\lambda_5}\boldsymbol{b}_2 d\tau & \int\limits_{4T_0}^{5T_0} e^{\boldsymbol{A}\lambda_5}\boldsymbol{b}_2 d\tau \\ \hline
\int\limits_{0}^{3T_0} e^{\boldsymbol{A}\lambda_6}\boldsymbol{b}_1 d\tau & \int\limits_{3T_0}^{6T_0} e^{\boldsymbol{A}\lambda_6}\boldsymbol{b}_1 d\tau & \int\limits_{0}^{2T_0} e^{\boldsymbol{A}\lambda_6}\boldsymbol{b}_2 d\tau & \int\limits_{2T_0}^{4T_0} e^{\boldsymbol{A}\lambda_6}\boldsymbol{b}_2 d\tau & \int\limits_{4T_0}^{6T_0} e^{\boldsymbol{A}\lambda_6}\boldsymbol{b}_2 d\tau
\end{array} \right] \tag{4.47}
$$

The $\boldsymbol{C}^{\mathrm{D}}$-matrix is for the multirate example is given by the $\bar{N} \times N$ block matrix:

$$
\boldsymbol{C}^{\mathrm{D}} = \begin{bmatrix}
\boldsymbol{0} & \boldsymbol{0} & \boldsymbol{0} & \boldsymbol{0} & \boldsymbol{0} & \boldsymbol{c}_1 \\
\boldsymbol{0} & \boldsymbol{0} & \boldsymbol{c}_1 & \boldsymbol{0} & \boldsymbol{0} & \boldsymbol{0} \\
\boldsymbol{0} & \boldsymbol{0} & \boldsymbol{0} & \boldsymbol{0} & \boldsymbol{0} & \boldsymbol{c}_2 \\
\boldsymbol{0} & \boldsymbol{c}_2 & \boldsymbol{0} & \boldsymbol{0} & \boldsymbol{0} & \boldsymbol{0} \\
\boldsymbol{0} & \boldsymbol{0} & \boldsymbol{0} & \boldsymbol{c}_2 & \boldsymbol{0} & \boldsymbol{0}
\end{bmatrix} \tag{4.48}
$$

Inserting the open-loop system matrices, $\boldsymbol{G}^{\mathrm{D}}$, $\boldsymbol{H}^{\mathrm{D}}$ and $\boldsymbol{C}^{\mathrm{D}}$ into the discrete state equation presented in equation 4.23 yields a model on state-space form. The model is, however, not explicitly presented here due to its size. The obtained state-space model corresponds well with the sampling scheme presented in figure 4.14. As an example, when the state subvector $\boldsymbol{x}_{\boldsymbol{c}}(kT + T_0)$ is described, it only depends on the states $\boldsymbol{x}_6(k)$ and the inputs $u_{\mathrm{c}1}(kT)$ and $u_{\mathrm{c}2}(kT)$ due to the zeros in the $\boldsymbol{G}^{\mathrm{D}}$ and $\boldsymbol{H}^{\mathrm{D}}$ matrices.

Similar to the previous example, the position response of the obtained state-space model is compared to the response of the open-loop system presented in figure 4.13 implemented in MATLAB Simulink. The simulation results are shown in figure 4.15, where the first subplot shows the inputs for the two models. The second and third subplots compares the position response of the two blocks from the two models.
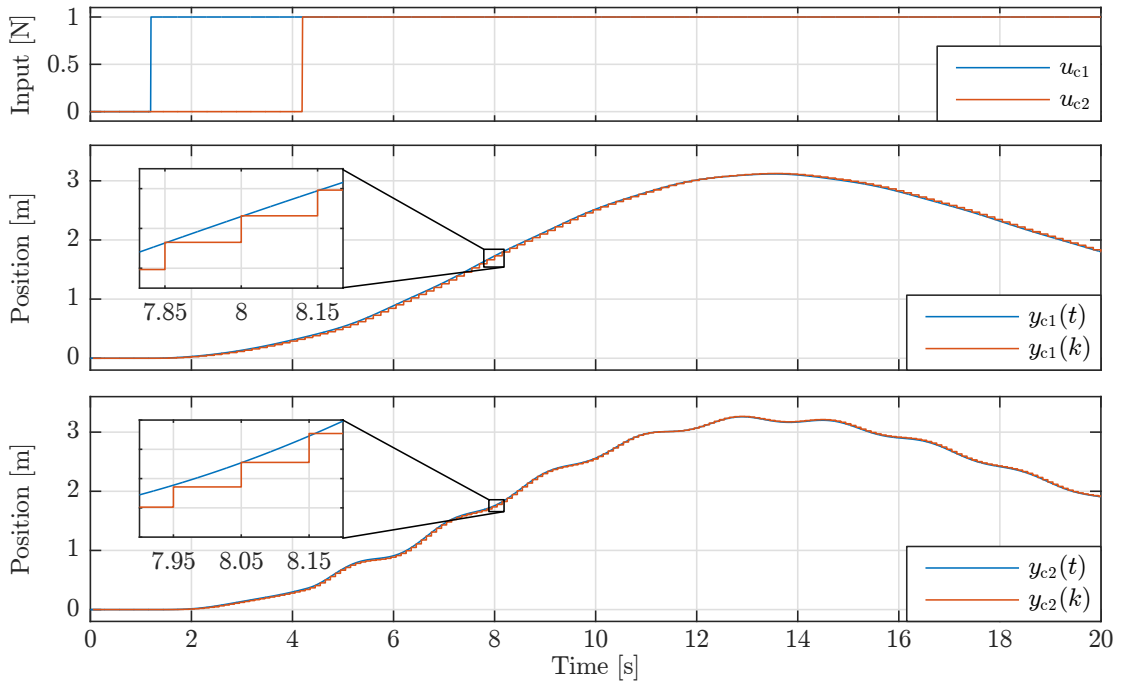
Fig. 4.15: Simulation results for a MATLAB Simulink implementation of figure 4.13 and for Araki and Yamamoto's state-space model, utilising different but similar sampling rates.

It is evident from figure 4.15, that applying Araki and Yamamoto's method yields a state-space model which describes the positions of the two carts at time steps equal to $T/2$ and $T/3$ for the first and second cart, respectively. This is possible since Araki and Yamamoto's method describes the discrete states at a time step equal to the STP.

Remark 4.3.N: As evident from equation 4.45, applying Araki and Yamamoto's method yields a state-space model with more inputs and corresponding outputs than the state-space model describing the system continuously. The number of inputs and outputs are, however, as previously stated, equal. The total number of inputs in the input vector corresponds to the number of samples occuring during the BTP for each of the two carts. This might be a concern if the state-space model is to be used for controller design why conventional methods for this may not be applicable. This is investigated later in this thesis.

Multirate System with Vastly Different Sampling Rates:
This example serves to apply the Araki and Yamamoto's method to the MSD system where vastly different sampling rates corresponding to the 5.4 MW DFPT are utilised. Thus, in accordance with the equivalent Kalman and Bertram example, the sampling time for the first input is $T_1 = 0.15$ s while the sampling time for the second input is $T_2 = 0.0039$ s. This yields a BTP of $T = 3.15$ s while the STP becomes $T_0 = 1.875 \times 10^{-4}$ s. Then, $N = 16800$, $N_1 = 21$ and $N_2 = 800$.

As N is very high, all state vectors and system matrices will have very large dimensions.

As an example, the state vector $\boldsymbol{x}(k)$ will be 67200×1-dimensional. Thus, this section does not present any of the state vectors or matrices which form the state-space model. A state space model is, however, formulated as it was done for the two previous examples.

Similar to the previous examples, a comparison is made of the simulation results from the Simulink model and the discrete state-space model. The results are shown in figure 4.16.
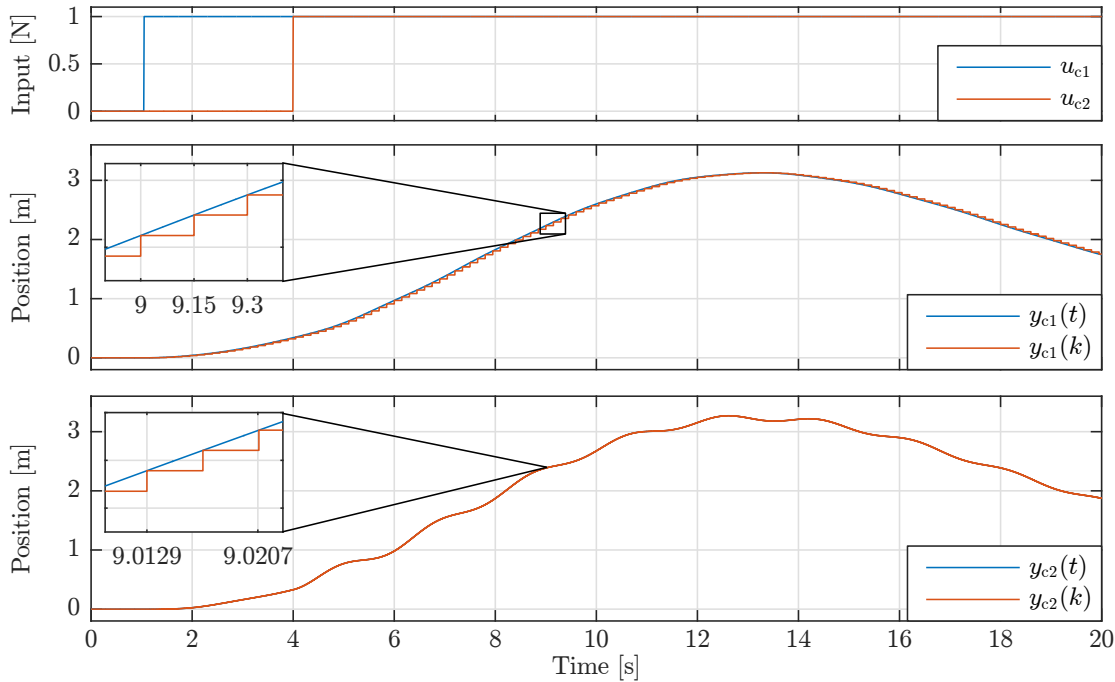
Fig. 4.16: Simulation results for a model implemented in MATLAB Simulink and for Araki and Yamamoto's state-space model, both utilising vastly different sampling rates.

It is clear that simulating the state-space model yields outputs which describes the position of the carts at time steps equal to $T_1 = 0.15$ s for the first cart and $T_2 = 0.0039$ s for the second cart.

Based on the presented general theory and various examples it can be concluded that applying Araki and Yamamoto's method to the MSD system yields a time-invariant discrete-time state-space model. Again a few final and general remarks are made regarding the method:

Remark 4.3.O: Applying Araki and Yamamoto's method to a multirate system increases the number of inputs and outputs in the resulting discrete model compared to a continuous state-space model. This may result in conventional controller design not being directly applicable. Furthermore, this unconventional form may also be a concern when conventional tools for MIMO system analysis are to be applied. This is however evaluated later in this thesis.

Remark 4.3.P: The time step of the model produced by Araki and Yamamoto's method is equal to the BTP, but is in contrary to Kalman and Bertram's method, able to describe the system states at time steps equal to the STP. Thus, the discrete model from Araki and Yamamoto's method can be utilised as a simulation tool regardless of the size of the BTP relative to the system's time constants.

Remark 4.3.Q: The main disadvantage of Araki and Yamamoto's method is its inability to include discrete dynamic elements. This is, however, a necessity when a discrete multirate state-space model of the DFPT is to be formulated due to its discrete chamber activations. Thus to make the method directly applicable for the DFPT, Araki and Yamamoto's method must be expanded to furthermore include the description of discrete dynamic elements.

It can be concluded that Araki and Yamamoto's method can be applied to a multirate sampled system to obtain a multirate model which meets all the desirable characteristics formulated in section 4.1, i.e. a linear time-invariant model on state-space form. It is, however, not immediately able to include discrete dynamic elements which is also necessary to utilise the method on the DFPT. To overcome the concerns related to the application of both the Araki and Yamamoto's method and the Kalman and Bertram's method on modelling the DFPT, the remainder of this chapter seeks to develop a new method. Thus next section describes how the ability of Araki and Yamamoto's method of describing the system states at time steps equal to the STP, can be combined with the ability of including discrete dynamic elements, as it is the case for the Kalman and Bertram's method.

4.4 A New Method: A Unified Non-minimal Realisation

Kalman and Bertram's unified approach can describe any type of sampling system with any kind of system element as long as they can be described on a conventional state-space form or difference equation form. This includes multirate and non-synchronous sampling arrangements with various combinations of discrete and continuous elements. The main disadvantage of the method is that the states are only updated with time steps equal to the BTP, and thus when the BTP becomes long relative to the system sampling rates, the model may not describe the system dynamics.

Araki and Yamamoto's non-minimal realisation seeks to overcome this issue by the lifting technique. Similarly to Kalman and Bertram's method, this method updates the states with time steps equal to the BTP, but a number of intermediate states are also calculated. These intermediate states are calculated, such that they are separated by a time step equal to the STP, thus by expanding the state vector in this fashion, the Araki and Yamamoto model also contains transient state transitions, which are too fast to be described at BTP time steps. The disadvantage of Araki and Yamamoto's method is that it only describes continuous systems, and does not take any discrete elements into consideration.

The new method developed by the authors of this thesis and presented in this section

seeks to combine the methods of Kalman and Bertram and Araki and Yamamaoto to form a unified non-minimal realisation. The purpose of doing this, is to obtain a general method for describing a system containing any combination of continuous and discrete elements with any type of sampling arrangement, while still retaining the dynamic properties of the system in the model. The derived method should produce a time-invariant discrete model in a state-space form, and should furthermore be able to describe both open- and closed-loop type systems.

Before applying the new method to the MSD system, some general definitions used to combine the two methods will first be presented. The theory presented in the next section builds upon the theory of sections 4.2 and 4.3, and thus understanding these two methods separately is essential for understanding the new method. As previously, the direct application of the new method will likely not be obvious from the presented definitions and equations, why the theory is followed by a few demonstrating examples.

Doubly Expanded State Vector and Model Form:
As in Kalman and Bertram's method, a combined vector containing the continuous, discrete and sample-and-hold states is defined:

$$\boldsymbol{x}_{\text{comb}} \equiv \begin{bmatrix} \boldsymbol{x_c}^\mathsf{T} & \vdots & \boldsymbol{x_d}^\mathsf{T} & \vdots & \boldsymbol{x_s}^\mathsf{T} \end{bmatrix}^\mathsf{T} \qquad \begin{matrix} [\mathbf{3} \times \mathbf{1}] \\ [n \times 1] \end{matrix} \qquad (4.49)$$

Then by Araki and Yamamoto's expanded discrete-time state vector definition in equation 4.26, a doubly, or equivalently lifted, expanded state vector describing all the continuous, discrete and sample-and-hold states of the system at steps corresponding to the STP may be defined:

$$\boldsymbol{x}(k) \equiv \begin{bmatrix} \boldsymbol{x}_1(k) \\ \vdots \\ \boldsymbol{x}_{N-1}(k) \\ \boldsymbol{x}_N(k) \end{bmatrix} = \begin{bmatrix} \boldsymbol{x}_{\text{comb}}((k-1)T + T_0) \\ \vdots \\ \boldsymbol{x}_{\text{comb}}((k-1)T + (N-1)T_0) \\ \boldsymbol{x}_{\text{comb}}(kT) \end{bmatrix} \qquad \begin{matrix} [\boldsymbol{N} \times \mathbf{1}] \\ [Nn \times 1] \end{matrix} \qquad (4.50)$$

With N still being defined as the number of STPs per BTP. Using this definition of the state vector, a model of the form given in equation 4.23 may be written:

$$\boldsymbol{x}(k+1) = \boldsymbol{G}^{\boldsymbol{\Psi}}\boldsymbol{x}(k) + \boldsymbol{H}^{\boldsymbol{\Psi}}\boldsymbol{u}(k) \qquad (4.51\text{a})$$

$$\boldsymbol{y}(k) = \boldsymbol{C}^{\boldsymbol{\Psi}}\left(\boldsymbol{U_1}\,\boldsymbol{x}(k+1) + \boldsymbol{U_2}\,\boldsymbol{x}(k)\right) \qquad (4.51\text{b})$$

where the matrices $\boldsymbol{G}^{\boldsymbol{\Psi}}$, $\boldsymbol{H}^{\boldsymbol{\Psi}}$ and $\boldsymbol{C}^{\boldsymbol{\Psi}}$ are the discrete equivalents to the $\boldsymbol{A}$, $\boldsymbol{B}$ and $\boldsymbol{C}$ matrices in a continuous state-space model. The input vector $\boldsymbol{u}(k)$ and the output vector $\boldsymbol{y}(k)$ here are equivalent to the ones defined in equation 4.23, and the same holds true for the two block matrices $\boldsymbol{U_1}$ and $\boldsymbol{U_2}$, why the reader is referred to the previous section.

In the following sections the transition matrices and their content are defined.

System Elements:
The three system elements are the continuous, discrete and sample-and-hold elements, and their transition matrices are again exactly as what was defined in section 4.2 from Kalman and Bertram's method.

Open-Loop System Matrices:
The definition of the $\boldsymbol{G^\Psi}$-matrix is similar to the definition of $\boldsymbol{G}^{\mathrm{D}}$, but it differs in that now the last column consists of the transition matrices $\boldsymbol{\Psi}_l(\boldsymbol{\Phi}, \boldsymbol{D}, \boldsymbol{S})$ where $l = \{1, \ldots, N\}$:

$$\boldsymbol{G^\Psi} \equiv \begin{bmatrix} \boldsymbol{0} & \cdots & \boldsymbol{0} & \boldsymbol{\Psi}_1 \\ \vdots & \ddots & \vdots & \vdots \\ \boldsymbol{0} & \cdots & \boldsymbol{0} & \boldsymbol{\Psi}_N \end{bmatrix} \qquad \begin{matrix} [\boldsymbol{N} \times \boldsymbol{N}] \\ [Nn \times Nn] \end{matrix} \qquad (4.52)$$

As in Kalman and Bertram's method, the $\boldsymbol{\Psi}_l(\boldsymbol{\Phi}, \boldsymbol{D}, \boldsymbol{S})$ matrices are functions of system element matrices, and the approach for deriving them is identical to what was presented for Kalman and Bertram.

The $\boldsymbol{H^\Psi}$-matrix distributes the inputs throughout the BTP, and ensures that the correct inputs are given to the correct time steps. The general form of the $\boldsymbol{H^\Phi}$-matrix is very similar to that of $\boldsymbol{H}^{\mathrm{D}}$:

$$\boldsymbol{H^\Psi} \equiv \begin{bmatrix} \boldsymbol{H}_1^\Psi(\boldsymbol{v}_l(\boldsymbol{\Phi}, \boldsymbol{D}, \boldsymbol{S}, \boldsymbol{d}, \boldsymbol{s})) & \cdots & \boldsymbol{H}_{\boldsymbol{p}}^\Psi(\boldsymbol{v}_l(\boldsymbol{\Phi}, \boldsymbol{D}, \boldsymbol{S}, \boldsymbol{d}, \boldsymbol{s})) \end{bmatrix} \qquad \begin{matrix} [\boldsymbol{1} \times \boldsymbol{p}] \\ [Nn \times \bar{N}] \end{matrix} \qquad (4.53)$$

where p is equal to the number of inputs in the system, such that each block in the matrix is a submatrix, which distributes the inputs related to 1 of p inputs. To derive the individual entries of the $\boldsymbol{H^\Psi}$ matrix, the approach of Kalman and Bertram for defining the $\boldsymbol{v}_l$ matrices in equation 4.3a, wherein the inputs and state transitions in the sampling scheme are considered, is used, and how to do this is illustrated in later examples. This has the benefit of readily allowing the inclusion of discrete elements, which the method of Araki and Yamamoto does not directly allow.

Regarding the $\boldsymbol{C^\Psi}$-matrix, it must now account for the double expansion of the state vector, such that the DDE and SHE states are also included. This can be done by defining the conventional continuous $\boldsymbol{C}$-matrix with respect to the combined vector of CDE, DDE and SHE states in equation 4.49. Then the definition of $\boldsymbol{C}^{\mathrm{D}}$ can be used to calculate $\boldsymbol{C^\Psi}$, and the reader is referred to the previous section for this.

Having presented the tools and theory necessary for applying the new combined method to the mass spring damper system, the next section presents various examples similar to the ones presented for both Kalman and Bertram's and Araki and Yamamaoto's methods.

4.4.1   Various Examples

This section presents two examples of applying the new unified non-minimal realisation method to the MSD system. The application of the method to single rate systems is now considered trivial, why only the two multirate examples are considered.

Multirate System with Similar Sampling Rates:

The system under consideration is illustrated in figure 4.17 and is again the MSD system, but to illustrate how discrete elements may be included, discrete first order low-pass filters have been placed on the inputs. Such filters could emulate the discrete effects of a digital controller or discrete chamber activations as is the case in a DFPT. The filters both have break frequencies of 1000 Hz and are for lower frequencies defined to have unity gain.
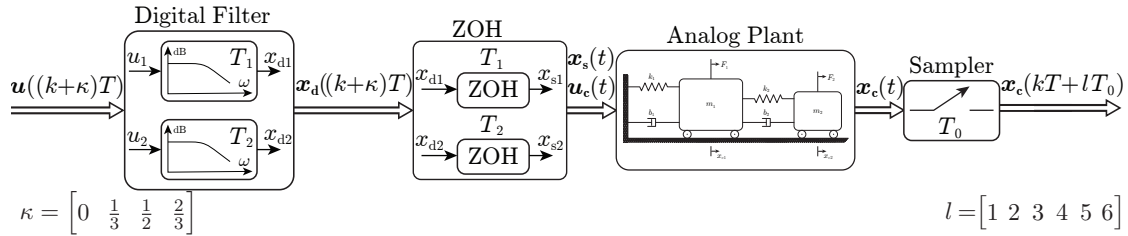
Fig. 4.17: Block diagram representation of the physical open-loop MSD system with discrete input dynamics, with sampled outputs and zero-order held analog plant inputs operated at multiple rates.

The first system input is updated at a rate of $T_1 = T/2 = 0.15\,\text{s}$ and the corresponding filter also updates with the same rate. Similarly, the second input is updated at a rate of $T_2 = T/3 = 0.1\,\text{s}$, with the second filter also operating at this rate. The BTP of this sampling system is then $T = 0.3\,\text{s}$, and the STP is $T_0 = 0.05\,\text{s}$, and with $N = 6$, $N_1 = 2$ and $N_2 = 3$.

To derive a model of the system, a four step procedure, similar to the one defined by Kalman and Bertram, is defined:

1. Defining the state variables.
2. Calculating the various transition matrices ($\boldsymbol{\Psi}, \boldsymbol{D}, \boldsymbol{S}$).
3. Starting from kT, then deriving transition equations for the sampling operations and sample-free time-intervals for a BTP.
4. Combining and simplifying transition equations to obtain a time-invariant model.

Step 1: For the system depicted in figure 4.17, there are $\gamma = 4$ CDE states, $\delta = 2$ DDE states and $\sigma = 2$ SHE states. From the figure, it can be seen that the DDE states are defined as being equal to the output of the filters, or equivalently the input of the hold circuit. Similarly, the SHE states are defined as being equal to the output of the hold circuit. The combined vector of all the system states is exactly the same as defined in equation 4.49. Thus the doubly expanded 48×1-dimensional state vector can be defined:

$$\boldsymbol{x}(k) = \begin{bmatrix} \boldsymbol{x}_1(k) \\ \boldsymbol{x}_2(k) \\ \boldsymbol{x}_3(k) \\ \boldsymbol{x}_4(k) \\ \boldsymbol{x}_5(k) \\ \boldsymbol{x}_6(k) \end{bmatrix} = \begin{bmatrix} \boldsymbol{x}_{\text{comb}}((k-1)T + T_0) \\ \boldsymbol{x}_{\text{comb}}((k-1)T + 2\,T_0) \\ \boldsymbol{x}_{\text{comb}}((k-1)T + 3\,T_0) \\ \boldsymbol{x}_{\text{comb}}((k-1)T + 4\,T_0) \\ \boldsymbol{x}_{\text{comb}}((k-1)T + 5\,T_0) \\ \boldsymbol{x}_{\text{comb}}(kT) \end{bmatrix} \tag{4.54}$$

Step 2: For the CDE, the 8×8 transition matrix is as defined by equation 4.6, with block matrix entries as defined in equation 4.5, and is thus not repeated here.

The transition matrices associated with the *hold* elements can now be defined. The inputs to the *hold* elements are simply the discrete filter outputs, and thus when defining the transition matrix S_7, and remembering that all matrices are simply modified identity matrices, only the 5th column in the 7th row will have an entry other than zero, corresponding to the state of the first filter. The S_8-matrix is constructed in the same fashion, but with the 6th column in the 8th row:

$$S_7 = \begin{bmatrix} \boldsymbol{I} & \boldsymbol{0} & \boldsymbol{0} \\ \boldsymbol{0} & \boldsymbol{I} & \boldsymbol{0} \\ \boldsymbol{0} & \begin{matrix} 1 & 0 \\ 0 & 0 \end{matrix} & \begin{matrix} 0 & 0 \\ 0 & 1 \end{matrix} \end{bmatrix} \qquad S_8 = \begin{bmatrix} \boldsymbol{I} & \boldsymbol{0} & \boldsymbol{0} \\ \boldsymbol{0} & \boldsymbol{I} & \boldsymbol{0} \\ \boldsymbol{0} & \begin{matrix} 0 & 0 \\ 0 & 1 \end{matrix} & \begin{matrix} 1 & 0 \\ 0 & 0 \end{matrix} \end{bmatrix} \tag{4.55}$$

To define the transition matrices related to the discrete low-pass filters, the governing equation for the filter must be known. Thus the first order difference equation of the form is presented:

$$x_{\text{d}i}(k+1) = -D\,x_{\text{d}i}(k) + d\,u_{\text{d}i}(k) \tag{4.56}$$

where the coefficients D and d together determine the gain and break frequency of the filter, which are chosen such that the filter has unity gain and attenuates signals over $1000\,\text{Hz}$. It may be seen that the filter depends only on its own internal state, and thus the the matrices $\boldsymbol{D}_5$ and $\boldsymbol{D}_6$ may be defined:

$$\boldsymbol{D}_5 = \begin{bmatrix} \boldsymbol{I} & \boldsymbol{0} & \boldsymbol{0} \\ \boldsymbol{0} & \begin{matrix} -D_1 & 0 \\ 0 & 1 \end{matrix} & \boldsymbol{0} \\ \boldsymbol{0} & \boldsymbol{0} & \boldsymbol{I} \end{bmatrix} \qquad \boldsymbol{D}_6 = \begin{bmatrix} \boldsymbol{I} & \boldsymbol{0} & \boldsymbol{0} \\ \boldsymbol{0} & \begin{matrix} 1 & 0 \\ 0 & -D_2 \end{matrix} & \boldsymbol{0} \\ \boldsymbol{0} & \boldsymbol{0} & \boldsymbol{I} \end{bmatrix} \tag{4.57}$$

Regarding the inputs acting through the filters, the vectors $\boldsymbol{d}_5$ and $\boldsymbol{d}_6$ may be defined:

$$\boldsymbol{d}_5 = \begin{bmatrix} \boldsymbol{0} \\ d_1 \\ 0 \\ \boldsymbol{0} \end{bmatrix} \qquad \boldsymbol{d}_6 = \begin{bmatrix} \boldsymbol{0} \\ 0 \\ d_2 \\ \boldsymbol{0} \end{bmatrix} \tag{4.58}$$

This definition of the $\boldsymbol{d}$ input matrices is slightly different from the one used in Kalman and Bertram's method. Having rigorously used the definitions of Kalman and Bertram, the matrices should have had two columns, but due to utilising the input vector definition of Araki and Yamamoto, it is not possible to always use vector-matrix products, since they do not consider both inputs at all sampling instances, why $\boldsymbol{d}$ is here defined as a vector.

Step 3: For this step the top part of figure 4.18, which illustrates the real progression of system states, is presented. By use of the figure, the individual $\boldsymbol{\Psi}_l$ matrices and entries of the $\boldsymbol{H}^{\boldsymbol{\Psi}}$ matrix may be derived by considering the transitions from $\boldsymbol{x}(k)$ to the $l = \{1, \dots, N\}$ $\boldsymbol{x}_l(k+1)$ vectors.

Multirate System:
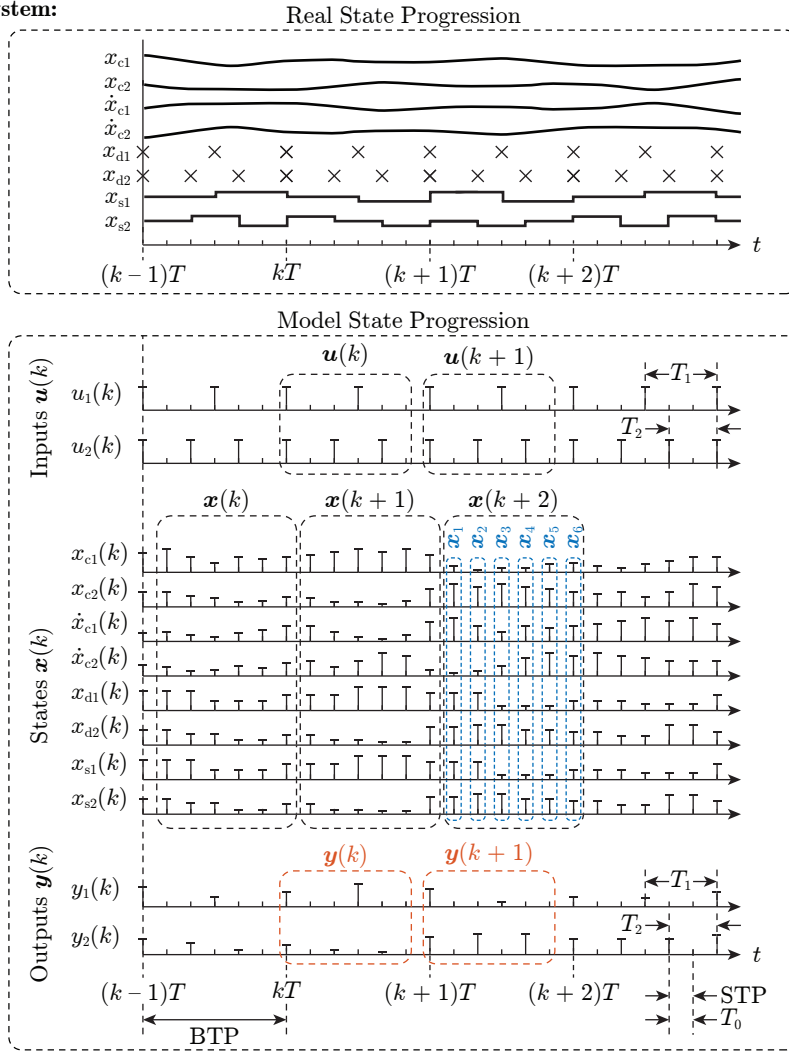
Fig. 4.18: In the top: the real state progression of continuous, discrete and piecewise constant *hold* states for a multirate system. In the bottom: the progression of the model states.

Thus to define $\boldsymbol{x}_1(k+1)$: Examining the top part of figure 4.18 and examning the open interval $[kT \quad kT + T_0[$, corresponding to examining the interval $[\boldsymbol{x}_6(k) \quad \boldsymbol{x}_1(k+1)[$ for the model state progression in the lower part of the figure. It may be seen that the first state transition is related to the DDE, where sampling new inputs and calculating new outputs occurs (multiplication of $\boldsymbol{D}$ and $\boldsymbol{d}$ to $\boldsymbol{x}_6(k)$ and $\boldsymbol{u}(k)$ respectively). Subsequently the sampling and holding of the DDE outputs by the SHEs occurs (multiplication by $\boldsymbol{S}$), and finally a continuous CDE state transition of length T_0 happens (multiplication by $\boldsymbol{\Phi}(T_0)$):

$$\boldsymbol{x}_1(k+1) = \underbrace{\boldsymbol{\Phi}(T_0)\boldsymbol{S}_8\boldsymbol{S}_7\boldsymbol{D}_6\boldsymbol{D}_5}_{\boldsymbol{\Psi}_1}\,\boldsymbol{x}_6(k) + \underbrace{\boldsymbol{\Phi}(T_0)\boldsymbol{S}_7\boldsymbol{d}_5}_{\boldsymbol{v}_1}\,u_1(kT) + \underbrace{\boldsymbol{\Phi}(T_0)\boldsymbol{S}_8\boldsymbol{d}_6}_{\boldsymbol{v}_2}\,u_2(kT) \qquad (4.59a)$$

Similarly for defining $\boldsymbol{x}_2(k+1)$, it may be seen that in addition to all the transitions occuring for $\boldsymbol{x}_1(k+1)$ a continuous CDE transition of length T_0 happens. Thus all the previous transitions (contained in $\boldsymbol{\Psi}_1$) and inputs (contained in $\boldsymbol{v}_1$ and $\boldsymbol{v}_2$) are carried over and finally multiplied by $\boldsymbol{\Phi}(T_0)$:

$$\boldsymbol{x}_2(k+1) = \underbrace{\boldsymbol{\Phi}(T_0)\boldsymbol{\Psi}_1}_{\boldsymbol{\Psi}_2}\,\boldsymbol{x}_6(k) + \underbrace{\boldsymbol{\Phi}(T_0)\boldsymbol{v}_1}_{\boldsymbol{v}_3}\,u_1(kT) + \underbrace{\boldsymbol{\Phi}(T_0)\boldsymbol{v}_2}_{\boldsymbol{v}_4}\,u_2(kT) \tag{4.59b}$$

For $\boldsymbol{x}_3(k+1)$ all the previous transitions are again carried over. Thus starting from where $\boldsymbol{x}_2(k+1)$ ended, it may be seen that the next state update is that of $x_6 = x_{d2}$ (multiplication by $\boldsymbol{D}_6$), with a subsequent update of $x_8 = x_{s2}$ (multiplication by $\boldsymbol{S}_8$), and finally concluded by a continuous CDE transition of length T_0. Furthermore, a new input is also sampled, why the input $u_2(kT + 2T_0)$ is introduced:

$$\boldsymbol{x}_3(k+1) = \overbrace{\boldsymbol{\Phi}(T_0)\boldsymbol{S}_8\boldsymbol{D}_6\boldsymbol{\Psi}_2}^{\boldsymbol{\Psi}_3}\,\boldsymbol{x}_6(k) + \overbrace{\boldsymbol{\Phi}(T_0)\boldsymbol{v}_3}^{\boldsymbol{v}_5}\,u_1(kT) + \overbrace{\boldsymbol{\Phi}(T_0)\boldsymbol{S}_8\boldsymbol{D}_6\boldsymbol{v}_4}^{\boldsymbol{v}_6}\,u_2(kT)$$
$$+ \underbrace{\boldsymbol{\Phi}(T_0)\boldsymbol{S}_8\boldsymbol{d}_6}_{\boldsymbol{v}_2}\,u_2(kT+2T_0) \tag{4.59c}$$

The approach for defining $\boldsymbol{x}_4(k+1)$, $\boldsymbol{x}_5(k+1)$ and $\boldsymbol{x}_6(k+1)$ is exactly the same, why it is not explained, and only the final result is presented:

$$\boldsymbol{x}_4(k+1) = \overbrace{\boldsymbol{\Phi}(T_0)\boldsymbol{S}_7\boldsymbol{D}_5\boldsymbol{\Psi}_3}^{\boldsymbol{\Psi}_4}\,\boldsymbol{x}_6(k) + \overbrace{\boldsymbol{\Phi}(T_0)\boldsymbol{S}_7\boldsymbol{D}_5\boldsymbol{v}_5}^{\boldsymbol{v}_7}\,u_1(kT) + \overbrace{\boldsymbol{\Phi}(T_0)\boldsymbol{v}_6}^{\boldsymbol{v}_8}\,u_2(kT) \tag{4.59d}$$
$$+ \underbrace{\boldsymbol{\Phi}(T_0)\boldsymbol{v}_2}_{\boldsymbol{v}_4}\,u_2(kT+2T_0) + \underbrace{\boldsymbol{\Phi}(T_0)\boldsymbol{S}_7\boldsymbol{d}_5}_{\boldsymbol{v}_1}\,u_1(kT+3T_0)$$

$$\boldsymbol{x}_5(k+1) = \overbrace{\boldsymbol{\Phi}(T_0)\boldsymbol{S}_8\boldsymbol{D}_6\boldsymbol{\Psi}_4}^{\boldsymbol{\Psi}_5}\,\boldsymbol{x}_6(k) + \overbrace{\boldsymbol{\Phi}(T_0)\boldsymbol{v}_7}^{\boldsymbol{v}_9}\,u_1(kT) + \overbrace{\boldsymbol{\Phi}(T_0)\boldsymbol{S}_8\boldsymbol{D}_6\boldsymbol{v}_8}^{\boldsymbol{v}_{10}}\,u_2(kT) \tag{4.59e}$$
$$+ \underbrace{\boldsymbol{\Phi}(T_0)\boldsymbol{S}_8\boldsymbol{D}_6\boldsymbol{v}_4}_{\boldsymbol{v}_6}\,u_2(kT+2T_0) + \underbrace{\boldsymbol{\Phi}(T_0)\boldsymbol{v}_1}_{\boldsymbol{v}_3}\,u_1(kT+3T_0) + \underbrace{\boldsymbol{\Phi}(T_0)\boldsymbol{S}_8\boldsymbol{d}_6}_{\boldsymbol{v}_2}\,u_2(kT+4T_0)$$

$$\boldsymbol{x}_6(k+1) = \overbrace{\boldsymbol{\Phi}(T_0)\boldsymbol{\Psi}_5}^{\boldsymbol{\Psi}_6}\,\boldsymbol{x}_6(k) + \overbrace{\boldsymbol{\Phi}(T_0)\boldsymbol{v}_9}^{\boldsymbol{v}_{11}}\,u_1(kT) + \overbrace{\boldsymbol{\Phi}(T_0)\boldsymbol{v}_{10}}^{\boldsymbol{v}_{12}}\,u_2(kT) \tag{4.59f}$$
$$+ \underbrace{\boldsymbol{\Phi}(T_0)\boldsymbol{v}_6}_{\boldsymbol{v}_8}\,u_2(kT+2T_0) + \underbrace{\boldsymbol{\Phi}(T_0)\boldsymbol{v}_3}_{\boldsymbol{v}_5}\,u_1(kT+3T_0) + \underbrace{\boldsymbol{\Phi}(T_0)\boldsymbol{v}_2}_{\boldsymbol{v}_4}\,u_2(kT+4T_0)$$

Deriving the model state transitions in this fashion results in the lower part of figure 4.18.

Step 4: The next step is to combine all the individual transition equations presented in equation 4.59, into a single matrix-vector representation. Having already defined the state vector in equation 4.54, a matrix- vector form may be readily obtained as:

$$\underbrace{\begin{bmatrix} \boldsymbol{x}_1(k+1) \\ \boldsymbol{x}_2(k+1) \\ \boldsymbol{x}_3(k+1) \\ \boldsymbol{x}_4(k+1) \\ \boldsymbol{x}_5(k+1) \\ \boldsymbol{x}_6(k+1) \end{bmatrix}}_{\boldsymbol{x}(k+1)} = \underbrace{\begin{bmatrix} & \boldsymbol{\Psi}_1 \\ & \boldsymbol{\Psi}_2 \\ \boldsymbol{0} & \boldsymbol{\Psi}_3 \\ & \boldsymbol{\Psi}_4 \\ & \boldsymbol{\Psi}_5 \\ & \boldsymbol{\Psi}_6 \end{bmatrix}}_{\boldsymbol{G}^{\boldsymbol{\Psi}}} \underbrace{\begin{bmatrix} \boldsymbol{x}_1(k) \\ \boldsymbol{x}_2(k) \\ \boldsymbol{x}_3(k) \\ \boldsymbol{x}_4(k) \\ \boldsymbol{x}_5(k) \\ \boldsymbol{x}_6(k) \end{bmatrix}}_{\boldsymbol{x}(k)} + \underbrace{\begin{bmatrix} \overbrace{\boldsymbol{v}_1 \quad 0}^{\boldsymbol{H}_1^{\boldsymbol{\Psi}}} & \overbrace{\boldsymbol{v}_2 \quad 0 \quad 0}^{\boldsymbol{H}_2^{\boldsymbol{\Psi}}} \\ \boldsymbol{v}_3 \quad 0 & \boldsymbol{v}_4 \quad 0 \quad 0 \\ \boldsymbol{v}_5 \quad 0 & \boldsymbol{v}_6 \quad \boldsymbol{v}_2 \quad 0 \\ \boldsymbol{v}_7 \quad \boldsymbol{v}_1 & \boldsymbol{v}_8 \quad \boldsymbol{v}_4 \quad 0 \\ \boldsymbol{v}_9 \quad \boldsymbol{v}_3 & \boldsymbol{v}_{10} \quad \boldsymbol{v}_6 \quad \boldsymbol{v}_2 \\ \boldsymbol{v}_{11} \quad \boldsymbol{v}_5 & \boldsymbol{v}_{12} \quad \boldsymbol{v}_8 \quad \boldsymbol{v}_4 \end{bmatrix}}_{\boldsymbol{H}^{\boldsymbol{\Psi}}} \underbrace{\begin{bmatrix} u_1(kT) \\ u_1(kT+3T_0) \\ u_2(kT) \\ u_2(kT+2T_0) \\ u_2(kT+4T_0) \end{bmatrix}}_{\boldsymbol{u}(k)} \tag{4.60a}$$

where $\boldsymbol{G}^{\boldsymbol{\Psi}}$ is a 48×48 matrix, and $\boldsymbol{H}^{\boldsymbol{\Psi}}$ is a $48 \times (2+3)$ matrix, wherein the left-right separataion is in accordance with the sorting of the first and second input. The output vector is given by:

$$\underbrace{\begin{bmatrix} y_1(kT) \\ y_1(kT+3T_0) \\ y_2(kT) \\ y_2(kT+2T_0) \\ y_2(kT+4T_0) \end{bmatrix}}_{\boldsymbol{y}(k)} = \underbrace{\begin{bmatrix} \boldsymbol{0} & \boldsymbol{0} & \boldsymbol{0} & \boldsymbol{0} & \boldsymbol{0} & \boldsymbol{c}_1 \\ \boldsymbol{0} & \boldsymbol{0} & \boldsymbol{c}_1 & \boldsymbol{0} & \boldsymbol{0} & \boldsymbol{0} \\ \boldsymbol{0} & \boldsymbol{0} & \boldsymbol{0} & \boldsymbol{0} & \boldsymbol{0} & \boldsymbol{c}_2 \\ \boldsymbol{0} & \boldsymbol{c}_2 & \boldsymbol{0} & \boldsymbol{0} & \boldsymbol{0} & \boldsymbol{0} \\ \boldsymbol{0} & \boldsymbol{0} & \boldsymbol{0} & \boldsymbol{c}_2 & \boldsymbol{0} & \boldsymbol{0} \end{bmatrix}}_{\boldsymbol{C}^{\boldsymbol{\Psi}}} \boldsymbol{x}(k) \tag{4.60b}$$

where $\boldsymbol{c}_1$ and $\boldsymbol{c}_2$ are the first and second row of a $\boldsymbol{C}$-matrix, which selects the two first entries from a vector defined in accordance with equation 4.49.

As done previously, a Simulink implementation of the system represented by figure 4.17 has been made, and both the system and model represented by equation 4.60 has been simulated. The results of these simulations are presented in figure 4.19.
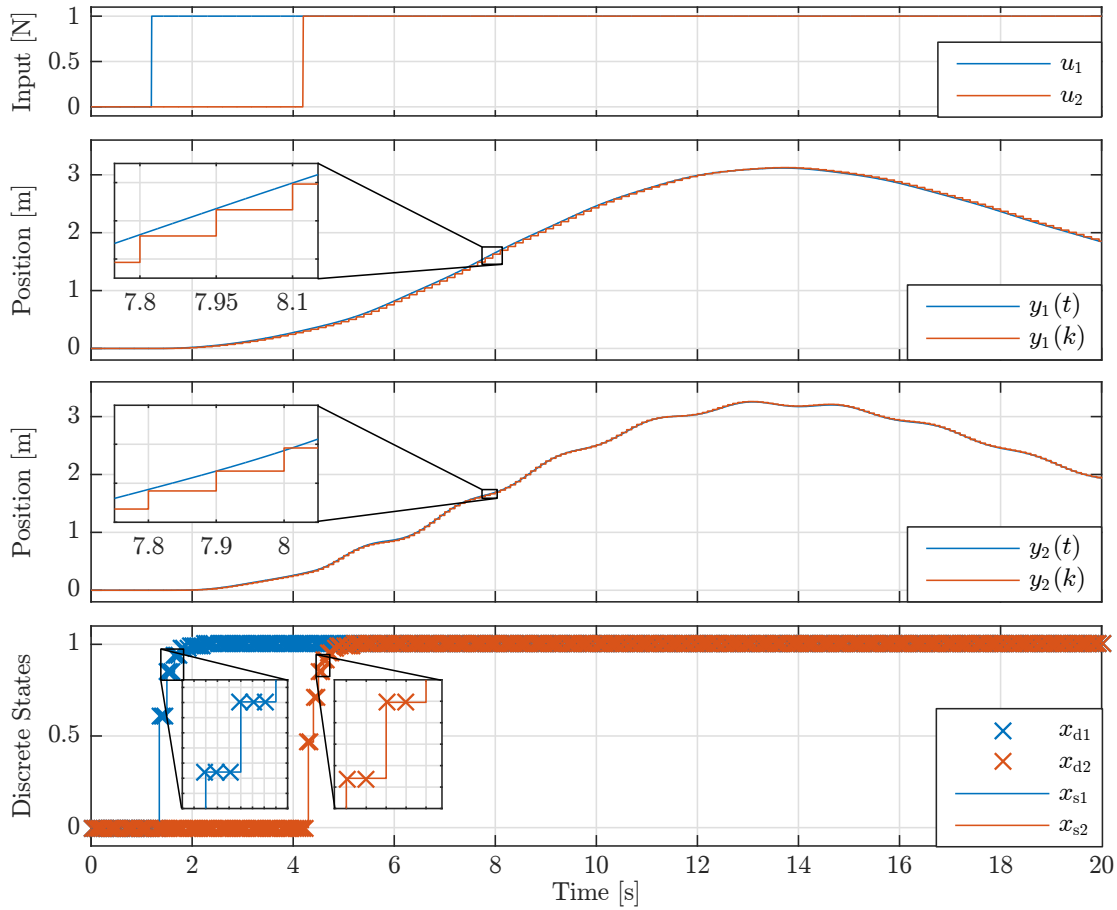
Fig. 4.19: Simulation results for a MATLAB Simulink implementation of figure 4.17 and for the model represented by equation 4.60, both utilising similar but different update rates.

Based on the second and third subplot it is evident that like Araki and Yamamoto's method, the new method yields a state-space model, which describes the positions of the two carts at two different rates. The fourth subplot illustrates the DDE and SHE states, where the form of the state progression illustrated in the bottom part of figure 4.18 is repeated again, wherein the states are calculated for every STP, but only updated at the correct rates.

This concludes the example regarding the application of the new unified non-minimal realisation method to the multirate mass spring damper MIMO system with discrete input dynamics. Again a few remarks on the method are made:

Remark 4.4.A: The new unified non-minimal realisation method can successfully describe a multirate MIMO system including continuous, discrete and sample-and-hold elements operating at various rates. Furthermore, the presented model structure is time-invariant and able to describe both open- and closed-loop system configurations.

Remark 4.4.B: This new model structure results in the DDE and SHE states attaining values for every step of the STP within the BTP, which is technically not correct when considering that the real DDE states are only available at rates of T_1 and T_2, as illustrated in the top part of figure 4.18. However, even though the model calculates these extra intermediate states, they are held constant, and only updated at the correct rates.

Remark 4.4.C: The multirate sample-and-hold elements could also be considered as a single element with periodically varying non-uniform rate. Thus the generality of the method with regard to describing any kind of sampling system is not lost.

Remark 4.4.D: The bottom block row in the model represented by equation 4.60a, which calculates the BTP to BTP or $kT \rightarrow (k+1)T$ transition, and not the intermediate steps, is the same as the model obtained by Kalman and Bertram's method.

Remark 4.4.E: The remarks regarding the increased number of inputs and outputs and usefulness of the model as a simulation made for Araki and Yamamoto's method also apply to this new unified non-minimal realisation, but are not repeated here.

The next task is to investigate, how the unified non-minimal realisation method handles systems wherein the sampling and update rates are vastly different.

Multirate System with Vastly Different Sampling Rates:
This example applies the new unified non-minimal realisation to the MSD system with discrete input dynamics, which is depicted in figure 4.17, where the vastly different sampling rates correspond to the activations rates in the 5.4 MW DFPT. Thus, the rate of the first input and associated discrete filter is $T_1 = 0.15$ s while the sampling time for the second input is $T_2 = 0.0039$ s. This yields a BTP of $T = 3.15$ s while the STP becomes $T_0 = 1.875 \times 10^{-4}$ s. Then, $N = 16800$, $N_1 = 21$ and $N_2 = 800$.

As N is very high, all state vectors and system matrices will have very large dimensions.

As an example, the state vector $\boldsymbol{x}(k)$ will be $N\,n \times 1 = 134200 \times 1$-dimensional. Thus, none of the state vectors or matrices which form the state-space model are shown.

Similar to the previous examples, a comparison is made of the simulation results from the Simulink model and the discrete state-space model, and the results is presented in figure 4.20.
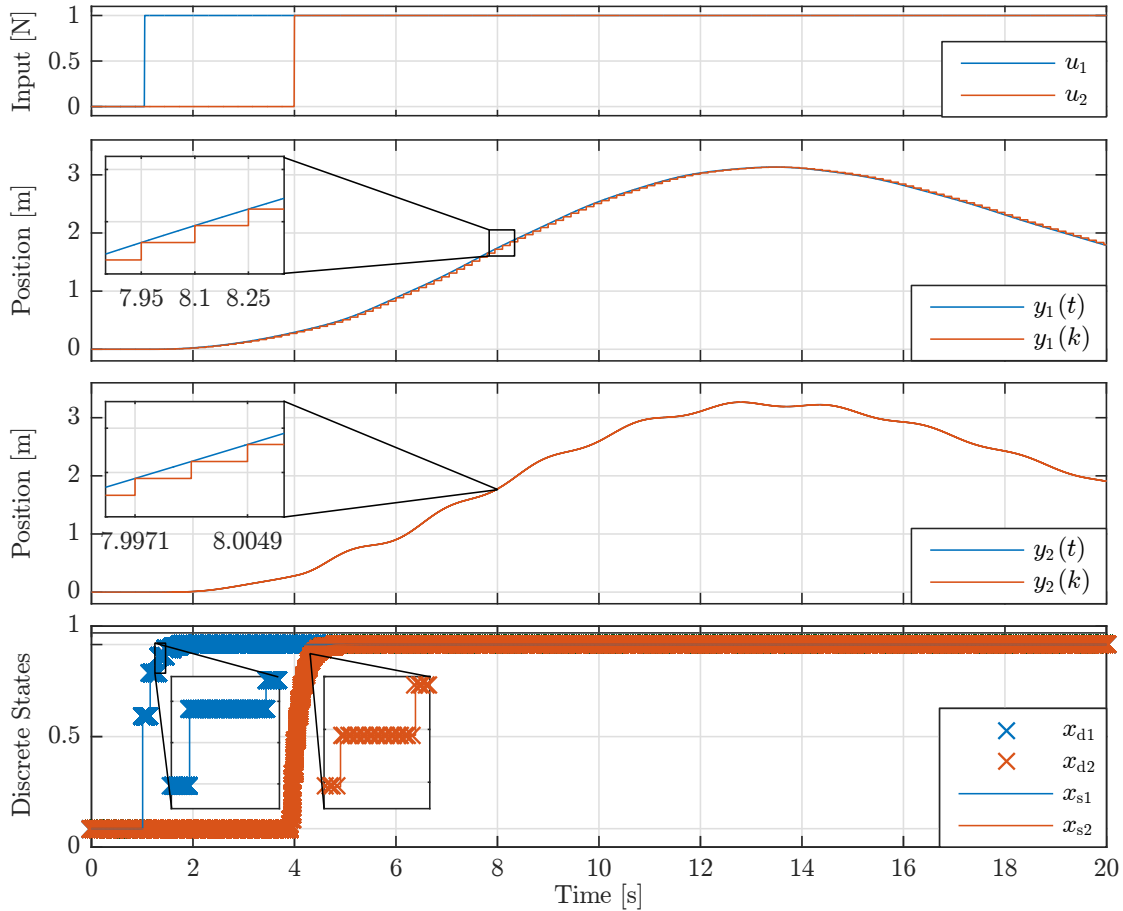
Fig. 4.20: Simulation results for a MATLAB Simulink implementation of figure 4.17 and for the model represented by equation 4.60, both utilising vastly different update rates.

The results are very similar to those presented in the previous example, it may, however, now be seen that this model formulation is able to correctly simulate brief transient events, even when the BTP becomes large.

This generally concludes the application of the new unified non-minimal realisation to the two different examples and thus also concludes the development of a method able to produce a model of a multirate sampled system. To conclude the section and chapter a few general remarks on the method and its application to the DFPT are made:

Remark 4.4.F: The new unified non-minimal realisation method produces a discrete-time state-space model, which has the following properties:

- Linear time-invariant system descriptions for both SISO and MIMO systems.
- Handles both open- and closed-loop configurations.
- Any combination of discrete and continuous system elements can be modelled.
- The discrete and sample-and-hold elements can operate with conventional, non-uniform or non-synchronous update rates, or any combination of these, although the rate must be periodic if the final model should have a finite form.
- System transient events can be correctly simulated even when the BTP is significant longer compared to system time constants, unlike Kalman and Bertram's method.
- The number of states is greatly increased by the lifting approach, and can cause computational issues, if intelligent algorithms are not utilised.

The method generally appears a suitable candidate for modelling the DFPT, with none of the obvious disadvantages of either Kalman and Bertram's or Araki and Yamamoto's methods, why it is decided to proceed to modelling the DFPT. The challenge of an increased number of inputs and outputs still remains, and will be further considered in chapter 6. Since the unified non-minimal realisation method will be used in subsequent chapters, the abbreviation UNMR is introduced. Before the developed UNMR method is utilised for obtaining a multirate model of the DFPT, an algorithm which can be used for software implementation to utilise the UNMR method is presented.

4.4.2   Unified Non-minimal Realiasation Algorithm

It is the intention that the developed unified non-minimal realisation method can be applied to systems with similar as well as vastly different sampling rates. Therefore a calculation algorithm, suitable for software implementation in e.g. MATLAB is be developed. Ideally such an algorithm should be defined in the most general form, meaning it should be applicable for multirate systems with any number of inputs, outputs and sampling rates. To develop such an algorithm is an extensive and time consuming process and may therefore also be difficult to understand and apply. Since the intention of this section is to present an algorithm which potential readers of this thesis relatively easy can understand and more importantly apply, it is chosen to present a simplified version of the more general algorithm, which only is applicable for a limited range of multirate systems. This includes systems with $i = 2$ inputs, $o = 2$ outputs, and $p = 2$ sampling rates/periods.

It should be noted that many different kinds of algorithms could be developed to calculate the required data for formulating a LTI state-space representation of the form utilised in the UNMR method. Hence, the algorithm presented in this section is merely one of many possible approaches why it may not be of the most compact form nor the most computationally efficient. However, the algorithm has during this thesis proven to work successfully, which is deemed to be sufficient and further work used on improvements is therefore considered needless.

In contrast to the previous parts of this chapter, where relatively compact mathematical notations have been utilised when for instance a if-statement is presented, the algorithm presented in this section will use notations strongly inspired from MATLAB-code language. The use of such notations should provide the reader with a more foreseeable

algorithm, which is intended to make the algorithm easier to understand and apply. Prior to the presentation of the algorithm some of these utilised notations are briefly described:

- When a zero-matrix, $\boldsymbol{M}_0$, or an identity-matrix, $\boldsymbol{M}_{\text{eye}}$, of the dimensions $[m \times n]$ is defined, it is written as:
$$\boldsymbol{M}_0 = \boldsymbol{0}(m, n) \qquad\qquad \boldsymbol{M}_{\text{eye}} = \boldsymbol{I}(m, n)$$

- When the mth row, the nth column, or the entry of the mth row and the nth column in a matrix, $\boldsymbol{M}$, must be selected, it is done as:
$$\boldsymbol{M}(m, :) \qquad\qquad \boldsymbol{M}(:, n) \qquad\qquad \boldsymbol{M}(m, n)$$

- When a for-loop going from $h = 1$ to $h = k$ with steps of size j it is written as:
$$\text{for } h = 1 : j : k$$
$$\text{Intended math} - \text{operation}$$
$$\text{end}$$

In addition to the notations defined above, the algorithm for the UNMR method make use of the notations defined in sections 4.2 to 4.4. The algorithm is presented in a number of steps and remarks related to the individual steps might be included. This is done in the aim of providing the reader with additional information to why the related step is performed. The algorithm steps are defined as followed:

Algorithm Step 1 - Defining Sampling Period & Numbers:
Define the system parameters T_h, T, T_0, N_h, N and l_h. Note that $h = \{1, ..., p\}$.

Algorithm Step 2 - Transition Matrices:
1. Define the length, n, of the state vector $\boldsymbol{x}_{\textbf{comb}}$.
2. Define the transition matrix, $\boldsymbol{\Phi}(t)$, and evaluate at $t = T_0$.
3. For each sampling rate, T_h, for $h = \{1, ..., p\}$, define the transition matrices $\boldsymbol{D}_h$ and $\boldsymbol{S}_h$.
4. For each input, u_h, for $h = \{1, ..., i\}$, define either $\boldsymbol{d}_h$ or $\boldsymbol{s}_h$ depending on the specific system. Furthermore for the use in proceeding calculations define the input transition vector, $\boldsymbol{u}_h$, defined as:
$$\text{if} \quad \boldsymbol{d}_h \neq 0$$
$$\boldsymbol{u}_h = \boldsymbol{d}_h$$
$$\text{else}$$
$$\boldsymbol{u}_h = \boldsymbol{s}_h$$
$$\text{end}$$
5. Define the output transition matrix, $\boldsymbol{C}$, of size $[o \times n]$ for the state vector, $\boldsymbol{x}_{\textbf{comb}}$.

Algorithm Step 3 - Transition Action Matrix:
Define a transition action matrix, $\boldsymbol{M}_{\text{action}} = \boldsymbol{0}$, of size $[p \times N]$, which describes at which multiples of T_0 a T_h-state transitions can occur. Instances at which state transition occurs are represented by a 1-entry in $\boldsymbol{M}_{\text{action}}$, and are defined as:
$$\text{for } h = 1 : p$$
$$\text{for} \quad j = 1 : l_h : N$$
$$\boldsymbol{M}_{\text{action}}(h, j) = 1$$
$$\text{end}$$
$$\text{end}$$

Remark 4.4.G: The four step procedure for the UNMR method presented in section 4.4.1 does not define a transition action matrix. This is because the information provided by $\boldsymbol{M}_{\text{action}}$ is contained in the model state progression figures presented during this chapter, e.g figure 4.14. However, when the sampling rates of a system becomes vastly different, it is inconvenient to make a state progressions figure and furthermore such a figure cannot be utilised in a software algorithm, why the alternative transition action matrix, $\boldsymbol{M}_{\text{action}}$, is defined.

Algorithm Step 4 - Intermediate State & Input Matrices:
Define an intermediate state matrix ,$\boldsymbol{\Psi}_k$, for each T_0-transition in T (hence $k = \{1, ..., N\}$):
$$\begin{aligned} &\text{for} \quad k = 1 : 1 : N \\ &\qquad \boldsymbol{\Psi}_k = \boldsymbol{I}(n, n) \\ &\text{end} \end{aligned}$$

For the lifted input vector define a intermediate input matrix, $\boldsymbol{V}_k$, of size $[n \times l_1 + l_2]$, for each T_0-transition in T:
$$\begin{aligned} &\text{for} \quad k = 1 : 1 : N \\ &\qquad \boldsymbol{V}_k = \boldsymbol{0}(n, l_1 + l_2) \\ &\text{end} \end{aligned}$$

The intermediate input matrix, $\boldsymbol{V}_k$, is hereafter changed to include columns of 1-entries corresponding to when a lifted input, e.g $u_h(kT + T_j)$ for $h = \{1, ..., i\}$ and $j = \{1, ..., p\}$, starts to affect the state vector $\boldsymbol{x}_k$:
$$\begin{aligned} &h = 0 \\ &\text{for} \quad j = 1 : 1 : p \\ &\qquad \text{for} \quad k = 1 : l_j : N \\ &\qquad\qquad h = h + 1 \\ &\qquad\qquad \boldsymbol{V}_k(:, h) = \boldsymbol{1}(n, 1) \\ &\qquad \text{end} \\ &\text{end} \end{aligned}$$

Remark 4.4.H: The intermediate state and input matrices will later in this algorithm include the same information as the matrix $\boldsymbol{\Psi}$ and the vectors $\boldsymbol{v}$ in the T_0-transition equation presented in step 3 in section 4.4. E.g. the $\boldsymbol{\Psi}_1$ matrix in equation 4.59a will simply be denoted as $\boldsymbol{\Psi}_1$ in the algorithm, and $\boldsymbol{v}_1$ and $\boldsymbol{v}_2$ will in addition to some zero-columns be included in the matrix, $\boldsymbol{V}_1$, in the algorithm.

Algorithm Step 5 - Calculating Transition Equations Data
Calculate the data contained in the T_0-transition equations by:
$$\begin{aligned} &\text{for } h = 1 : 1 : N \\ &\quad \text{if} \quad \boldsymbol{M}_{\text{action}}(:, h) = \begin{bmatrix} 1 & 1 \end{bmatrix}^{\mathsf{T}} \\ &\qquad \boldsymbol{\Psi}_h = \boldsymbol{\Phi}(T_0)\boldsymbol{S}_2\boldsymbol{S}_1\boldsymbol{D}_2\boldsymbol{D}_1\boldsymbol{\Psi}_h \\ &\qquad \text{for} \quad j = 1 : 1 : l_1 + l_2 \\ &\qquad\qquad \text{if} \quad \boldsymbol{V}_h(:, j) = \boldsymbol{1}(N, 1) \\ &\qquad\qquad\qquad \text{if} \quad j \leq N_1 \\ &\qquad\qquad\qquad\qquad \boldsymbol{V}_h(:, j) = \boldsymbol{\Phi}(T_0)\boldsymbol{u}_1 \\ &\qquad\qquad\qquad \text{else} \\ &\qquad\qquad\qquad\qquad \boldsymbol{V}_h(:, j) = \boldsymbol{\Phi}(T_0)\boldsymbol{u}_2 \\ &\qquad\qquad\qquad \text{end} \\ &\qquad\qquad \text{end} \\ &\qquad \text{end} \end{aligned}$$

$$\text{elseif} \quad \boldsymbol{M}_{\text{action}}(:,h) = \begin{bmatrix} 1 & 0 \end{bmatrix}^{\mathsf{T}}$$
$$\boldsymbol{\Psi}_h = \boldsymbol{\Phi}(T_0)\boldsymbol{S}_1\boldsymbol{D}_1\boldsymbol{\Psi}_{h-1}$$

$$\text{for} \quad j = 1:1:l_1 + l_2$$
$$\text{if} \qquad \boldsymbol{V}_h(:,j) = \boldsymbol{1}(N,1)$$
$$\boldsymbol{V}_h(:,j) = \boldsymbol{\Phi}(T_0)\boldsymbol{u}_1\boldsymbol{V}_h(:,j)$$
$$\text{elseif} \qquad j > N_1$$
$$\boldsymbol{V}_h(:,j) = \boldsymbol{\Phi}(T_0)\boldsymbol{V}_{h-1}(:,j)$$
$$\text{else}$$
$$\boldsymbol{V}_h(:,j) = \boldsymbol{\Phi}(T_0)\boldsymbol{u}_1\boldsymbol{V}_{h-1}(:,j)$$
$$\text{end}$$
$$\text{end}$$
$$\text{end}$$

$$\text{elseif} \quad \boldsymbol{M}_{\text{action}}(:,h) = \begin{bmatrix} 0 & 1 \end{bmatrix}^{\mathsf{T}}$$
$$\boldsymbol{\Psi}_h = \boldsymbol{\Phi}(T_0)\boldsymbol{S}_2\boldsymbol{D}_2\boldsymbol{\Psi}_{h-1}$$

$$\text{for} \quad j = 1:1:l_1 + l_2$$
$$\text{if} \qquad \boldsymbol{V}_h(:,j) = \boldsymbol{1}(N,1)$$
$$\boldsymbol{V}_h(:,j) = \boldsymbol{\Phi}(T_0)\boldsymbol{u}_2\boldsymbol{V}_h(:,j)$$
$$\text{elseif} \qquad j > N_1$$
$$\boldsymbol{V}_h(:,j) = \boldsymbol{\Phi}(T_0)\boldsymbol{u}_2\boldsymbol{V}_{h-1}(:,j)$$
$$\text{else}$$
$$\boldsymbol{V}_h(:,j) = \boldsymbol{\Phi}(T_0)\boldsymbol{V}_{h-1}(:,j)$$
$$\text{end}$$
$$\text{end}$$
$$\text{end}$$

$$\text{else}$$
$$\boldsymbol{\Psi}_h = \boldsymbol{\Phi}(T_0)\boldsymbol{\Psi}_{h-1}$$
$$\text{for} \quad j = 1:1:l_1 + l_2$$
$$\boldsymbol{V}_h(:,j) = \boldsymbol{\Phi}(T_0)\boldsymbol{V}_{h-1}(:,j)$$
$$\text{end}$$
$$\text{end}$$

Remark 4.4.I: From the algorithm used to calculate the data for the T_0-transition it should be apparent, why the definitions presented in algorithm step 2-4 have been made. More precisely the need for $\boldsymbol{u}_h$ for $h = \{1,...,i\}$, $\boldsymbol{M}_{\text{action}}$ and the preallocation of $\boldsymbol{\Psi}_j$ and $\boldsymbol{V}_j$ for $j = \{1,...,N\}$.

Algorithm Step 6 - LTI Matrix-vector Representation

By the use of the data contained in the T_0-transition ($\boldsymbol{\Psi}_i$ and $\boldsymbol{V}_i$), the state transition matrix, $\boldsymbol{G}^{\boldsymbol{\Psi}}$, the input transition matrix, $\boldsymbol{H}^{\boldsymbol{\Psi}}$ and the output transition matrix, $\boldsymbol{C}^{\boldsymbol{\Psi}}$, can be formulated.

1. The state transition matrix is calculated by defining a temporary matrix, $\boldsymbol{\Psi}_{\text{temp}}$, of size $[Nn \times n]$ containing the data of $\boldsymbol{\Psi}_h$ for $h = \{1,...,N\}$:

$$h = 0$$
$$\text{for} \quad j = 1:1:N$$
$$\boldsymbol{\Psi}_{\text{temp}}(h+1:h+n,n) = \boldsymbol{\Psi}_j$$
$$h = h + n$$
$$\text{end}$$

$$\boldsymbol{G}^{\boldsymbol{\Psi}} = \begin{bmatrix} \boldsymbol{0}(Nn, Nn-n) & \boldsymbol{\Psi}_{\text{temp}} \end{bmatrix}$$

2. Input transition matrix:

$$h = 0$$
$$\text{for} \quad j = 1 : 1 : N$$
$$\quad \boldsymbol{H}^{\boldsymbol{\Psi}}(h + 1 : h + n, n) = \boldsymbol{V}_j$$
$$\quad h = h + n$$
$$\text{end}$$

3. The output transition matrix is defined by initially preallocating $\boldsymbol{C}^{\boldsymbol{\Psi}}$ to be a zero-matrix of size $[l_1 + l_2 \times Nn]$, and hereafter the entrance of $\boldsymbol{C}^{\boldsymbol{\Psi}}$ is changed in accordance to the following algorithm:

$$h = 0$$
$$\text{for} \quad j = 1 : 1 : p$$
$$\quad \text{if} \quad j = 1$$
$$\quad\quad \text{for} \quad k = 1 : 1 : N$$
$$\quad\quad\quad \text{for} \quad m = 0 : 1 : N_j - 1$$
$$\quad\quad\quad\quad \text{if} \quad (m = 0 \ \& \ k = N) \ || \ ml_j = k$$
$$\quad\quad\quad\quad\quad \boldsymbol{C}^{\boldsymbol{\Psi}}(m + 1, h : h + n) = \boldsymbol{C}(h, :)$$
$$\quad\quad\quad\quad \text{else}$$
$$\quad\quad\quad\quad\quad \boldsymbol{C}^{\boldsymbol{\Psi}}(m + 1, h : h + n) = \boldsymbol{0}(1, n)$$
$$\quad\quad\quad\quad \text{end}$$
$$\quad\quad\quad \text{end}$$
$$\quad\quad\quad h = h + n$$
$$\quad\quad \text{end}$$
$$\quad\quad h = 0$$
$$\quad \text{else}$$
$$\quad\quad \text{for} \quad k = 1 : 1 : N$$
$$\quad\quad\quad \text{for} \quad m = 0 : 1 : N_j - 1$$
$$\quad\quad\quad\quad \text{if} \quad (m = 0 \ \& \ k = N) \ || \ ml_j = k$$
$$\quad\quad\quad\quad\quad \boldsymbol{C}^{\boldsymbol{\Psi}}(m + l_1, h : h + n) = \boldsymbol{C}(h, :)$$
$$\quad\quad\quad\quad \text{else}$$
$$\quad\quad\quad\quad\quad \boldsymbol{C}^{\boldsymbol{\Psi}}(m + l_1, h : h + n) = \boldsymbol{0}(1, n)$$
$$\quad\quad\quad\quad \text{end}$$
$$\quad\quad\quad \text{end}$$
$$\quad\quad\quad h = h + n$$
$$\quad\quad \text{end}$$
$$\quad\quad h = 0$$
$$\quad \text{end}$$
$$\text{end}$$

Remark 4.4.J: The notation & and || used in the if-statements presented in the calculations of the output transition matrix, $\boldsymbol{C}^{\boldsymbol{\Psi}}$, simply means *and* and *or* respectively.

This concludes the presentation of the software algorithm for the UNMR method. The next chapter concerns the development of a DFPT multirate model and the UNMR method will along with this sections presented algorithm be part of this development.

Multirate DFPT Modelling

This chapter presents how a linear multirate model of the 10 kW DFPT is derived. The chapter starts with a presentation of various continuous and discrete linear models which each represents different subelements of the DFPT. Based on these models, the developed unified non-minimal realisation method will be applied to create a linear multirate DFPT model. The chapter ends with a validation of the derived model and comments upon what challenges must be addressed before a 5.4 MW DFPT multirate model can be derived.

DFPT Modelling Preface:

The problem this thesis seeks to answer is how to develop a LTI multirate model of a utility-scale WT DFPT such that conventional analysis and control design tools can be applied. The problem of obtaining a LTI multirate DFPT model has been divided into three subtasks which are presented in section 1.5.1. These include how to linearly model a full stroke operated DDM, how to address the challenge of having a non-uniform sample rate in the time-domain and lastly how to develop a linear multirate model.

Each subtask is studied and solved individually. A linear model of a DDM, has been studied by Johansen et al. (2016) and Pedersen et al. (2016a) and a method for handling non-uniform sampling rate was proposed in unpublished work by Pedersen et al. (2016a) and utilised by the authors of this thesis in Junker et al. (2016). The third and last subtask is studied in chapter 4 where the UNMR method is developed and shown to successfully model the multirate MSD system while fulfilling all the desired characterisitics. The aim of this chapter is therefore to combine the solutions from the three subtasks such that a linear multirate model of a DFPT can be formulated. To investigate this, the fictive 10 kW DFPT, which is introduced exclusively as a DFPT system used to evaluate the applicability of methods onto a DFPT, is utilised. The 10 kW DFPT is a highly simplified version of the 5.4 MW DFPT used for a utility-scale WT. This significantly eases the application and evaluation of various method. The main specifications of the fictive 10 kW DFPT is reiterated here in order to ease the understanding of the linear multirate model derivation of the 10 kW DFPT presented in this chapter.

The 10 kW DFPT consists of two DDMs, a DD pump and motor, connected by a high and low pressure line. The pressure in the low pressure line is assumed constant. The DD pump contains one pressure chamber which can be discretely activated twice per pump shaft rotation (full stroke operation), due to the lobed pump shaft geometry. The DD motor contains three pressure chambers where each chamber can be discretely activated once per motor shaft rotation (full stroke operation). The motor is assumed to be operated at a constant speed of 1500 rpm and the pump shaft speed is variable but with a rated value equal to 1500 rpm. The following section presents the approach for

applying the solutions of the subtasks to the 10 kW DFPT system.

5.1 Multirate Modelling Approach

Before the UNMR method can be applied to obtain a multirate 10 kW DFPT model, some preliminary considerations and decisions are made. These are presented in the following.

The UNMR method offers an approach for creating a linear multirate model of a system which elements can be described by a combination of continuous and discrete linear models. This method was developed based on the MSD system where linear descriptions of the system elements are well known. However, for the DFPT, linear descriptions of the different system elements are no longer well known why linear descriptions of the DFPT's elements must be obtained prior to applying the UNMR method.

There is no specific requirements to which type of linear model can be used to describe the system elements in the DFPT, other than being time-invariant and that the chosen models should be a reasonable approximation of the true system dynamics. Thus several different types and combinations of linear models might be utilised. The choice of which types of models are chosen to represent the different system elements in the DFPT is depicted in figure 5.1. The figure is made to be a linear equivalent representation of the non-linear simulation model of the DFPT presented in figure 3.1. In addition to presenting the different types of linear models which will be utilised to make a multirate DFPT model, figure 5.1 furthermore aims to present how the different system elements interact with each other.
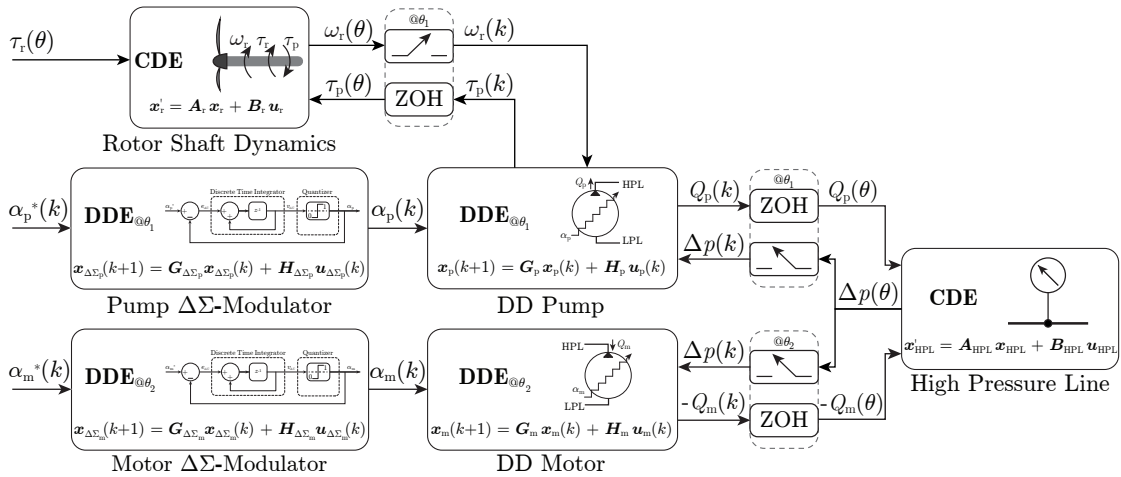
Fig. 5.1: Linear open loop multirate DFPT model described in the spatial-domain, which is valid for both 10 kW DFPT and 5.4 MW DFPT. Each block in the figure represents a continuous or a discrete linear state space representation of a system element in the DFPT. Inputs for the multirate model is the rotor torque, τ_r, and the displacement references $\alpha_p{}^*$ and $\alpha_m{}^*$ for the pump and motor, respectively. The notation $@\theta_1$ and $@\theta_2$ specifies the sampling rate of the pump and motor, respectively.

A few general remarks can be made to figure 5.1.

Remark 5.1.A: All models are linear as this is a necessity in order to apply the UNMR method. As a consequence the NREL turbine model, which describes a nonlinear relation between the exogenous wind input, v, and the rotor torque, τ_r has been omitted. Instead the rotor torque, τ_r, is simply seen as a disturbance input to the rotor shaft dynamics.

Remark 5.1.B: The derived multirate DFPT model is intended to be used for a deterministic control approach. Thus, noise/disturbance terms cannot be included in the linear descriptions of the respective system elements, and when such terms are present they will therefore be neglected before the UNMR method is applied.

Remark 5.1.C: As presented in section 1.5.1 the challenge of non-uniform time-domain activation rate of a variable-speed DDM may be solved by considering the machine in the spatial angle-domain, where the angle between successive chamber activations is constant. Therefore all linear models presented in figure 5.1 are either derived in the spatial angle-domain or transformed from the time-domain. This transformation from the time-domain to the spatial angle-domain means that the linear multirate model which is developed in this chapter will be on an angle-invariant form instead of time-invariant.

Remark 5.1.D: The challenge of choosing appropriate linear representations of the different system elements is limited to the DDMs of the pump and motor, as approaches for a linear descriptions of the remaining system elements (Newtons's II law, continuity equation and $\Delta\Sigma$-modulators) are considered well established. It is chosen to use a discrete convolution sum model to describe the dynamics of the DDMs.

Linear DFPT System Elements:

In addition to the general remarks made to the multirate DFPT model, some elaborating comments can be made to the individual system elements depicted in figure 5.1:

DD Pump: The DD pump is operated using full stroke operation, which effectively means that the pump displacement only can be changed at specific pump angles (piston positions). These positions are given by the angular distance between cylinder chambers denoted by θ_1. To include this vital characteristic, a discrete approximation with a sampling interval of θ_1 is chosen to describe the pump flow, Q_p, and pump torque, τ_p in the spatial angle-domain. The notation @θ_1 presented in figure 5.1 simply means that the discrete model uses the sampling interval θ_1. The discrete model of the pump is based on the convolution sum model of impulse responses proposed by Johansen et al. (2016), which in Junker et al. (2016) has been successfully utilised by the authors for describing the pump flow and torque.

DD Motor: Like for the DD pump, the DD motor is operated by the use of full stroke operation, why a similar discrete modelling approach is chosen. In this case the sampling interval is denoted θ_2 and corresponds to the angular distance between cylinders in the motor.

$\Delta\Sigma$-Modulator: These system elements are included in the multirate DFPT model in order to facilitate the use of conventional control structures where the control output will be a non-binary displacement reference, e.g α_p^* for the pump. The purpose of the $\Delta\Sigma$-modulator is thus to convert a non-binary displacement input into a binary chamber activation sequence, which can be given as an input to one of the DDMs. The dynamics of a $\Delta\Sigma$-modulator are mathematically described by equations 3.19 and 3.20, which include a discrete integrator and a non-linear quantizer. The discrete representation is in this chapter linearised, and the conventional sampling time of such a discrete model is replaced with the sampling rate θ_1 or θ_2 depending on which DDM the $\Delta\Sigma$-modulator is connected to.

High Pressure Line: This dynamic element is modelled by the continuity equation, which is represented in the time-domain. Thus the equation is transformed into the spatial domain and furthermore linearised in order to be implemented in the multirate DFPT model.

Rotor Shaft Dynamics: The rotational analogue to Newton's II law is used to describe the dynamics of the rotor shaft. Similar to the HPL, the dynamics of the rotor are transformed into the spatial-domain and afterwards linearised in order to have a feasible representation for the multirate DFPT model.

ZOH Elements: The ZOH elements in figure 5.1 are essential when DDE and CDE must be connected and therefore a zero-order-hold approximation will be applied for the DFPT's flow, torque and pressure dynamics.

Multirate DFPT Modelling Procedure:

Having defined the types of linear models needed to describe the dynamics of the DFPT, a procedure for deriving the multirate DFPT model is presented. The procedure furthermore serves as a guideline for how the remainder of this chapter progresses. The bolded headlines depicts the remaining sections of this chapter, and the elaborating text beneath describes the content of each section:

1. **Linear System Element Representation:** Deriving linear representations of the DFPT elements presented in figure 5.1. These will be presented in a generalised form, meaning that the linear representations will be valid for both the 5.4 MW and 10 kW DFPT.

   - The linear models of the DDMs will initially be derived for the 5.4 MW DFPT. This is deemed to provide the reader with a better understanding of how the convolution sum model works including its applicability and limitations. However when the 10 kW multirate model later is evaluated, associated model parameters will be presented.
   - The general form of the remaining linear system elements included in the multirate DFPT model is identical for both the 5.4 MW and 10 kW power rating.

2. Application of the unified non-minimal realisation method:

Generalised DFPT Modelling:
Step 1: Defining the state variables. This is done in the most generalised form when possible, thus being applicable for both 5.4 MW and 10 kW DFPT.
Step 2: Calculating the various transition matrices ($\boldsymbol{\Psi}, \boldsymbol{D}, \boldsymbol{S}$), once again in a generalised form when possible.

10 kW DFPT Modelling:
Step 3: Based on the sampling rates of the 10 kW DFPT and starting from kT, the transition equations are derived for the sampling operations and sample-free angle-intervals for an entire BTP.
Step 4: Combining and simplifying transition equations to obtain a linear angle-domain and angle-invariant model of the 10 kW DFPT.

3. 10 kW Model Validation: Validate the derived 10 kW multirate DFPT model using the associated simulation model derived in chapter 3. Establish if the UNMR method is applicable for the 5.4 MW DFPT and identify the tasks which must be addressed prior to the potential development of a 5.4 MW multirate DFPT model.

This concludes the consideration made prior to the development of the of a multirate DFPT model and the next section will proceed with deriving linear system element representations.

5.2 Linear System Element Representations

The content of this section takes its starting point in some of the linear models presented in Junker et al. (2016). The work of this section, while using the same type of models as presented in Junker et al. (2016), will generally differ in the aspect that the purpose is now to carry out the necessary groundwork to later derive a MIMO multirate model, whereas in the referenced work the goal was to create two decentralised SISO models.

The models of the system elements will next be presented, starting with the discrete representations of the $\Delta\Sigma$-modulators and DDMs continued by the continuous representations of the rotor dynamics and the HPL pressure dynamics.

5.2.1 Linear $\Delta\Sigma$-Modulater Representation

The $\Delta\Sigma$-modulator is used for transforming a non-binary displacement reference to a bianry one. A linear representation of the $\Delta\Sigma$-modulator is made in accordance with Reiss (2008), and depicted in figure 5.2, where the $\Delta\Sigma$-modulator connected to the DD pump is shown. Reiss (2008) proposes to view the first order non-linear quatizer as a noise term, $n_{\Delta\Sigma}$. This description may be used, as the linear binary output, α_{p}, will contain the average of the input, $\alpha_{\mathrm{p}}{}^*$, in addition to a bit stream, $n_{\Delta\Sigma}$, considered as noise.
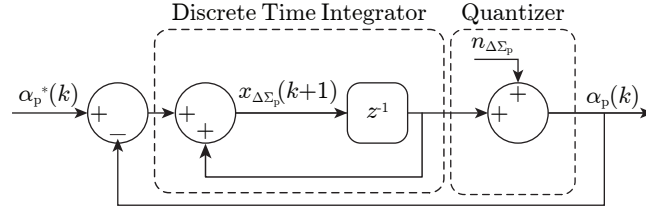
Fig. 5.2: Linear representation of a first order $\Delta\Sigma$-modulator for the DD pump. Inspired by Reiss (2008).

From figure 5.2 two difference equations describing the linear dynamics of the $\Delta\Sigma$-modulator can be derived:

$$x_{\Delta\Sigma_{\mathrm{p}}}(k+1) = x_{\Delta\Sigma_{\mathrm{p}}}(k) + \alpha_{\mathrm{p}}{}^*(k) - \alpha_{\mathrm{p}}(k) \tag{5.1a}$$

$$\alpha_{\mathrm{p}}(k) = x_{\Delta\Sigma_{\mathrm{p}}}(k) + n_{\Delta\Sigma}(k) \tag{5.1b}$$

Equation 5.1b can be viewed as an output equation, and by the definition of equation 5.1a, this output is described by a single sample delayed input and the quantization error represented by a digital differentiated noise term.

By defining a state variable, $x_{\Delta\Sigma_{\mathrm{p}}}$, and inserting equation 5.1b into equation 5.1a a discrete state-space representation of the $\Delta\Sigma$-modulator can be formulated as:

$$x_{\Delta\Sigma_{\mathrm{p}}}(k+1) = \overbrace{[0]}^{G_{\Delta\Sigma_{\mathrm{p}}}} x_{\Delta\Sigma_{\mathrm{p}}}(k) + \overbrace{[1]}^{H_{\Delta\Sigma_{\mathrm{p}}}} \overbrace{\alpha_{\mathrm{p}}{}^*(k)}^{u_{\Delta\Sigma_{\mathrm{p}}}[k]} - [1]\, n_{\Delta\Sigma_{\mathrm{p}}}(k) \tag{5.2a}$$

$$y_{\Delta\Sigma_{\mathrm{p}}}(k) = \alpha_{\mathrm{p}}(k) = \underbrace{[1]}_{C_{\Delta\Sigma_{\mathrm{p}}}} x_{\Delta\Sigma_{\mathrm{p}}}(k) + [1]\, n_{\Delta\Sigma_{\mathrm{p}}}(k) \tag{5.2b}$$

An identical approach can used to derive the $\Delta\Sigma$-modulator for the DD motor, where the subscript m is used instead of p.

Remark 5.2.A: To accurately describe the noise term, $n_{\Delta\Sigma}$, a non-linear description must be utilised. As non-linear representations cannot be accommodated when the UNMR method must be applied, and furthermore because it is the intend to apply deterministic control, the noise term in equations 5.2a and 5.2b will be omitted in the future model development.

5.2.2 Linear DDM Representations

As evident from the previous discussion and with reference to figure 5.1, linear descriptions of the DDM flows and torques are necessary to form a multirate DFPT model. Such descriptions may be derived by considering the volumetric displacement of a single pressure chamber as proposed in Johansen et al. (2016). Then by considering the flow produced by a single pressure chamber as the discrete impulse response of an entire DDM, a linear description of the DDM flow may be obtained. In the following the proposed approach is applied to both the DD pump and DD motor. The derivation of linear DDM models are based on the 5.4 MW DFPT as the high number of chambers in its DDMs

significantly eases the understanding of how these are linearly modelled. The derived type of linear DDM model are however also utilised for modelling the DDMs in the 10 kW DFPT.

5.2.2.A Pump Flow Response

Figure 5.3 illustrates the normalised volumetric displacement of a single pressure chamber in the DD pump of the 5.4 MW DFPT. The pumping stroke is initiated by actively closing the LPV at TDC (maximum chamber volume). This pressurises the fluid in the chamber until the pressure is above p_{H} which causes the HPV to passively open at θ_{HPV}, and the pump starts producing flow. As the piston passes BDC (minimum chamber volume), the chamber pressure starts to decrease and at a pressure level below p_{H}, the pumping stroke ends as the HPV is passively closed. Subsequently, at a chamber pressure below p_{L} the LPV passively opens.
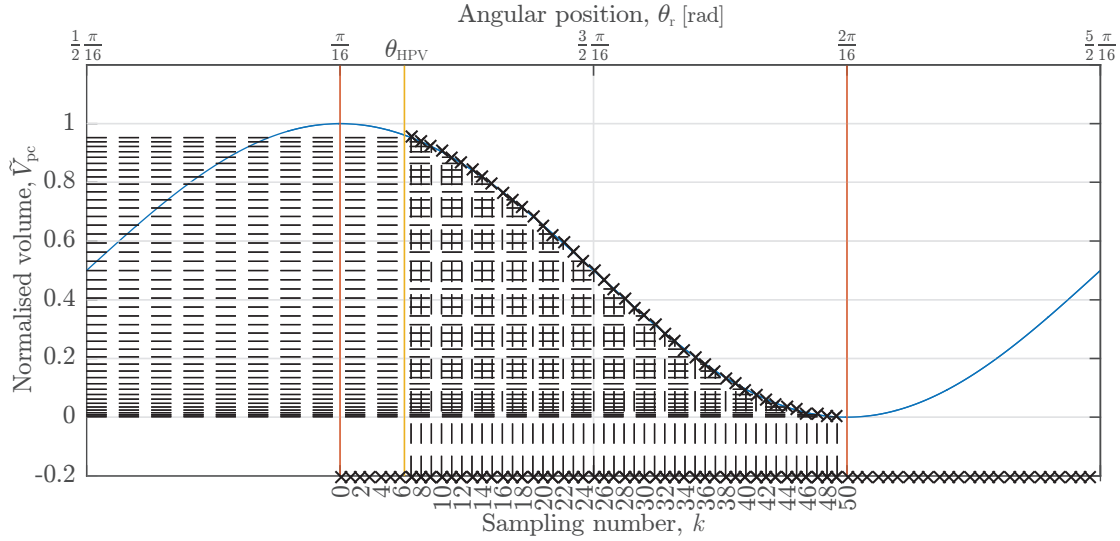
Fig. 5.3: Normalised volumetric displacement of a single pump pressure chamber. The upper x-axis denotes the angular shaft position, and the bottom x-axis illustrates the corresponding sampling instances for the 5.4 MW DFPT (Only every second instance is numbered).

The pumping stroke interval may be subdivided into a number of smaller intervals of width equal to the angle between subsequent chambers, and thus the flow through the HPV at any discrete instant k within the pumping stroke may be approximated by:

$$Q_{\mathrm{HPV}}(k) \approx \frac{V_{\mathrm{pc}}(\theta(k+1)) - V_{\mathrm{pc}}(\theta(k))}{\theta_1} = \underbrace{\frac{x_{\mathrm{p,stroke}} A_{\mathrm{pp}}}{\theta_1}}_{k_{Q_{\mathrm{p}}}} \Delta \tilde{V}_{\mathrm{pc}}(k) \qquad (5.3)$$

where $\tilde{V}_{\mathrm{pc}}(k)$ is the normalised displacement fraction at the kth position, the product $x_{\mathrm{p,stroke}} A_{\mathrm{pp}}$ is the maximum volumetric displacement of a single chamber, and θ_1 is the distance between sampling instances. These discrete instances are aligned with physical location of the pressure chambers, and correspond to the points at which a decision to

initiate a pumping stroke for a single chamber can be made, and the distance between them is given by:

$$\theta_1 = \frac{2\,\pi}{N_{\mathrm{pc}}\,N_{\mathrm{cr}}\,N_{\mathrm{l}}} \tag{5.4}$$

Remark 5.2.B: The flow approximation of equation 5.3 effectively assumes that fluid compressibility effects are negligible, such that the chamber pressure is constant, which it is not.

The normalised displacement fractions may be calculated by considering the volume change between sampling instances:

$$\Delta \tilde{V}_{\mathrm{pc}}(k) = \begin{cases} 0 & \text{for } \theta(k),\, \theta(k+1) \notin [\theta_{\mathrm{HPV}};\frac{2\pi}{16}] \\ \tilde{V}_{\mathrm{pc}}(\theta(k+1)) - \tilde{V}_{\mathrm{pc}}(\theta_{\mathrm{HPV}}) & \text{for } \theta(k) < \theta_{\mathrm{HPV}} < \theta(k+1) \\ \tilde{V}_{\mathrm{pc}}(\theta(k+1)) - \tilde{V}_{\mathrm{pc}}(\theta(k)) & \text{for } \theta(k),\, \theta(k+1) \in [\theta_{\mathrm{HPV}};\frac{2\pi}{16}] \\ \tilde{V}_{\mathrm{pc}}(\frac{2\pi}{16}) - \tilde{V}_{\mathrm{pc}}(\theta(k)) & \text{for } \theta(k) < \frac{2\pi}{16} < \theta(k+1) \end{cases} \tag{5.5}$$

Remark 5.2.C: Ideally a full pumping stroke lasts from TDC to BDC, i.e. the interval $\left[\frac{\pi}{16};\frac{2\pi}{16}\right]$, however, because of passive valve actuation some of the stroke must be used to create the necessary pressure differences, why in accordance with figure 5.3 and equation 5.5 flow does not occur from sample $k = 0$.

In full stroke operation, the stroke cannot be interrupted, and thus when starting the stroke at $k = 0$, flow is produced from $k = 6$ until $k = 50$. Thus, a total of 51 samples are used to describe a full pumping stroke (5.4 MW DFPT). Considering the stroke as an impulse response, and subsequent strokes as shifted impulse responses, then a convolution sum type model may be formulated:

$$\tilde{\alpha}_{\mathrm{p}}(k) = -\sum_{m=0}^{k} \Delta \tilde{V}_{\mathrm{pc}}(k-m)\,\alpha_{\mathrm{p}}(m) \tag{5.6a}$$

$$Q_{\mathrm{p}}(k) = k_{Q_{\mathrm{p}}}\,\omega_{\mathrm{r}}(k)\,\tilde{\alpha}_{\mathrm{p}}(k) \tag{5.6b}$$

Here the upper equation represents the impulse response model, with the lower equation being the scaling of the normalised flow response. $\alpha_{\mathrm{p}}(m)$ is a binary displacement input sequence, which determines whether subsequent pressure chambers are activated or not.

Remark 5.2.D: It has in section 3.3.1 been defined that the flow, Q_{p}, is positive when given a binary displacement input, α_{p}, different from zero (note that α_{p} cannot be negative). Therefore a minus term in front of the summation in equation 5.6 is included to cancel out the negative normalised volumetric displacement contained in $\Delta \tilde{V}_{\mathrm{pc}}(k)$, which is the result of the definitions made in equation 5.3.

As evident from equation 5.6, the scaling is non-linear since it is a product of the shaft speed (a model state) and the convolution sum. Thus by use of a first order Taylor approximation the scaling is linearised:

$$\Delta Q_{\mathrm{p,lin}}(k) = k_{Q_{\mathrm{p}}}\tilde{\alpha}_{\mathrm{p0}}\,\Delta\omega_{\mathrm{r}}(k) + k_{Q_{\mathrm{p}}}\omega_{\mathrm{r0}}\,\Delta\tilde{\alpha}_{\mathrm{p}}(k) \tag{5.7}$$

The choice of the linearisation constants, $\tilde{\alpha}_{\text{p0}}$ and ω_{r0}, will not be considered in this section, but are later discussed in section 5.4.1, however one remark to equation 5.7 is made:

Remark 5.2.E: A consequence of applying the Taylor approximation is a linearised flow expression, which first term does not depend on the current displacement input, $\alpha_{\text{p}}(k)$, represented within $\tilde{\alpha}_{\text{p}}(k)$. This effectively means that even though the input to the pump is $\alpha_{\text{p}} = 0(\tilde{\alpha}_{\text{p}} = 0)$, the linear flow model will output a non-zero flow if $\tilde{\alpha}_{\text{p0}} \neq 0$. This does not bear any physical meaning, why by solely considering equation 5.7 $\tilde{\alpha}_{\text{p0}} = 0$ should be chosen as the linearisation constant.

The convolution sum of equation 5.6a may be written in a state-space formulation by defining a number of states corresponding to the previous inputs:

$$
\overbrace{\begin{bmatrix} \alpha_{\text{p}}(k) \\ \alpha_{\text{p}}(k-1) \\ \alpha_{\text{p}}(k-2) \\ \vdots \\ \alpha_{\text{p}}(k-p_{\text{p}}+1) \end{bmatrix}}^{\boldsymbol{x}_{\text{p}}(k+1)} = \overbrace{\begin{bmatrix} 0 & 0 & \cdots & 0 & 0 \\ 1 & 0 & \cdots & 0 & 0 \\ 0 & 1 & \cdots & 0 & 0 \\ \vdots & \vdots & \ddots & \vdots & \vdots \\ 0 & 0 & \cdots & 1 & 0 \end{bmatrix}}^{\boldsymbol{G}_{\text{p}}} \overbrace{\begin{bmatrix} \alpha_{\text{p}}(k-1) \\ \alpha_{\text{p}}(k-2) \\ \alpha_{\text{p}}(k-3) \\ \vdots \\ \alpha_{\text{p}}(k-p_{\text{p}}) \end{bmatrix}}^{\boldsymbol{x}_{\text{p}}(k)} + \overbrace{\begin{bmatrix} 1 \\ 0 \\ 0 \\ \vdots \\ 0 \end{bmatrix}}^{\boldsymbol{H}_{\text{p}}} \overbrace{\alpha_{\text{p}}(k)}^{u_{\text{p}}(k)} \tag{5.8a}
$$

$$
\tilde{\alpha}_{\text{p}}(k) = \begin{bmatrix} \Delta\tilde{V}_{\text{pc}}(1) & \Delta\tilde{V}_{\text{pc}}(2) & \Delta\tilde{V}_{\text{pc}}(3) & \cdots & \Delta\tilde{V}_{\text{pc}}(p_{\text{p}}) \end{bmatrix} \boldsymbol{x}_{\text{p}}(k) + \begin{bmatrix} \Delta\tilde{V}_{\text{pc}}(0) \end{bmatrix} u_{\text{p}}(k) \tag{5.8b}
$$

By combining equations 5.7 and 5.8b a new discrete output equation, which describes the pump flow as a linear combination of other states, may be derived:

$$
y_{Q_{\text{p}}}(k) = Q_{\text{p,lin}}(k) = k_{Q_{\text{p}}}\tilde{\alpha}_{\text{p0}}\underbrace{\omega_{\text{r}}(k)}_{x_{\text{r}}(k)} + \omega_{\text{r0}}\underbrace{k_{Q_{\text{p}}}\Delta\tilde{\boldsymbol{V}}_{\text{pc}}(1{:}p)}_{\boldsymbol{C}_{\text{p}}} \boldsymbol{x}_{\text{p}}(k) + \omega_{\text{r0}}\underbrace{k_{Q_{\text{p}}}\Delta\tilde{\boldsymbol{V}}_{\text{pc}}(0)}_{D_{\text{p}}} \underbrace{u_{\text{p}}(k)}_{y_{\Delta\Sigma\text{p}}(k)} \tag{5.9}
$$

Noting that the Δ notation from equation 5.7 has been omitted to simplify the notation. ω_{r} is the state related to the rotor shaft dynamics, why it is denoted as such, and ω_{r0} its corresponding linearisation point. The DD pump input $u_{\text{p}}(k) = \alpha_{\text{p}}(k)$ is defined as the $\Delta\Sigma$-modulator output $y_{\Delta\Sigma\text{p}}(k)$, as illustrated in figure 5.1.

Remark 5.2.F: In the 5.4 MW DFPT, $D_{\text{p}} = 0$, but not in the 10 kW DFPT, why it has been included in equation 5.9 for the completeness of the state-space formulation.

Remark 5.2.G: The linear combination in equation 5.9 is a combination of both purely discrete states and sampled continuous states. This mixture is a non-issue in the UNMR method, since a DDE, which the pump is represented as, is defined to have sampling actions at its corresponding inputs.

To illustrate the applicability of the utilised linear DDM flow models, a model comparison between the linear and non-linear model of the DD pump in the 5.4 MW DFPT is made. In this comparison the linear flow model is based on the operating point of $\tilde{\alpha}_{\text{p0}} = 0$ and $\omega_{\text{r0}} = 10.5\,\text{rpm}$. Similarly the non-linear model is simulated at a constant speed of ω_{r0} and additionally a constant pressure in the HPL of $p_{\text{H}} = 360\,\text{bar}$. The flow dynamics for a single pressure chamber are for the linear and non-linear model presented in figure 5.4.
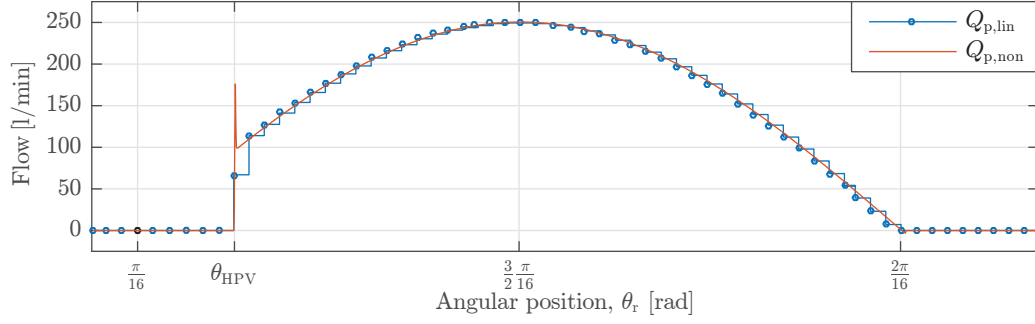
Fig. 5.4: Comparison of linear and non-linear flow response for a single pressure chamber in the DD pump of the 5.4 MW DFPT. At $\theta_r = \frac{\pi}{16}$ the decision to activate the next pressure chamber is taken, e.g. a binary input of 1 is given as input to both the linear and non-linear DD pump. Subsequent chambers are not activated.

From figure 5.4, it can be seen that the linear flow, $Q_{p,lin}$, deviates from the non-linear flow, $Q_{p,non}$, at the angle, θ_{HPV}, where the HPV is passively opened. The cause of this deviation is due to the omitted pressure dynamics in the linear flow model. Furthermore, a small deviation exist when the pumping stroke ends and the piston passes BDC (difficult to detect in figure 5.4). The deviation is the result of backflow from the HPL and into the pressure chamber as the passive closing of the HPV does not occur instantaneously. Despite these deviations, the discrete representation of the motor flow is seen to be a good fit of the continuous non-linear flow in the majority of the pumping stroke, why the presented flow modelling approach is considered valid.

Before proceeding to how the pump torque may be modelled, a final remark is made:

Remark 5.2.H: It is evident, that the greater the number of pressure chambers, the better the resolution obtained by the discrete model is. Thus for the descaled 10 kW drivetrain, this method will yield somewhat poor approximations of the actual flow waveform.

5.2.2.B Pump Torque Response

By use of the previously considered DD pump flow, an expression for the torque may be derived by considering input-output power conservation in the pump:

$$P_p = Q_p \, \Delta p = \tau_p \, \omega_r \quad \Rightarrow \quad \tau_p = \frac{Q_p \, \Delta p}{\omega_r} \tag{5.10}$$

Combining equations 5.6b and 5.10 yields a discrete expression for the torque independent of the shaft speed:

$$\tau_p(k) = \frac{Q_p(k) \, \Delta p(k)}{\omega_r(k)} = k_{Q_p} \, \Delta p(k) \, \tilde{\alpha}_p(k) \tag{5.11}$$

This is a non-linear expression, why it is linearised by a first order Taylor approximation:

$$\Delta \tau_{p,lin}(k) = k_{Q_p} \tilde{\alpha}_{p0} \, \Delta\Delta p(k) + k_{Q_p} \Delta p_0 \, \Delta\tilde{\alpha}_p(k) \tag{5.12}$$

Remark 5.2.I: Equation 5.12 is used to calculate the torque produced by a single pressure chamber. When a chamber pressurises the fluid, the pressure it is working against is that of the HPL, p_H, and not the pressure difference, Δp, as such Δp_0 should be set equal to the linearisation value of p_H.

Remark 5.2.J: In contrast to the linearised flow expression seen in equation 5.7, the first term of the linearised torque expression has physical meaning, since the produced pump torque is dependent on the pressure in the HPL. Solely considering the torque expression in equation 5.12 thus suggest, that choosing the linearisation constant $\tilde{\alpha}_{\mathrm{p}0} \neq 0$ would yield the best torque approximation.

As previously, a new discrete output equation, which now describes the pump torque as a linear combination of other states, may again be formed by combining equations 5.8b and 5.12:

$$y_{\tau_\mathrm{p}}(k) = \tau_{\mathrm{p,lin}}(k) = k_{Q_\mathrm{p}} \tilde{\alpha}_{\mathrm{p}0} \underbrace{\Delta p(k)}_{x_{\mathrm{HPL}}(k)} + \Delta p_0 \underbrace{k_{Q_\mathrm{p}} \Delta \tilde{\boldsymbol{V}}_{\mathrm{pc}}(1{:}p)}_{\boldsymbol{C}_\mathrm{p}} \boldsymbol{x}_\mathrm{p}(k) + \Delta p_0 \underbrace{k_{Q_\mathrm{p}} \Delta \tilde{\boldsymbol{V}}_{\mathrm{pc}}(0)}_{D_\mathrm{p}} \underbrace{u_\mathrm{p}(k)}_{y_{\Delta\Sigma\mathrm{p}}(k)} \quad (5.13)$$

Noting that the Δ notation from equation 5.12 has also been omitted to simplify the notation. Δp_{HPL} is the state related to the HPL pressure dynamics, why it is denoted as such, and like before the DD pump input $u_\mathrm{p}(k) = \alpha_\mathrm{p}(k)$ is defined as the $\Delta\Sigma$-modulator output $y_{\Delta\Sigma\mathrm{p}}(k)$, as illustrated in figure 5.1.

Similarly as for the linear flow response, it is chosen to make a model comparison between the linear and non-linear torque response. The comparison is seen in figure 5.5 and is made under the same conditions as the previously presented flow comparison in figure 5.4.
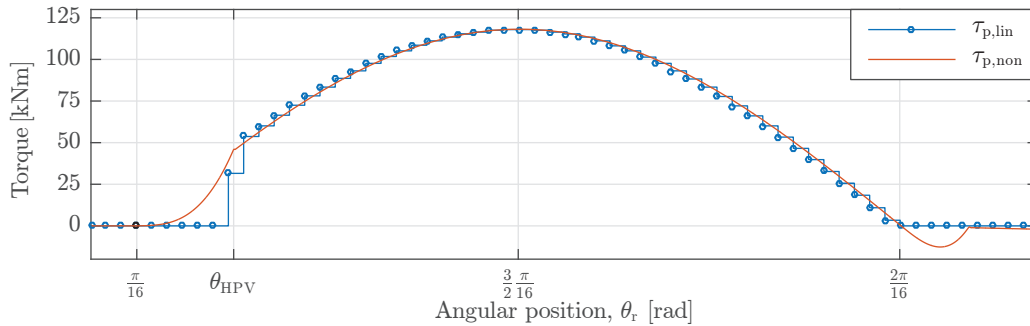

Fig. 5.5: Comparison of linear and non-linear torque response for a single pressure chamber in the DD pump of the 5.4 MW DFPT. At $\theta_\mathrm{r} = \frac{\pi}{16}$ the decision to activate the next pressure chamber is taken, e.g. a binary input of 1 is given as input to both the linear and non-linear DD pump. Subsequent chambers are not activated.

Figure 5.5 shows torque deviations between the linear and non-linear model at the beginning and ending of the pumping stroke. Similarly to the flow deviations, these are explained by the omitted pressure dynamics. As the linear torque response is a function of the linear flow response, it also is no surprise that the comparison shown figures 5.4 and 5.5 shows resemblances. The presented results are deemed sufficient to validate the DDM modelling approach.

5.2.2.C Motor Flow Response

Very similarly to the approach utilised for the pump, a discrete impulse response model may be derived for the DD motor flow.

The motoring stroke is initiated at some angle $\theta_\mathrm{m} = \theta_\mathrm{LPV}$ before the BDC, such that when the LPV is actively closed, the chamber pressure increases above p_H, which passively opens the HPV. Then near the TDC, the HPV is actively closed and the motoring stroke ends, such that the chamber pressure decreases, causing the LPV to passively open when the chamber pressure is below p_L.
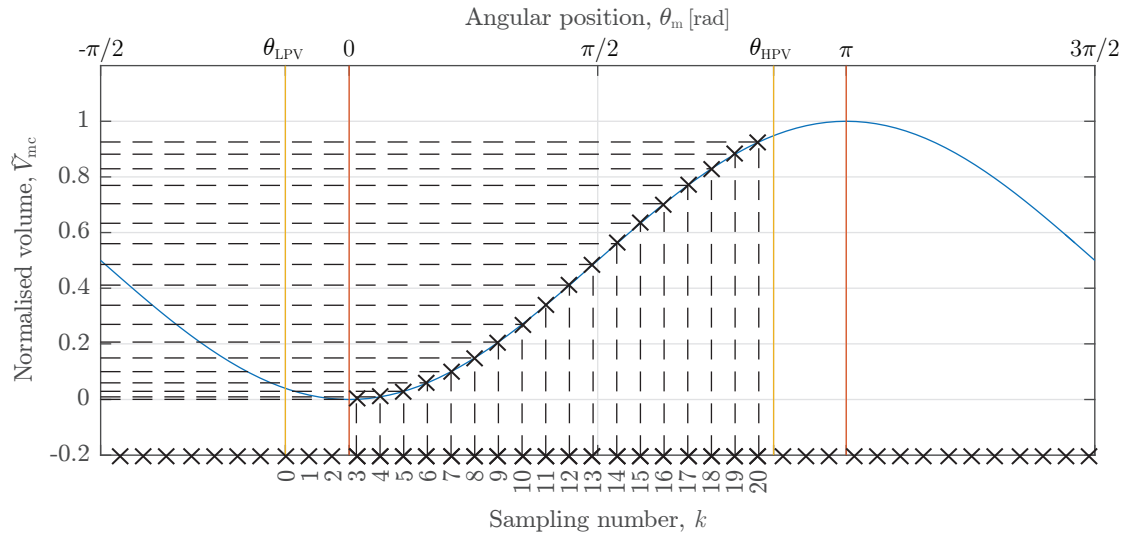
Fig. 5.6: Normalised volumetric displacement of a single motor pressure chamber. The upper x-axis denotes the angular shaft position, and the bottom x-axis illustrates the corresponding sampling instances for the DD motor in the 5.4 MW DFPT. Illustration taken from the previously presented work in Junker et al. (2016).

The sampling intervals are now simply defined by:

$$\theta_2 = \frac{2\,\pi}{N_\mathrm{mc}\,N_\mathrm{ec}} \tag{5.14}$$

The convolution type model may now be obtained as:

$$\tilde{\alpha}_\mathrm{m}(k) = \sum_{m=0}^{k} \Delta \tilde{V}_\mathrm{mc}(k-m)\,\alpha_\mathrm{m}(m) \qquad Q_\mathrm{m}(k) = k_{Q_\mathrm{m}}\,\omega_\mathrm{m}\,\tilde{\alpha}_\mathrm{m}(k) \tag{5.15}$$

It is worth noting, that for the motor, the shaft speed is constant, such that the scaling of the convolution sum is thus linear, why linearisation like for the pump is not necessary. k_{Q_m} is defined similarly as for k_{Q_p} Like before, a state-space formulation may again be obtained, where the number of states is now 20 (5.4 MW DFPT), and the output equation may be written as:

$$y_{Q_\mathrm{m}}(k) = Q_\mathrm{m}(k) = \omega_\mathrm{m}\,\underbrace{k_{Q_\mathrm{m}}\Delta \tilde{\boldsymbol{V}}_\mathrm{mc}(1{:}p)}_{\boldsymbol{C}_\mathrm{m}}\,\boldsymbol{x}_\mathrm{m}(k) + \omega_\mathrm{m}\,\underbrace{k_{Q_\mathrm{m}}\Delta \tilde{\boldsymbol{V}}_\mathrm{mc}(0)}_{D_\mathrm{m}}\,\underbrace{u_\mathrm{m}(k)}_{y_{\Delta\Sigma\mathrm{m}}(k)} \tag{5.16}$$

To make the validation of the DDM modelling approach complete, a model comparison between the linear and non-linear flow response of the motor in the 5.4 MW DFPT is made. The simulation results of the non-linear model is made at a constant speed of 1500 rpm and additionally a constant pressure in the HPL of $p_H = 360$ bar. The flow dynamics for a single pressure chamber are for both models presented in figure 5.7.
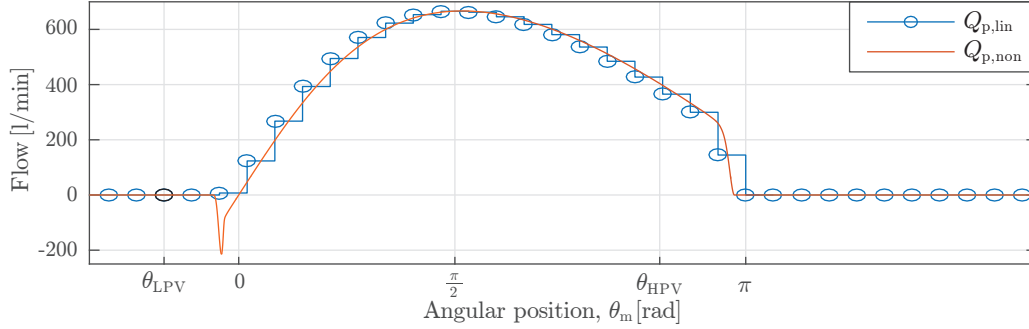
Fig. 5.7: Comparison of linear and non-linear flow response for a single pressure chamber in the DD motor of the 5.4 MW DFPT. At θ_{LPV} the decision to activate the next pressure chamber is taken, e.g. a binary input of 1 is given as input to both the linear and non-linear DD motor. Subsequent chambers are not activated.

From figure 5.7 it can once again be established that the linear DDM modelling approach gives reasonable approximation of the non-linear motor flow. As for the linear DD pump, small deviations exist between the linear and non-liner model, which primary cause is the omitted pressure dynamics in the linear approximation. In addition to the comments presented for validating the linear DD pump model, the following remarks are considered valid for the linear DD motor model:

Remark 5.2.K: As expected the linear motor flow does not include the initial back flow originating from the passive opening of the HPV valve. As a result the linear motor model's average intake flow is larger than that of the non-linear simulation model. To compensate for the initial back flow, a negative displacement fraction could have been utilised, yielding a constant back flow approximation. However, as the back flow is pressure dependent, this would presumably still result in a poor initial flow correspondence between the two models.

Remark 5.2.L: Evaluating the effective displacement during one motoring stroke for the two models yields very similar volumes, with the linear discrete model being slightly larger caused by the unmodelled behaviour of the initial back flow. If close to identical effective displacements are desired, this could be done by changing θ_{HPV} to the angle where the HPV starts closing or to where the HPV is in the middle of the closing operation, as an alternative to when it is fully closed. It should be noted that doing so comes with the cost of a decreased fit between the discrete and continuous flow waveform.

Having derived linear descriptions of both the DD pump and motor flows, it is now possible to consider deriving linear expressions for the pressure dynamics of the HPL

and motion dynamics of the pump/rotor shaft.

5.2.3 | Linear Rotor Dynamics

The rotor and pump are connected by a mutual shaft why the following section uses the terms rotor shaft and pump shaft interchangeably. The time-domain rotor dynamics are described by equation 3.1. To be able to combine it with the models just derived for the DDMs, the time-domain dynamics must be transformed to the spatial angle-domain.

Spatial Transformation:
The spatial angle-domain transformation of a time-domain differential equation, as initially proposed by Heemels et al. (1999), is defined by rewriting a time derivative as an angular derivative of the time. Here shown for the pump shaft position:

$$\frac{d\,\theta_{\mathrm{r}}(t)}{dt} = \omega_{\mathrm{r}}(t) \Rightarrow \frac{d\,t(\theta_{\mathrm{r}})}{d\theta_{\mathrm{r}}} = \frac{1}{\omega_{\mathrm{r}}(\theta_{\mathrm{r}})} \tag{5.17}$$

Remark 5.2.M: The interpretation of this equation is that $t(\theta_{\mathrm{r}})$ is the point in time at which the angular position is $\theta = \theta_{\mathrm{r}}$. For the shaft speed, the interpretation is similar, such that $\omega_{\mathrm{r}}(\theta_{\mathrm{r}})$ is the shaft speed at position θ_{r}. (Heemels et al. 1999)

By the chain rule, the velocity derivative may be expanded, and by use of equation 5.17 a spatial derivative of the angular velocity can be written as:

$$\frac{d\,\omega_{\mathrm{r}}}{dt} = \frac{d\,\omega_{\mathrm{r}}}{d\theta_{\mathrm{r}}}\frac{d\,\theta_{\mathrm{r}}}{dt} \Rightarrow \frac{d\,\omega_{\mathrm{r}}}{d\theta_{\mathrm{r}}} = \frac{d\,\omega_{\mathrm{r}}}{dt}\frac{d\,t}{d\theta_{\mathrm{r}}} = \dot{\omega}_{\mathrm{r}}\frac{1}{\omega_{\mathrm{r}}} \tag{5.18}$$

Remark 5.2.N: The main disadvantage of the transformation is that the shaft cannot change its rotation from anti-clockwise to clockwise, or vice versa, since this would result in division by zero. Although this issue is trivial for a WT drivetrain, other applications wherein this is problematic can easily be proposed.

Remark 5.2.O: The spatial transformation's use of equation 5.18 will result in a non-linear spatial-domain description of an otherwise linear time-domain description why linearisation is necessary.

Linearised Spatial Domain Dynamics:
The continuous spatial domain motion dynamics of the pump shaft can be obtained as:

$$\frac{d\,\omega_{\mathrm{r}}}{d\theta_{\mathrm{r}}} = \frac{1}{J_{\mathrm{rp}}\,\omega_{\mathrm{r}}}\left(\tau_{\mathrm{r}} - d_{\mathrm{r}}\omega_{\mathrm{r}} - \frac{\tau_{\mathrm{p}}}{\eta_{\mathrm{p}}}\right) \tag{5.19}$$

This is a non-linear equation, since the states are no longer linearly independent. Heemels et al. (1999) furthermore presents a linearisation approach for the spatial domain dynamics, when only small perturbations near a steady-state solution are considered, which results in:

$$\frac{d\,\Delta\omega_{\mathrm{r}}}{d\theta_{\mathrm{r}}} = \Delta\omega_{\mathrm{r}}' = \frac{1}{J_{\mathrm{rp}}\,\omega_{\mathrm{r}0}}\left(\Delta\tau_{\mathrm{r}} - d_{\mathrm{r}}\Delta\omega_{\mathrm{r}} - \frac{\Delta\tau_{\mathrm{p,lin}}}{\eta_{\mathrm{p}}}\right) \tag{5.20}$$

where ω_{r0} is the steady state velocity used for the linearisation. Δ terms correspond to small perturbations near the steady state solution, and $\Delta\tau_r$ corresponds to a disturbance input. The mark ($'$) denotes the spatial state derivative.

Remark 5.2.P: This method of linearisation is somewhat unconventional compared to the more traditional method of first order Taylor approximations. It has, however, been shown to work well for spatial-domain equations previously in Junker et al. (2016). A conventional linearisation would result in the damping term $d_r\Delta\omega_r$ being cancelled, which is generally undesirable.

Equation 5.20 may then be rewritten to a more convenient state formulation:

$$\underbrace{\omega_r'}_{x_r'} = \underbrace{-\frac{d_r}{J_{rp}\,\omega_{r0}}}_{A_r}\,\underbrace{\omega_r}_{x_r}\,\underbrace{-\frac{1}{J_{rp}\,\omega_{r0}\,\eta_p}\,\tau_{p,lin}}_{B_r\quad u_r}+\frac{1}{J_{rp}\,\omega_{r0}}\tau_r \tag{5.21}$$

Noting that the Δ notation from equation 5.20 has been omitted to simplify the notation. The input to this continuous spatial-domain rotor dynamics equation is the linearised discrete pump torque, which according to figure 5.1 acts through a hold element.

Remark 5.2.Q: The rotor torque term, τ_r, which effectively describes the wind's influence on the rotor velocity, will from this point forward be viewed as a noise term. As a result it will be neglected since the intention to utilise a deterministic controller approach does not allow for a model representation with noise inputs.

5.2.4 Linear HPL Dynamics

To obtain the spatial-domain HPL pressire dynamics the approach is the same: Expand the time derivative by the chain rule and then apply the transformation of equation 5.17:

$$\frac{d\,\Delta p}{dt} = \frac{d\,\Delta p}{d\theta_r}\frac{d\,\theta_r}{dt} \Rightarrow \frac{d\,\Delta p}{d\theta_r} = \frac{d\,\Delta p}{dt}\frac{d\,t}{d\theta_r} = \Delta\dot{p}\,\frac{1}{\omega_r} \tag{5.22}$$

It can now be seen that the spatial HPL pressure dynamics can be obtained by dividing the time-domain dynamics in equation 3.2 by the shaft speed to obtain:

$$\frac{d\,\Delta p}{d\theta_r} = \frac{\beta_H}{V_H\,\omega_r}\,(Q_p - Q_m - k_l\,\Delta p) \tag{5.23}$$

This is a non-linear equation, and by using the approach suggested by Heemels et al. (1999), the following linearised dynamics may be obtained:

$$\frac{d\,\Delta\Delta p}{d\theta_r} = \Delta\Delta p' = \frac{\beta_H}{V_H\,\omega_{r0}}\,(\Delta Q_{p,lin} - \Delta Q_m - k_l\,\Delta\Delta p) \tag{5.24}$$

Equation 5.24 is rewritten to a more convenient state formulation:

$$\underbrace{\Delta p'}_{x_{HPL}'} = \underbrace{-\frac{\beta_H\,k_l}{V_H\,\omega_{r0}}}_{A_{HPL}}\underbrace{\Delta p}_{x_{HPL}} + \underbrace{\frac{\beta_H}{V_H\,\omega_{r0}}}_{B_{HPL}}\big(\underbrace{Q_{p,lin}}_{u_{HPL_p}} - \underbrace{Q_m}_{u_{HPL_m}}\big) \tag{5.25}$$

Noting that the double Δ notation from equation 5.24 has been omitted to simplify the notation. The inputs to this continuous spatial HPL pressure dynamics equation are the linearised discrete pump flow and discrete motor flow, which according to figure 5.1 both act through hold elements.

Remark 5.2.R: The employed spatial transformation describes all states with respect to the pump shaft position. This does not introduce any problems in the case of constant pump speed, but consider the case of varying pump speed, then when seen from the time-axis, the pump shaft position axis stretches linearly, whereas the motor shaft position axis remains fixed. When combining the different linear descriptions of the system elements, e.g. the flows $Q_{p,lin}$ and Q_m, the motor axis and pump axis are in effect superimposed on one and another. From a mathematical point of view this is somewhat problematic since the motor states now are described relative to an axis which they do not belong to. However, keeping in mind that the derived models are to serve as a linear tool for analysis and controller design, and such models are often only accurate representations in the vicinity of the linearisation point, the spatial transformation is considered applicable.

Having derived and defined linear descriptions for all the elements in the DFPT, the next task becomes combining these subelements into a single DFPT multirate model. This will be done by the use of the developed UNMR method, and is the topic of the following sections.

5.2.5 DFPT Modelling Dimensions

The equations derived in the previous sections are generally applicable to both the full power 5.4 MW DFPT and the 10 kW DFPT. The only changes lie in different parameter values, linearisation points and finally a different number of pressure chambers, and thus also different number of states in the DDM models. For this reason table 5.1 is presented, wherein the number of states for the individual system element representations in the two versions of the DFPT are tabulated.

	5.4 MW DFPT	10 kW DFPT
Continuous states, γ		
HPL state	1	1
Rotor state	1	1
Discrete states, δ		
DD Pump states, p_p	50	1
Pump $\Delta\Sigma$ state	1	1
DD motor states, p_m	20	1
Motor $\Delta\Sigma$ state	1	1
Sample-and-hold states, σ	3	3
Total, n	**77**	**9**

Tab. 5.1: The number of states in the full power 5.4 MW and the downscaled 10 kW DFPTs.

A few remarks can me made for the information presented in table 5.1:

Remark 5.2.S: As previously presented the dynamics of the rotor and HPL can be described in a similar fashion for the 5.4 MW and 10 kW DFPT as it is only the model parameters which are different. From equation 5.20 and thus using the notation from the UNMR method this leads to $\gamma = 2$.

Remark 5.2.T: The discrete representation of the DFPT's DDMs are the only models which differ for the 5.4 MW and 10 kW DFPT. This is the result of a different number of pressure chambers in the DDMs. Using the convolution sum modelling approach described in section 5.2.2 it is found that 50 and 20 states are required to describe the dynamics of DD pump and motor for the 5.4 MW DFPT. It is furthermore found that these numbers of states reduces to 1 for both the DD pump and motor for 10 kW DFPT. From this it can be seen that the number of discrete states, δ, is equal to 72 and 4 for the 5.4 MW and 10 kW DFPT, respectively.

Remark 5.2.U: The sample-and-hold states are required whenever an output from a discrete model must be used as an input to a continuous model. From figure 5.1 it is evident that this is the case for the torque, τ_p, and the flows Q_p and Q_m. Thus for the sample-and-hold states, $\sigma = 3$ for both the 5.4 MW and 10 kW DFPT.

When the transition matrices for the different elements of the DFPT must be formed, associated model parameters and operating (or linearisation) points must be chosen. As this chapter only concerns the evaluation of the 10 kW DFPT, only parameters and the operating point associated with the 10 kW DFPT will be presented. This is done in section 5.4.1.

5.3 Generalised DFPT Modelling

The work presented in the following two sections will proceed as defined in the four step procedure outlined in section 4.4, such that first the state variables are defined, following this the transition matrices are determined based on the previously presented linear equations. Thereafter the transition equations may be derived by considering the sampling operations in the system, such that they may be combined to form a lifted time-, or more accurately, angle-invariant model. The two first steps are presented in this section and will be derived, such that they are generally applicable to both the 10 kW and 5.4 MW DFPT, whereas the last two steps presented in section 5.4 will focus solely on the 10 kW DFPT.

In order to derive a DFPT multirate model, the four step procedure of the UNMR method makes use of all the preceding linear subelement models to define state variables and system transition matrices. The authors are therefore well aware, that it is challenging for the reader to follow these derivations, without going back and forth between several of this chapter's sections. Thus, at the end of this chapter, a multirate model validation is presented, which serves as indication that the following sections derivations are made correctly.

5.3.1 Step 1: State Variable Definition

The combined vector of all system states is, as always, defined as:

$$\boldsymbol{x}_{\text{comb}} \equiv \left[\ \boldsymbol{x_c}^{\mathsf{T}} \ \vdots\ \boldsymbol{x_d}^{\mathsf{T}}\ \vdots\ \boldsymbol{x_s}^{\mathsf{T}}\ \right]^{\mathsf{T}} \qquad \begin{array}{c} [\mathbf{3 \times 1}] \\ [n \times 1] \end{array} \qquad (5.26)$$

The individual state vectors for the system elements may then be separately defined.

With reference to figure 5.1, it may be seen that there are two CDEs, and thus this vector simply consists of the rotor speed state and HPL to LPL pressure difference state, such that $\gamma = 2$:

$$\boldsymbol{x_c} = \left[\ x_{\text{r}}^{\mathsf{T}} \quad x_{\text{HPL}}^{\mathsf{T}}\ \right]^{\mathsf{T}} \qquad [\gamma \times 1] \qquad (5.27)$$

There are four DDEs in the system, namely the two DDMs and their associated $\Delta\Sigma$-modulators. These DDE states may be combined to form the vector:

$$\boldsymbol{x_d} = \left[\ \boldsymbol{x_p}^{\mathsf{T}} \quad x_{\Delta\Sigma_{\text{p}}}^{\mathsf{T}} \quad \boldsymbol{x_m}^{\mathsf{T}} \quad x_{\Delta\Sigma_{\text{m}}}^{\mathsf{T}}\ \right]^{\mathsf{T}} \qquad \begin{array}{c} [\mathbf{4 \times 1}] \\ [\delta \times 1] \end{array} \qquad (5.28)$$

where $\delta = p_{\text{p}} + 1 + p_{\text{m}} + 1$, and noting that $\boldsymbol{x_p}$ and $\boldsymbol{x_m}$ are vectors, and not just scalars.

Regarding the three SHEs, which are used when interconnecting a DDE and SHE, the last subvector may be formed:

$$\boldsymbol{x_s} = \left[\ x_{\tau_{\text{p,lin}}}^{\mathsf{T}} \quad x_{Q_{\text{p,lin}}}^{\mathsf{T}} \quad x_{Q_{\text{m}}}^{\mathsf{T}}\ \right]^{\mathsf{T}} \qquad [\sigma \times 1] \qquad (5.29)$$

Remark 5.3.A: In equations 5.27 to 5.29 both the scalars and bold vectors are transposed. It would have been sufficient only to transpose the vectors. However, for consistency, every entry in the state block vectors is transposed.

Remark 5.3.B: The lifted state vector and lifted input/output vectors, also previously denoted as double expanded vectors, would normally have been defined in step 1. However, their definition is specific to the system and the corresponding sampling scheme, why it is decided to wait until step 3, when the 10 kW DFPT is considered, to define them.

Having defined the state vectors for the system elements, and their dimensions, it is now possible to proceed to defining the transition matrices.

5.3.2 Step 2: System Transition Matrices

In the following, the transition matrices describing the dynamics of the DFPT's system elements are defined. First the CDEs will be considered, since these are the main dynamic elements. Following this the DDEs are considered, and finally the SHEs.

Continuous Dynamic Elements

With reference to the continuous state vector, $\boldsymbol{x}_{\mathrm{c}}$, equations 5.21 and 5.25 may be combined to form a single state-space formulation of the continuous linear spatial-domain rotor and HPL dynamics:

$$
\begin{bmatrix} x_{\mathrm{r}}' \\ x_{\mathrm{HPL}}' \end{bmatrix} = \underbrace{\begin{bmatrix} A_{\mathrm{r}} & 0 \\ 0 & A_{\mathrm{HPL}} \end{bmatrix}}_{\boldsymbol{A}_{\mathrm{c}}} \begin{bmatrix} x_{\mathrm{r}} \\ x_{\mathrm{HPL}} \end{bmatrix} + \underbrace{\begin{bmatrix} B_{\mathrm{r}} & 0 & 0 \\ 0 & B_{\mathrm{HPL}} & -B_{\mathrm{HPL}} \end{bmatrix}}_{\boldsymbol{B}_{\mathrm{c}}} \begin{bmatrix} u_{\mathrm{r}} \\ u_{\mathrm{HPL_p}} \\ u_{\mathrm{HPL_m}} \end{bmatrix} \tag{5.30}
$$

Remark 5.3.C: It may be seen that there are no direct cross-couplings between the two CDEs, since $\boldsymbol{A}_{\mathrm{c}}$ is merely a diagonal matrix, which also makes sense, since the elements are not physically directly connected. However, some cross-couplings exist when considering the flows and torques produced by the DDMs.

With $\boldsymbol{A}_{\mathrm{c}}$ and $\boldsymbol{B}_{\mathrm{c}}$ defined, equation 4.5 may be used to calculate $\boldsymbol{G}_{\mathrm{c}}(\tau)$ and $\boldsymbol{H}_{\mathrm{c}}(\tau)$, such that $\boldsymbol{\Phi}(\tau)$ may finally be formed:

$$
\boldsymbol{\Phi}(\tau) = \begin{bmatrix} \boldsymbol{G}(\tau) & \boldsymbol{0} & \boldsymbol{H}(\tau) \\ \boldsymbol{0} & \boldsymbol{I} & \boldsymbol{0} \\ \boldsymbol{0} & \boldsymbol{0} & \boldsymbol{I} \end{bmatrix} \begin{matrix} \} \gamma \text{ rows} \\ \} \delta \text{ rows} \\ \} \sigma \text{ rows} \end{matrix} \qquad \begin{matrix} [\mathbf{3 \times 3}] \\ [n \times n] \end{matrix} \tag{5.31}
$$

Discrete Dynamic Elements

To define the DDE transition matrices, the dimensions are firstly considered. With reference to the discrete state vector, $\boldsymbol{x}_{\mathrm{d}}$, it is obvious that within the discrete section of the block transition matrices, there should be a further four block rows. These four block rows describe the transitions occurring at sampling rates θ_1 and θ_2, and thus two DDE state transition matrices denoted $\boldsymbol{D}_{\mathrm{p}}$ and $\boldsymbol{D}_{\mathrm{m}}$ must be defined.

The DDE state transition matrix, $\boldsymbol{D}_{\mathrm{p}}$, will describe the transitions occurring at θ_1, which thus includes the block states transitions of $\boldsymbol{x}_{\Delta\Sigma_{\mathrm{p}}}$ and $\boldsymbol{x}_{\mathrm{p}}$. Then starting with the DD pump element, which is represented by the state-space form of the convolution sum (equation 5.8a), the input must be defined with respect to the other states. The input to a DDM is the output of the corresponding $\Delta\Sigma$-modulator, and thus by considering the $\Delta\Sigma$ output equation (equation 5.2b), the following can be obtained:

$$
u_{\mathrm{p}}(k) = y_{\Delta\Sigma_{\mathrm{p}}}(k) = C_{\Delta\Sigma_{\mathrm{p}}} x_{\Delta\Sigma_{\mathrm{p}}}(k) \; \Rightarrow \; \boldsymbol{x}_{\mathbf{p}}(k{+}1) = \boldsymbol{G}_{\mathrm{p}} \boldsymbol{x}_{\mathbf{p}}(k) + \boldsymbol{H}_{\mathrm{p}} C_{\Delta\Sigma_{\mathrm{p}}} x_{\Delta\Sigma_{\mathrm{p}}}(k) \tag{5.32}
$$

With reference to the definition of $\boldsymbol{x}_{\mathbf{comb}}$ and $\boldsymbol{x}_{\mathbf{d}}$ in section 5.3.1, then the transition of equation 5.32 must be included in the first block row in the discrete section of D_{p} as presented in equation 5.33.

Regarding the DD pump's $\Delta\Sigma$-modulator, it may be seen by examining equation 5.2a, that the $\Delta\Sigma$-state do not depend on any other model states, but instead on an external sampled input, why a $\boldsymbol{d}_{\mathrm{p}}$-vector must furthermore be defined. Based on the state-space

formulation of the $\Delta\Sigma$-modulator seen in equation 5.2a, the second block row in the discrete section of $\boldsymbol{D}_{\mathrm{p}}$ and $\boldsymbol{d}_{\mathrm{p}}$ may be written as seen in equation 5.33:

$$\boldsymbol{D}_{\mathrm{p}} = \begin{bmatrix} \boldsymbol{I} & \boldsymbol{0} & \boldsymbol{0} \\ \boldsymbol{0} & \begin{matrix} \boldsymbol{G}_{\mathrm{p}} & \boldsymbol{H}_{\mathrm{p}}C_{\Delta\Sigma_{\mathrm{p}}} & \boldsymbol{0} & \boldsymbol{0} \\ \boldsymbol{0} & G_{\Delta\Sigma_{\mathrm{p}}} & \boldsymbol{0} & \boldsymbol{0} \\ \boldsymbol{0} & \boldsymbol{0} & \boldsymbol{I} & \boldsymbol{0} \\ \boldsymbol{0} & \boldsymbol{0} & \boldsymbol{0} & 1 \end{matrix} & \boldsymbol{0} \\ \boldsymbol{0} & \boldsymbol{0} & \boldsymbol{I} \end{bmatrix} \begin{matrix} \\ \left.\vphantom{\begin{matrix}\\\\\\\\\end{matrix}}\right\} \begin{matrix} \boldsymbol{4} \text{ rows} \\ \boldsymbol{\delta} \text{ rows} \end{matrix} \\ \\ \end{matrix} \qquad \boldsymbol{d}_{\mathrm{p}} = \begin{bmatrix} \boldsymbol{0} \\ \boldsymbol{0} \\ H_{\Delta\Sigma_{\mathrm{p}}} \\ 0 \\ 0 \\ \boldsymbol{0} \end{bmatrix} \qquad (5.33)$$

Remembering that all transition matrices start as simple diagonal matrices, wherein the rows corresponding to the states which undergoes a transition are modified, such that the dynamics of the transitions are accounted for and that other states are unaffected.

The DDE state transition matrix, $\boldsymbol{D}_{\mathrm{m}}$, is defined in a similar manner. For the DD motor element, the input-output relation is defined as:

$$u_{\mathrm{m}}(k) = y_{\Delta\Sigma_{\mathrm{m}}}(k) = C_{\Delta\Sigma_{\mathrm{m}}} x_{\Delta\Sigma_{\mathrm{m}}}(k) \qquad (5.34)$$

This discrete dynamic transition is included in the third block row of $\boldsymbol{D}_{\mathrm{m}}$, whereas the transitions of the DD motor's associated $\Delta\Sigma$-modulator is contained in the fourth block row of $\boldsymbol{D}_{\mathrm{m}}$ and $\boldsymbol{d}_{\mathrm{m}}$ as can be seen in equation 5.35.

$$\boldsymbol{D}_{\mathrm{m}} = \begin{bmatrix} \boldsymbol{I} & \boldsymbol{0} & \boldsymbol{0} \\ \boldsymbol{0} & \begin{matrix} \boldsymbol{I} & 0 & 0 & \boldsymbol{0} \\ 0 & 1 & 0 & 0 \\ 0 & 0 & \boldsymbol{G}_{\mathrm{m}} & \boldsymbol{H}_{\mathrm{m}}C_{\Delta\Sigma_{\mathrm{m}}} \\ 0 & 0 & 0 & G_{\Delta\Sigma_{\mathrm{m}}} \end{matrix} & \boldsymbol{0} \\ \boldsymbol{0} & \boldsymbol{0} & \boldsymbol{I} \end{bmatrix} \begin{matrix} \leftarrow p_{\mathrm{p}} \text{ rows} \\ \leftarrow 1 \text{ row} \\ \leftarrow p_{\mathrm{m}} \text{ rows} \\ \leftarrow 1 \text{ row} \end{matrix} \qquad \boldsymbol{d}_{\mathrm{m}} = \begin{bmatrix} \boldsymbol{0} \\ \boldsymbol{0} \\ 0 \\ \boldsymbol{0} \\ H_{\Delta\Sigma_{\mathrm{m}}} \\ \boldsymbol{0} \end{bmatrix} \qquad (5.35)$$

In the matrices in equations 5.33 and 5.35, the dimensions of the discrete section and the rows therein have been indicated in the right hand side, to illustrate the number of states used for describing the different system components.

5.3.2.C Sample-and-Hold Elements

The SHE states are simply scalars, and not vectors like some of the DDE states, thus for the SHE transition matrices, $\boldsymbol{S}_{\mathrm{p}}$ and $\boldsymbol{S}_{\mathrm{m}}$, the sample-and-hold section will contain three rows.

Defining the SHE transition matrices is done by considering the output equations, which were derived in conjunction with the convolution sum impulse response models for the pump and motor. The SHE transition matrix, $\boldsymbol{S}_{\mathrm{p}}$, will contain the SHE states described by the sampling rate, θ_1, which includes the pump torque and pump flow. Based on the linearised pump torque described by equation 5.13 and the linearised pump flow described by equation 5.9, it is possible to write row one and two in the sample-and-hold

section in $\boldsymbol{S}_\mathrm{p}$:

$$
\boldsymbol{S}_\mathrm{p} = \left.\left[
\begin{array}{cccccccccc}
& \boldsymbol{I} & & & \boldsymbol{0} & & & & \boldsymbol{0} & \\
& \boldsymbol{0} & & & \boldsymbol{I} & & & & \boldsymbol{0} & \\
0 & k_{Q_\mathrm{p}}\alpha_{\mathrm{p}0} & \Delta p_0\,\boldsymbol{C}_\mathrm{p} & \Delta p_0\,D_\mathrm{p}\,C_{\Delta\Sigma_\mathrm{p}} & \boldsymbol{0} & 0 & 0 & 0 & 0 \\
k_{Q_\mathrm{p}}\alpha_{\mathrm{p}0} & 0 & \omega_{\mathrm{r}0}\,\boldsymbol{C}_\mathrm{p} & \omega_{\mathrm{r}0}\,D_\mathrm{p}\,C_{\Delta\Sigma_\mathrm{p}} & \boldsymbol{0} & 0 & 0 & 1 & 0 \\
0 & 0 & \boldsymbol{0} & 0 & \boldsymbol{0} & 0 & 0 & 0 & 1
\end{array}
\right]\right\}\begin{array}{l}\text{3 rows}\\\sigma\text{ rows}\end{array}
$$

(5.36)

Note that D_p is the pump displacement, and not the $\boldsymbol{D}_\mathrm{p}$-matrix defined in the previous section.

The SHE transition matrix, $\boldsymbol{S}_\mathrm{m}$, includes the SHE transition of the motor flow described by equation 5.16 of which dynamics is written in the third row in the sample-and-hold section as:

$$
\boldsymbol{S}_\mathrm{m} = \left[
\begin{array}{cccccccc}
\boldsymbol{I} & & & \boldsymbol{0} & & & \boldsymbol{0} & \\
\boldsymbol{0} & & & \boldsymbol{I} & & & \boldsymbol{0} & \\
& \boldsymbol{0} & 0 & \boldsymbol{0} & 0 & 1 & 0 & 0 \\
\boldsymbol{0} & \boldsymbol{0} & 0 & \boldsymbol{0} & 0 & 0 & 1 & 0 \\
& \boldsymbol{0} & 0 & \omega_\mathrm{m}\,\boldsymbol{C}_\mathrm{m} & \omega_\mathrm{m}\,D_\mathrm{m}\,C_{\Delta\Sigma_\mathrm{m}} & 0 & 0 & 0
\end{array}
\right]
$$

(5.37)

Thereby transition matrices for all the elements in the system have been defined, and it is now possible to proceed to deriving the transitions equations. However, before this is done, some considerations regarding normalising the states are made, since deriving the transition equations will include a large number of matrix products.

5.3.3   Normalisation of State Vector

Prior to deriving and evaluating the transition equations for the $10\,\mathrm{kW}$ DFPT multirate model, it is chosen to normalise the combined state vector, $\boldsymbol{x_{comb}}$. This is done to reduce potential numerical calculation issues arising from having states of different magnitudes. E.g considering that the state vector is initially described in SI-units, why the pressure, Δp has a magnitude in the order of 10^7, whereas the DDM flows, Q_p and Q_m, have magnitudes in the order of 10^{-4}.

The normalisation of the state vector is done in accordance with Phillips and Parr (2011), which defines the general state transformation as the continuous counterpart to:

$$
\boldsymbol{x}(k) = \boldsymbol{P}\boldsymbol{v}(k)
$$

(5.38)

Where $\boldsymbol{v}(k)$ is the normalised state vector and $\boldsymbol{P}$ is a diagonal transformation matrix containing appropriate gains for normalising the state vector $\boldsymbol{x}(k)$. By inserting equation 5.38 into a general discrete state equation, a transformed state and input matrix

can be derived.

$$\boldsymbol{x}(k+1) = \boldsymbol{G}\boldsymbol{x}(k) + \boldsymbol{H}\boldsymbol{u}(k) \tag{5.39a}$$

$$\boldsymbol{P}\boldsymbol{v}(k+1) = \boldsymbol{G}\boldsymbol{P}\boldsymbol{v}(k) + \boldsymbol{H}\boldsymbol{u}(k) \tag{5.39b}$$

$$\boldsymbol{v}(k+1) = \underbrace{\boldsymbol{P}^{-1}\boldsymbol{G}\boldsymbol{P}}_{\boldsymbol{G}_v}\boldsymbol{v}(k) + \underbrace{\boldsymbol{P}^{-1}\boldsymbol{H}}_{\boldsymbol{H}_v}\boldsymbol{u}(k) \tag{5.39c}$$

Here $\boldsymbol{G}_v$ and $\boldsymbol{H}_v$ represents the transformed state and input matrix, respectively.

The state normalisation on the multirate DFPT model is performed according to equation 5.39, where the transition matrices $\boldsymbol{\Phi}$, $\boldsymbol{D}$ and $\boldsymbol{S}$ can be viewed as the state matrix $\boldsymbol{G}$, and the $\boldsymbol{d}$-vector can be considered as the input matrix $\boldsymbol{H}$.

The transformation matrix for both DFPT models can be defined as:

$$\boldsymbol{P} = \begin{bmatrix} \begin{matrix} \mathrm{nom}(\omega_\mathrm{r}) & 0 \\ 0 & \mathrm{nom}(\Delta p) \end{matrix} & \boldsymbol{0} & \boldsymbol{0} \\ \boldsymbol{0} & \boldsymbol{I} & \boldsymbol{0} \\ \boldsymbol{0} & \boldsymbol{0} & \begin{matrix} \mathrm{nom}(\tau_\mathrm{p}) & 0 & 0 \\ 0 & \mathrm{nom}(Q_\mathrm{p}) & 0 \\ 0 & 0 & \mathrm{nom}(Q_\mathrm{m}) \end{matrix} \end{bmatrix} \tag{5.40}$$

Where $\mathrm{nom}(\omega_\mathrm{r})$ represents a function which equals the nominal/rated value of ω_r. In a similar manner $\mathrm{nom}(\Delta p)$ represents the rated pressure difference between the HPL and LPL and so on.

Remark 5.3.D: An identity gain matrix is used for the discrete states in the transition matrix, $\boldsymbol{P}$, as these states only can obtain a binary value corresponding to whether a chamber is active or inactive.

The state transformation is performed between step 2 and 3 of the UNMR method, and will not be elaborated upon further. For simplicity the notation change of the state vector from $\boldsymbol{x}$ to $\boldsymbol{v}$ and proceeding notation changes from $\boldsymbol{G}$ to $\boldsymbol{G}_v$ and $\boldsymbol{H}$ to $\boldsymbol{H}_v$ is omitted. Thus, the notation of the transition matrices defined in step 1 and 2 will not change in step 3, even though $\boldsymbol{x}_{\mathbf{comb}}$ now represents the normalised state vector and $\boldsymbol{\Phi}$, $\boldsymbol{D}$ and $\boldsymbol{S}$ the normalised state matrices and finally $\boldsymbol{d}$ the normalised input matrix.

5.4 10 kW DFPT Modelling

In the remainder of this chapter, the focus will lie on applying the UNMR method to the 10 kW DFPT with the aim of deriving a multirate model. As discussed previously, this is done since the two sampling rates are different but similar, such that all the transition equations become relatively simple and can be displayed for the reader. Thereby the focus lies on the application of the method why the technical details of the computer algorithms which are utilised for more complex sampling schemes are not presented.

This sections initially presents the model parameters needed in order to evaluate the transition matrices derived in step 2 of the UNMR method, hereafter the section will

proceed with step 3 and 4, which are the derivation of transition equations and of a spatial-domain counterpart to an LTI multilrate model.

5.4.1   Model Parameters

Operating Point:
During the development of a linear model, which makes use of linearised mathematical descriptions, an operating point must be defined before the model can be evaluated. In general, several approaches for defining an operating point can be made:

Remark 5.4.A: Choose the operating point as where the system is expected to operate most frequently. A consequence of utilising linearised descriptions is that these often are only a valid description of the system's true dynamics close to the operating point. Thus, by defining the operating point as where the system is expected to operate most frequently, one might achieve a model which is "most often" representative of the system's true dynamics. As this approach does not consider how the stability might change within the system's operating range, controller design often make use of relative large stability margins (gain and phase margins). This seeks to ensure stable system operation in the entire operating range.

Remark 5.4.B: Choose a conservative operating point with regards to stability of the system. There exist several methods for determining the most conservative operating point, and depending on the system of interest one method might be more suitable than the other. In general, these methods often include parameter variations while performing a measure of the system's stability using Bode plots (or the MIMO equivalent SVD-plot) or alternatively pole-zero mapping. Common for all these methods is that they can get extensive and time consuming to perform as the operating range of the system increases. Furthermore the methods does not always provide a qualitative and definitive measure of the "most" conservative operating point.

When an operating point for the 5.4 MW DFPT multirate model must be determined it could be beneficial to apply one of the above presented approaches. However, for the purely fictional 10 kW DFPT these approaches are deemed somewhat unsuitable. Firstly because the 10 kW DFPT was introduced as an evaluation platform which utilises different but similar sampling rates of the two DDMs, and thus the system's operating range has not been defined, why the knowledge to choose the operating point as where the system is expected to operate most frequently has not been defined. Secondly, if the operating point should be based on the stability of the system, one must rely on the model being representative. As this has not yet been concluded, effort put into determining a conservative operating point at the current stage makes little sense.

In essence, the method of choosing the operating point is not considered essential for the 10 kW DFPT model, as the primary objective is to evaluate if the UNMR method can be applied to develop a multirate DFPT model. Thus, the linearisation constant have simply been chosen as the rated operating conditions of the system:

- $\omega_{r0} = 1500\,\mathrm{rpm}$
- $\Delta p_0 = 350\,\mathrm{bar}$
- $\tilde{\alpha}_{p0} = 0$

Choosing $\tilde{\alpha}_{p0}$ based on rated system conditions does makes little sense, and is therefore chosen based on the following remarks:

Remark 5.4.C: Defining $\tilde{\alpha}_{p0} = 0$ will ensure that the pump flow always will be zero, when a zero displacement is given to the pump.

Remark 5.4.D: Defining $\tilde{\alpha}_{p0} = 0$, furthermore, provides the option of giving both the linear and non-liner model an unit-step as input in later model comparison, without the characteristics of the utilised $\Delta\Sigma$-modulators becoming non-linear.

Remark 5.4.E: After the applicability of utilising the UNMR method to derive a multirate DFPT model has been evaluated, it might be beneficial to reconsider the choice of operating point before potential linear system analysis and controller design is performed on the multirate model.

10 kW DFPT Multirate Model Parameters:
In addition to the operating point, the model parameters must be known before the 10 kW multirate model can be evaluated. Many of these parameters have already been defined during the development of the 10 kW DFPT non-linear simulation model and can be found in tables 3.1, 3.3 and 3.4. However additional parameters have to be defined for the discrete representations of the DDMs. This is done in accordance with equations 5.3 to 5.5 for the DD pump and the equivalent counterparts for the DD motor and the parameters are presented in table 5.2.

Lastly the normalisation gains utilised in the transformation matrix $\boldsymbol{P}$ must be defined. As previously described, these are chosen as the rated values of the respective states in the state vector $\boldsymbol{x}_{\mathbf{comb}}$ and can furthermore be found in table 5.2.

Remark 5.4.F: Table 5.2 presents the parameter values in units deemed appropriate for display, however, when the parameters are utilised in the model development, values are transformed into SI-units.

With the operating point and model parameters defined, the derivations and evaluations of the state transition equations for the 10 kW DFPT multirate model are presented next.

Description	Parameter	Value
10 kW DD Pump		
Sampling rate	θ_1 [rad]	π
Pump flow constant	k_{Q_p} [m³/rad]	1.942×10^{-6}
Normalised displacement vector	$\Delta \boldsymbol{V}_{pc}$ [-]	$\begin{bmatrix} -0.892 & 0 \end{bmatrix}^\mathsf{T}$
10 kW DD Motor		
Sampling rate	θ_2 [rad]	$\frac{2}{3}\pi$
Flow constant	k_{Q_m} [m³/rad]	1.906×10^{-6}
Normalised displacement vector	$\Delta \boldsymbol{V}_{mc}$ [-]	$\begin{bmatrix} 0.559 & 0.371 \end{bmatrix}^\mathsf{T}$
Transformation Gains		
Rotor speed	$\mathrm{nom}(\omega_r)$ [rpm]	1500
HPL & LPV pressure difference	$\mathrm{nom}(\Delta p)$ [bar]	350
Rotor torque	$\mathrm{nom}(\tau_p)$ [Nm]	63.66
Pump flow	$\mathrm{nom}(Q_p)$ [m³/s]	2.86×10^{-4}
Motor flow	$\mathrm{nom}(Q_m)$ [m³/s]	2.86×10^{-4}

Tab. 5.2: Parameters used for modelling the 10 kW DFPT Multirate Model.

5.4.2 Step 3: Deriving Transition Equations

Step 3 in the UNMR method seeks to derive the transition equations throughout a BTP in the system. For this to be possible, the sampling scheme for the 10 kW DFPT must be defined. As previously presented the DFPT's pump and motor have 2 and 3 chamber activations per revolution, respectively. This results in two discrete update rates of the system, $\theta_1 = \pi$ and $\theta_2 = 2\pi/3$, and they yield an STP of $\theta_0 = \pi/3$ and a BTP of $\theta_{\mathrm{BTP}} = 2\pi$. The $\Delta\Sigma$-modulators are operated at the same rate as their corresponding DDM. The number of STPs per BTP is then $N = 6$, the number of θ_1s per BTP is $N_1 = 2$ and the number of θ_2s per BTP is $N_2 = 3$.

From the above definitions it is possible to visualise the sampling scheme as it was done for the MSD system, and the sampling scheme is depicted in figure 5.8. As previously, the top part illustrates an example of the real state progression, while the bottom part illustrates their progression in the model produced by the UNMR method.

The double expanded $Nn \times 1 = 6 \cdot 9 \times 1$ state vector for the 10 kW DFPT is given by:

$$\boldsymbol{x}(k) = \begin{bmatrix} \boldsymbol{x}_1(k) \\ \boldsymbol{x}_2(k) \\ \boldsymbol{x}_3(k) \\ \boldsymbol{x}_4(k) \\ \boldsymbol{x}_5(k) \\ \boldsymbol{x}_6(k) \end{bmatrix} = \begin{bmatrix} \boldsymbol{x}_{\mathrm{comb}}((k-1)\theta_{\mathrm{BTP}} + \theta_0) \\ \boldsymbol{x}_{\mathrm{comb}}((k-1)\theta_{\mathrm{BTP}} + 2\,\theta_0) \\ \boldsymbol{x}_{\mathrm{comb}}((k-1)\theta_{\mathrm{BTP}} + 3\,\theta_0) \\ \boldsymbol{x}_{\mathrm{comb}}((k-1)\theta_{\mathrm{BTP}} + 4\,\theta_0) \\ \boldsymbol{x}_{\mathrm{comb}}((k-1)\theta_{\mathrm{BTP}} + 5\,\theta_0) \\ \boldsymbol{x}_{\mathrm{comb}}(k\theta_{\mathrm{BTP}}) \end{bmatrix} \tag{5.41}$$
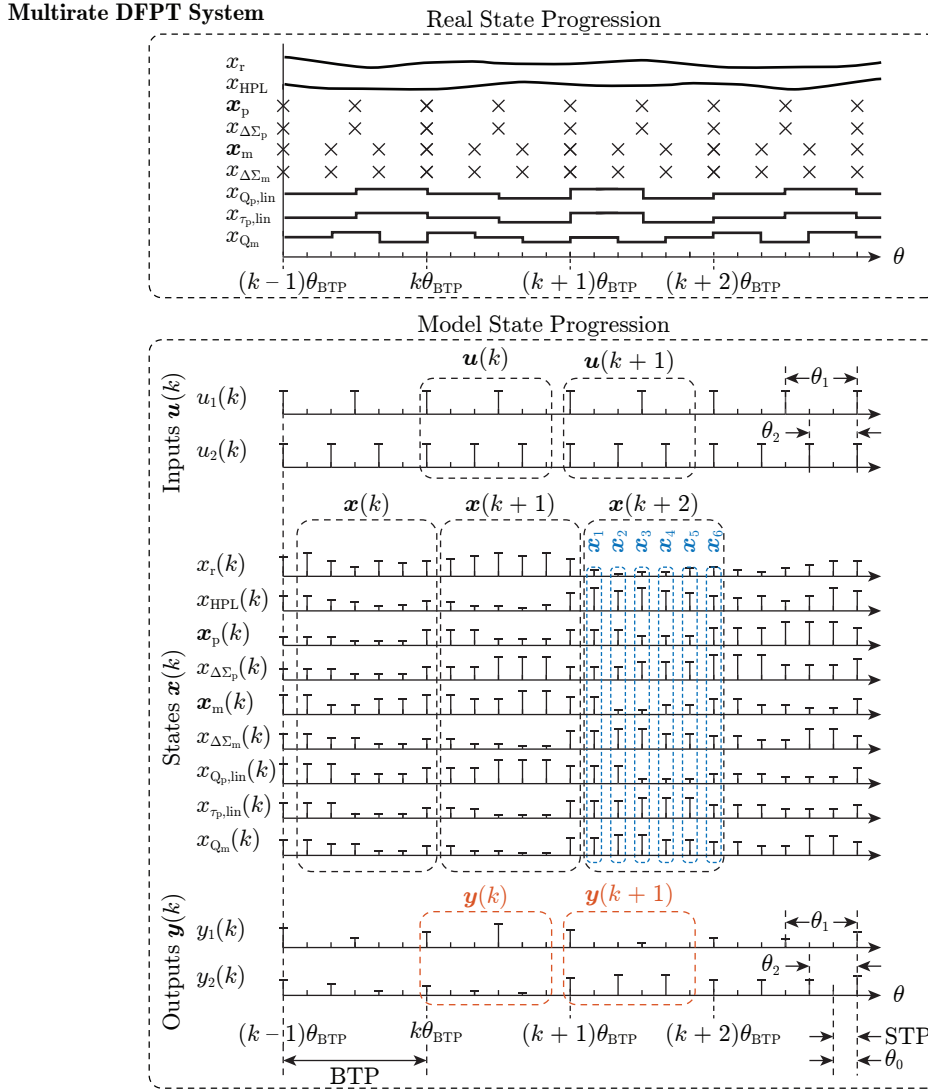
Fig. 5.8: Progression of real system states and model states for the 10 kW DFPT.

The lifted input and output vectors are given by:

$$
\boldsymbol{u}(k) = \begin{bmatrix} u_1(k\theta_{\text{BTP}}) \\ u_1(k\theta_{\text{BTP}} + \theta_1) \\ u_2(k\theta_{\text{BTP}}) \\ u_2(k\theta_{\text{BTP}} + \theta_2) \\ u_2(k\theta_{\text{BTP}} + 2\theta_2) \end{bmatrix}
\qquad
\boldsymbol{y}(k) = \begin{bmatrix} y_1(k\theta_{\text{BTP}}) \\ y_1(k\theta_{\text{BTP}} + \theta_1) \\ y_2(k\theta_{\text{BTP}}) \\ y_2(k\theta_{\text{BTP}} + \theta_2) \\ y_2(k\theta_{\text{BTP}} + 2\theta_2) \end{bmatrix}
\tag{5.42}
$$

Step 3 and 4 for developing the multirate DFPT model are very similar to when step 3 and 4 for the MSD multirate model was developed. This is the case, since the sampling scheme is very similar and also that the structure with DDEs acting through SHEs on CDEs is similar, why deriving the transition equations will follow the same procedure, merely with some of the matrices exchanged.

Defining $\boldsymbol{x}_1(k+1)$ is done by examining the top part of figure 5.8 and examining the open interval $[k\theta_{\mathrm{BTP}} \quad k\theta_{\mathrm{BTP}}+\theta_0[$, corresponding to examining the interval $[\boldsymbol{x}_6(k) \quad \boldsymbol{x}_1(k+1)[$ for the model state progression in the lower part of the figure. The first transitions are the internal transitions related to both DDMs and the related sampling of new inputs (multiplication of both $\boldsymbol{D}_{\mathrm{p}}$ and $\boldsymbol{D}_{\mathrm{m}}$ on $\boldsymbol{x}_6(k)$ and $\boldsymbol{d}_{\mathrm{p}}$ to $u_1(k\theta_{\mathrm{BTP}})$ and finally $\boldsymbol{d}_{\mathrm{m}}$ to $u_2(k\theta_{\mathrm{BTP}})$). This is followed by the sampling and holding of the DDE states (multiplication of $\boldsymbol{S}_{\mathrm{p}}$ and $\boldsymbol{S}_{\mathrm{m}}$). Finally the first transition is concluded by a continuous CDE transition of length θ_0 (multiplication by $\boldsymbol{\Phi}(\theta_0)$):

$$\boldsymbol{x}_1(k+1) = \underbrace{\boldsymbol{\Phi}(\theta_0)\boldsymbol{S}_{\mathrm{m}}\boldsymbol{S}_{\mathrm{p}}\boldsymbol{D}_{\mathrm{m}}\boldsymbol{D}_{\mathrm{p}}}_{\boldsymbol{\Psi}_1}\boldsymbol{x}_6(k) + \underbrace{\boldsymbol{\Phi}(\theta_0)\boldsymbol{S}_{\mathrm{p}}\boldsymbol{d}_{\mathrm{p}}}_{\boldsymbol{v}_1}u_1(k\theta_{\mathrm{BTP}}) + \underbrace{\boldsymbol{\Phi}(\theta_0)\boldsymbol{S}_{\mathrm{m}}\boldsymbol{d}_{\mathrm{m}}}_{\boldsymbol{v}_2}u_2(k\theta_{\mathrm{BTP}}) \quad \text{(5.43a)}$$

Similarly for defining $\boldsymbol{x}_2(k+1)$, it may be seen that in addition to all the transitions occuring for $\boldsymbol{x}_1(k+1)$, a continuous CDE transition of length θ_0 happens. Thus all the previous transitions (contained in $\boldsymbol{\Psi}_1$) and inputs (contained in $\boldsymbol{v}_1$ and $\boldsymbol{v}_2$) are carried over and finally multiplied by $\boldsymbol{\Phi}(\theta_0)$:

$$\boldsymbol{x}_2(k+1) = \underbrace{\boldsymbol{\Phi}(\theta_0)\boldsymbol{\Psi}_1}_{\boldsymbol{\Psi}_2}\boldsymbol{x}_6(k) + \underbrace{\boldsymbol{\Phi}(\theta_0)\boldsymbol{v}_1}_{\boldsymbol{v}_3}u_1(k\theta_{\mathrm{BTP}}) + \underbrace{\boldsymbol{\Phi}(\theta_0)\boldsymbol{v}_2}_{\boldsymbol{v}_4}u_2(k\theta_{\mathrm{BTP}}) \quad \text{(5.43b)}$$

For $\boldsymbol{x}_3(k+1)$ all the previous transitions are again carried over. Thus starting from where $\boldsymbol{x}_2(k+1)$ ended, it may be seen that the next states updates are those of $x_{\Delta\Sigma_{\mathrm{m}}}$ and $\boldsymbol{x}_{\mathrm{m}}$ (multiplication by $\boldsymbol{D}_{\mathrm{m}}$), with a subsequent update of $x_{Q_{\mathrm{m}}}$ (multiplication by $\boldsymbol{S}_{\mathrm{m}}$), and finally concluded by a continuous CDE transition of length θ_0. Furthermore, a new input is also sampled, why the input $u_2(k\theta_{\mathrm{BTP}} + 2\theta_0)$ is introduced:

$$\boldsymbol{x}_3(k+1) = \overbrace{\boldsymbol{\Phi}(\theta_0)\boldsymbol{S}_{\mathrm{m}}\boldsymbol{D}_{\mathrm{m}}\boldsymbol{\Psi}_2}^{\boldsymbol{\Psi}_3}\boldsymbol{x}_6(k) + \overbrace{\boldsymbol{\Phi}(\theta_0)\boldsymbol{v}_3}^{\boldsymbol{v}_5}u_1(k\theta_{\mathrm{BTP}}) + \overbrace{\boldsymbol{\Phi}(\theta_0)\boldsymbol{S}_{\mathrm{m}}\boldsymbol{D}_{\mathrm{m}}\boldsymbol{v}_4}^{\boldsymbol{v}_6}u_2(k\theta_{\mathrm{BTP}})$$
$$+ \underbrace{\boldsymbol{\Phi}(\theta_0)\boldsymbol{S}_{\mathrm{m}}\boldsymbol{d}_{\mathrm{m}}}_{\boldsymbol{v}_2}u_2(k\theta_{\mathrm{BTP}}+2\theta_0) \quad \text{(5.43c)}$$

The approach for defining $\boldsymbol{x}_4(k+1)$, $\boldsymbol{x}_5(k+1)$ and $\boldsymbol{x}_6(k+1)$ is exactly the same, why it is not explained, and only the final result is presented:

$$\boldsymbol{x}_4(k+1) = \overbrace{\boldsymbol{\Phi}(\theta_0)\boldsymbol{S}_{\mathrm{p}}\boldsymbol{D}_{\mathrm{p}}\boldsymbol{\Psi}_3}^{\boldsymbol{\Psi}_4}\boldsymbol{x}_6(k) + \overbrace{\boldsymbol{\Phi}(\theta_0)\boldsymbol{S}_{\mathrm{p}}\boldsymbol{D}_{\mathrm{p}}\boldsymbol{v}_5}^{\boldsymbol{v}_7}u_1(k\theta_{\mathrm{BTP}}) + \overbrace{\boldsymbol{\Phi}(\theta_0)\boldsymbol{v}_6}^{\boldsymbol{v}_8}u_2(k\theta_{\mathrm{BTP}})$$
$$+ \underbrace{\boldsymbol{\Phi}(\theta_0)\boldsymbol{v}_2}_{\boldsymbol{v}_4}u_2(k\theta_{\mathrm{BTP}}+2\theta_0) + \underbrace{\boldsymbol{\Phi}(\theta_0)\boldsymbol{S}_{\mathrm{p}}\boldsymbol{d}_{\mathrm{p}}}_{\boldsymbol{v}_1}u_1(k\theta_{\mathrm{BTP}}+3\theta_0) \quad \text{(5.43d)}$$

$$\boldsymbol{x}_5(k+1) = \overbrace{\boldsymbol{\Phi}(\theta_0)\boldsymbol{S}_{\mathrm{m}}\boldsymbol{D}_{\mathrm{m}}\boldsymbol{\Psi}_4}^{\boldsymbol{\Psi}_5}\boldsymbol{x}_6(k) + \overbrace{\boldsymbol{\Phi}(\theta_0)\boldsymbol{v}_7}^{\boldsymbol{v}_9}u_1(k\theta_{\mathrm{BTP}}) + \overbrace{\boldsymbol{\Phi}(\theta_0)\boldsymbol{S}_{\mathrm{m}}\boldsymbol{D}_{\mathrm{m}}\boldsymbol{v}_8}^{\boldsymbol{v}_{10}}u_2(k\theta_{\mathrm{BTP}})$$
$$+ \underbrace{\boldsymbol{\Phi}(\theta_0)\boldsymbol{S}_{\mathrm{m}}\boldsymbol{D}_{\mathrm{m}}\boldsymbol{v}_4}_{\boldsymbol{v}_6}u_2(k\theta_{\mathrm{BTP}}+2\theta_0) + \underbrace{\boldsymbol{\Phi}(\theta_0)\boldsymbol{v}_1}_{\boldsymbol{v}_3}u_1(k\theta_{\mathrm{BTP}}+3\theta_0)$$
$$+ \underbrace{\boldsymbol{\Phi}(\theta_0)\boldsymbol{S}_{\mathrm{m}}\boldsymbol{d}_{\mathrm{m}}}_{\boldsymbol{v}_2}u_2(k\theta_{\mathrm{BTP}}+4\theta_0) \quad \text{(5.43e)}$$

$$\boldsymbol{x}_6(k+1) = \overbrace{\boldsymbol{\Phi}(\theta_0)\boldsymbol{\Psi}_5}^{\boldsymbol{\Psi}_6}\boldsymbol{x}_6(k) + \overbrace{\boldsymbol{\Phi}(\theta_0)\boldsymbol{v}_9}^{\boldsymbol{v}_{11}}u_1(k\theta_{\mathrm{BTP}}) + \overbrace{\boldsymbol{\Phi}(\theta_0)\boldsymbol{v}_{10}}^{\boldsymbol{v}_{12}}u_2(k\theta_{\mathrm{BTP}})$$
$$+ \underbrace{\boldsymbol{\Phi}(\theta_0)\boldsymbol{v}_6}_{\boldsymbol{v}_8}u_2(k\theta_{\mathrm{BTP}}+2\theta_0) + \underbrace{\boldsymbol{\Phi}(\theta_0)\boldsymbol{v}_3}_{\boldsymbol{v}_5}u_1(k\theta_{\mathrm{BTP}}+3\theta_0) + \underbrace{\boldsymbol{\Phi}(\theta_0)\boldsymbol{v}_2}_{\boldsymbol{v}_4}u_2(k\theta_{\mathrm{BTP}}+4\theta_0) \quad \text{(5.43f)}$$

Remark 5.4.G: The order in which the matrices are multiplied is very important if the correct transfer matrices are to be obtained. The multiplication order must correspond with the state update order of the actual system, otherwise the correct result will not be obtained. It is, however, possible to change the order of the DDE matrices, since they are not dependent upon each other. Thus, the following holds true which is relevant in equation 5.43a: $\boldsymbol{D}_{\mathrm{m}}\boldsymbol{D}_{\mathrm{p}} = \boldsymbol{D}_{\mathrm{p}}\boldsymbol{D}_{\mathrm{m}}$

Having derived all the individual transition equations step 3 is concluded, and it is possible to proceed to step 4.

5.4.3   Step 4: Combining The Transition Equations

Using the definition of the state vector as given by equation 5.41, a spatial-domain counterpart to a linear time-invariant (angle-invariant) state-space model may be formed as:

$$
\underbrace{\begin{bmatrix} \boldsymbol{x}_1(k+1) \\ \boldsymbol{x}_2(k+1) \\ \boldsymbol{x}_3(k+1) \\ \boldsymbol{x}_4(k+1) \\ \boldsymbol{x}_5(k+1) \\ \boldsymbol{x}_6(k+1) \end{bmatrix}}_{\boldsymbol{x}(k+1)} = \underbrace{\begin{bmatrix} & \boldsymbol{\Psi}_1 \\ & \boldsymbol{\Psi}_2 \\ \boldsymbol{0} & \boldsymbol{\Psi}_3 \\ & \boldsymbol{\Psi}_4 \\ & \boldsymbol{\Psi}_5 \\ & \boldsymbol{\Psi}_6 \end{bmatrix}}_{\boldsymbol{G}^{\boldsymbol{\Psi}}} \underbrace{\begin{bmatrix} \boldsymbol{x}_1(k) \\ \boldsymbol{x}_2(k) \\ \boldsymbol{x}_3(k) \\ \boldsymbol{x}_4(k) \\ \boldsymbol{x}_5(k) \\ \boldsymbol{x}_6(k) \end{bmatrix}}_{\boldsymbol{x}(k)} + \underbrace{\begin{bmatrix} \overbrace{\boldsymbol{v}_1 \quad 0}^{\boldsymbol{H}_1^{\boldsymbol{\Psi}}} & \overbrace{\boldsymbol{v}_2 \quad 0 \quad 0}^{\boldsymbol{H}_2^{\boldsymbol{\Psi}}} \\ \boldsymbol{v}_3 \quad 0 & \boldsymbol{v}_4 \quad 0 \quad 0 \\ \boldsymbol{v}_5 \quad 0 & \boldsymbol{v}_6 \quad \boldsymbol{v}_2 \quad 0 \\ \boldsymbol{v}_7 \quad \boldsymbol{v}_1 & \boldsymbol{v}_8 \quad \boldsymbol{v}_4 \quad 0 \\ \boldsymbol{v}_9 \quad \boldsymbol{v}_3 & \boldsymbol{v}_{10} \quad \boldsymbol{v}_6 \quad \boldsymbol{v}_2 \\ \boldsymbol{v}_{11} \quad \boldsymbol{v}_5 & \boldsymbol{v}_{12} \quad \boldsymbol{v}_8 \quad \boldsymbol{v}_4 \end{bmatrix}}_{\boldsymbol{H}^{\boldsymbol{\Psi}}} \underbrace{\begin{bmatrix} u_1(k\theta_{\mathrm{BTP}}) \\ u_1(k\theta_{\mathrm{BTP}} + 3\theta_0) \\ u_2(k\theta_{\mathrm{BTP}}) \\ u_2(k\theta_{\mathrm{BTP}} + 2\theta_0) \\ u_2(k\theta_{\mathrm{BTP}} + 4\theta_0) \end{bmatrix}}_{\boldsymbol{u}(k)}
$$

$$\text{(5.44a)}$$

The output vector may then be calculated by:

$$
\underbrace{\begin{bmatrix} y_1(k\theta_{\mathrm{BTP}}) \\ y_1(k\theta_{\mathrm{BTP}} + 3\theta_0) \\ y_2(k\theta_{\mathrm{BTP}}) \\ y_2(k\theta_{\mathrm{BTP}} + 2\theta_0) \\ y_2(k\theta_{\mathrm{BTP}} + 4\theta_0) \end{bmatrix}}_{\boldsymbol{y}(k)} = \underbrace{\begin{bmatrix} \boldsymbol{0} & \boldsymbol{0} & \boldsymbol{0} & \boldsymbol{0} & \boldsymbol{0} & \boldsymbol{c}_1 \\ \boldsymbol{0} & \boldsymbol{0} & \boldsymbol{c}_1 & \boldsymbol{0} & \boldsymbol{0} & \boldsymbol{0} \\ \boldsymbol{0} & \boldsymbol{0} & \boldsymbol{0} & \boldsymbol{0} & \boldsymbol{0} & \boldsymbol{c}_2 \\ \boldsymbol{0} & \boldsymbol{c}_2 & \boldsymbol{0} & \boldsymbol{0} & \boldsymbol{0} & \boldsymbol{0} \\ \boldsymbol{0} & \boldsymbol{0} & \boldsymbol{0} & \boldsymbol{c}_2 & \boldsymbol{0} & \boldsymbol{0} \end{bmatrix}}_{\boldsymbol{C}^{\boldsymbol{\Psi}}} \boldsymbol{x}(k) \qquad \text{(5.44b)}
$$

Exactly which states that will be included in the lifted output vector will be decided when the control strategy is considered.

The model represented by equation 5.44a has been constructed by combining the solutions to the three individual challenges of DFPT modelling. For this reason great uncertainty about the suitability of the individual solutions when combined is present, which is why the next section focuses on validating this new model.

5.5   10 kW Model Validation

Traditionally, a linear model validation aims to establish if the model's linear representations are a reasonable approximation of their non-linear counterparts. The linear subelements used to comprise the multirate model have to some extent already been validated.

- The linear discrete models of the DDMs in the 5.4 MW DFPT are validated in section 5.2.2 and previously by Johansen et al. (2016), Junker et al. (2016), Pedersen et al. (2016a), and Pedersen (2016).
- The use of a linearised $\Delta\Sigma$-Modulator expands beyond DFPT modelling and its successful usage in Junker et al. (2016), Pedersen et al. (2016a), Pedersen (2016), and Reiss (2008) suffices as indication of its validity.
- The subelements models used to describe rotor and HPL dynamics is based on the transformation approach which applicability have been established by Heemels et al. (1999) and furthermore successfully utilised by the authors in Junker et al. (2016), why these types of models furthermore are considered as valid linear approximation.

Further validation of the individual linear DFPT subelement models is therefore considered redundant and instead this section seeks to determine if the derived 10 kW multirate DFPT model has successfully combined the individual solutions of the three subchallenges presented in section 1.5.1 such that it can be confirmed if the challenge of multirate DFPT modelling is solved. For convenience the three subchallenges of modelling a DFPT are reiterated together with their solution:

Challenge I - DD Machine Modelling This challenge entails how a linear description of the discrete nature of operating the DDMs in full stroke operation can be formulated. The solution of this challenge consists of describing the DDM's dynamics by a convolution sum model of shifted impulse responses.

Challenge II - Non-uniform Activation Sequence This challenge entails how a discrete model of a DDM can be derived when the machine speed varies, creating a non-uniform chamber activation sequence in the time-domain. This challenge is solved by deriving all linear subelement models in the spatial-domain.

Challenge III - Multirate Activation Sequences A DFPT model contains two DDMs which chamber activation sequences are not synchronised, creating a multirate modelling challenge. This challenge is solved by the use of the developed UNMR method.

Individual solutions to challenge I and II already have been presented by the authors as well as others (Heemels et al. 1999; Junker et al. 2016; Pedersen et al. 2016a) and a solution to challenge III is presented in section 4.4. Therefore, what remain is how to combine these separate solutions in a multirate model describing an entire DFPT. The derived 10 kW DFPT multirate model, includes the individual solutions to the three DFPT modelling challenges. Thus, if simulation results from the DFPT multirate model and its subelements can be presented, which exhibits the appropriate sampling rates of the 10 kW DFPT and furthermore displays correct DDE, SHE and CDE transitions, the DFPT multirate model and the UNMR method's applicability to a DFPT are considered validated.

5.5.1   Multirate Model Validation

To evaluate if simulation results from the DFPT multirate model exhibits the appropriate sampling rates of the 10 kW DFPT, and if dynamic and discrete transitions occurs in the correct order it is desired to make model comparison between the multirate model and the non-liner simulation model. If there does not exist a reasonable correlation between the discrete linear subelements and their continuous non-linear counterparts, it will become exceedingly difficult to evaluate if the discrete multirate model exhibits the correct timing of transitions. E.g. if there exist the correct delay between when an input given to a DDM and the associated flow response starts or if the discrete representation of the DDM flow's described at multi-plums of θ_1 and θ_2 yields the correct representation of the HPL dynamics described at multi-plums of the system's STP. Thus, having similar flow and torque waveforms in the multirate and non-linear simulation model is important to complete the desired evaluation.

Unfortunately the low number of 2 and 3 chamber activations per revolution for the pump and motor in the 10 kW DFPT, respectively, results in discrete approximations of the DDMs' torque and flow responses with poor resolution. To illustrate the significance of such poor approximations, the linear discrete and non-linear continuous motor flow responses of the 10 kW DFPT is compared in figure 5.9 and remarks are made.
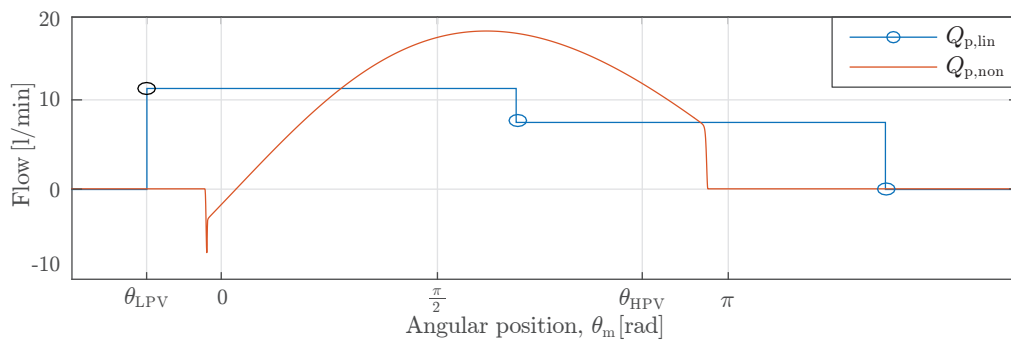
Fig. 5.9: Comparison of linear and non-linear flow response for a single pressure chamber in the DD motor of the 10 kW DFPT. At θ_{LPV} the decision to activate the next pressure chamber is taken, e.g. a binary input of 1 is given as input to both the linear and non-linear DD motor model. Subsequent chambers are not activated.

Remark 5.5.A: Comparing the discrete flow response of the 10 kW DD motor in figure 5.9, with the discrete flow response of the 5.4 MW DD motor previously presented in figure 5.7, it is evident that reducing the number of chamber activations per revolution significantly diminishes the discrete flow approximation of the continuous non-linear flow waveform. This issue is a direct result of the limitations imposed by using an impulse response modelling approach, which only describes the flow at discrete instances where a chamber activation can occur.

Remark 5.5.B: From figure 5.9 it is apparent that the discrete model of the DD motor yields a poor fit of the continuous non-linear flow waveform, however, from calculations it is found that the discrete linear model still exhibits a reasonable approximation of the effective displacement during a motoring stroke operation. A

comparison of the discrete and continuous model of the 10 kW DD pump comes with similar conclusions.

The 10 kW DFPT model only serves as an evaluation tool, where the applicability of the UNMR method can be investigated, why it is not considered an issue that the 10 kW discrete DDM models are poor approximations of the actual continuous dynamics.

However, having similar flow and torque waveforms in the multirate and non-linear simulation model during a multirate model validation will ease the evaluation, of whether the multirate model's dynamic transitions occurs in correct order and at correct rates, significantly. Thus, in the following model comparison it is chosen to utilise the linear discrete 10 kW DDM models in the otherwise continuous non-linear DFPT model. This makes the model comparison ideal for determining if the multirate model is capable of combining different subelement models correctly, and if the dynamic transitions occurs in the right order, hereby making it possible to determine the applicability of the UNMR method both the 10 kW and 5.4 MW DFPT.

Model Comparison:
The initial 10 kW simulation model contains three non-linear dynamic descriptions. The $\Delta\Sigma$-modulators' quantizers and the DDM torque and flow expressions. Introducing the linear discrete descriptions of the DDMs in this model, effectively means that only the quantizers remains non-linear. However, the characteristics of the quantizer only exhibits non-linear behaviour when given non-binary inputs, meaning that the entire simulation model is linear if the displacements inputs, $\alpha_p{}^*$ and $\alpha_p{}^*$, are limited to binary values. This makes the model comparison fairly easy as the simulation model and the multirate model should have close to identical simulation results in the defined multirate sampling instances. It is, however, important to note that this comparison primarily serves as a validation with respect to if the transitions occurs at the correct instances in the multirate DFPT model.

Remark 5.5.C: As the model comparison is performed under circumstances where both the multirate model and the simulation model exhibits linear characteristics, it would have been logical to expect identical simulation result. However, as previously described, the multirate model is described in the spatial-domain. The transformation from the time-domain to the spatial-domain introduces a non-linear term and thus requires linearisation. As a result some deviations between the discrete multirate model and the simulation model in the rotor and HPL dynamics may exist if the DFPT is operated sufficiently far away from the linearisation point during the model comparison.

Figure 5.10 depicts the model comparison with regard to the discrete and sample-and-hold states. The first subplot depicts the displacement inputs given to both the non-linear model and the discrete multirate model. The second and third subplot depicts the outputs of the DFPT's two $\Delta\Sigma$-modulators. It should be noted that the non-linear model simulation results are plotted as a continuous signal, whereas the multirate model is plotted as discrete data points for the discrete model states and ZOH-approximations for the SHE-states and the continuous states. Comparing subplot one to three it can be

seen that when an input is changed, the corresponding $\Delta\Sigma$-modulator's output changes after a sampling delay of either θ_1 or θ_2. E.g. the displacement input to the pump, $\alpha_\mathrm{p}{}^*$, changes to 1 after π, which result in the corresponding $\Delta\Sigma$-modulator's output changing to 1, $\theta_1 = \pi$ later. This corresponds well with how the state transition is expected to occur, and thus indicates that the multirate model describes the dynamics of the DFPT correctly.
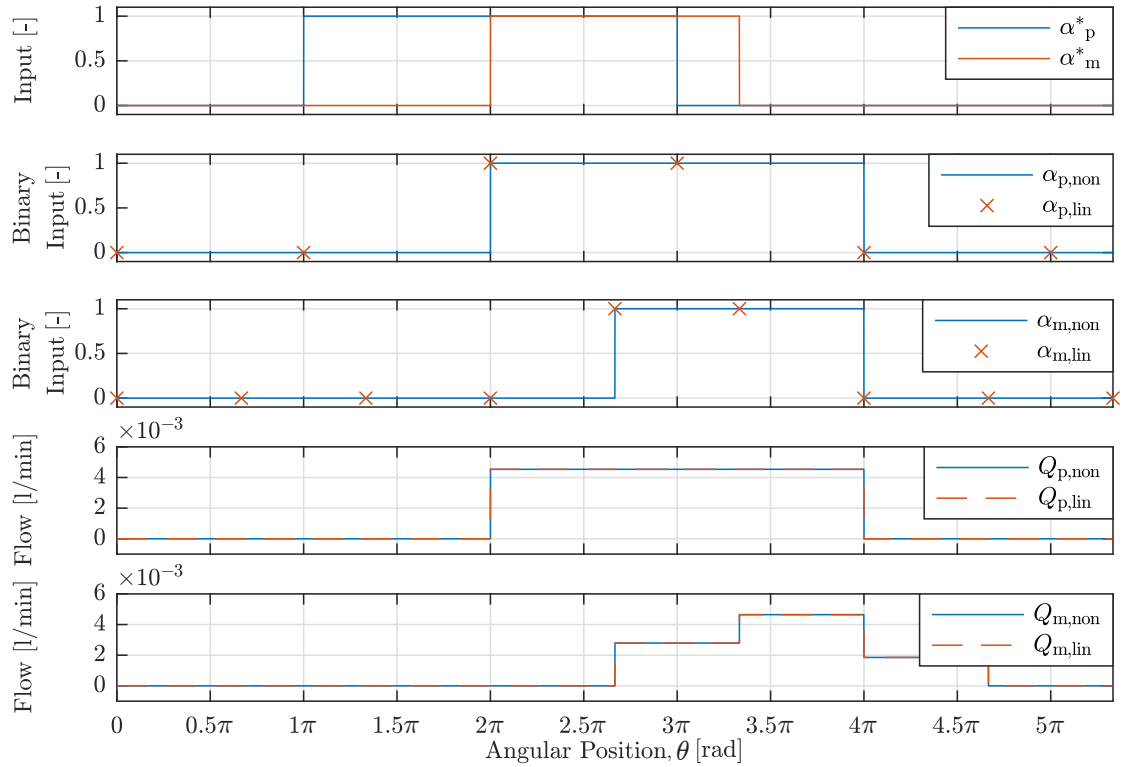
Fig. 5.10: Model comparison between $10\,\mathrm{kW}$ linear multirate model and the $10\,\mathrm{kW}$ non-linear simulation model, which includes linear descriptions of DDMs. Subplot one to three shows the non-binary displacement inputs, α^*, and binary displacement inputs, α, given to the DDMs and subplot four and five the pump and motor flow, Q_p and Q_m, respectively.

Subplot four and five in figure 5.10 depicts the flow waveforms, Q_p and Q_m. It is no surprise that these flow waveforms have identical magnitude and characteristics as they are based on identical linear discrete models. However, prior to this comparison, a concern was if the multirate model was capable of describing the SHE-state ($Q_\mathrm{p,lin}$ and $Q_\mathrm{m,lin}$) transitions at the correct angles. Subplot four and five shows that the SHE-state transition occurs at the same angles as the non-linear model.

Figure 5.10 indicates that the multirate model's discrete and sample-and-hold state transitions occurs at the right angle, and furthermore with the correct sampling rates. With this established, the second part of the model validation compares simulation results from the discrete multirate model and simulation model with regard to the continuous states ω_r and Δp. This can be seen in figure 5.11.
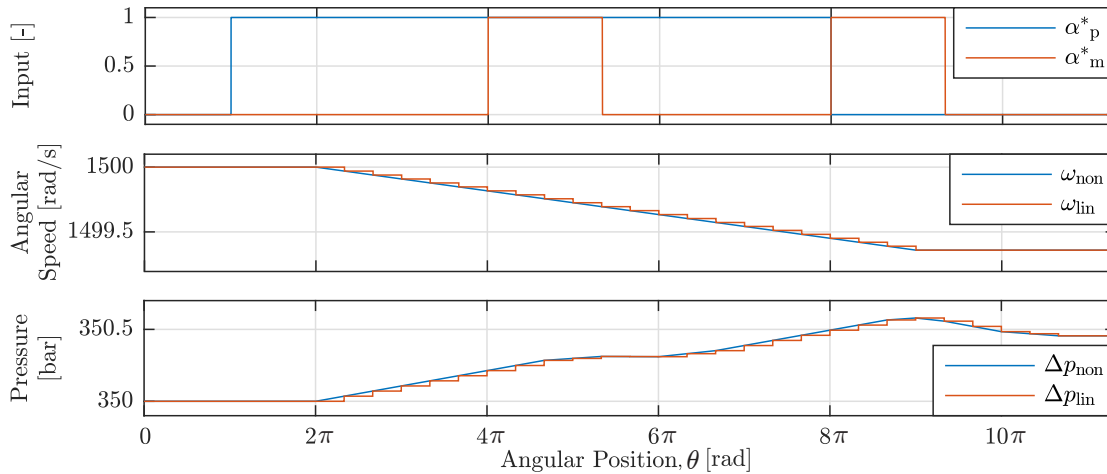
Fig. 5.11: Model comparison between 10 kW linear multirate model and the 10 kW non-linear simulation model, which includes linear descriptions of DDMs. Subplot one shows the non-binary displacement inputs, α^*, given to the DDMs and subplot two and three shows the angular rotor speed ω_r and the pressure difference Δp, respectively.

The first subplot of figure 5.11 shows the displacement inputs given to the non-linear model and the linear multirate model. In this comparison the simulation is run over a larger change in angular position in the desire to capture larger changes in the angular speed of the rotor shaft, ω_r, and in the pressure difference between the HPL and LPL, Δp. However studying subplot two and three in figure 5.11 shows that relatively small changes occur. The small change in angular speed is because the inertia of the rotor shaft is relatively large, compared to the torque the DD pump can produce, whereas the relatively large volume in the HPL results in small pressure changes.

Examining subplot two and three in figure 5.11 it can be seen that the multirate model's ZOH-approximations fits the continuous waveforms produced by the non-linear model. The ZOH-approximations changes with a step size of the multirate model's STP, which is in accordance with the theory presented in chapter 4. The results of figure 5.11 again confirms that the transitions occurring in the multirate model are correct. This furthermore shows that the spatial transformation of Newton's II law and the continuity equation utilised in the derivations of the multirate model are correct, since they provide the same values of ω_r and Δp as the time-domain non-linear model.

Multirate Validation Considerations:
The above presented result concludes the validation of the linear discrete multirate model describing the 10 kW DFPT. From this validation it can be established that the 10 kW DFPT multirate model can describe the dynamic state transition at the correct angular positions and with the appropriate sampling rates. The derived multirate model includes discrete convolution sum models of the two DDMs, which is the proposed solution to the DFPT modelling subchallenge I. Furthermore these discrete models are described in the spatial-domain, hereby creating uniform sampling rates which solves subchallenge II. As the sampling rates of the two discrete DDM models are different, the UNMR method for

producing a multirate model also solves subchallenge III. Hereby it can be concluded that the multirate model successfully solves all initially proposed DFPT modelling subchallenges and thus a method which is able to produce a linear time-variant (angle-invariant) model of a DFPT on state-space form have successfully been developed.

The multirate model validation does not include a comparison where the simulation model contains the non-linear DDM models, however, such a comparison and corresponding validation was made for the individual DDMs prior to the mulrirate model comparison. Therefore considering all the results presented in section 5.5, there is no indication that the derived UNMR method cannot be successfully applied to describe the 5.4 MW DFPT as the discrete DDM models have a better fit when compared to their corresponding non-linear DDM models due to a relatively high number of pressure chambers.

When the multirate model is to be expanded to the 5.4 MW DFPT some comments can be made:

Remark 5.5.D: With the exception of the discrete DDM models all other subelement in the DFPT remains the same for both the 10 kW and 5.4 MW DFPT. Furthermore, the discrete DDM models of the 5.4 MW DFPT have in this thesis been developed, why only the choice of a suitable operating point remains, before step 3 of the UNMR method can be applied to the 5.4 MW DFPT.

Remark 5.5.E: Step 3 of the UNMR method consists of deriving transition equations for each STP period within a BTP period. Doing this by hand, as presented in this chapter is cumbersome and ill advised in the case of a large ratio between a system's BTP and STP, however, utilising the presented algorithm from section 4.4.2 should simplify step 3 significantly.

Remark 5.5.F: Step 4 of the UNMR method should be straight forward to apply to the 5.4 MW DFPT, where the spatial-domain's equivalence to a linear time-invariant state space model is defined. However, the BTP will be significantly larger than the STP, why the dimensions of the lifted state vector, the state transition matrix and the input transition matrix will be relatively large. This might arise a computational memory issue, when step 3 and 4 must be performed for the 5.4 MW DFPT multirate model.

Results indicating that the UNMR method can be applied to the 5.4 MW DFPT have been presented. Furthermore, the tasks that have to be adressed before a 5.4 MW multirate DFPT model can be derived have been presented. Related comments upon these tasks suggest that the only potential task remaining is how to handle the relatively large memory requirements needed to compute the necessary data for deriving the multirate model. Thus, knowledge has been attained to answer first part of this thesis' problem statement, why the remainder of thesis will focus on the second part, concerning the utilisation of conventional linear MIMO analysis and controller design tools on the developed multirate DFPT model. To simplify the investigation of applicability of such tools on a multirate model produced by the UNMR method next chapter will take basis in the previously derived multirate model of the MSD system.

6

Multirate Mass Spring Damper Control

This chapter seeks to investigate the applicability of various methods for system analysis and controller design on the Mass Spring Damper (MSD) system described by the unified non-minimal realisation method. Initially, the prerequisites necessary for controller design are presented. This is followed by investigating the applicability of the Relative Gain Array (RGA) and Singular Value Decomposition (SVD) on the model for analysing system cross couplings and frequency response, respectively. Finally, a controller for the MSD system is designed.

6.1 Lifted Multirate Analysis and Control Challenges

Chapter 4 has solved the task of deriving a method which is able to produce a LTI model describing both continuous, discrete and sample-and-hold elements on discrete-time state-space form. This method, refereed to as the Unified Non-minimal Realisation (UNMR) method, was in chapter 5 successfully applied on the downscaled DFPT and its applicability towards the full power 5.4 MW DFPT was confirmed. In addition to these already solved tasks, this thesis also seeks to investigate the following remaining tasks:

- Can conventional methods such as the RGA and SVD be directly applied to the model produced by the UNMR method in order to investigate cross couplings and frequency response in the MIMO system?

- Is it possible to apply conventional controller design methods on a model produced by the UNMR method to obtain a controller that is able to control the states?

- How is the additional entries in the input and output vector of the discrete model handled with regard to system analysis, controller design and subsequent implementation of the controller?

Instead of handling these tasks based on the DFPT system it is chosen to consider the simpler MSD system including the discrete filters as this is just as qualified a platform for evaluating if and how these tasks can be solved. To further simplify, this chapter mainly considers the example with different but similar sampling rates ($T_1 = 0.15$ s and $T_1 = 0.10$ s) unless otherwise noted as this reduces the state-space model dimensions significantly. It is important to note that the objective of applying conventional analysis and controller design methods is to investigate if these methods can be directly applied to the derived multirate model and comment upon potential limitations. Thus, this chapter does not seek to qualitatively or quantitatively analyse the system or design a controller that yields high performance reference tracking.

Different methods for designing controllers exist. Due to the large number of states, primarily a consequence of the large number of pressure chambers in the DFPT, it is chosen to test the applicability of designing a Linear Quadratic Regulator (LQR). Before the controller design method is applied, the controllability of the multirate model describing the MSD system derived in section 4.3 is investigated.

6.2 Controllability of Multirate Model

A system described by a state-space model is considered state controllable if all states can be brought from any initial state to any final state within a finite time by its inputs. In general this is obviously a highly desirable feature of a system.

One approach for determining this is by evaluating the rank of the controllability matrix which is given by (Skogestad and Postlethwaite 2001):

$$\boldsymbol{R}_{\mathrm{c}} = \begin{bmatrix} \boldsymbol{H}^{\boldsymbol{\Psi}} & \boldsymbol{G}^{\boldsymbol{\Psi}}\boldsymbol{H}^{\boldsymbol{\Psi}} & \boldsymbol{G}^{\boldsymbol{\Psi}2}\boldsymbol{H}^{\boldsymbol{\Psi}} & \dots & \boldsymbol{G}^{\boldsymbol{\Psi}Nn-1}\boldsymbol{H}^{\boldsymbol{\Psi}} \end{bmatrix} \tag{6.1}$$

where the product Nn describes the total number of states for the given system. State controllability is achieved if the controllability matrix has full rank, i.e. if $\mathrm{rank}(\boldsymbol{R}_{\mathrm{c}}) = Nn = 48$ for the multirate MSD model. The rank of the controllability matrix is, however, found to $\mathrm{rank}(\boldsymbol{R}_{\mathrm{c}}) = 9$ and thus only 9 states are controllable.

To the best of the authors' knowledge, no method exists for directly determining which states are the controllable ones. As an alternative some comments and remarks are made regarding why full state controllability cannot be achieved:

Remark 6.2.A: Due to the derived linear multirate model being a non-minimal realisation it contains states which are not necessary for describing the system dynamics. This is due to the fact that the state vector $\boldsymbol{x}(k+1)$ can be described only using the state subvector $\boldsymbol{x}_6(k)$. As previously stated, the states $\boldsymbol{x}_1(k)$ to $\boldsymbol{x}_5(k)$ are only included such that the system dynamics can be described at time steps equal to the STP. This also means that from a control point of view a large number of states are redundant and thus may not be controllable.

Remark 6.2.B: The UNMR method forms an expanded state vector which describes the continuous, discrete and sample-and-hold elements at time steps equal to the STP. As the sample-and-hold elements are modelled as ideal, they can be described by a direct input-output coupling, why these states are redundant.

Remark 6.2.C: Considering the input vector, it is evident that the input $\boldsymbol{u}_1$ can only be given twice during a BTP while the input $\boldsymbol{u}_2$ can be given three times. Thus, it makes sense that the states which are described at instants when no input can be given are uncontrollable.

Remark 6.2.D: The state vector formulated by the UNMR method is given on a rather unconventional form, at least in the sense of LTI systems, as several of the states describes the same physical state, only shifted in time. Due to this unconventional form, it can be argued that if the state subvector $\boldsymbol{x}_6(k)$ (excluding the sample-

and-hold states) is controllable, then the state subvectors $\boldsymbol{x}_1(k)$ to $\boldsymbol{x}_5(k)$ should also be bounded to some extent. Thus, for a state-space model on this form, the requirements to controllability may be relaxed.

To confirm that the uncontrollable states are a consequence of the non-minimal realisation, the model is converted to a minimal realisation using the MATLAB command *minreal* since this eliminates the states which are uncontrollable and unobservable. Utilisation of the *minreal*-function requires a state-space model where the output equation is given on the conventional form, i.e. $\boldsymbol{y}(k) = \boldsymbol{C}\boldsymbol{x}(k) + \boldsymbol{D}\boldsymbol{u}(k)$. The state equation is therefore combined with the output equation formulated from the UNMR method to obtain an output equation given by:

$$\boldsymbol{y}(k) = \underbrace{\boldsymbol{C}^{\boldsymbol{\Psi}}(\boldsymbol{U_1}\boldsymbol{G}^{\boldsymbol{\Psi}} + \boldsymbol{U_2})}_{\boldsymbol{C}_{\mathrm{c}}}\boldsymbol{x}(k) + \underbrace{\boldsymbol{C}^{\boldsymbol{\Psi}}\boldsymbol{U_1}\boldsymbol{H}^{\boldsymbol{\Psi}}}_{\boldsymbol{D}_{\mathrm{c}}}\boldsymbol{u}(k) \tag{6.2}$$

Converting to a minimal realisation eliminates 42 states and thus only 6 states remain in the state-space model. This corresponds well with the fact that the state subvectors $\boldsymbol{x}_1(k)$ to $\boldsymbol{x}_5(k)$ are redundant and that the sample-and-hold elements can be described by a direct input-output coupling. The 6 remaining states describe the 4 continuous and 2 discrete states at steps equal to the BTP.

Remark 6.2.E: As the sample-and-hold elements can be described by a direct input-output coupling these states could have been omitted when the state-space model was formulated using the UNMR method as the states do not contribute with any dynamics. The reason for including the states describing the sample-and-hold elements in the unified non-minimal realisation is that this allows for describing imperfect sampling operations.

The redundancy of the 42 states which are eliminated can also be confirmed by considering the poles of the non-minimal realisation model, which are shown in figure 6.1.
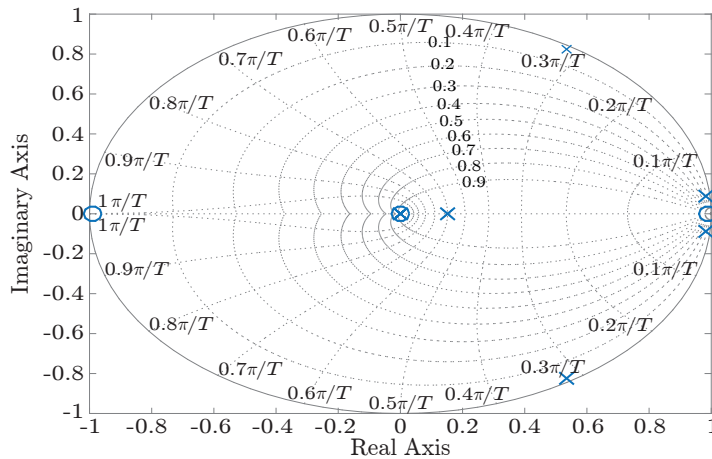
Fig. 6.1: Pole-zero map showing the pole and zero location for the MSD system including discrete filters and different but similar sampling rates.

42 poles are located in the origin corresponding to the eliminated states. A pole in the origin corresponds to a state which does not contribute with any additional dynamics to the system. This is exactly the case for the lifted state subvectors $\boldsymbol{x}_1(k)$ to $\boldsymbol{x}_5(k)$ and the sample-and-hold states in $\boldsymbol{x}_6(k)$.

Remark 6.2.F: The location of the two complex conjugate pole pairs, associated with the continuous states in the multirate model, is the same as the poles for a conventional ZOH discretisation of the MSD system.

As previously stated, the model produced by the UNMR method does not yield full rank of the controllability matrix. This does, however, not mean that the system can not be controlled. As an example, the behaviour of the states describing the sample-and-hold elements is of no interest from a control point-of-view why the lack of controllability is not considered an issue. The lack of controllability of the states describing the continuous elements in $\boldsymbol{x}_1(k)$ to $\boldsymbol{x}_5(k)$ might, however, pose a problem when a controller is to be designed. This is investigated in a later section in this chapter.

Having investigated the controllability of the multirate model, the next sections seeks to evaluate if the RGA and SVD can be applied to the multirate model such that models on this form can be analysed with respect to cross couplings and frequency response.

6.3 MIMO Analysis Tools

Before a controller is designed for a MIMO system, the control engineer is often interested in analysing the system. Analysis with regard to the system's frequency response and potential cross couplings between the system's multiple inputs and outputs is often of high interest as it provides valuable information with respect to determining a suitable control structure for the given system. As an example, a decentralised control structure may not yield the desired tracking performance if the system contains a high degree of cross couplings.

This section investigates if the RGA and SVD are directly applicable on the model produced by the UNMR method in order to analyse cross couplings and frequency response for the system. If these MIMO analysis tools are directly applicable on the multirate MSD then it can be assumed that they can be utilised on the multirate DFPT model. It is important to note that the purpose of the section is not to develop new analysis methods, but only to apply already known methods. Thus the following section initially investigates the applicability of the Relative Gain Array (RGA).

6.3.1 Relative Gain Array

The RGA can be utilised for obtaining a measure of the degree of influence each input has on each output, i.e. cross couplings. In addition to a cross coupling analysis, the RGA can be utilised for pairing controlled outputs with inputs if decentralised control is to be applied.

In order to utilise the RGA, a discrete transfer function matrix, denoted $\boldsymbol{G}_{\mathrm{MSD}}$, is in-

troduced which describes the dynamics between each of the inputs and outputs and is calculated by (Skogestad and Postlethwaite 2001):

$$G_{\mathrm{MSD}}(z) = C_c \left(zI - G^{\Psi} \right)^{-1} H^{\Psi} + D_c \tag{6.3}$$

G_{MSD} has dimension 5×5, according to the number of inputs and outputs. The 5×5 RGA matrix of the MSD system can be calculated by (Skogestad and Postlethwaite 2001):

$$\mathrm{RGA}(G_{\mathrm{MSD}}) = \mathbf{\Lambda}(G_{\mathrm{MSD}}) = G_{\mathrm{MSD}} \times \left(G_{\mathrm{MSD}}^{-1} \right)^{\intercal} \tag{6.4}$$

where $\times$ denotes element-by-element multiplication. Each RGA element, λ_{ij}, in $\mathbf{\Lambda}(G_{\mathrm{MSD}})$ is a complex number why $|\lambda_{ij}|$ is computed and utilised for analysing the cross couplings. As the input-output couplings depend on the frequency at which the system is excited, the RGA elements are generally evaluated as function of frequency. Analysis of the frequency response of discrete systems is limited to below the Nyquist frequency due to aliasing effects, and for single rate systems the Nyquist frequency is simply half the sampling frequency. However, for multirate systems the Nyquist frequency is not as easily defined, and therefore it is chosen to simply denote the Nyquist frequency as half the BTP rate for simplicity, such that:

$$f_{\mathrm{Nyq}} = \frac{f_T}{2} = \frac{1/T}{2} \ \ [\mathrm{Hz}] \tag{6.5}$$

For the MSD system utilising different but similar sampling rates, the input and output vectors are repeated in equation 6.6. The vectors are shown here for clarity and the entries will be the inputs and outputs between which the cross couplings can be investigated.

$$\boldsymbol{u}(k) = \begin{bmatrix} u_1(kT) \\ u_1(kT + 3T_0) \\ u_2(kT) \\ u_2(kT + 2T_0) \\ u_2(kT + 4T_0) \end{bmatrix} \qquad \boldsymbol{y}(k) = \begin{bmatrix} y_1(kT) \\ y_1(kT + 3T_0) \\ y_2(kT) \\ y_2(kT + 2T_0) \\ y_2(kT + 4T_0) \end{bmatrix} \tag{6.6}$$

The magnitudes of the $5 \cdot 5 = 25$ RGA elements are computed and plotted as function of the frequency for G_{MSD}. It is, however, found that the plots were inconclusive with regard to analysing cross couplings which is also why the plots are not shown here. Some remarks are made upon why the RGA cannot be directly applied to G_{MSD} for analysing couplings:

Remark 6.3.A: A conventional MIMO state-space formulation describes the multiple inputs and outputs at the same instant in time. The model produced by the UNMR method, however, formulates an input and output vector where the entries are shifted in time as seen in equation 6.6. This is a consequence of obtaining a linear time-invariant state-space model of the multirate system. The RGA is not formulated to account for couplings across time but only as a tool for investigating couplings between inputs and outputs described at the same time instants.

Remark 6.3.B: As the entries in the input and output vector are shifted in time, it does not make physical sense to analyse certain combinations of inputs and outputs with respect to cross couplings. This is evident if, for example, the cross couplings between the input $u_1(kT + T_1)$ and the output $y_2(kT + T_2)$, as seen in equation 6.6, are to be investigated. This does not make sense as $kT + T_1$ occurs later in time than $kT + T_2$. This is also the case for other combinations of inputs and outputs why an RGA analysis cannot be used for analysing cross couplings between all inputs and outputs given by the state-space model.

Remark 6.3.C: In order to get meaningful information from the RGA all combinations between inputs and outputs must make physical sense. Thus, it is not possible to simply extract specific RGA elements, λ_{ij}, which are considered to make physical sense from $\mathbf{\Lambda}(\boldsymbol{G}_{\mathrm{MSD}})$ and analyse these individually with respect to cross couplings.

Considering equation 6.6, it is clear that the only input-output pair which are described at the same instant in time is the first and third entries in the two vectors. Thus, rather than applying the RGA to the full 5×5 $\boldsymbol{G}_{\mathrm{MSD}}$ transfer function matrix, the four transfer functions describing the dynamics between the first and third entries at time kT are extracted from $\boldsymbol{G}_{\mathrm{MSD}}$ to obtain a new transfer function matrix, $\boldsymbol{G}_{\mathrm{MSD13}}$. The 2×2 RGA element matrix are then computed:

$$\mathbf{\Lambda}(\boldsymbol{G}_{\mathrm{MSD13}}) = \boldsymbol{G}_{\mathrm{MSD13}} \times (\boldsymbol{G}_{\mathrm{MSD13}}^{-1})^\intercal = \begin{bmatrix} \lambda_{11} & \lambda_{12} \\ \lambda_{21} & \lambda_{22} \end{bmatrix} \tag{6.7}$$

Remark 6.3.D: Performing a RGA analysis on the transfer function, $\boldsymbol{G}_{\mathrm{MSD13}}$, does not provide a definitive answer to all the input-output couplings present in the system, but merely an indication of which cross coupling might be expected.

Plotting the magnitude of the computed RGA elements in equation 6.7 as function of frequency yields the RGA plot in figure 6.2.

Some comments regarding the validity of extracting these transfer functions and performing a RGA analysis on them are now made:

Remark 6.3.E: If the RGA is calculated for the continuous MSD system (equation 4.1) as a function of frequency, then it has been observed that the magnitude of the elements is exactly the same as illustrated in figure 6.2. By this argument it is considered a valid approach to extract the BTP to BTP transfer functions for the lifted multirate model.

The filters present in the multirate model, which are not present in the continuous model, should not affect any cross couplings, since they are present in both input paths. Furthermore the Nyquist frequency, which is $f_{\mathrm{Nyq}} = 1.67\,\mathrm{Hz} = 10.4\,\mathrm{rad/s}$, is two decades lower than the break frequency of the filters, meaning that the frequency response of the discrete multirate model should be completely unaffected by the presence of the filters.

If a quantitative cross coupling analysis were to be performed, some comments upon figure 6.2 could be made.
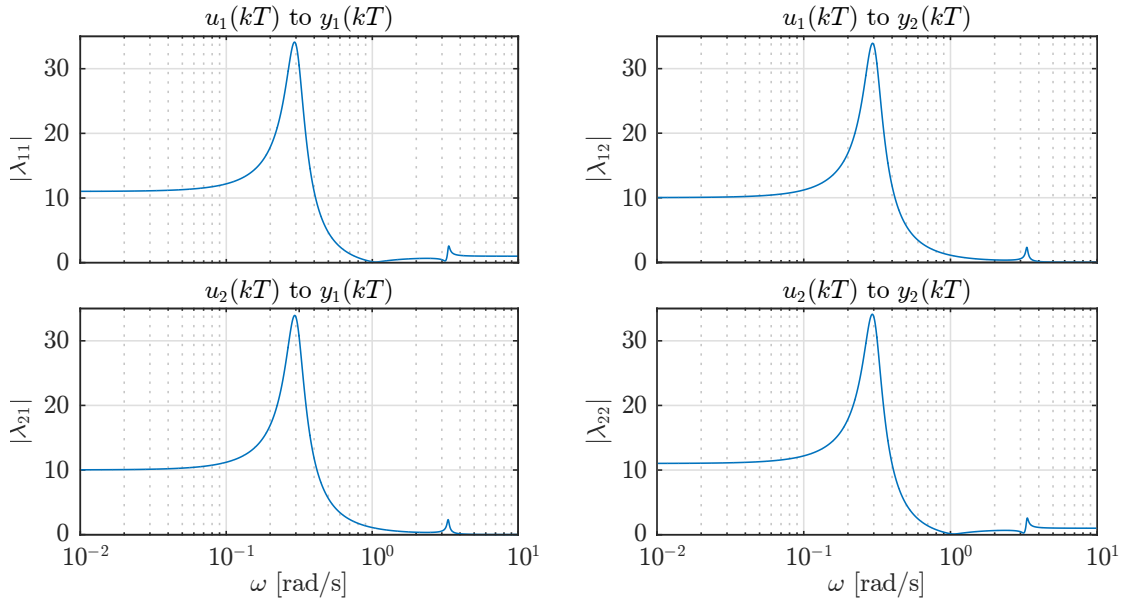
Fig. 6.2: Magnitude of RGA elements in $\mathbf{\Lambda}(\boldsymbol{G}_{\mathrm{MSD13}})$ as function of frequency.

- The RGA frequency response depicts two resonance peaks, one at $\sim 0.3\,\mathrm{rad/s}$ and a second at $\sim 3\,\mathrm{rad/s}$, which corresponds to the natural frequency of mass 1 and 2 respectively in the MSD system.
- Above frequencies of $\sim 0.3\,\mathrm{rad/s}$, u_1 only affects y_1 and u_2 only affects y_2 as $|\lambda_{11}| = 1$ and $|\lambda_{22}| = 1$. This also makes physical sense for the MSD system, due to the filtering effect that is the direct result of the natural frequencies of the MSD systems two masses.

From the RGA investigation presented in this section, it can be concluded that the RGA cannot be directly applied to the lifted model, produced by the UNMR method, for analysing cross couplings between all inputs and outputs described in the model. This is due to the entries in the input and output vector being shifted in time relative to each other. The RGA can only be applied to analyse the cross couplings between the inputs and outputs which are described at the same instants in time, if the corresponding transfer functions are extracted from the full transfer function matrix. In order to analyse couplings across time another tool is needed. As this chapter seeks to investigate if conventional methods can be applied to a model on the given form no further effort is put into obtaining a tool which is able to analyse cross couplings across time.

Having investigated the applicability of the RGA, the next section seeks to determine the applicability of the SVD for analysing the MIMO multirate model frequency response.

6.3.2 Singular Value Decomposition

The gain of a SISO system can be investigated by considering a Bode plot as it only depends on the input excitation frequency. When a MIMO system is considered the gain, however, depends on the direction of the input vector in addition to the frequency.

(Skogestad and Postlethwaite 2001)

Thus since the Bode plot is not applicable, the gain of MIMO systems can instead be analysed by decomposing the transfer function matrix into its singular values. For the 5×5 $\boldsymbol{G}_{\text{MSD}}$, 5 singular values are computed, denoted by $\sigma_{1\ldots 5}^{\Psi}$, for each evaluated frequency. Two of these singular values will correspond to a maximum and minimum singular value, denoted by $\hat{\sigma}$ and $\check{\sigma}$, respectively. $\hat{\sigma}$ and $\check{\sigma}$ describes the maximum and minimum gain of the system for any input direction. The singular values of the transfer function matrix $\boldsymbol{G}_{\text{MSD}}$ can be computed as function of the frequency by applying the MATLAB function svd to $\boldsymbol{G}_{\text{MSD}}$.

Figure 6.3 shows the five singular values for $\boldsymbol{G}_{\text{MSD}}$ as function of frequency. In order to evaluate if the singular values are meaningful and can be used for analysing the system gain, the two singular values, σ_1 and σ_2, of the transfer function matrix formed from the continuous state-space model describing the MSD (equation 4.1), are also computed and included in the plot.
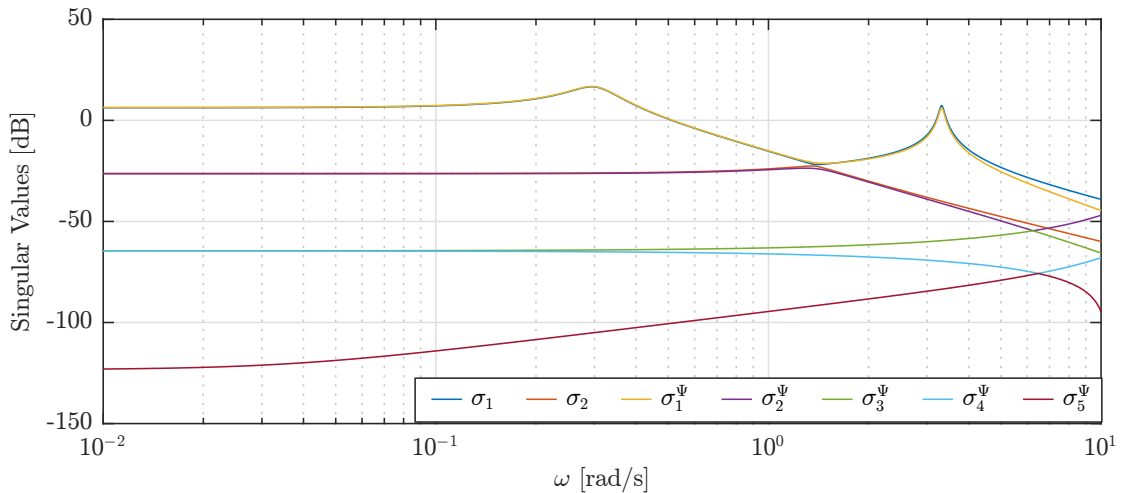
Fig. 6.3: Singular values of $\boldsymbol{G}_{\text{MSD}}$ where $\hat{\sigma} = \sigma_1^{\Psi}$ and $\check{\sigma} = \sigma_5^{\Psi}$. Singular values of continuous transfer function matrix, where $\hat{\sigma} = \sigma_1$ and $\check{\sigma} = \sigma_2$, are also plotted.

Some comments and remarks are made upon the singular values plotted in figure 6.3:

Remark 6.3.F: Similarities exist between certain of the singular values computed from $\boldsymbol{G}_{\text{MSD}}$ and the continuous model. The maximum values, $\hat{\sigma}$, of $\boldsymbol{G}_{\text{MSD}}$ and the continuous representation are similar, however, the minimum values, $\check{\sigma}$, are not equal. For $\boldsymbol{G}_{\text{MSD}}$, $\check{\sigma}$ is significantly lower than for the continuous model. No apparent physical interpretation of the minimum singular value of $\boldsymbol{G}_{\text{MSD}}$ is found.

The comparison to the contiuous system is still considered valid, since the break frequency of the discrete filters is significantly higher (1000 Hz), why these should not modify the gain of the system for inputs below the Nyquist frequency.

Remark 6.3.G: The singular values of $\boldsymbol{G}_{\text{MSD}}$ are calculated by considering the resulting

system gain for all possible directions of the input vector. As previously stated certain combinations of inputs and outputs does not make physical sense, e.g. the input-output pairs which has relations going backwards in time. The gain of these combinations are, however, also included when the singular values are computed, why certain of the singular values may not make physical sense.

Remark 6.3.H: As some of the input-output pairs do not make physical sense, the singular values computed from the full 5×5 transfer function matrix $\boldsymbol{G}_{\text{MSD}}$ do not immediately make sense.

Attempting to account for this by merely calculating the singluar values for the 2×2 transfer function matrix $\boldsymbol{G}_{\text{MSD13}}$, as was done in the RGA analysis, produces singular values which are different in DC-gain and with different break frequency than the continuous system, why this approach is not considered valid for calculating the SVD of lifted multirate models.

Remark 6.3.I: The increasing deviation between σ_1 and σ_1^{Ψ} and σ_2 and σ_2^{Ψ} at increasing frequencies is due to the frequency response of the discrete system nearing the Nyquist frequency ($10.4\,\text{rad/s}$).

Based on figure 6.3 and the presented remarks it is concluded that the SVD tool is not directly applicable to a model produced by the UNMR method. The reason for this is similar to what was presented for the RGA, which is that the SVD is not directly capable of accounting for the model containing entries in the input and output vector which are shifted in time relative to each other. It is, however, still possible to determine the maximum gain of the system, which could be useful when doing a sensitivity analysis to determine an appropriate linearsation point.

The discrete-time multirate model on state-space form produced by the UNMR method has been investigated with regard to controllability and the applicability of conventional analysis tools such as the RGA and SVD. It can generally be concluded that despite the derived multirate model being linear time-invariant, these conventional tools are not directly applicable. The next section seek to determine a suitable control structure and design a controller.

6.4 Optimal Control of Multirate System

The control engineer is generally free to choose whatever control law he fancies, whether it be a linear or non-linear compensation, and subsequently stability may relatively easily be proved (at least in the linear case). However, the challenge of determining what constitutes good or appropriate controller gains still remains.

The work in this thesis is limited to considering only linear time (or angle) invariant multirate models, why it is also natural to consider only linear control laws. In this subset of control theory, there are a number of different possibilities, including transfer function based PID and lag-lead controllers or state-space based state feedback arrangements. Having developed a multirate model in a state-space formulation it is decided to focus

on state feedback possibilities.

Determining the controller gains for a state controller may be done by conventional pole placement methods, such as Ackermann's formula, or by optimisation based minimum cost methods. Owing to the large number of states in a full scale DFPT model, the latter method will here be used to derive a method for determining the controller gains.

6.4.1   Conventional State Feedback

The conventional state feedback control law is normally written in the form:

$$\boldsymbol{u}(k) = -\boldsymbol{K}\boldsymbol{x}(k) \tag{6.8}$$

Determining the controller gain matrix, $\boldsymbol{K}$, may then be done by setting up a minimum cost optimisation problem. The problem is typically formulated using a quadratic performance index of the form (MathWorks 2017):

$$J(k) = \sum_{i=k}^{\infty} \left[\boldsymbol{x}(i)^{\mathsf{T}}\boldsymbol{Q}\boldsymbol{x}(i) + \boldsymbol{u}(i)^{\mathsf{T}}\boldsymbol{R}\boldsymbol{u}(i) + 2\boldsymbol{x}(i)^{\mathsf{T}}\boldsymbol{N}\boldsymbol{u}(i) \right] \tag{6.9}$$

where $\boldsymbol{Q}$ and $\boldsymbol{R}$ are weighting matrices for the control error and control effort, respectively. The cross term weighting matrix $\boldsymbol{N}$ is often set equal to zero, such that this term is omitted.

This problem, also known as the discrete-time linear quadratic regulator (LQR) problem may be solved by using the MATLAB command *dlqr($\boldsymbol{G}$,$\boldsymbol{H}$,$\boldsymbol{Q}$,$\boldsymbol{R}$,$\boldsymbol{N}$)*. Alternatively the proof is provided in appendix D.2, wherein an analytical expression for the gain matrix and the discrete-time Riccati equation are derived under the assumption of $\boldsymbol{N} = 0$.

The gain matrix may be calculated analytically by (MathWorks 2017):

$$\boldsymbol{K} = \left(\boldsymbol{R} + \boldsymbol{H}^{\mathsf{T}}\boldsymbol{P}\boldsymbol{H}\right)^{-1}\left(\boldsymbol{H}^{\mathsf{T}}\boldsymbol{P}\boldsymbol{G} + \boldsymbol{N}^{\mathsf{T}}\right) \tag{6.10}$$

The expression depends on the state equation matrices $\boldsymbol{G}$ and $\boldsymbol{H}$, as well as the effort weighting matrices $\boldsymbol{R}$ and $\boldsymbol{N}$. The matrix $\boldsymbol{P}$ is obtained by solving the discrete-time algebraic Riccati equation, which is given by (MathWorks 2017):

$$0 = \boldsymbol{G}^{\mathsf{T}}\boldsymbol{P}\boldsymbol{G} - \boldsymbol{P} + \boldsymbol{Q} - \left(\boldsymbol{G}^{\mathsf{T}}\boldsymbol{P}\boldsymbol{H} + \boldsymbol{N}\right)\left[\boldsymbol{R} + \boldsymbol{H}^{\mathsf{T}}\boldsymbol{P}\boldsymbol{H}\right]^{-1}\left(\boldsymbol{H}^{\mathsf{T}}\boldsymbol{P}\boldsymbol{G} + \boldsymbol{N}^{\mathsf{T}}\right) \tag{6.11}$$

Considering the MSD system with similar sampling rates, and solving the LQR problem with $\boldsymbol{N} = 0$, then a control law of the following form is obtained:

$$\begin{bmatrix} u_1(kT) \\ u_1(kT + 3T_0) \\ u_2(kT) \\ u_2(kT + 2T_0) \\ u_2(kT + 4T_0) \end{bmatrix} = \begin{bmatrix} \boldsymbol{0} & \boldsymbol{0} & \boldsymbol{0} & \boldsymbol{0} & \boldsymbol{0} & \boldsymbol{K}_1 \\ \boldsymbol{0} & \boldsymbol{0} & \boldsymbol{0} & \boldsymbol{0} & \boldsymbol{0} & \boldsymbol{K}_2 \\ \boldsymbol{0} & \boldsymbol{0} & \boldsymbol{0} & \boldsymbol{0} & \boldsymbol{0} & \boldsymbol{K}_3 \\ \boldsymbol{0} & \boldsymbol{0} & \boldsymbol{0} & \boldsymbol{0} & \boldsymbol{0} & \boldsymbol{K}_4 \\ \boldsymbol{0} & \boldsymbol{0} & \boldsymbol{0} & \boldsymbol{0} & \boldsymbol{0} & \boldsymbol{K}_5 \end{bmatrix} \begin{bmatrix} \boldsymbol{x}_1(k) \\ \boldsymbol{x}_2(k) \\ \boldsymbol{x}_3(k) \\ \boldsymbol{x}_4(k) \\ \boldsymbol{x}_5(k) \\ \boldsymbol{x}_6(k) \end{bmatrix} \tag{6.12}$$

where $\boldsymbol{K}_{1\dots5}$ are 1×8 vectors of the form $\begin{bmatrix} k_1 & k_2 & k_3 & k_4 & k_5 & k_6 & 0 & 0 \end{bmatrix}$.

Some general comments may be made upon this control law:

Remark 6.4.A: All control signals for the entire BTP are calculated using only $\boldsymbol{x}_6(k)$. To reiterate the definition of how the signals in the model are arranged relative to one and another, the lower part of figure 4.18 is presented again as figure 6.4.
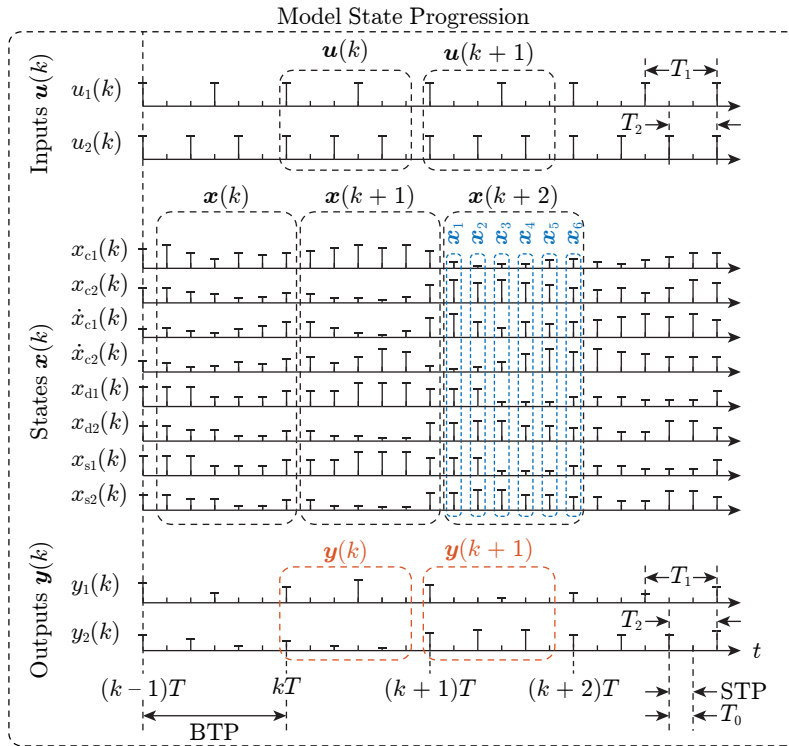
Fig. 6.4: Model signal and state progression for MSD system with similar sampling rates.

Then it may be seen that when calculating $\boldsymbol{u}(k)$, which is needed to calculate $\boldsymbol{x}(k+1)$, then $\boldsymbol{x}_6(k)$, which corresponds to the final state value of the previous BTP, is simply the newest available data (as seen from the model), why it is only logical to utilise this dataset for feedback.

However, when operating the actual system, signals will not appear as full blocks updated only at BTP time steps. The signals will appear one after another with STP time steps. Thus when calculating the control signals, e.g. for $u_1(kT + 3T_0)$ there will be newer data available than $\boldsymbol{x_6}(k)$, why it would be desirable to use the newest available data for feedback.

While this is a non-issue for a system with similar sampling rates, and a short BTP relative to the system time constants, it becomes problematic when the BTP becomes long, since this results in potentially very old data being used to generate future control signals.

Remark 6.4.B: Implementing the lifted control law given in equation 6.12 is a question of implementing five parallel control laws, and then shifting between them. It may be seen that all these control laws update with a period given by the BTP, but that they are shifted relative to each other with the periods T_1 and T_2. The five control laws then have to be merged into two control laws, that update at rates of T_1 and T_2, which is basically done by switching between them.

Remark 6.4.C: That the control law only utilises six of the states in $\boldsymbol{x}_6(k)$ for feedback corresponds well with only six controllable states in the minimal realisation.

Remark 6.4.D: Araki and Yamamoto (1986), whose work the lifting approach presented in this thesis is based upon, addresses this problem by presenting a control law which utilises the output vector $\boldsymbol{y}(k)$, or equivalently $\boldsymbol{x}(k)$ and $\boldsymbol{x}(k+1)$, for feedback:

$$\boldsymbol{u}(k) = -\boldsymbol{K}\boldsymbol{y}(k) = -\boldsymbol{K}\boldsymbol{C}^{\boldsymbol{\Psi}}(\boldsymbol{U}_1\boldsymbol{x}(k+1) + \boldsymbol{U}_2\boldsymbol{x}(k)) \qquad (6.13\text{a})$$

$$\begin{bmatrix} u_1(kT) \\ u_1(kT+3T_0) \\ u_2(kT) \\ u_2(kT+2T_0) \\ u_2(kT+4T_0) \end{bmatrix} = - \begin{bmatrix} \boldsymbol{k}_{11} & \boldsymbol{0} & \boldsymbol{k}_{13} & \boldsymbol{0} & \boldsymbol{0} \\ \boldsymbol{0} & \boldsymbol{k}_{22} & \boldsymbol{0} & \boldsymbol{k}_{24} & \boldsymbol{0} \\ \boldsymbol{k}_{31} & \boldsymbol{0} & \boldsymbol{k}_{33} & \boldsymbol{0} & \boldsymbol{0} \\ \boldsymbol{k}_{41} & \boldsymbol{0} & \boldsymbol{0} & \boldsymbol{k}_{44} & \boldsymbol{0} \\ \boldsymbol{0} & \boldsymbol{k}_{52} & \boldsymbol{0} & \boldsymbol{0} & \boldsymbol{k}_{55} \end{bmatrix} \begin{bmatrix} \boldsymbol{x}_6(k) \\ \boldsymbol{x}_3(k+1) \\ \boldsymbol{x}_6(k) \\ \boldsymbol{x}_2(k+1) \\ \boldsymbol{x}_4(k+1) \end{bmatrix} \qquad (6.13\text{b})$$

The $\boldsymbol{C}^{\boldsymbol{\Psi}}$, $\boldsymbol{U}_1$ and $\boldsymbol{U}_2$ rearrange the state vector, such that the vector in equation 6.13b is obtained. Note that $\boldsymbol{C}^{\boldsymbol{\Psi}}$ is defined in a manner such that all eight states of the MSD system are presented in each block vector in the output vector $\boldsymbol{y}(k)$. This leads to double feedback of states, which should be further considered upon using this control law. Furthermore, it may be seen that the gain matrix, which is presented here as it is defined in the source material, has a form which utilises the newest available data in the output vector, without using future data, which is not yet available.

This control law appears to be a suitable candidate for use in a lifted system. However, no procedure for determining the controller gains is provided, why other approaches are investigated.

The result of implementing a control law of the form given in equation 6.12 in the Simulink simulation model of the MSD system is shown in figure 6.5. In the simulation, the system is initialised with an initial position of 0.1 m and the controller then drives the masses back to their natural resting positions, such that all states are driven to zero. In general it may be concluded that a control law derived based on a multirate model of the system is able to stabilise the system. Furthermore, the control law only utilises data from the previous BTP, which, as may be seen from the figure, poses no problem in the case of similar sampling rates, wherein the BTP is significantly less than the time constants of the system (BTP $= 0.3$ s, $\tau_1 = 22$ s and $\tau_2 = 16.7$ s). The fact that all control signals are calculated for one BTP at a time is evident in the zooms, where the control signal fed into the system is seen as the bold line, which is merged from the individual signals in the lifted control vector $\boldsymbol{u}(k)$.
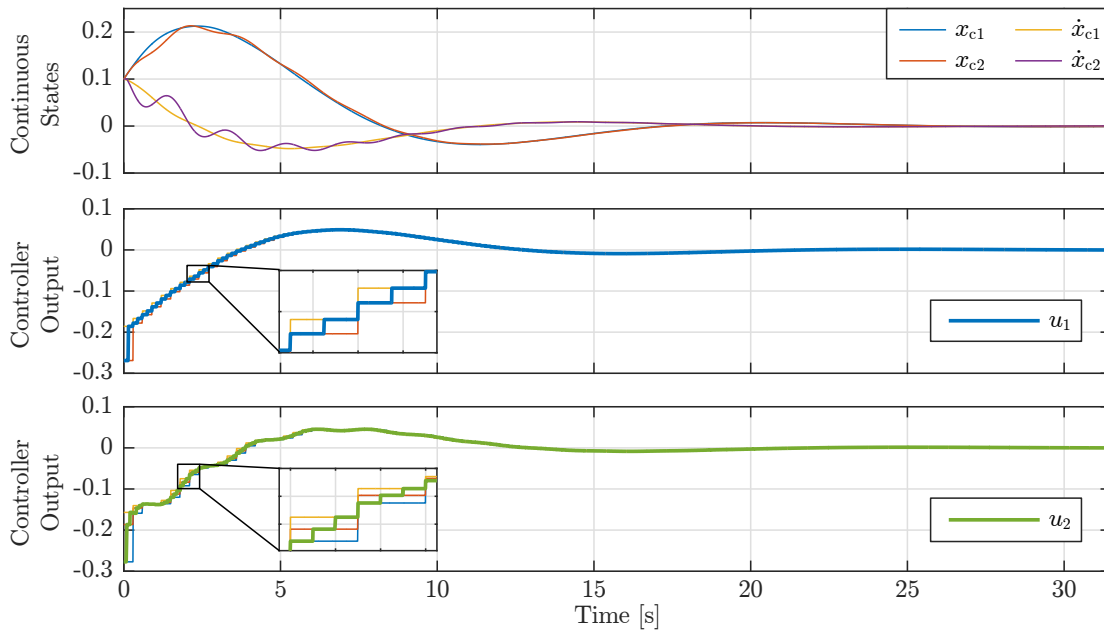
Fig. 6.5: State feedback control of MSD simulation model with similar sampling rates, with control law based on multirate model.

Considering the case of vastly different sampling rates, with a BTP of $T = 3.15\,\text{s}$, then compared to the time constants the BTP is still much smaller, and thus based on this, the update rate of the control signal is fast enough to control the system. However, all control signals are still based on data from the previous BTP, and thus upon nearing the end of the current BTP, control signals are based on data from as much as $3.15\,\text{s}$ ago, which seems unnecessary when sensors could provide data rates in the hundreds or thousands of Hertz.

Despite these considerations, a BTP update control law has been implemented on a system with similar sampling times of $T_1 = 0.15\,\text{s}$ and $T_2 = 0.126\,\text{s}$, but with a near irrational ratio, thereby resulting in a long BTP of $T = 3.15\,\text{s}$, and a short STP of $T_0 = 0.006\,\text{s}$. This BTP is equal to the vastly different sampling rate examples. The result of such a simulation, using the same initial conditions as previously, is shown in figure 6.6, where it may be seen that the response of the continuous states is practically no different than the case of similar sampling rates, where the BTP is significantly shorter. In the figure, the BTP update rate of the control signals is more readily apparent than in the previous figure. Furthermore it may be observed that while the update rate of the signal is very low, the merged control signal is relatively smoothly varying.

Remark 6.4.E: It is chosen to use similar sampling times with near irrational ratio, as an alternative to vastly different sampling times. This is because the use of vastly different sampling times requires $\boldsymbol{G^\Psi}$ and $\boldsymbol{H^\Psi}$ dimensions to become exceedingly large, why the use of sparse matrices to reduce memory consumption must be utilised when calculating a lifted LTI model. However, the use of sparse matrices
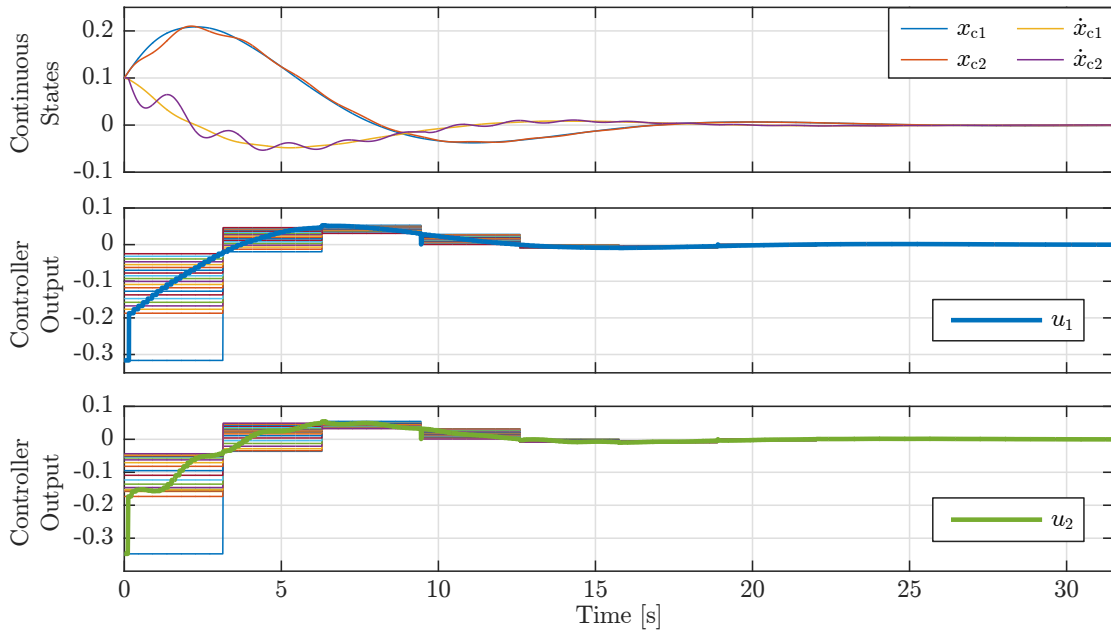
Fig. 6.6: State feedback control of MSD simulation model with similar sampling rates, but with a near irrational ratio resulting in a long BTP, and with control law based on the multirate model.

excludes the use of MATLAB's *dlqr* command, since it is not programmed to handle such matrices. Thus, similar sampling times with near irrational ratio is chosen instead, since this does not require the use of sparse matrices.

Remark 6.4.F: With regard to not having full rank in the controllability matrix, which may normally be problematic when utilising full state feedback, the simulation results appear to prove that the full rank requirement can be relaxed to simply having rank equal to the number of continuous and discrete states, $\gamma + \delta$, for a minimal realiation of the lifted system.

While control with only a BTP update rate appears to work rather well for the considered example of a deterministic model and deterministic control, there are some concerns regarding how well BTP control works when unmodelled disturbances act on the system.

In this section, it was attempted to utilise the standard tools for LQR controller design, which are available in MATLAB. This was done under the hypothesis that given a LTI model, then it would be possible to derive suitable controllers using conventional methods. While this was possible, controllers were limited to using data from the previous BTP for feedback. Thus the next section will consider the possibilities for using a control law, which calculates control signals with the newest available data.

6.4.2 Feedback with Newest Available Data

To be able to utilise the newest available data for feedback, some different options have been considered. The ideas generally revolve around reformulating the cost function or general form of the control law, and adapting the proof in appendix D.2 to derive a new

control law. To be able to do this, the proof is first summarised:

1. Given a cost function $J(k)$ and a guess for the form of the minimum cost value $\breve{J}(k)$, then the cost function may be rewritten to three terms: A quadratic term in $\boldsymbol{x}(k)$, a quadratic term in $\boldsymbol{u}(k)$ and a cross term in $\boldsymbol{x}(k)$ and $\boldsymbol{u}(k)$ (bilinear term).
2. The control law is then derived by finding the point at which the cost gradient is zero, and subsequently solving for $\boldsymbol{u}(k)$.
3. The control law may then be inserted into the cost function from step 1 to write it as a quadratic form in only $\boldsymbol{x}(k)$.
4. The minimum must hold for any $\boldsymbol{x}(k)$, why this can be omitted. The remaining matrix equation is known as the discrete-time Riccati equation, which must be solved, such that the feedback gains can be evaluated numerically.

Two possibilities for deriving something suitable are evident. The first is to derive a control law of the form (output feedback):

$$\boldsymbol{u}(k) = -\boldsymbol{K}\boldsymbol{y}(k) \tag{6.14}$$

The second is to analytically derive a control law in the conventional form together with an analytical expression for $\boldsymbol{K}$, and then attempt to reconstruct and factor separate terms for $\boldsymbol{U}_1\,\boldsymbol{x}(k+1) = \boldsymbol{x}_{1\ldots5}(k+1)$ and $\boldsymbol{U}_2\,\boldsymbol{x}(k) = \boldsymbol{x}_6(k)$. In essence the two possibilities should be equivalent, and they should both allow utilising the newest available data, such that they reach the same end result, however, their execution differ, why both possibilities in the following are investigated.

6.4.2.A Output Feedback

Considering the first option, the task is now to derive an output feedback control law. Typically this is done when not all states are measured, why only some states can be used for feedback. However, the reason for doing it in this case is that $\boldsymbol{y}(k)$ includes information from $\boldsymbol{x}(k+1)$, which makes it possible to use newer data for feedback.

The proof is attempted adapted by using the cost function $J(k)$ and minimum guess $\breve{J}(k)$ given as:

$$J(k) = \sum_{i=k}^{\infty} \left[\boldsymbol{y}(i)^{\mathsf{T}}\boldsymbol{Q}\boldsymbol{y}(i) + \boldsymbol{u}(i)^{\mathsf{T}}\boldsymbol{R}\boldsymbol{u}(i)\right] \qquad \breve{J}(k) = \boldsymbol{y}(k)^{\mathsf{T}}\boldsymbol{P}\boldsymbol{y}(k) \tag{6.15}$$

The proposed cost function differs from the one in the proof, that this one weighs the output instead of the states.

Then like in the proof, the cost function may be rewritten to:

$$J(k) = \boldsymbol{y}(k)^{\mathsf{T}}\boldsymbol{Q}\boldsymbol{y}(k) + \boldsymbol{u}(k)^{\mathsf{T}}\boldsymbol{R}\boldsymbol{u}(k) + J(k+1) \tag{6.16}$$

When substituting the minimum guess into the cost function in step 1 of the derivation, $\boldsymbol{y}(k+1)$ is obtained in the right hand side:

$$\boldsymbol{y}(k)^{\mathsf{T}}\boldsymbol{P}\boldsymbol{y}(k) = \boldsymbol{y}(k)^{\mathsf{T}}\boldsymbol{Q}\boldsymbol{y}(k) + \boldsymbol{u}(k)^{\mathsf{T}}\boldsymbol{R}\boldsymbol{u}(k) + \boldsymbol{y}(k+1)^{\mathsf{T}}\boldsymbol{P}\boldsymbol{y}(k+1) \tag{6.17}$$

By shifting the output equation, either in the conventional form or in the one with $\boldsymbol{x}(k+1)$, by one sample, $\boldsymbol{y}(k+1)$ may be eliminated from the equation. However, this also introduces the term $\boldsymbol{u}(k+1)$ to the equation. Simply shifting and inserting the control law in equation 6.14 merely reintroduces $\boldsymbol{y}(k+1)$, why this cannot be done. Alternatively, $\boldsymbol{u}(k+1)$ may be eliminated by solving the output equation explicitly for $\boldsymbol{u}(k)$ as a function of $\boldsymbol{x}(k)$. This has the effect of double defining the control law, and furthermore it rewrites the output feedback control law to a state feedback law instead. Generally this approach may then be concluded as being mathematically invalid.

Another possibility would be to attempt to write the cost function only in terms of $\boldsymbol{y}(k)$ and $\boldsymbol{u}(k)$, to do this a minimum guess of $\boldsymbol{y}(k-1)$ has been used to obtain:

$$\boldsymbol{y}(k-1)^{\mathsf{T}}\boldsymbol{P}\boldsymbol{y}(k-1) = \boldsymbol{y}(k)^{\mathsf{T}}\boldsymbol{Q}\boldsymbol{y}(k) + \boldsymbol{u}(k)^{\mathsf{T}}\boldsymbol{R}\boldsymbol{u}(k) + \boldsymbol{y}(k)^{\mathsf{T}}\boldsymbol{P}\boldsymbol{y}(k) \tag{6.18}$$

However, this results in $\boldsymbol{u}(k-1)$ appearing in the left hand side, when the cost function is rewritten to obtain the Riccati equation, why this approach also is concluded invalid.

Textbooks such as Lewis et al. (2012) also offer procedures for designing output feedback controllers. The procedures are, however, limited to considering systems with output equations of the form $\boldsymbol{y}(k) = \boldsymbol{C}\boldsymbol{x}(k)$, why it is not directly applicable to lifted systems, which include a direct transfer term in the output as illustrated in equation 6.2.

6.4.2.B Reconstructing $\boldsymbol{U}_1\,\boldsymbol{x}(k+1)$ and $\boldsymbol{U}_2\,\boldsymbol{x}(k)$

Reconstructing $\boldsymbol{U}_1\,\boldsymbol{x}(k+1)$ and $\boldsymbol{U}_2\,\boldsymbol{x}(k)$ in the control law is equivalent to using an output feedback control as illustrated in the following:

$$\boldsymbol{u}(k) = -\boldsymbol{K}\boldsymbol{y}(k) = -\boldsymbol{K}\boldsymbol{C}^{\boldsymbol{\Psi}}\left(\boldsymbol{U}_1\boldsymbol{x}(k+1) + \boldsymbol{U}_2\boldsymbol{x}(k)\right) \tag{6.19}$$

However, it may be simpler to reconstruct the terms for a state feedback law, than to derive an output feedback law.

Using the same cost function as in equation 6.15 with a minimum guess $\check{J}(k)$ of the form:

$$\check{J}(k) = \boldsymbol{x}(k)^{\mathsf{T}}\boldsymbol{P}\boldsymbol{x}(k) \tag{6.20}$$

Then step 1 of the derivation may be completed by inserting the output equation and state equation to rewrite the cost function to:

$$J(k) = \boldsymbol{x}(k)^{\mathsf{T}}[\boldsymbol{C}_{\mathrm{c}}^{\mathsf{T}}\boldsymbol{Q}\boldsymbol{C}_{\mathrm{c}} + \boldsymbol{G}^{\mathsf{T}}\boldsymbol{P}\boldsymbol{G}]\boldsymbol{x}(k) + \boldsymbol{u}(k)^{\mathsf{T}}[\boldsymbol{D}_{\mathrm{c}}^{\mathsf{T}}\boldsymbol{Q}\boldsymbol{D}_{\mathrm{c}} + \boldsymbol{R} + \boldsymbol{H}^{\mathsf{T}}\boldsymbol{P}\boldsymbol{H}]\boldsymbol{u}(k) \tag{6.21}$$
$$+ 2\boldsymbol{u}(k)^{\mathsf{T}}[\boldsymbol{D}_{\mathrm{c}}^{\mathsf{T}}\boldsymbol{Q}\boldsymbol{C}_{\mathrm{c}} + \boldsymbol{H}^{\mathsf{T}}\boldsymbol{P}\boldsymbol{G}]\boldsymbol{x}(k)$$

Step 2 is then carried out by taking the derivative with respect to $\boldsymbol{u}(k)$ to obtain:

$$\frac{\delta J(k)}{\delta \boldsymbol{u}(k)} = 2\left[\boldsymbol{D}_{\mathrm{c}}^{\mathsf{T}}\boldsymbol{Q}\boldsymbol{D}_{\mathrm{c}} + \boldsymbol{R} + \boldsymbol{H}^{\mathsf{T}}\boldsymbol{P}\boldsymbol{H}\right]\boldsymbol{u}(k) + 2\left[\boldsymbol{D}_{\mathrm{c}}^{\mathsf{T}}\boldsymbol{Q}\boldsymbol{C}_{\mathrm{c}} + \boldsymbol{H}^{\mathsf{T}}\boldsymbol{P}\boldsymbol{G}\right]\boldsymbol{x}(k) \tag{6.22}$$

Now there are two possibilities, the first is to reconstruct $\boldsymbol{U}_1\,\boldsymbol{x}(k+1)$ and $\boldsymbol{U}_2\,\boldsymbol{x}(k)$ (or $\boldsymbol{y}(k)$), and the second is to solve directly for $\boldsymbol{u}(k)$, as is normally done.

Consider the first option, by rearranging equation 6.22 it is possible to write the term $\boldsymbol{D}_{\mathrm{c}}^{\mathsf{T}}\boldsymbol{Q}\,\boldsymbol{y}(k)$, and then subsequently solve for the remaining $\boldsymbol{u}(k)$ to obtain analytic expressions for the feedback gains, and a control law that utilises both the newest available data with the $\boldsymbol{y}(k)$ term and also data from the previous BTP with the $\boldsymbol{x}(k)$ term:

$$\boldsymbol{u}(k)=-[\boldsymbol{R}+\boldsymbol{H}^{\mathsf{T}}\boldsymbol{P}\boldsymbol{H}]^{-1}\boldsymbol{H}^{\mathsf{T}}\boldsymbol{P}\boldsymbol{G}\,\boldsymbol{x}(k)+[\boldsymbol{R}+\boldsymbol{H}^{\mathsf{T}}\boldsymbol{P}\boldsymbol{H}]^{-1}\overbrace{[\boldsymbol{D}_{\mathrm{c}}^{\mathsf{T}}\boldsymbol{Q}\boldsymbol{D}_{\mathrm{c}}\boldsymbol{u}(k)+\boldsymbol{D}_{\mathrm{c}}^{\mathsf{T}}\boldsymbol{Q}\boldsymbol{C}_{\mathrm{c}}\boldsymbol{x}(k)]}^{\boldsymbol{D}_{\mathrm{c}}^{\mathsf{T}}\boldsymbol{Q}\,\boldsymbol{y}(k)} \quad \text{(6.23a)}$$
$$= -\boldsymbol{K_x}\boldsymbol{x}(k) - \boldsymbol{K_y}\boldsymbol{y}(k) \quad \text{(6.23b)}$$

Remark 6.4.G: The authors acknowledge that this control law may not be mathematically valid, since $\boldsymbol{y}(k)$ is also a function of $\boldsymbol{u}(k)$. Thereby making the equation implicit in $\boldsymbol{u}(k)$.

To use this control law, the solution to the corresponding Riccati equation $\boldsymbol{P}$ must be obtained, such that the feedback gains can be calculated. Typically the Riccati equation is derived by inserting the control law into the cost function, and then writing all the terms as quadratic terms on $\boldsymbol{x}(k)$. This is, however, not possible with the above control law, why the second option is now considered. Alternatively, and more conventionally, the cost function derivative (equation 6.22) may be explicitly solved for $\boldsymbol{u}(k)$:

$$\boldsymbol{u}(k) = - [\boldsymbol{D}_{\mathrm{c}}^{\mathsf{T}}\boldsymbol{Q}\boldsymbol{D}_{\mathrm{c}}+\boldsymbol{R}+\boldsymbol{H}^{\mathsf{T}}\boldsymbol{P}\boldsymbol{H}]^{-1}[\boldsymbol{D}_{\mathrm{c}}^{\mathsf{T}}\boldsymbol{Q}\boldsymbol{C}_{\mathrm{c}}+\boldsymbol{H}^{\mathsf{T}}\boldsymbol{P}\boldsymbol{G}]\boldsymbol{x}(k) \quad \text{(6.24)}$$

Remark 6.4.H: If equation 6.23 had been used, terms with $\boldsymbol{y}(k)$ would have appeared when attempting to derive the Riccati equation. Of course, these could have been eliminated with the output equation, however, this would merely introduce terms with $\boldsymbol{u}(k)$ instead.

Solving the output equation explicitly for $\boldsymbol{u}(k)$ would doubly define the control law, thereby conflicting with the definition in equation 6.23.

Using this control law (equation 6.24) and the output equation, then it is possible to arrive at the following Riccati equation:

$$0 = \boldsymbol{G}^{\mathsf{T}}\boldsymbol{P}\boldsymbol{G} - \boldsymbol{P} + \overbrace{\boldsymbol{C}_{\mathrm{c}}^{\mathsf{T}}\boldsymbol{Q}\boldsymbol{C}_{\mathrm{c}}}^{\tilde{\boldsymbol{Q}}}$$
$$- \big(\boldsymbol{G}^{\mathsf{T}}\boldsymbol{P}\boldsymbol{H}+\underbrace{\boldsymbol{C}_{\mathrm{c}}^{\mathsf{T}}\boldsymbol{Q}\boldsymbol{D}_{\mathrm{c}}}_{\tilde{\boldsymbol{N}}}\big)\big[\underbrace{\boldsymbol{D}_{\mathrm{c}}^{\mathsf{T}}\boldsymbol{Q}\boldsymbol{D}_{\mathrm{c}}+\boldsymbol{R}}_{\tilde{\boldsymbol{R}}}+\boldsymbol{H}^{\mathsf{T}}\boldsymbol{P}\boldsymbol{H}\big]^{-1}(\boldsymbol{D}_{\mathrm{c}}^{\mathsf{T}}\boldsymbol{Q}\boldsymbol{C}_{\mathrm{c}}+\boldsymbol{H}^{\mathsf{T}}\boldsymbol{P}\boldsymbol{G}) \quad \text{(6.25)}$$

It may be noted that if the $\tilde{\boldsymbol{Q}}$, $\tilde{\boldsymbol{R}}$ and $\tilde{\boldsymbol{N}}$ definitions are made, then the above equation is the same as the standard Riccati equation given in equation 6.11. The matrices $\tilde{\boldsymbol{Q}}$, $\tilde{\boldsymbol{R}}$ and $\tilde{\boldsymbol{N}}$ should be real and symmetric like their regular counterparts. This has the advantage of making it possible to simply solve the equation by use of MATLAB's *dlqr* command using the redefinitions to obtain $\boldsymbol{P}$, then $\boldsymbol{K_y}$ may be calculated:

$$\boldsymbol{K_y} = [\boldsymbol{R}+\boldsymbol{H}^{\mathsf{T}}\boldsymbol{P}\boldsymbol{H}]^{-1}\boldsymbol{D}_{\mathrm{c}}^{\mathsf{T}}\boldsymbol{Q} = \begin{bmatrix} \boldsymbol{0} & k_{12} & \boldsymbol{0} & k_{14} & k_{15} \\ \boldsymbol{0} & k_{22} & \boldsymbol{0} & k_{24} & k_{25} \\ \boldsymbol{0} & k_{32} & \boldsymbol{0} & k_{34} & k_{35} \\ \boldsymbol{0} & k_{42} & \boldsymbol{0} & k_{44} & k_{45} \\ \boldsymbol{0} & k_{52} & \boldsymbol{0} & k_{54} & k_{55} \end{bmatrix} \quad \text{(6.26)}$$

where each entry in the matrix is a 1×8 vector. A comment may be made upon on the form of $\boldsymbol{K_y}$:

Remark 6.4.I: Remembering the definition of $\boldsymbol{u}(k)$ and $\boldsymbol{y}(k)$:

$$\boldsymbol{u}(k) = \begin{bmatrix} u_1(kT) \\ u_1(kT + 3T_0) \\ u_2(kT) \\ u_2(kT + 2T_0) \\ u_2(kT + 4T_0) \end{bmatrix} \qquad \boldsymbol{y}(k) = \begin{bmatrix} y_1(kT) \\ y_1(kT + 3T_0) \\ y_2(kT) \\ y_2(kT + 2T_0) \\ y_2(kT + 4T_0) \end{bmatrix} \tag{6.27}$$

It may be seen that the form of $\boldsymbol{K_y}$ causes newer data than is available to be used when calculating the control signals. Consider e.g. $u_1(kT)$ then the signal $y_1(kT + 3T_0)$ is used, which occurs three STPs later in time, than the control signal. Thus it would be impossible to actually implement this control law, which also corresponds well with the lack of mathematical validity noted previously.

As such, it is concluded that it is difficult, if not impossible, to derive a control law, which utilises the newest available data, for a lifted multirate system with use of the standard LTI control theory tools available in MATLAB.

Remark 6.4.J: The control design difficulties arise from wishing to derive a control law with an update rate equal to the STP based on a LTI model which updates at a rate equal to the BTP. In essence, what has been attempted done, is to derive a periodically time-varying control law from a time-invariant plant model. Achieving this could potentially be possible by re-deriving the LQR proof, while using a STP summation instead of the BTP summation currently used.

As mentioned in section 4.3, there appears to be a large number of papers regarding the multirate control of lifted systems, and also papers utilising optimal control formulations. Therefore it is concluded that it is definitely possible to obtain an optimal controller with the desired properties, it is, however, beyond the scope of this thesis to derive these tools, why they are not further considered.

Despite a strong desire to use a control law which calculates control signals using the newest available data, figure 6.6 shows that a BTP control law works rather well. Furthermore, the controller used for that simulation was derived by simply using MATLAB's *dlqr* command, i.e. a standard LTI controller design algorithm. Thus, while it is concluded that STP control is difficult to achieve using standard LTI design algorithms, it is also concluded that BTP control works rather well.

This chapter set out to investigate the applicability of conventional MIMO control and analysis tools on the multirate MSD system. It is generally found that the use of such tools can to some extend be applied to analyse a lifted multirate system, and that optimal control could be used to formulate a control law capable of controlling the MSD system at a feedback update rate of the BTP. Next chapter seeks to establish if these conclusions furthermore are valid for the $10\,\text{kW}$ multirate DFPT model.

Multirate DFPT Control

The purpose of this chapter is to investigate the applicability of the LTI control and analysis tools, which were applied to the MSD system, to the 10 kW DFPT. This includes a brief study of the applicability of the RGA on the DFPT multirate model and the design of a deterministic optimal controller. The designed controller is hereafter implemented in the 10 kW non-linear DFPT simulation model to establish if the developed control works as a proof of concept. Lastly, the application of the unified non-minimal realisation method to the 5.4 MW DFPT and subsequent control thereof is discussed.

7.1 Applicability of MIMO Analysis to 10 kW DFPT

In the previous chapter it was concluded that MIMO analysis of a lifted multirate system is somewhat difficult to apply, because of couplings across time, which cannot automatically be accounted, and which do not always make sense (e.g. backwards in time). However, it still appears to be possible to extract some information by selectively extracting relevant transfer function from the transfer function matrix.

Consider now the case of the DFPT. To obtain a linear multirate model of this system, it is necessary to transform all time-domain equations to the spatial-domain. The question now becomes, how does this transformation affect frequency response analysis tools.

Generally, the transformation transforms the time axis to an angle axis:

$$ t \quad \xrightarrow[\text{Transformation}]{\text{Spatial}} \quad \theta \tag{7.1} $$

In fact, by investigating the transformation as used in equation 5.18 to transform the rotor dynamics, and in equation 5.20 for the linear case. Then it may be seen that in the linear case, the transformation is actually simply just a scaling of the coefficients by a constant scalar. Scalar products are by definition commutative, and thereby it does not matter if the transformation is applied before or after mathematical operations are performed. It is merely up to the engineer to do whatever is convenient in the given situation.

Thus, by this argument, it is argued that frequency response analysis is equally applicable for spatial-domain models as it is for time-domain models, only that the x-axis uses a different angular frequency as illustrated by:

$$ f = \frac{1}{T} \left[\frac{\text{rad}}{\text{s}} \right] \quad \xrightarrow[\text{Transformation}]{\text{Spatial}} \quad f_{\theta_{\text{BTP}}} = \frac{1}{\theta_{\text{BTP}}} \left[\frac{1}{\text{rad}} \right] \tag{7.2} $$

Remark 7.1.A: The reader should be careful to distinguish the angular frequency as defined for frequency reponse analysis of spatial-domain models from the conventional term angular frequency. As the conventional term merely represents the angular velocity in the time-domain.

To investigate this scaling of the x-axis, the continuous linear time-domain dynamics and linear spatial-domain dynamics of the rotor (equations 3.1 and 5.20) are considered in a transfer function form:

$$\text{Time-domain} \quad \dot{\omega}_r = \frac{1}{J_{rp}}\left(\tau_r - d_r\,\omega_r - \frac{\tau_p}{\eta_p}\right) \quad \Rightarrow \omega_r = \frac{1}{s + \frac{d_r}{J_{rp}}}\left(\frac{1}{J_{rp}}\tau_r - \frac{1}{J_{rp}\eta_p}\tau_p\right) \tag{7.3}$$

$$\text{Spatial-domain} \quad \omega_r' = \frac{1}{J_{rp}\,\omega_{r0}}\left(\tau_r - d_r\omega_r - \frac{\tau_{p,lin}}{\eta_p}\right) \Rightarrow \omega_r = \frac{1}{s + \frac{d_r}{J_{rp}\,\omega_{r0}}}\left(\frac{1}{J_{rp}\,\omega_{r0}}\tau_r - \frac{1}{J_{rp}\,\omega_{r0}\,\eta_p}\tau_{p,lin}\right) \tag{7.4}$$

Then by examining the location of the pole for either case, then it may be seen that in the time-domain the pole is located at $s = -d_r/J_{rp}$, but that in the spatial-domain the pole has been shifted to $s = -d_r/(J_{rp}\,\omega_{r0})$. That is to say the pole has simply been multiplied by the factor $1/\omega_{r0}$, and thus the x-axis scaling is also simply this factor. It may be noted that this pole location is merely equal to the A_r constant in the rotor dynamics state equation given by equation 5.21.

In chapter 5 it was concluded that the time-domain response of the multirate DFPT model corresponded well with the simulation model. Having clarified whether or not frequency response analysis is applicable to spatial-domain models, it now becomes interesting to investigate if the model behaves correctly in the angular frequency domain. To be able to consider the frequency response of the multirate DFPT model, it is necessary to define which states are present in the output. Therefore the first output is chosen as the rotor speed, such that $y_1 = \omega_r$, and the second output is chosen as the pressure, such that $y_2 = \Delta p$. Having decided upon the outputs, it is possible to form the 5×5 transfer function matrix $\boldsymbol{G}_{10kW}$ by use of equation 6.3.

Cross Couplings in the DFPT:
Considering the DFPT, it has an evident cross coupling in the pump torque/flow/pressure relationship, in that the torque affects the rotor velocity, thereby affecting the pump flow, which subsequently affects the pressure. The control engineer may therefore be interested in analysing the degree of these cross couplings for a DFPT such that an appropriate control algorithm can be chosen. Therefore, this section seeks to investigate if the RGA can be applied to the DFPT multirate model formulated by utilising the UNMR method to yield information regarding cross couplings. As such, it is important to note that the RGA is not applied to the 10 kW DFPT with the objective of qualitatively or quantitatively analysing cross coupling nor is it to determine an appropriate control structure.

To apply the RGA, the BTP to BTP transfer function are extracted from the 5×5 transfer function matrix $\boldsymbol{G}_{10kW}$ and by omitting the across time transfer functions, the matrix 2×2 dimensional $\boldsymbol{G}_{10kW13}$ may be formed. The results of calculating the RGA for this matrix are presented in figure 7.1.
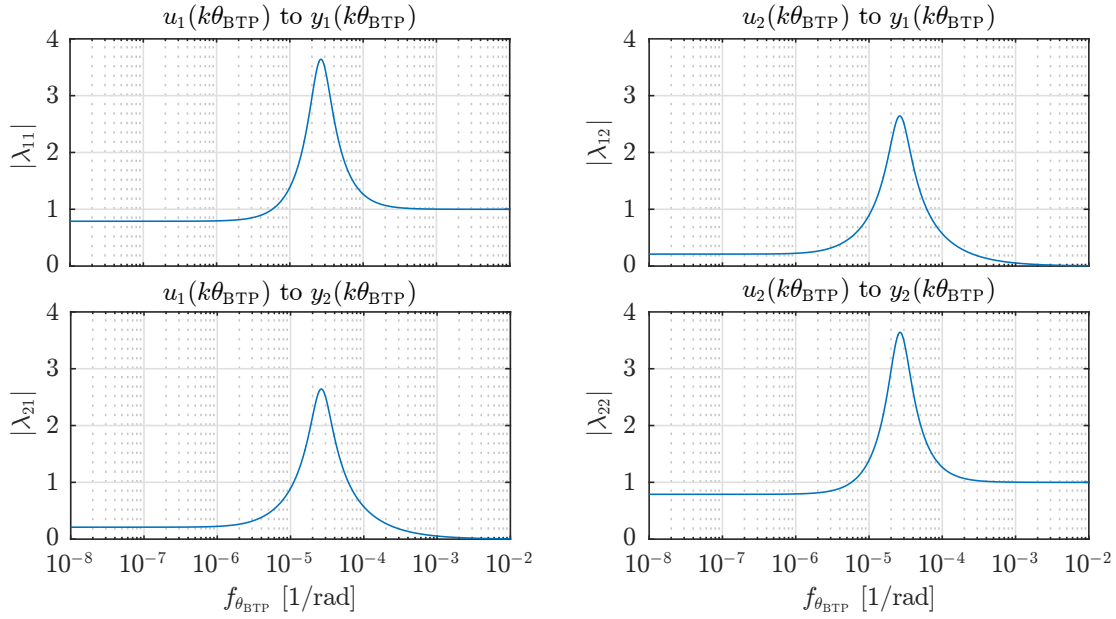
Fig. 7.1: Magnitude of RGA elements in $\mathbf{\Lambda}(\boldsymbol{G}_{10\mathrm{kW}13})$ as function of frequency.

The RGA elements appear normal and similar to what would be expected for a system with cross couplings. The magnitude of the x-axis is small, however, this is explained by the location of the poles associated with the HPL and rotor dynamics, which in the continuous case are at $s = 8.2 \times 10^{-6}$ and $s = 1.21.2 \times 10^{-5}$, meaning that all dynamics should be in the vicinity of these locations, which corresponds very well with the figure. The upper limit of the x-axis is given by the Nyquist frequency in the spatial-domain, which may be found by considering BTP which in section 6.3 was defined to represent the sampling period of the multirate model. Thus, the Nyquist frequency may then be defined similarly as for time-domain models:

$$f_{\theta_{\mathrm{BTP}},\mathrm{Nyq}} = \frac{f_{\theta_{\mathrm{BTP}}}}{2} = 0.08\,\mathrm{rad}^{-1} \tag{7.5}$$

Remark 7.1.B: To perform this analysis a new linearisation point, wherein $\alpha_{\mathrm{p0}} = 0.5$, was chosen. If this had not been done, there would be no mutual correlation between the torque and pressure, which would mean that the system would have appeared completely decoupled.

Remark 7.1.C: The authors acknowledge that arguments with regard to a discrete model have been made by considering properties of the continuous equations. While not strictly correct, it is still correct in the sense that it gives some idea of the true result, and since the purpose is not qualitative or quantitative analysis, this is deemed sufficient.

With regard to analysis of cross couplings, it gives essential information to the control engineer when determining an appropriate control structure. In this thesis, however, only true MIMO optimal full state feedback control is considered why the actual information

151

which can be drawn from an RGA analysis is not of interest. Based on the presented, it is, however concluded that meaningful information regarding the degree of cross couplings in a DFPT can be drawn from applying the RGA to the multirate DFPT model produced by the UNMR method. The RGA is not directly applicable due to certain input-output dynamics described by the multirate model do not make physical sense which the RGA is not directly capable of accounting for. However, applying the RGA to the BTP to BTP transfer functions from the given transfer function matrix makes it possible to analyse the degree of cross couplings of a DFPT.

Gain in the DFPT:
In the previous chapter it was shown that, unlike the RGA analysis, it was not possible to just merely extract the BTP to BTP transfer functions, and thereby obtain meaningful results. For this reason the SVD analysis of the DFPT is omitted.

7.2 Optimal Control of 10 kW DFPT

This section investigates the applicability of the conventional deterministic LQR control problem to the 10 kW DFPT multirate model. It is important to note that the objective of the designed full state feedback control is not to obtain high performing reference tracking. This is due to the fact that the 10 kW DFPT is a purely fictive system why the tracking performance is of no interest. Instead, the controller is designed as a proof-of-concept to determine if the conventional deterministic LQR control problem can be applied to the 10 kW DFPT multirate model produced by the UNMR method, such that, a controller which is able to control the DFPT is obtained.

Considering full state feedback control of the DFPT, then the controllability of the system is important. Calculating the controllability matrix for the multirate model of the 10 kW DFPT, then like for the MSD system, the rank of this matrix is equal to 9. Considering the states in the individual subvectors of the lifted state vector, then there are $\gamma = 2$ CDE states, $\delta = 4$ DDE states and finally $\sigma = 3$ SHE states. Given that the SHE states describe the idealised sampling operations, then these states are generally uncontrollable, since they describe direct input-output couplings. This leaves 6 states in the last subvector, which is also the number of controllable states in a minimal realisation (by MATLAB's *minreal* command) of the multirate 10 kW DFPT model. Accounting for the remaining 3 controllable states in the lifted multirate model is difficult.

However, the relaxed controllability requirement, stating that the number of controllable states of a minimal realisation should be equal to $\gamma + \delta$, is still considered valid, why the 10 kW DFPT is considered controllable.

The following weighting matrices are defined for the LQR optimal control problem applied to the 10 kW DFPT multirate model:

$$\boldsymbol{Q} = \mathrm{diag}\left(\boldsymbol{Q_1}, \boldsymbol{Q_1}, \boldsymbol{Q_1}, \boldsymbol{Q_1}, \boldsymbol{Q_1}, \boldsymbol{Q_1}\right) \qquad\qquad \boldsymbol{R} = \boldsymbol{I} \qquad\qquad (7.6)$$

where $\boldsymbol{R}$ is a 5×5 matrix corresponding in dimension to the lifted input vector, and similarly $\boldsymbol{Q}$ is a 54×54 matrix, or equivalently 6×6 block matrix, corresponding to the

lifted state vector. The matrices $\boldsymbol{Q_1}$ on the diagonal of $\boldsymbol{Q}$ are 9×9 weighting matrices for the individual subvectors in the lifted state vector, and are defined as:

$$\boldsymbol{Q_1} = \text{diag}\,(50000, 10000, 0, 0, 0, 0, 0, 0, 0) \tag{7.7}$$

Thereby the rotor speed and pressure states are weighted at every time step in the lifted vector.

Using these matrices in the conventional state feedback formulation of the optimal LQR problem as presented in section 6.4.1 yields a BTP update control law of the form given in equation 6.12.

Remark 7.2.A: The weighting matrices are not determined with the objective of obtaining high performance reference tracking but merely as a proof of concept to conclude if the resulting optimal control law is able to control the HPL pressure and rotor speed in the downscaled 10 kW DFPT.

The resulting control law is implemented in the 10 kW DFPT non-linear simulation model in order to evaluate its applicability. The simulation is run by setting a rotor speed reference and pressure difference reference of $\omega_r{}^* = 1500$ rpm and $\Delta p^* = 350$ bar, respectively. The full state feedback LQR optimal control problem is, however, by default, designed to drive all states to zero. Thus in order to track ω_r and Δp to the stated non-zero references, the control law is reformulated such that the ω_r and Δp states are transformed to a rotor speed error and pressure difference error defined as $e_{\omega_r} = \omega_r{}^* - \omega_r$ and $e_{\Delta p} = \Delta p^* - \Delta p$, respectively. The defined error states are multiplied with the entries in the gain matrix $\boldsymbol{K}$ which are computed for driving the original states, ω_r and Δp, to zero. It can be shown that this reformulation is equivalent to implementing a pre-compensator gain to the states which are to be driven to a non-zero reference.

Similar to the multirate control law implemented for the MSD system, the resulting gain matrix $\boldsymbol{K}$ has five rows meaning that five control signals are computed. Only two inputs ($u_1 = \alpha_p{}^*$ and $u_2 = \alpha_m{}^*$) can be given to the DFPT why the five calculated controller outputs must be merged to two control signals. This is done in a similar manner to the MSD system by switching between the five calculated controller outputs at specified instants.

As presented in chapter 5, the linear multirate model of the 10 kW DFPT is developed in the spatial-domain (DD pump angle). This also means that when the control law is to be implemented in the simulation model, the discrete triggering must be done as function of the DD pump angle. This discrete triggering applies to both the BTP sampling of all states at the angular instant of θ_{BTP} and the switching between the five computed control signals in order to obtain $\alpha_p{}^*$ and $\alpha_m{}^*$.

The simulation results are plotted in figure 7.2 where the simulation is initiated with a rotor speed of $\omega_r = 1515$ rpm and a HPL to LPL pressure difference of $\Delta p = 360$ bar. Furthermore, the only exogenous input affecting the DFPT is the rotor torque which is set constant to $\tau_r = 64.3$ Nm corresponding to the linearisation reactive pump torque in the linear model. As the exogenous input is constant, it is considered deterministic. The

top plots show the rotor speed and pressure difference response and the lower plot show
the inputs to the DSMs, α_p^* and α_m^*.
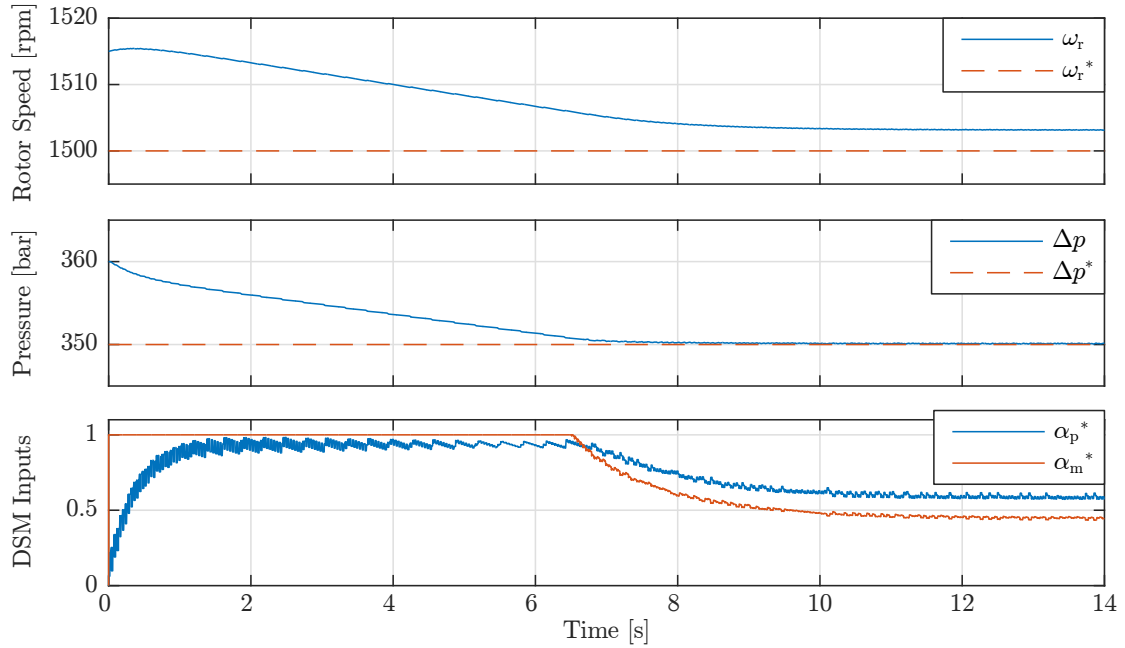
Fig. 7.2: Simulation results of rotor speed and HPL to LPL pressure difference from 10 kW DFPT
simulation model including DSM inputs.

α_m^* is seen to saturate at a value of 1 which is due to a saturation block located at
both DSM inputs in the simulation model. This is done in order to avoid integrator
wind-up in the DSMs as they include a discrete-time integrator. The simulation results
show that the implemented full state feedback controller is able to track the rotor speed
and pressure difference to a steady state value. The rotor speed, however, has a steady
state error. The steady state error could potentially have been removed by introducing
an integral term but has not been done as high tracking performance is not the objective
in this thesis. It should furthermore be noted that the exogenous input τ_r is constant
why the controllers ability to reject stochastic disturbances is not evaluated.

Based on the simulation it can be concluded that the BTP update control law calculated
from the optimal LQR problem is able to control the 10 kW DFPT. This does, however,
not imply that the control law can also be implemented on the full scale 5.4 MW DFPT.
The 5.4 MW DFPT has significantly more chamber activation per BTP which means
that the controlled outputs may vary more within a BTP which could lead to a problem
since the state feedback is only sampled at intervals equal to the BTP. In addition to
this, the rotor torque is in the 5.4 MW DFPT a function of the exogenous wind speed
input which is highly varying which could also pose a problem due to the state feedback
BTP sampling rate. Thus the next section seeks to preliminary investigate the control
challenges regarding implementation on the 5.4 MW DFPT.

7.3 Challenges upon Application to 5.4 MW DFPT

During the development of a multirate modelling method, application to the 10 kW DFPT and control hereof, a number of challenges are identified. These challenges will in this section be discussed, primarily, in relation to the 5.4 MW DFPT.

Deterministic Control of DFPT with Stochastic Exogenous Inputs:
Considering the task of applying the UNMR method to the full scale 5.4 MW DFPT, only deterministic control with an update rate equal to the BTP has been considered. This has been shown to work acceptably in the case of deterministic systems, but how well does this type of control work for systems under the influence of stochastic exogenous inputs. A wind turbine is an example of such a system, since it has the wind speed as a stochastic exogenous input for the drivetrain. To be able to properly discuss the potential problems of applying a deterministic control algorithm for controlling a WT DFPT, the reader must be familiar with the basics of WT operation why a brief introduction to this is presented in the following. WT operation is further elaborated in appendix B.

For a WT, the objective is generally to maximise power production without exceeding the ratings and limitations of the various subsystems (e.g. drivetrain or pitch system). A measure for optimal power production is the Tip-Speed Ratio (TSR), which is defined as a ratio between the wind speed and rotor speed. WT operation can be divided into several regions which are constrained by the wind speed acting on the WT. For wind speeds above the cut in wind speed and below the rated speed, an optimum TSR is obtained by controlling the DD pump reactive torque. For wind speeds above the rated value, both the blade pitch angle and reactive pump torque is used for obtaining an optimum TSR. This thesis is not concerned with the control of the pitch system why only the region in which an optimum TSR is obtained by controlling the reactive pump torque is considered. An optimum TSR is in this region obtained by maintaining a combination of optimal values of the reactive pump torque and rotor speed. This region is referred to as region II when it is considered in the rotor speed frame and is depicted in figure 7.3.
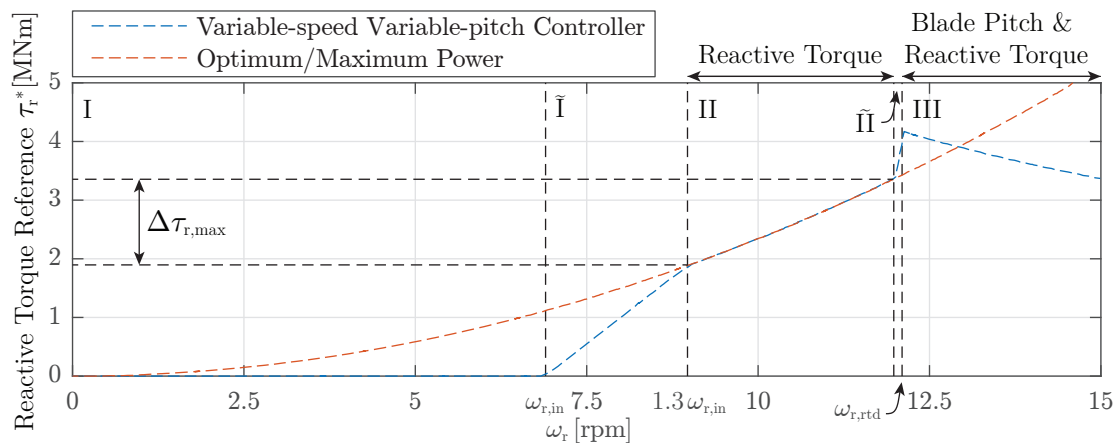
Fig. 7.3: Ideal reactive torque for maximum power production as a function of ω_r for the 5.4 MW WT. Overlaid are the operating regions for the WT. Based on data in Jonkman et al. (2009)

Despite that the TSR depends directly on the rotor speed, the control task of obtaining an optimum TSR is considered as a torque control problem, as this can be shown to avoid utilisation of the highly fluctuating wind speed as feedback. Instead a reactive torque reference is calculated as a function of the desired rotor speed which means that the rotor speed is indirectly controlled to obtain an optimum TSR and hereby maximising the power production.

In addition to the controlled reactive torque, it is desired to control the pressure in the HPL connecting the DD pump and motor to a constant reference since the highest efficiency of the DDMs are obtained when they are operated at their rated pressure. The concern of applying the control law which utilises state feedback only updated at intervals equal to the BTP on the 5.4 MW DFPT is then, how much these controlled outputs can vary during the BTP. As the the exogenous wind speed directly affects the rotor speed which is to be indirectly controlled, by accelerating it, it is desired to investigate the maximum acceleration of the rotor due to the wind, such that the maximum change in speed during one BTP can be calculated.

The change in rotor speed, $\Delta\omega_{\mathrm{r}}$, will be calculated by the use of equation 7.8:

$$\Delta\omega_{\mathrm{r}} = \dot{\omega}_{\mathrm{r,max}}\, T_{\mathrm{max}} \tag{7.8}$$

Where $\dot{\omega}_{\mathrm{r,max}}$ and T_{max} are the maximum acceleration and maximum time period for a BTP, respectively. These maximum values will be found based on an engineering assessment of what changes might occur within region II operation of a WT (see figure B.5). The results of this investigation should not be seen as conclusive, but merely as a well founded indication on the result of implementing the BTP control on the 5.4 MW DFPT.

To determine the maximum time period of a BTP, the sampling scheme of the 5.4 MW DFPT is established. The sampling rates of the DD pump and motor are determined using equations 5.4 and 5.14 respectively.

$$\theta_1 = \frac{2\,\pi}{N_{\mathrm{pc}}\,N_{\mathrm{cr}}\,N_{\mathrm{l}}} = \frac{2\,\pi}{25\cdot 4\cdot 16} = 0.0039\,\mathrm{rad} \quad \theta_2 = \frac{2\,\pi}{N_{\mathrm{mc}}\,N_{\mathrm{ec}}} = \frac{2\,\pi}{7\cdot 6} = 0.1496\,\mathrm{rad} \tag{7.9}$$

With the sampling periods for the system defined, it is now possible to define a STP of $\theta_0 = 1.87 \times 10^{-4}\,\mathrm{rad}$ and a BTP of $\theta_{\mathrm{BTP}} = \pi\,\mathrm{rad}$.

Remark 7.3.A: The number of STPs per BTP is then found to $N = 16800$, and with a combined state vector of dimension $n \times 1 = 77 \times 1$ (for detail see table 5.1) it should be evident that the double expanded state vector of dimension $Nn \times 1$ will become exceedingly large along with the lifted system matrices $\boldsymbol{G}^{\boldsymbol{\Psi}}$ and $\boldsymbol{H}^{\boldsymbol{\Psi}}$. This is why, as previously stated, sparse matrices must be utilised when forming the discrete state-space model of the 5.4 MW DFPT using the UNMR method.

In figure B.5 the operating range of the rotor speed in region II is seen to be $[1.3\omega_{\mathrm{r,in}}\ 0.99\omega_{\mathrm{r,trd}}] = [8.97\ 11.98]$ rpm and from this, the BTP period initially determined in the spatial-domain can be transformed into the time-domain. This yields a BTP range of $[T_{\min}\ T_{\max}] = [\theta_{\mathrm{BTP}}/\omega_{\mathrm{r,in}}\ \theta_{\mathrm{BTP}}/\omega_{\mathrm{r,trd}}] = [2.5\ 3.34]$ s.

A measure of the maximum rotor acceleration, $\dot{\omega}_{r,max}$, is estimated by considering Newton's second law of rotation:

$$\dot{\omega}_{r,max} = \frac{\Delta\tau_{r,max}}{J_{rp}} \tag{7.10}$$

where $\Delta\tau_{r,max} = \tau_{rtd} - \tau_{min}$. These torques represent the maximum and minimum rotor torque within region II operation. Defining $\Delta\tau_{r,max}$ as such, assumes that the exogenous wind speed changes instantaneously from the cut-in wind speed, v_{in}, to the rated wind speed, v_{rtd}, which for the purpose of these calculation might be considered a conservative choice. τ_{rtd} and τ_{min} are calculated using equation B.5 and associated parameters from table B.1, and hereby is $\dot{\omega}_{r,max}$ found to:

$$\dot{\omega}_{r,max} = \frac{3.28\,\text{MNm} - 1.84\,\text{MNm}}{38.8\,\text{Mkg m}^2} = 0.0372\,\text{rad/s}^2 \tag{7.11}$$

Having determined $\dot{\omega}_{r,max}$ and T_{max}, equation 7.8 is applied to calculate the maximum change in rotor speed and is found to $\Delta\omega_r = 1.19\,\text{rpm}$. Comparing this deviation with the rotor speed within the operating range of $[8.97\ 11.98]\,\text{rpm}$ it is significant in size, which gives way for the following remarks:

Remark 7.3.B: The calculated maximum change in rotor speed should be considered as the absolute maximum change which is expected to occur during a BTP, as it is based upon the most conservative choices of BTP time period and rotor acceleration. In fact, the calculated maximum rotor speed change is based on the assumption that the WT is operated at the cut-in wind speed when a BTP is initiated followed by an immediate increase in the wind speed to rated its value, resulting in a constant acceleration of $\dot{\omega}_{r,max}$ during the entire BTP.

Considering BTP control of a DFPT it is clear that a constant acceleration during an entire BTP is highly unlikely, because as the rotor speed start to increase so will the pressure in the HPL. This will effectively result in an increased reactive pump torque creating a negative change in rotor acceleration. Thus, this confirms that the preceding calculations are based upon most conservative assumptions.

Remark 7.3.C: A rotor speed change of $\Delta\omega_r = 1.19\,\text{rpm}$ during a BTP, could potentially result in a significant control error when the feedback control states are updated, and depending on the magnitudes of the controller gains, this might lead to stability issues.

Remark 7.3.D: In the preceding calculations only the exogenous wind input's effect on the rotor velocity has been considered, however, the second control output, Δp will also be affected. The effect the exogenous wind input has on Δp should also be investigated before the applicability of BTP control is determined for the 5.4 MW DFPT.

The preceding calculations indicate that implementing the BTP updated control law on the 5.4 MW DFPT might pose stability issues. However, the calculations are based on an engineering assessment why tests on a simulation model must be conducted in order to finally conclude the applicability of the BTP control.

Control of Uncontrollable States:

In contrast to the 10 kW DFPT, where the controlled outputs are the rotor speed and pressure, the controlled outputs for the 5.4 MW DFPT are the pump torque, τ_r and the HPL to LPL pressure difference, Δp. However, the torque is a SHE state, which for idealised sample-and-hold operations results in the state being non-minimal and therefore also uncontrollable, why reference tracking of this state is likely not possible. It may therefore be necessary to reformulate the model using an integral state, where the integral state is equal to the torque tracking error.

Including an integral state in a standard discrete state-space formulation is considered relatively trivial, and the procedure is well established in literature, e.g. Ogata (1987). However, when an integral state must be included in the lifted multirate state-space model, the procedure is no longer well documented and it gives rise to the following considerations:

Remark 7.3.E: If it is intended to apply a BTP control strategy, for the 5.4 MW DFPT, where the state feedback is only sampled at a rate equal to the BTP, it also makes sense to define the integral state at the identical BTP update rate. Defining the integral states at a sampling period equal to the BTP in which the multirate model is described, should make it possible to include an integral state without reformulating the UNMR method, but merely by adding an additional step. It is expected that a textbook procedure of how to include an integral state as the one described in Ogata (1987) should be somewhat directly applicable.

Remark 7.3.F: Alternatively, if the challenges of designing a control law which utilises control feedback updates at a rate of the STP, it would make sense to introduce an integral state with a STP update rate. Doing so, however requires a reformulation of the UNMR method, as an integral state must be defined in the expanded state vector also referred to as the combined state vector. This procedure is more time consuming and a textbook approach will not directly be applicable, however, to the authors knowledge there is no indication that it should not be possible.

Time-domain Implementation of Spatial-domain Control Law:

In the spatial-domain there are no challenges with regard to implementing the control law, nor are there any problems in the time-domain when the rotor speed is constant. But when the rotor speed changes, the time until a BTP is completed will vary. During a BTP $N_1 = \theta_{\text{BTP}}/\theta_1$ and $N_2 = \theta_{\text{BTP}}/\theta_2$ displacement inputs to the DD pump and DD motor can be given, respectively. In the angle-domain these are fully synchronised, but in the time-domain, then if the pump speed is decreasing the motor will potentially require more than N_2 displacement inputs before the BTP is completed and the pump has had N_1 displacement inputs. As the BTP is described by the pump angle, the problem only concerns inputs given to the DD motor. The issues related to updating the motor's control signal is attempted illustrated in figure 7.4.

Figure 7.4 is based upon how the spatial-domain control law is implemented in the 10 kW non-linear simulation model, which is merely one of multiple implementation approaches. The figure displays the relation between the angular position of the 10 kW DFPT DDMs,
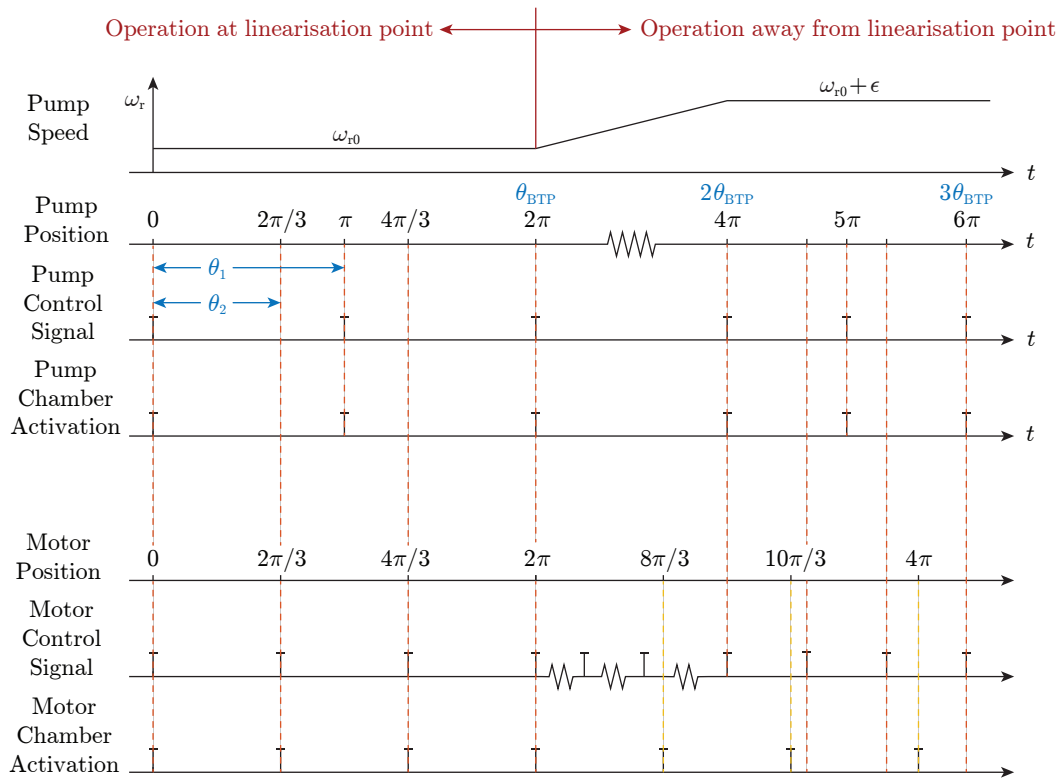
Fig. 7.4: The figure depicts the control update challenges related to the time-domain implementation of the spatial-domian control law. In scenario 1, depicted to the left, the DD pump is operated at the multirate model's operating point. In scenario 2, depicted to the right, the DD pump speed has increased and is above the multirate model's operating point. The figure's control rates and associated chamber activations are based upon the downscaled 10 kW DFPT.

and the associated control signal update rates along with the chamber activation sequence. In the first scenario, seen in the left part of the figure, the speed of DDMs are operated in the multirate model's operating point, why control updates and associated chamber activations are synchronised. In the second scenario, seen in the right part of the figure, the DD pump is operated above the multirate model's operating point. As the pump angle triggers the spatial-domain control structure, the control signal for the pump and associated chamber activations remain synchronised. However, the DD motor's control signal, which are triggered by the pump angle, and associated chamber activations are no longer synchronised. As a result the motor control signal is updated at a faster rate than the associated chamber activations, and as a result not all calculated displacement inputs will be given to DD motor during a BTP.

The use of a model based control approach means that the designed BTP control is limited by the restrictions of the developed multirate DFPT model. For the 10 kW DFPT, which exhibits similar sampling rates, this means that at each BTP update instant determined by the pump angle, three displacement inputs for the motor are calculated regardless of how many inputs the motor requires during the following BTP. Assuming that BTP control is based on a model derived from the UNMR method, the issues related to

159

a non-uniform number of motor displacement inputs per BTP, can only be addressed during the time-domain implementation of the spatial-domain control law. Upon this implementation the following considerations have been made:

Remark 7.3.G: For each BTP, N_2 displacement inputs have been calculated for the DD motor when utilising the spatial-domain control law. The challenges, however, lies in when these displacement inputs should be updated:

- The displacement input could be updated at a rate of θ_2 triggered by the DD pump angle. This would result in the update being equally spaced within a BTP as depicted in figure 7.4. If the pump is operated at a speed below the multirate model's operating point, it could result in the same displacement input being given to the motor multiple times before the pump angle triggers an update in the motor displacement.
- The displacement input could be updated at a rate of θ_2 triggered by the DD motor angle. If the pump is operated at a speed below the multirate model's operating point, this could result in more than N_2 inputs being required for the DD motor during a BTP. This, however, leads to an issue when the N_2+1 input must be given as no such input has yet been calculated. An argument could be made that above the N_2 input, all displacement inputs are zero as the utilised spatial control law is restricted to a maximum of N_2 potential chamber activations during a BTP. Alternatively, the N_2^{th} displacement input could be held for the remainder of the BTP or the displacement input sequence could be repeated until the BTP is completed.

This concludes the discussion of the identified challenges related to the currently utilised DFPT multirate modelling and BTP updated control law. The discussion has taken basis in the experience acquired while working with the modelling and control of the downscaled 10 kW DFPT. Furthermore, these challenges have been put into perspective by considering the full scale 5.4 MW DFPT in the aim of emphasising the remaining challenges related to model based control of a utility-scale DFPT using the developed non-minimal realisation method. The next chapter will continue the discussion, however the focus will no longer be limited to control related challenges but aims to discuss all aspects of the work presented in this thesis, and additionally suggest future topics of studies within the area of model based control of a DFPT.

8

Discussion

The purpose of this discussion is to reflect on some of the choices taken throughout the work documented in this thesis, and their possible alternatives. The discussion is separated into three parts. Each part reflects on a different part of the thesis, such that the first part considers the task of DFPT modelling, the second part the analysis and control of lifted models and finally the third part considers alternative methods for deriving models and model based controllers together with discussing the methodical approach used in the project. This discussion should be seen as an addition to the discussions regarding results and application of methods, which have been presented throughout the report. The final part of the chapter is concluded with some considerations regarding the future work and application of the UNMR method to the 5.4 MW DFPT.

DFPT Modelling:

The purpose of deriving a linear multirate model of a DFPT was to obtain a tool, which could be used for analysing system properties with regard to control and furthermore also for designing controllers. For the model to be useful for this, three desirable characteristics were defined, which may briefly be summarised as:

- MIMO representation with transfer characteristics for all input and output combinations in the system.
- Linear time-invariant (or angle-invariant in the case of the DFPT).
- State-space formulation.

Generally the proposed UNMR method satisfies all of these requirements. However, the lifting approach, which the UNMR methods makes use of, is necessary to obtain an LTI description, increases the number of inputs and outputs of the LTI model by combining inputs occurring at different points in time in a single vector. Thereby the lifting approach somewhat violates the first requirement, since some of the transfer functions will be acausal since they describe input-output combinations backward in time. The lifting approach is, however, the only possibility for deriving a LTI model. As such, when retrospectively considering the desirable characteristics with the experience of applying conventional MIMO analysis tools to the model in mind, they appear conflicting to some extent.

Despite this, the proposed UNMR method does produce a LTI model of a multirate system, which includes both continuous, discrete and sample-and-hold elements by use of the lifting technique. Something which hitherto appears not to be described in literature. This is seen as a major result of this thesis.

Considering the DFPT, to apply the UNMR method, the activation rates in the DDMs must be uniform, which they are not for variable-speed operation in the time-domain. Obtaining uniform rates is possible by transforming all time-domain equations to the spatial angle-domain, where the angle between chamber activations is constant. The

employed spatial-transformation casts all states with respect to the pump shaft position. This does not introduce any problems in the case of constant pump speed, but consider the case of varying pump speed, then when seen from the time-axis, the pump shaft position axis stretches linearly, whereas the motor shaft position axis remains fixed. When combining the different linear descriptions of the system elements, the motor axis and pump axis are in effect superimposed on one and another. From a mathematical point of view this is somewhat problematic since now the motor states are described relative to an axis which they do not belong to. On the other hand, the purpose of the model is to serve as a linear tool for analysis and controller design, and such models are often only accurate representations in the vicinity of the linearisation point, and there is no reason that such arguments should not be applicable for the spatial-transformation as well.

As such, it has been shown that application of the UNMR method to the DFPT is possible, and when comparing simulation results, it may be seen that simulation results have good coherence with a time-domain simulation model of the DFPT in the vicinity of the linearisation point. This is seen as a major result of the thesis, as not only has the multirate modelling challenge been solved, but the individual solutions to the subchallenges of DFPT modelling have been combined to form a working linear angle-invariant model of the DFPT.

Consider the desire of having a globally valid, but not necessarily globally accurate, linear model, then the spatial-transformation must be reconsidered. The transformation as defined in equations 5.17 and 5.18 results in non-linear equations when applied, since all states are then divided by the pump speed. An alternative, which has not been investigated, is to consider these fractions as the states of the equations, then as seen from the fractions the equations are linear. This, however, appears to become problematic when considering the spatial-domain rotor dynamics, since how can it be possible to describe the dynamics of the pump/rotor speed state, when it is already included in all other states. Should the global validity of the model be an absolute requirement, then it appears that it is not merely possible to apply the spatial-transformation as done in this thesis, and a different or additional coordinate transformation would likely be necessary.

Nonetheless, the model is accurate at the operating point, and valid in the vicinity thereof as shown in section 5.5. Therefore the modelling approach is considered successful, especially when considering the fact that the purpose of such a model is merely to act as a mathematical tool for correctly describing the input-output relations of a system both in the time-domain, or more accurately the angle-domain, and the frequency domain.

Controller Design and Linear Analysis using Lifted Model:
The task of controlling a DFPT, may be likened to the task of controlling a power electronic back-to-back converter, which has one side connected to the grid and the other connected to a variable-speed motor. In these situations the converters are usually controlled in a decentralised strategy under the assumption of a stiff DC-link voltage. The purpose of the grid-side converter is then typically to control the DC-link such that it is maintained at some constant value, and the purpose of the motor-side converter

is then to control the motor with respect to some control objective, typically torque or speed. Such a decentralised control algorithm has previously been successfully utilised by the authors wherein the pressure level, Δp, may be likened to the DC-link voltage. The obvious disadvantage of such a decentralised strategy is that no conclusions with regard to stability can be made without assuming a constant pressure level. Furthermore, this absolutely requires that the pressure level is one of the controlled outputs, which may not necessarily be possible in the case of desiring motor torque control to satisfy grid connection requirements. This is where this thesis takes its starting point, the desire to analyse and control the system without making significant assumptions regarding the controlled outputs. With the hypothesis of the general applicability of conventional, well known and well documented tools offered by linear control theory to any LTI model, this thesis set out to derive a model, and the results of this have just been discussed.

The model produced by the UMNR method makes no requirements with regard to what the controlled outputs should be, and thus it is merely up to the engineer to choose something suitable.

The aforementioned acausal input-output combinations produced by the lifting approach limit the direct applicability of analysis tools. This limitation occurs since the tools have been derived for non-lifted systems with only causal input-output combinations. It may be possible to reformulate the tools to account for these couplings, however, this thesis has been concerned with model development and application of already existing tools, and not the derivation of new tools. As such, the application of analysis tools has been focused on how the conventional tools may be used to extract useful information, instead of focusing on complete re-derivations.

Determining to which extent the conventional tools may be applied to a lifted model, required extensive investigation of the results, and did not prove to be a trivial task, which contrasted greatly with the assumption, the conducted work was initiated by. However, having clarified the necessary modifications and limitations in interpretation upon application of the tools, the utilisation of them is fairly trivial in that it is exactly like applying them to non-lifted systems.

Considering the control of a lifted model. Then by the lifting approach a conventional discrete state-space model is produced with a single slow rate equal to the BTP. Designing state feedback controllers using such a model obviously limits the feedback signals to being updated once per BTP. This slow rate BTP is generally of no problem in the case of deterministic systems, but if the system has stochastic exogenous inputs, then this slow update rate of the feedback has potential for becoming problematic. While this was not an unexpected issue, it has proven to be more demanding than anticipated to derive a control law, which utilises a faster update rate, while limited to utilising standard linear quadratic regulator algorithms available in MATLAB.

With regard to control and analysis of the DFPT. It was determined that the spatial-transformation does not impose any limits on frequency response analysis, and subsequently it was determined that the derived 10 kW DFPT model appears to behave as expected in the frequency domain. The spatial-transformation does, however, introduce

a challenge when combined with the lifting approach. In the time-domain, the number of chamber activations per second in the DD pump and motor is somewhat similar in the 5.4 MW DFPT, since the vastly different operating speeds compensate for the vastly different number of chambers. However, upon transforming to the spatial-domain, the number of activations per revolution is of different order of magnitudes for the two DD machines. This causes the number of STPs per BTP to become very large, such that the dimensions of the lifted vectors and matrices become excessively large, whereby the computer memory consumption is increased to the point that it exceeds the memory available in a state-of-the-art personal computer. The challenge of memory consumption could potentially be handled by utilising a minimal realisation of the multirate model. This is possible since only the continuous and discrete states in the last subvector remain after applying MATLAB's *minreal* command, and these correspond exactly with the states which are utilised for feedback in the control law. All remaining states simply have a zero gain associated with them, why the gains for the minimal realisation are the same as for the model produced by the UNMR method.

The spatial-transformation inadvertently results in all control updates being triggered as a function of the pump shaft position. The challenges related to this and varying pump speed were extensively discussed in the previous chapter, with regard to the time-domain implementation of a spatial-domain control law.

Alternative Solutions and Approaches:
The objective of this thesis was to determine a suitable method for obtaining a LTI model of a DFPT which includes both continuous and discrete elements, whereto the conventional control theory tools may be applied. It may then be argued that while this has been satisfied (although somewhat limited with regard to analysis), the solution to this problem has highlighted a number of underlying issues, which indicate that obtaining a linear time-, or angle-, invariant model is not an optimal solution with regard to DFPT modelling and control.

Expanding this thesis' horizon to including linear time-variant models would remove the necessity of the lifting approach and thereby also acausal input-output combinations. The derivation of a time-varying model would be relatively easy for a reader familiar with the work in this thesis. Consider the transition equations derived in step 3 of the UNMR method, here all transitions are derived starting from the last subvector in the previous BTP. If instead a time-variant model is to be obtained, then it is simply a question of deriving the transitions starting from the previous STP instead. While simple to derive, time-variant models introduces the challenge of switching between periodically varying models and their associated control laws. Furthermore, how conventional control theory tools can be applied to periodically time-varying models must be considered. Is it merely possible to apply them piecewise per STP in a BTP, and how to handle the possibility of a very large number of STPs per BTP, whereby this approach quickly becomes unpractical. Additionally, while time-variant models would be relatively simple to derive, they would still be subject to the limitations of the spatial-domain transformation, why this would not be more applicable than for the UNMR method.

Hitherto unpublished work by Pedersen et al. (2016a) seems to indicate that hybrid modelling approaches can describe the DFPT, but that the derivation of control laws based on such models might be difficult. This is a topic which has not been considered by the authors, since the goal was here to derive LTI type models.

Finally the methodical approach for the project has resulted in challenges related to lifted LTI type models and the spatial-transformation only surfacing after already having derived multirate models for both the MSD and DFPT. If an alternative chronological order of conducting the presented work had been utilised, the challenges related to analysis and control of lifted models could potentially have been revealed at an earlier stage, which would have allowed the authors to choose a different modelling approach, potentially changing to time-variant descriptions. However, as mentioned time-variant descriptions would, in addition to being subject to switching challenges, still be subject to the spatial-domain transformation. Thereby, having changed the chronological order, the challenges related to the spatial-transformation would have remained hidden until a later stage in the project work. So while the order could have been changed to discover some things at an earlier stage, the end result would necessarily not be significantly changed.

Having discussed the proposed UNMR method and the challenges related to its application, it may generally be concluded that the method does make it possible to derive a LTI type model of a multirate system with continuous and discrete elements, which may easily occur when multiple sensors with different bandwidths are utilised, and this is seen as a major result of the thesis.

However, while this is possible, the limitations associated with combining the UNMR method and the spatial-transformation are more encompassing than anticipated. Problem free implementation of a multirate spatial-domain control law necessitates fixed-speed operation of the two machines. This is in contrast to what the spatial-transformation was originally intended for, which was exactly to allow variable-speed operation. Thus, before proceeding to applying the UNMR method to the 5.4 MW DFPT, it is the recommendation of the authors that future work should further investigate the spatial-transformation to obtain problem free implementation of the control, and furthermore also to perform an in-depth literature study to determine how STP rate controllers can be designed using lifted BTP rate models.

Conclusion

This thesis set out to answer the problem of deriving a linear time-invariant (LTI) multi-rate model of a utility-scale wind turbine digital fluid power transmission (DFPT) with the purpose of analysis and controller design utilising conventional linear control tools. The task is challenging owing to the system's two digital displacement machines (DDMs), which operate with unequal and non-uniform rates in the time-domain, and which act upon the continuous time-domain pressure and rotor dynamics.

The underlying hypothesis supporting this work, was that given a LTI model, the tasks of analysis and controller design should prove to be somewhat trivial, and easy to carry out for any engineer accustomed to multivariable linear control theory.

To break down the problem into more manageable subtasks, a linear mass spring damper system was introduced, and used for development of a new unified non-minimal realisation (UNMR) method for deriving a LTI multirate model. Regarding the UNMR method for modelling multirate systems a number of conclusions are made:

- The UNMR method combines Kalman and Bertram (1959), who describe any kind of sampled-data system with continuous, discrete and sample-and-hold elements, and Araki and Yamamoto (1986), who describes a method for deriving an LTI model of a multirate system with only continuous elements by the lifting approach.

- The UNMR method produces a LTI model, by lifting the individual signals into a vector encompassing all signals in a single common time period (the basic time period (BTP)). Thereby, the UNMR method combines multiple fast-rate signals into a single slow-rate signal and thus it is possible to derive a LTI model of a multirate system.

With respect to the control properties and applicability of conventional control and analysis tools, on a model produced by the UNMR method, some conclusions may be made:

- A lifted model can never attain full rank in the controllability matrix. This is a consequence of how a lifted model per definition is not a minimal realisation. However, it was generally found that the full rank requirement may be relaxed to having rank equal to the number of continuous and discrete states in the minimal realisation of the multirate model.

- For analysing cross couplings in a multiple-input multiple-output (MIMO) system the relative gain array (RGA) is commonly used. Since the input and output vector in the developed multirate model contain entries which are shifted in time relative each other, then the transfer function matrix contains input-output relations describing dynamics both forward and backward in time. The functions backward in time are acausal and do not make physical sense. Since the RGA is only defined for conventional causal continuous or discrete systems, it is concluded that it cannot

be directly applied.

However, it was generally found possible to extract the causal BTP to BTP transfer functions from the matrix, and perform the analysis and obtain realistic results.

- For analysing the gain of a MIMO system the singular value decomposition (SVD) is commonly used. For the same reason the RGA is not directly applicable, it is concluded that the SVD cannot be directly applied. In contrast to the RGA analysis, the causal BTP to BTP transfer functions could not be used to obtain meaningful results from a SVD analysis.

  However, it was found that calculating the SVD for the full transfer function matrix, did yield the correct maximum singular value, while the minimum value did not appear to have any physical meaning. Thus it is possible to determine the maximum gain of the system.

- Designing stable optimal linear quadratic state feedback controllers based on a lifted model for the case of a deterministic system was generally found to be possible. The feedback signals for the control law are, however, limited to updating at the BTP rate. This could pose a problem in systems where the BTP is significantly longer than the sampling times in the system and furthermore the system is influences by stochastic disturbances.

The UNMR method's applicability on a DFPT is evaluated using a downscaled 10 kW DFPT, which dynamic characteristics are similar to those of the full rate 5.4 MW DFPT. To apply the UNMR method to the DFPT, the non-uniform time-domain rates must be handled. Uniform rates are obtained by transforming all equations from the time-domain to a spatial angle-domain. Having done this, it has been shown that a multirate DFPT model can be obtained by utilising the UNMR method, and some conclusions may be drawn from the results:

- Frequency response analysis of spatial-domain models is possible.

- Deriving control laws and analysing BTP to BTP couplings for a DFPT is possible.

- Expansion to the full rating DFPT is difficult, because of a large number of states, which are only further expanded when applying the UNMR method. The large number of states necessitates the use of sparse matrices to conserve memory, which the LTI toolbox algorithms included in MATLAB are not programmed to handle.

By these conclusions, the problem statement of this thesis is considered answered. It is possible to derive a LTI multirate model of a utility-scale wind turbine DFPT, and furthermore, it is possible to apply conventional LTI multivariable control and analysis tools to the model. The tools cannot, however, be applied without taking the lifted nature of the model into consideration, which slightly limits the applicability of conventional tools. Thus, while it is possible to obtain LTI models, the derivation of them and subsequent analysis and controller design is far from trivial. It is the opinion of the authors that the task is sufficiently difficult, that other approaches to solving the DFPT modelling challenge should be considered, wherein the model is not limited to being linear.

Bibliography

Aalborg University 2016

Aalborg University (2016). *Hydrive: Hydrostatic Drive Train Transmission for Renewable Energy Applications.* On going project. URL: `vbn.aau.dk/da/projects/hydrive-hydrostatic-drive-train-transmission-for-renewable-energy-applications(2d952f9d-7b4d-4a8c-9a22-00d06d394efb).html`.

Amit 1980

N. Amit (1980). "Optimal Control of Multirate Digital Control Systems". PhD thesis. Department of Aeronautics, Astronautics, and Department of Mechanical Engineering - Stanford University. URL: `searchworks.stanford.edu/view/1010867`.

Andersen 2003

T. Andersen (2003). *Fluid Power System, Modelling and Analysis.* 2nd edition. Internally published. Institute of Energy Technology - Aalborg University.

Araki et al. 1986

M. Araki and K. Yamamoto (1986). "Multivariable Multirate Sampled-Data Systems: State-Space Description, Transfer Characteristics. and Nyquist Criterion". In: *IEEE Transactions on Automatic Control* 31.2, pp. 145–154. DOI: `10.1109/TAC.1986.1104205`.

Armstrong et al. 2006

B. S. R. Armstrong and Y. Qinghui (2006). "Multi-Level control of Hydraulic Gerotor Motors and Pumps". English. In: *Proceedings of the 2006 American Control Conference,* pp. 4619–4626. ISBN: 1-4244-0209-3. DOI: `10.1109/ACC.2006.1657450`.

Åström et al. 1984

K. J. Åström and B. Wittenmark (1984). *Computer Controlled Systems: Theory and Design.* Ed. by T. Kailath. 1st edition. Prentice Hall. ISBN: 0-13-164319-3.

Carroll et al. 2014

J. Carroll, A. McDonald, D. McMillan, and J. Feuchtwang (2014). "Offshore Availability for Wind Turbines with a Hydraulic Drive Train". In: *Proceedings of the 2014 Renewable Power Generation Conference.* URL: `pure.strath.ac.uk/portal/files/38339848/Carroll_etal_RPG2014_hydraulic_drive_train.pdf`.

Chapple et al. 2012

P. Chapple, M. Niss, and K. E. Thomsen (2012). "Wind turbines with variable hydraulic transmissions and electrically excited synchronous generators directly connected to the grid". In: *Proceedings of the ASME Symposium on Fluid Power and Motion Control.*

Danish Ministry of Climate, Energy and Building 2012

Danish Ministry of Climate, Energy and Building (2012). *DK Energy Agreement.* URL: `www.efkm.dk/sites/kebmin.dk/files/climate-energy-and-building-policy/denmark/energy-agreements/FAKTA%20UK%201.pdf`.

Echavarria et al. 2008

E. Echavarria, B. Hahn, G. J. W. van Bussel, and T. Tomiyama (2008). "Reliability

of Wind Turbine Technology Through Time". In: *Journal of Solar Energy Egineering*.
DOI: 10.1115/1.2936235.

Ehsan et al. 1997
M. Ehsan, W. H. S. Rampen, and S. H. Salter (1997). "Modeling of Digital-Displacement
Pump-Motors and Their Application as Hydraulic Drives for Nonuniform Loads."
English. In: *Journal of Dynamic Systems, Measurement, and Control (2000)* 122.1,
pp. 210–215. ISSN: 0022-0434. DOI: 10.1115/1.482444. URL: dynamicsystems.
asmedigitalcollection.asme.org/article.aspx?articleid=1408408.

Elkraft System et al. 2004
Elkraft System and Eltra (2004). *Wind Turbines Connected to Grids with Voltages
above 100 kV: Technical regulation for the properties and the regulation of wind tur-
bines*. URL: http://www.energinet.dk/SiteCollectionDocuments/Engelske%
20dokumenter/El/Grid%20Code%203.2.5%20Wind%20Turbines%20connected%
20above%20100%20kV.pdf.

Franklin et al. 1981
G. F. Franklin and J. D. Powell (1981). *Digital Control of Dynamic Systems*. Ed. by
R. C. Dorf. 1st edition. Addison-Wesley. ISBN: 0-201-02891-3.

Gayo 2011
J. B. Gayo (2011). *RELIAWIND : Reliability-focused research on optimizing Wind
Energy system design, operation and maintenance: Tools, proof of concepts, guidelines
& methodologies for a new generation*. URL: setis.ec.europa.eu/energy-research/
sites/default/files/project/docs/Publishable%20Summary%20-%20110513_
Reliawind_Final%20Publishable%20Summary%20to%20EC.pdf.

Glasson 1983
D. P. Glasson (1983). "Development and Applications of Multirate Digital Control".
In: *IEEE Control Systems Magazine* 3.4, pp. 2–8. DOI: 10.1109/MCS.1983.1104772.

Global Wind Energy Council 2015
Global Wind Energy Council (2015). *Global Wind Report*. Tech. rep. URL: www.gwec.
net/wp-content/uploads/vip/GWEC-Global-Wind-Report_2016.pdf.

Global Wind Energy Council 2016
– (2016). *Global Wind Report*. Tech. rep. URL: www.gwec.net/wp-content/uploads/
vip/GWEC_PRstats2016_EN_WEB.pdf.

Guo et al. 2016
Y. Guo and F. Liao (2016). "Design og Optimal Output Regulators for Dual-Rate
Linear Discrete-Time Systems Based on the Lifting Technique". In: *Mathematical Pro-
blems in Engineering*. DOI: 10.1155/2016/2879724.

Hahn et al. 2006
B. Hahn, M. Durstewitz, and K. Rohrig (2006). *Reliability of Wind Turbines: Experien-
ces of 15 years with 1,500 WTs*. Tech. rep. Institut fur Solare Energieversorgungstech-
nik (ISET) Verein an der Universitat Kassel. URL: renknownet2.iwes.fraunhofer.
de/pages/wind_energy/data/2006-02-09Reliability.pdf.

A. Hansen et al. 2004
A. Hansen, F. Iov, F. Blaabjerg, and L. Hansen (2004). "Review of Contemporary
Wind Turbine Concepts and their Market Penetration". In: *Wind Engineering*. DOI:
10.1260/0309524041590099.

L. H. Hansen et al. 2001a

L. H. Hansen, L. Helle, F. Blaabjerg, E. Ritchie, S. Munk-Nielsen, H. Bindner, P. Sørensen, and B. Bak-Jensen. (2001a). *Conceptual survey of Generators and Power Electronics for Wind Turbines*. Tech. rep. Risø National Laboratory, Roskilde, Denmark.

L. H. Hansen et al. 2001b

L. H. Hansen, P. H. Madsen, F. Blaabjerg, H. C. Christensen, U. Lindhard, and K. Eskildsen (2001b). "Generators and Power Electronics Technology for Wind Turbines". In: *IECON'01: The 27th Annual Conference of the IEEE Industrial Electronics Society*. DOI: `10.1109/IECON.2001.975598`.

R. H. Hansen 2013

R. H. Hansen (2013). "Design and Control of the Power Take-Off System for a Wave Energy Converter with Multiple Absorbers". PhD thesis. Department of Energy Technology, Aalborg University. ISBN: 978-87-92846-34-1.

Heemels et al. 1999

W. P. M. H. Heemels, R. J. A. Gorter, A. van Zijl, A. Van Zijl, S. Weiland, S. Weiland, M. R. Vonder, and M. R. Vonder (1999). "Asynchronous measurement and control: a case study on motor synchronization". In: *Control Engineering Practice* 7.12, pp. 1467–1482. ISSN: 0967-0661. DOI: `10.1016/S0967-0661(99)00113-6`.

Heikkila 2013

M. Heikkila (2013). "Displacement control of a mobile crane using a digital hydraulic power management system." In: *Mechatronics* 23.4, pp. 452–461. ISSN: 0957-4158. DOI: `10.1016/j.mechatronics.2013.03.009`.

Johansen et al. 2016

P. Johansen, D. B. Roemer, H. C. Pedersen, and T. O. Andersen (2016). "Discrete Linear Time Invariant Analysis of Digital Fluid Power Pump Control". In: *Journal of Dynamic System Measurement and Control, ASME*. Accepted for publication.

Johansen 2014

P. Johansen (2014). "Tribodynamic Modeling of Digital Fluid Power Motors". PhD thesis. ISBN: 978-87-92846-49-5. URL: `vbn.aau.dk/files/209376288/per_johansen.pdf`.

Jonkman et al. 2009

J. Jonkman, S. Butterfield, W. Musial, and G. Scott (2009). *Definition of a 5-MW Reference Wind Turbine for Offshore System Development*. Tech. rep. National Renewable Energy Laboratory. URL: `www.nrel.gov/docs/fy09osti/38060.pdf`.

Junker et al. 2016

P. Junker, T.-E. Lindberg, and K. B. Nielsen (2016). *Control of a 5 MW Digital Fluid Power Wind Turbine Transmission*. 3rd Semester MSc. Project at Department of Energy Technology at Aalborg University.

Kaidis 2013

C. Kaidis (2013). "Wind Turbine Reliability Prediction: A Scada Data Processing & Reliability Estimation Tool". MA thesis. Uppsala University. URL: `www.diva-portal.org/smash/get/diva2:707833/FULLTEXT01.pdf`.

Kalman et al. 1959

R. E. Kalman and J. E. Bertram (1959). "A Unified Approach To The Theory of

Sampling Systems". In: *Journal of the Franklin Institute* 267.5, pp. 405–436. DOI: 10. 1016/0016-0032(59)90093-6.

Kameda et al. 2014
T. Kameda, M. Uchida, O. Uehara, H. Dodson, A. Robertson, and W. Rampen (2014). "Hydraulic pump, method for maintaining same, and wind power generation device". Japanese. WO2014002522 A1. URL: patentscope.wipo.int/search/en/detail.jsf? docId=WO2014002522.

Lee 2006
S.-H. Lee (2006). "Multirate Digital Control System Design and its Application to Computer Disk Drives". In: *IEEE Transactions on Control Systems Technology* 14.1, pp. 124–133. DOI: 10.1109/TCST.2005.860530.

Lennevi 1993
J. Lennevi (1993). "On fluid Power Control: With Special Reference to Velocity Control of Hydrostatic Transmissions". ISBN: 9178711002. PhD thesis. Department of Mechanical Engineering, Linköping University.

Lewis 2012
F. L. Lewis (2012). *Feedback Control for Discrete-Time Systems*. URL: www.uta.edu/ utari/acs/ee5321/2013%20notes/2%20lqr%20dt%20and%20sampling.pdf.

Lewis et al. 2012
F. L. Lewis, D. L. Vrabie, and V. L. Syrmos (2012). *Optimal Control*. 3rd. Wiley. ISBN: 978-0-470-63349-6.

Li et al. 2008
H. Li and Z. Chen (2008). "Overview of different wind generator systems and their comparisons". In: *IET Renewable Power Generation* 2.2, pp. 123–138. DOI: 10.1049/ iet-rpg:20070044.

Liserre et al. 2011
M. Liserre, R. Càrdenas, M. Molinas, and J. Rodriguez (2011). "Overview of Multi-MW Wind Turbines and Wind Parks". In: *IEEE Transactions On Industrial Electronics* 58.4, pp. 1081–1095. DOI: 10.1109/TIE.2010.2103910.

MathWorks 2017
MathWorks (2017). *dlqr*. URL: www.mathworks.com/help/control/ref/dlqr.html.

NWTC Information Portal (FAST) 2016
NWTC Information Portal (FAST) (2016). *FAST: An aeroelastic computer-aided engineering (CAE) tool for horizontal axis wind turbines*. Last modified 19-March-2015. URL: nwtc.nrel.gov/FAST.

Ogata 1987
K. Ogata (1987). *Discrete-Time Control Systems*. 1st edition. Prentice Hall. ISBN: 0-13-216102-8.

Pedersen et al. 2016a
N. H. Pedersen, P. Johansen, and T. O. Andersen (2016a). "LQR Feedback Control Development for Wind Turbines Featuring a Digital Fluid Power Transmission System". In: *Proceedings of the 9th FPNI Ph.D. Symposium on Fluid Power*. DOI: 10.1115/FPNI2016-1537. URL: proceedings.asmedigitalcollection.asme.org/ proceeding.aspx?articleid=2588372.

Pedersen et al. 2016b

– (2016b). "Optimal Control of a Wind Turbine with Digital Fluid Power Transmission". Internally published at Aalborg University.

Pedersen 2016

N. H. Pedersen (2016). "Concept Identification for a Wind Turbine with a Digital Fluid Power Transmission".

Perez et al. 2013

J. N. P. Perez, F. P. G. Marquez, A. Tobias, and M. Papaelias (2013). "Wind Turbine Realiability Analysis". In: *Renewable and Sustainable Energy Reviews*. DOI: 10.1016/j.rser.2013.03.018.

Phillips et al. 2011

C. L. Phillips and J. M. Parr (2011). *Feedback Control Systems*. 5th edition. Prentice Hall. ISBN: 978-0-131-86614-0.

Poore et al. 2003

R. Poore and T. Lettenmaier (2003). *Alternative Design Study Report: WindPACT Advanced Wind Turbine Drive Train Designs Study*. Tech. rep. National Renewable Energy Laboratory. URL: nrel.gov/docs/fy03osti/33196.pdf.

Rajabhandharaks 2014

D. Rajabhandharaks (2014). "Control of hydrostatic transmission wind turbine". MA thesis. Department of Electrical Engineering at San Josè University. ISBN: 978-1-321-54788-7. URL: scholarworks.sjsu.edu/cgi/viewcontent.cgi?article=8060&context=etd_theses.

Rampen 2006

W. Rampen (2006). *Gearless Transmissions for Large Wind Turbines*. Tech. rep. Artemis Intelligent Power. URL: www.artemisip.com/wp-content/uploads/2016/03/2006-11-Gearless-Transmissions-Bremen.pdf.

Rampen et al. 1995

W. Rampen, J. Almond, and S. Salter (1995). "The digital displacement pump/motor operating cycle: experimental results demonstrating the fundamental characteristics". In: *Fluid Power Series* 7, pp. 321–332.

Reiss 2008

J. D. Reiss (2008). "Understanding Sigma-Delta Modulation: The Solved and Unsolved Issues". English. In: *Journal of the Audio Engineering Society* 56.1/2, pp. 49–64. ISSN: 1945-7006. URL: www.aes.org/e-lib/browse.cfm?elib=14375.

Roemer 2014

D. B. Roemer (2014). "Design and Optimization of Fast Switching Valves for Large Scale Digital Hydraulic Motors". PhD thesis. Department of Energy Technology, Aalborg University. ISBN: 978-87-92846-58-7.

Sasaki et al. 2014

M. Sasaki, A. Yuge, T. Hayashi, H. Nishino, M. Uchida, and T. Noguchi (2014). "Large Capacity Hydrostatic Transmission with Variable Displacement". In: *The 9th International Fluid Power Conference*. URL: www.artemisip.com/wp-content/uploads/2016/03/2014-03-24to26-9th-IFK-Aaacehn-MHI-DDT.pdf.

Schmitz et al. 2013

J. Schmitz, N. Vatheuer, and H. Murrenhoff (2013). "Hydrostatic Transmissions: A

Power Play in Wind Turbine Design". In: *Hydraulics & Pneumatics*. ISSN: 0018-814X. URL: hydraulicspneumatics.com/hydraulic-pumps-amp-motors/hydrostatic-transmissions-power-play-wind-turbine-design.

Silva et al. 2014

P. Silva, A. Giuffrida, N. Fergnani, E. Macchi, M. Cantu, R. Suffredini, M. Schiavetti, and G. Gigliucci (2014). "Performance prediction of a multi-MW wind turbine adopting an advanced hydrostatic transmission". In: *Energy*. DOI: 10.1016/j.energy.2013.11.034.

Singh et al. 2011

M. Singh and S. Santoso (2011). *Dynamic Models for Wind Turbines and Wind Power Plants*. Tech. rep. National Renewable Energy Laboratory. URL: www.nrel.gov/docs/fy12osti/52780.pdf.

Skogestad et al. 2001

S. Skogestad and I. Postlethwaite (2001). *Multivariable Feedback Control: Analysis and Design*. 2nd edition. Wiley. ISBN: 978-0-470-01168-3.

Sniegucki et al. 2013

M. Sniegucki, M. Gottfried, and U. Klingauf (2013). "Optimal Control of Digital Hydraulic Drives using Mixed-Integer Quadratic Programming". English. In: *IFAC Proceedings Volumes* 46, pp. 827–832. ISSN: 1474-6670. DOI: 10.3182/20130904-3-FR-2041.00013.

Stengel et al. 1977

R. F. Stengel and P. W. Berry (1977). "Stability and Control of Maneuvering High-Performance Aircraft". In: *Journal of Aircraft* 14.8, pp. 787–794. DOI: 10.2514/3.58854.

Tangirala et al. 2001

A. K. Tangirala, D. Li, R. S. Patwardhan, S. L. Shah, and T. Chen (2001). "Ripple-free conditions for lifted multirate control systems". In: *Auomatica* 37.10, pp. 1637–1645. DOI: 10.1016/S0005-1098(01)00116-9.

Tsutsumi et al. 2012

K. Tsutsumi, M. Shimizu, N. Caldwell, D. Dumnov, S. Laird, and V. Pappala (2012). "Wind Turbine Generator and Tidal Current Generator and Operation Method Thereof". US20120104752 A1. URL: appft1.uspto.gov/netacgi/nph-Parser?Sect1=PTO1&Sect2=HITOFF&d=PG01&p=1&u=/netahtml/PTO/srchnum.html&r=1&f=G&l=50&s1=20120104752.PGNR..

wind-turbine-models.com 2016a

wind-turbine-models.com (2016a). *Enercon E-126 7.580 (Turbine)*. URL: www.en.wind-turbine-models.com/turbines/14-enercon-e-126-7.580/picture-VWBtG9xFOe2.

wind-turbine-models.com 2016b

– (2016b). *NEG Micon NM 64/1500 (Turbine)*. URL: www.en.wind-turbine-models.com/turbines/64-neg-micon-nm-64-1500/picture-l6ZtqyAfQ6l.

wind-turbine-models.com 2016c

– (2016c). *Senvion 6.2M152 Onshore (Turbine)*. URL: www.en.wind-turbine-models.com/turbines/886-senvion-6.2m152-onshore/picture-2xGtA9Kc5ol.

wind-turbine-models.com 2016d

– (2016d). *Vestas V 164-8.0 (Turbine)*. URL: http://www.en.wind-turbine-models.
com/turbines/318-vestas-v-164-8.0.

wind-turbine-models.com 2016e

– (2016e). *Vestas V 66-1.65 (Turbine)*. URL: http://www.en.wind-turbine-models.
com/turbines/15-vestas-v-66-1.65/picture-2Jkt49JHDWV.

State of the Art Research

This appendix includes supplementary documentation on the studies conducted in order to complete the work presented in chapter 1. The intended purpose of this appendix is to supply the readers of this thesis with additional elaboration of some conclusions made during chapter 1. It furthermore presents what the authors considers relevant knowledge when a DFPT must be studied, however due to page limitations have not been allowed space in the primary part of this thesis.

The appendix covers a variety of topics, which in some way all are connected to the study of DFPT WT drivetrains. As a result this appendix is not intended to be read as a single coherent chapter, but instead as separate sections, which all serves as references to specific parts of chapter 1. This appendix includes the following sections:

A.1 WT Topologies

A. Hansen et al. (2004), L. H. Hansen et al. (2001b), Li and Chen (2008), and Singh and Santoso (2011) generally classify the drivetrain of modern utility-scale horizontal axis upwind WTs into four categories:

- **Type A:** Fixed-speed Wind Turbine
- **Type B:** Variable-slip Wind Turbine
- **Type C:** Doubly-fed Induction Generator Wind Turbine
- **Type D:** Full-converter Wind Turbine

Type A turbines operate with a fixed rotor speed, while **types B, C** and **D** are variable-speed WTs. Furthermore the general drivetrain topologies may also be classified by the power control strategy, the scale of the implemented power converter (full or partial) and if they are geared or direct-driven. Many different variations of these WT drivetrains and their control strategies exist, and it is beyond the scope of this work to classify every variation (Li and Chen 2008).

Fixed-speed and Variable-speed Topologies:

Fixed-speed turbines are generally simpler and more robust than their variable-speed counterparts. The design of fixed-speed WTs is inherently limited to only obtain maximum aerodynamic efficiency at one wind speed, as such they operate at less than optimum in real world conditions with varying wind speeds. Variable-speed turbines which usually employ some form of power converter to allow for variable speed operation. They are, in contrast to fixed-speed designs, designed to operate efficiently over a wide range of wind speeds, by adjusting the rotor speed for optimal wind power extraction. (A. Hansen et al. 2004)

Fixed-speed WTs may either employ blade pitch control or stall control, while variable-speed designs normally employ blade pitching mechanisms with some control algorithm for efficient operation. Generally, WTs that employ blade pitching are able to extract more energy from the wind, it does, however, come at the cost of additional machinery (the pitching mechanisms) and controllers. (Singh and Santoso 2011)

Fixed-speed WTs were mostly installed in the 1980's and 1990's, whereas the bulk of modern turbines currently being installed are variable-speed designs, which are able to operate more efficiently over a larger wind speed range. (A. Hansen et al. 2004)

In the following, the components which make up the type A, B, C and D drivetrain topologies will be elaborated upon. Furthermore, slight variations of the different topologies, which do not require their own classification, will also be briefly presented.

Type A: Fixed-speed Wind Turbine:

These are the most basic utility-scale WTs in operation today. They derive their name from the fact that they operate with less than 1% variation in rotor speed when operating, independently of the wind speed.

The generator in these WTs is a high speed asynchronous squirrel cage induction generator (SCIG). The high speed generator shaft is connected to the low speed main shaft (the rotor) via a multi-stage (full speed) gearbox, and the stator windings connect directly to the grid through a transformer. As such the rotational speed of the rotor is determined by the grid frequency, winding configuration and gear ratio of the gearbox. (Li and Chen 2008)

Figure A.1 diagrammatically shows a stall regulated fixed-speed WT topology, with included softstarter and reactive power compensation capacitor bank.

To allow for smoother connection to the grid a softstarter is normally included, which can reduce in-rush current and mechanical stresses from jerk during acceleration of the rotor from standstill. Furthermore, a SCIG requires reactive power to magnetise the stator side windings, a capacitor bank, as indicated in the figure, may be used as reactive power compensation. (L. H. Hansen et al. 2001a)
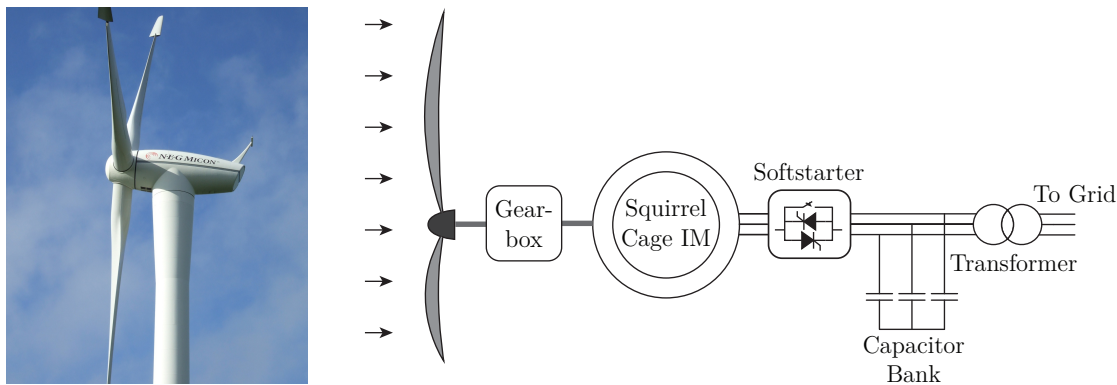
Fig. A.1: Stall regulated **type A** drivetrain, which includes a capacitor bank for reactive power compensation. The generator connects directly to the grid, and the turbine rotor connects to the SCIG via a gearbox. To the left, an example of the here illustrated stall regulated **type A** topology, a NEG Micon NM64/1500 1.5 MW wind turbine with a 64 m rotor and deployed tip brakes (wind-turbine-models.com 2016b).

Type B: Variable-slip Wind Turbine:

The variable-slip WT also utilises a high speed induction machine as the generator. However, instead of short circuited bars in the rotor, the rotor is now constructed from the copper windings. The rotor windings in the wound rotor induction generator (WRIG) are normally accessible through slip rings, although other concepts exist (e.g. Vestas' Optislip).

Like the fixed-speed WT, the high speed generator shaft is connected to the low speed main shaft (the rotor) via a multi-stage (full speed) gearbox, and the stator windings connect directly to the grid through a transformer. Since the WRIG stator windings are connected directly to the grid, the synchronous speed is fixed, and the rotor speed can thus only be varied by changing the machine slip. This allows for limited speed control in the range of 0-10 % above the synchronous speed. Furthermore, softstarters and capacitor banks are also used in this drivetrain topology. (A. Hansen et al. 2004; Li and Chen 2008)

The rotor windings are connected in series with a controlled resistor, variable speed operation is then obtained, by controlling the rotor currents. Increasing the rotor resistance has the effect of flattening the speed-torque curve for the IM, which widens the otherwise narrow operating range for power generation, and thereby operation at slip of up to 10 %. The energy extracted from the rotor circuit by the variable resistance is generally dissipated as heat, and thus the variable speed range depends on the power rating of the resistance. (Li and Chen 2008; Singh and Santoso 2011)

Figure A.2 diagrammatically shows a pitch regulated variable-slip WT topology, with included softstarter and reactive power compensation capacitor bank.
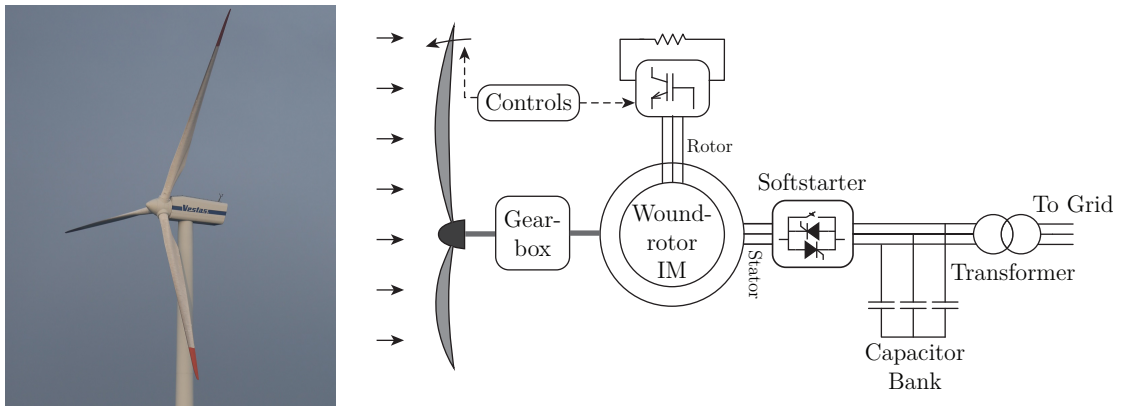
Fig. A.2: Pitch regulated **Type B** drivetrain, which includes a capacitor bank for reactive power compensation. The generator connects directly to the grid, and the turbine rotor connects to the WRIG machine via a gearbox. To the left, a Vestas V66 1.65 MW **type B** pitch regulated wind turbine with a 66 m rotor (wind-turbine-models.com 2016e).

The Opstislip concept by Vestas, incorporates the power converter into the rotor and optically transmits control signals to vary the rotor speed. The Optislip concept does away with brushes and slip rings, which require costly maintenance. (A. Hansen et al. 2004; L. H. Hansen et al. 2001a).

Type C: Doubly-fed Induction Generator Wind Turbine:

This drivetrain topology utilises a wound rotor induction machine as the generator, and combines it with a multi-stage (full speed) gearbox to connect to the turbine rotor. The stator windings are again connected directly to the grid though a transformer, while the rotor windings are connected to the grid through a power converter, thereby the name Double-fed Induction Generator (DFIG).

The power converter controls the rotor frequency, and thus also the rotor speed. This allows for limited speed control, typically in the range of $\pm 30\,\%$ of the synchronous speed, depending on the converter size. The power converter is normally rated at 30 % of the nominal generator rating. Furthermore, the addition of the rotor-side power converter makes active compensation of reactive power consumption and smooth grid connection possible, therefore the previously undertaken measures are no longer needed. This topology necessitates slip rings to connect the converter to the rotor windings, however, rotor power can be fed into the grid instead of simply being dissipated as heat. (A. Hansen et al. 2004; Li and Chen 2008)

Figure A.3 diagrammatically shows a pitch regulated DFIG WT topology.

Type D: Full-converter Wind Turbine:

This topology offers full variable speed operation of the WT. This is achieved by completely decoupling the generator from the grid by use of a full scale power converter, as such the generator frequency can be varied in the full speed range. Similarly to type C turbines, the power converter can perform reactive power compensation and smooth grid connection. The topology may be realised with a single-stage (medium speed) gearbox
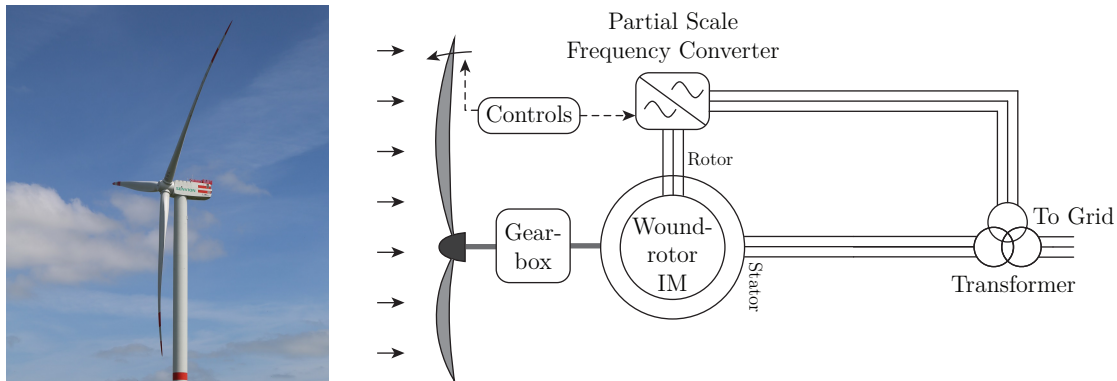
Fig. A.3: Pitch regulated **Type C** drivetrain. The generator connects directly to the grid, and the turbine rotor connects to the WRIG machine via a gearbox. To the left, a Senvion (formerly REpower) 6.2M152 6.15 MW **type C** pitch regulated wind turbine with a 152 m rotor (wind-turbine-models.com 2016c).

driven generator or by completely omitting the gearbox (a major contributor downtime) and implementing a direct drive generator. (A. Hansen et al. 2004; Roemer 2014)

The generator utilised in this topology is typically a synchronous machine (SM), which may either utilise electrical excitation (EESG) or permanent magnets (PMSG) to create a rotor-side magnetic fiel. The former does, however, require an additional power converter and slip rings. (Li and Chen 2008)

The full power converter can be realised as a back-to-back converter, and thereby the grid can be supplied with a fixed frequency voltage, while still allowing the turbine rotor speed to vary. (Roemer 2014)

Figure A.4 diagrammatically shows a pitch regulated permanent magnet WT topology.
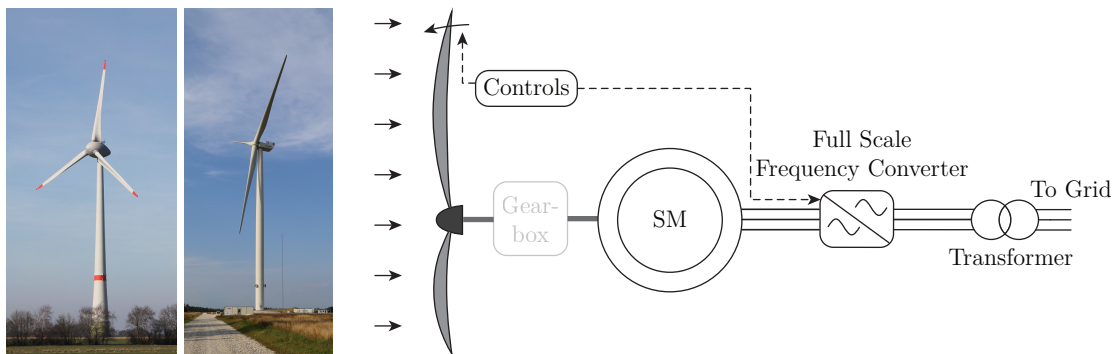
Fig. A.4: Pitch regulated **Type D** drivetrain. The generator connects to the grid through a full scale power converter, and the turbine rotor connects to the synchronous machine via an optional gearbox. To the left, a Enercon E-126 7.6 MW **type D** pitch regulated electrically excite direct drive wind turbine with a 127 m rotor, note how the large generator ($\varnothing$12 m) influences the nacelle design (wind-turbine-models.com 2016a). In the middle, a MHI Vestas V164 8 MW **type D** pitch regulated permanent magnet geared wind turbine with a 127 m rotor (wind-turbine-models.com 2016d).

This concludes the description of WT drivetrain topologies, and slight variations thereof, which are utilised in current production WTs. Having presented the general design and the components used in today's common utility WT, a basic foundation for studying the reliability of conventional WTs and common causes of breakdowns is attained.

A.2 Conventional WT Drivetrain Efficiency

Only the efficiency of currently installed wind turbines will be considered, why the efficiency study of type A and B are omitted. Liserre et al. (2011), who investigates currently installed multi-MW WTs and their drivetrains, finds that type C turbines are the most adopted for onshore applications owing to their lower weight and cost. However, for offshore applications, direct drive type D turbines have been preferred, due to heightened requirements for robustness and reliability. Furthermore Liserre et al. (2011) notes that for increasing power ratings, the generator for direct drive turbines may become too large and heavy for commercial applications, and that type D turbines with single-stage gearboxes become more attractive (e.g. the MHI Vestas V164).

Moreover, the use of WTs with power converters allows for control of active and reactive power, voltage and frequency, response during transient situations, influence on grid stability and improved power quality. All of which are important for interconnecting the turbine to the grid, and for which there are usually requirements (Elkraft System and Eltra 2004).

The efficiency of WTs generally improves when the generated power is close to the power rating of the WT. Multiple studies of WT drivetrain efficiency has been performed (see Poore and Lettenmaier (2003), Roemer (2014), and Silva et al. (2014)), the purpose of reiterating the results of these studies, is to determine the necessary efficiency of an alternative drivetrain design to be commercially viable.

Figure A.5 shows the efficiency of type C and permanent magnet type D, both direct drive and geared, turbines as a function of the percentile power generation.
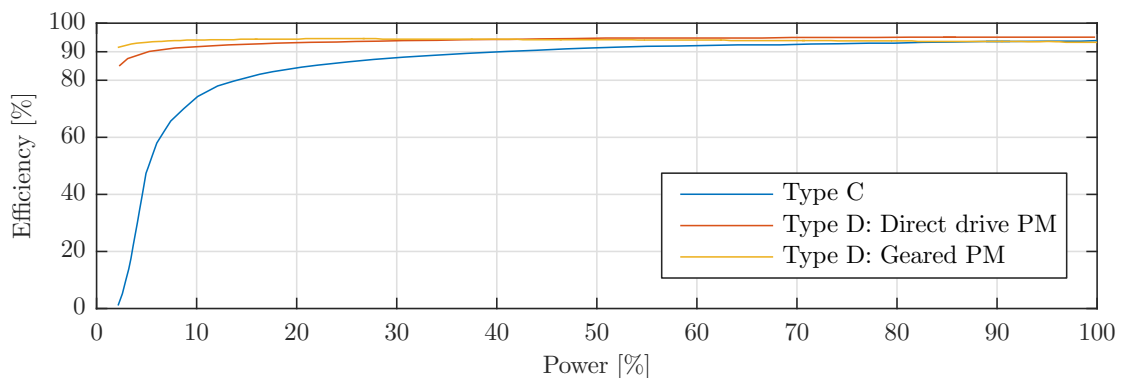

Fig. A.5: Efficiency of wind turbine topologies C and D (permanent magnet, direct drive and gear) as a function of the percentile rated power generation. Based on data for advanced models of 1.5 MW turbine topologies presented by Poore and Lettenmaier (2003).

From the figure it can be seen that close to rated power the efficiency of type C DFIG and type D geared and direct drive topologies is similar at ~95 %. Evident is also the advantage of the full variable speed operation range of the type D topology, where they are able to operate efficiently at much lower power levels. Poore and Lettenmaier (2003) states that electrically excited type D WTs have lower efficiencies than their PM counterparts, and as such data is not available for this variation of the type D topology. The age of the data source should be noted, and it must be expected that efficiency improvements have been made in recent years.

This concludes the investigation of modern utlity-scale WTs, which are currently installed and under production. Based on the results presented in this section, there are stringent requirements for alternative drivetrain topologies if they are to be a commercially viable.

A.3 A Intelligent FPT Design Example

A research project from *Institut fur angewandtes Stoffstrommanagement*, have designed a FPT based drivetrain is for a 1 MW WT. The design of the FPT drivetrain seen in figure A.6 employs two low speed fixed displacement pumps connected in parallel and four hydraulic displacement motors.
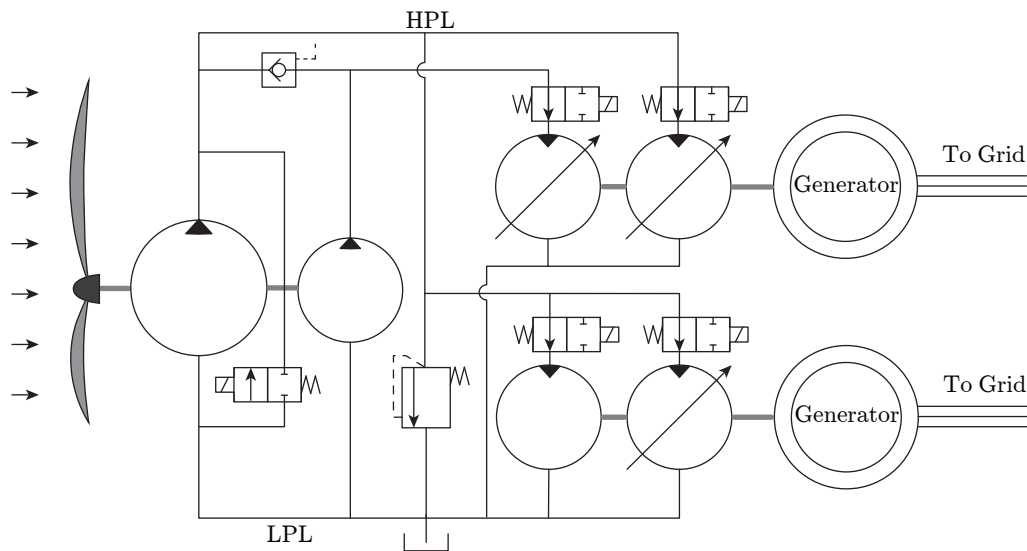
Fig. A.6: Design proposal from Schmitz et al. (2013) for a more efficient FPT based drivetrain.

The pumps are dimensioned to account for 80 % and 20 % of the total displacement respectively. When the drivetrain is operated at partial load, the 80 % displacement pump can be switched off by opening a valve from the HPL to LPL. The system contains three variable displacement motors and one fixed displacement motor. These are in pairs connected to two separate synchronous generators. Depending on the load acting on the drivetrain one pump and one or several of the motors can be switched off. As a result of this design, the efficiency of the drive train can be improved significantly during partial

load. With this intelligent design the maximum efficiency at partial load is found to be between 70 % and 80 %. Compared to conventional drivetrains this efficiency can not be considered impressive, and thus the presented FPT based drivetrain is not deemed as a competitive alternative for present WT drivetrains. (Schmitz et al. 2013)

A.4 Fluid Power Efficiency Maps

This section has the purpose of elaborating and supporting some of the statements made during the introduction chapter 1 regarding the efficiency of fluid power machines, FPT based drivetrains and DD machines.

A.4.1 Conventional Fluid Power Machines

A general issue with the FPT based drivetrains for WT are that these must be designed for a significant higher peak than the WT's average power output. Since the mechanical losses in conventional fluid power pumps and motors does not scale down with reduced power output, the FPT based drivetrains suffer from poor efficiencies at partial load. To illustrate this phenomenon the contour plots of a commercial available variable bent axis displacement pump (RexrothAV6M250) is depicted in figure A.7. The figure shows the pump's efficiency as a function of pressure and output speed at a displacement of 100 % and 20 % respectively. At full displacement the pump has a peak efficiency of 93 % and in more than 85 % of the operating range the efficiency is larger than 70 %. However when the displacement of the pump is reduced to 20 % the peak efficiency reduces to 81 % while in more than 35 % of the operating range the efficiency has diminished to less than 60 %.
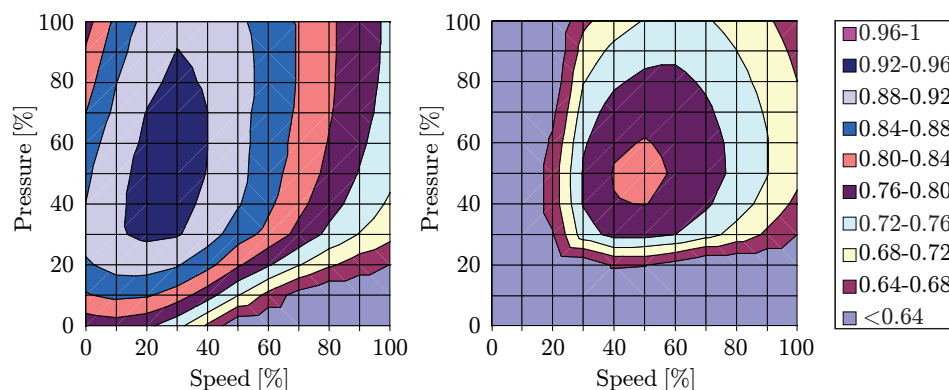
Fig. A.7: Contour plot of typical variable bent axis displacement pump. Left plot at 100 % displacement and right plot at 20 % displacement.(Rampen 2006)

A FPT has two stages of conversion. Stage 1 converts the rotational energy from the WT blades to a pressurised fluid in the HPL using one or several pumps. Stage 2 utilises the pressurised fluid to drive a hydraulic motor which then in turn transfers the energy to high speed rotational energy. Since two stages of conversion are present in the FPT, the overall efficiency of the transmission is determined by multiplication of the pump and

motor efficiency. If loses are present at different locations than in the pump and motor, these must furthermore be considered. The typical overall efficiency of commercially available FPT have the efficiency characteristic seen in figure A.8. From the figure it can be seen that the efficiency varies depending on the output speed and the load torque. For output speeds higher than 50 % the efficiency ranges between 60 % and 80 % depending on the load.
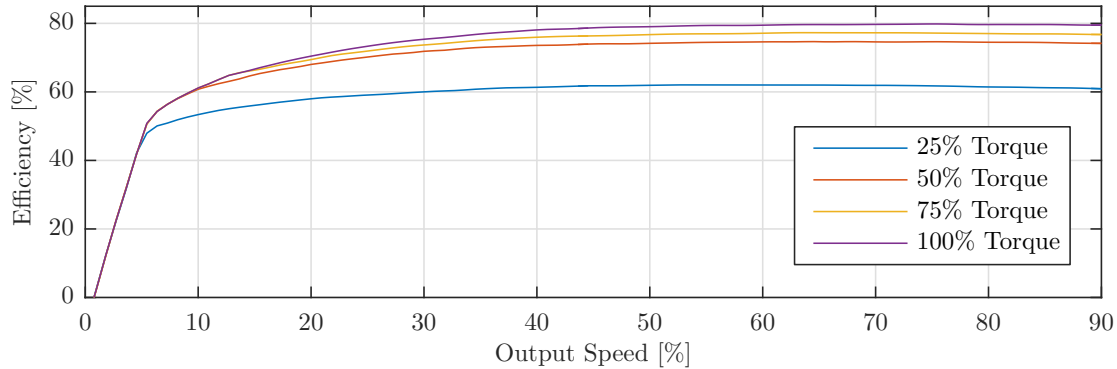

Fig. A.8: Overall efficiency as a function of output speed and torque for a typical commercial available FPT. (Rampen 2006)

Even though more intelligent designs of FPT based drivetrains are emerging, such as the one presented in figure A.6, the relatively poor efficiency at partial load makes FPT based drivetrains a poor alternative for many application including WTs.

A.4.2 Digital Displacement Machines

The efficiency of a typical variable DD pump is depicted in figure A.9. The figure shows the efficiency contour plot as a function of percentile speed and pressure for 100 % and 20 % displacement respectively.
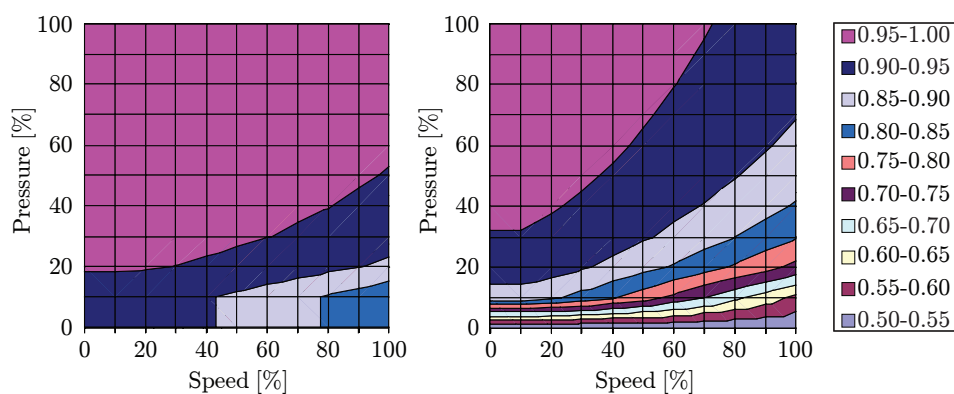
Fig. A.9: Contour plot of typical DD machine. Left plot at 100 % displacement and right plot at 20 % displacement.(Rampen 2006)

At full displacement the variable DD pump exhibits an efficiency of more than 90 % for more than 85 % of the entire working range. At a displacement of 20 % the efficiency generally decreases, however is still maintained above 80 % in more than 85 % of the complete working range. This can be considered as a significant improvement compared to conventional variable displacement pumps. The efficiency maps depicted in figure A.9 shows an efficiency of 95 % in a wide range of operation, and squaring this number to get an estimate of the overall efficiency of a DFPT yields 90 %, which is comparable to current WT transmissions (Rampen 2006). This suggest that utilisation of DFPT based drivetrains could be a viable solution when designing future WTs.

Wind Turbine Appendix

The purpose of this chapter is to present the essential knowledge regrading WT operation and modelling which has been utilised during this project in order to develop control of a DFPT based drivetrain. The chapter elaborates upon the overall control objectives and control strategies for the chosen NREL 5.4 MW WT. It continues with description of the governing mathematical equations used to describe the dynamics of the WT. The appendix ends with a presentation of the given wind profile used when the developed control of the DFPT is evaluated.

B.1 NREL 5 MW WT Introduction

The National Renewable Energy Laboratory (NREL) 5 MW reference WT is a three-bladed upwind variable-speed and variable-pitch design. The WT is a fictional concept developed by the U.S. Department of Energy for the purpose of supporting studies for assessing offshore wind technology. While purely fictional, the specifications of the NREL 5 MW WT are heavily based on the real REpower 5M WT. Owing to the research oriented purpose of the concept, the specifications of the WT are freely available, and the WT is commonly used as a reference in academic research. (Jonkman et al. 2009)

Complete simulation packages for the entire NREL 5.4 MW WT, which simulate aerodynamics, hydrodynamics, control & electrical servo dynamics and structural dynamics, are available, e.g. the FAST package (NWTC Information Portal (FAST) 2016). However, the focus of this project lies not on the modelling of the complete WT, but on the modelling and control of the DFPT based drivetrain. Therefore a greatly simplified representation of the NREL 5.4 MW WT is here considered, where only the torque and power generation are included.

Figure B.1 shows a simple block diagram of the WT under consideration, with inputs and outputs as described in section 1.3.1.

The exogenous wind speed input, v, to the WT, is an external and uncontrollable system input. For real life conditions it depends on the location, both globally and locally, in the sense that air currents are affected by nearby mountains, hills and vegetation. Mathematical modelling of the wind speed and the WT is further considered in appendix B.2.

The control input to the rotor pitch angle, β, shown in figure B.1 is generally determined by some wind power extraction strategy. The power extraction strategy is generally similar for variable-speed variable-pitch WTs, but specific with regard to parameters such as rated wind speed and so on. To fully understand the power extraction strategy,

NREL 5 MW
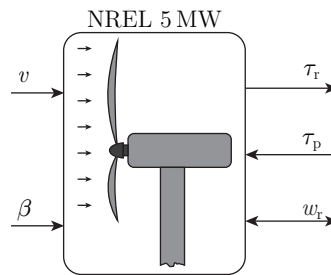
Fig. B.1: Inputs and outputs of the NREL 5.4 MW WT.

it is first necessary to consider the overall control objective for WTs.

Control Objective:

When operating a WT, typical overall objectives for the control strategy include:

Maximise Power Production: Power extraction from the wind should be maximised, without exceeding the maximum rating of the WT components, while still fulfilling operational criteria such as cut-in and cut-out wind speeds.

Minimise Wear Out: Mechnical loads caused by torque pulsations should be minimised, excitation of resonant modes in the structure should be avoided and tripping the electrical system should be avoided due to excessive loads.

Furthermore this is constrained by standards and requirements, implemented by grid operators, for the quality of the generated power. Evidently, these overall objectives are conflicting, as power production can hardly be maximised without stressing the components of the WT.

Control Strategy:

Jonkman et al. (2009) defines a number of operating regions for the NREL WT as a function of the wind speed. The four distinct regions are illustrated in figure B.2, where only region II & III are utilised for power production.

The four regions define the operation of the WT as:

Region I: Below the cut-in wind speed, v_{in}, where the generator torque is kept at zero and no power is being generated by the WT. In this region the wind is used to accelerate the rotor for start-up purposes.

Region II: Below the rated wind speed, v_{rtd}, and above the cut-in wind speed. The objective here is to maximise power capture from the wind, and this is done by maintaining a constant tip-speed ratio (TSR). The TSR, which is the relative speed of the rotor blade tip to the wind, is a measure of the fraction of power extracted from the wind.

Maintaining an optimal TSR is done by regulating the rotational speed of the turbine rotor by controlling the reactive pump torque. The rotor torque produced by the wind acting on the turbine is maximised when the pitch angle of the blades
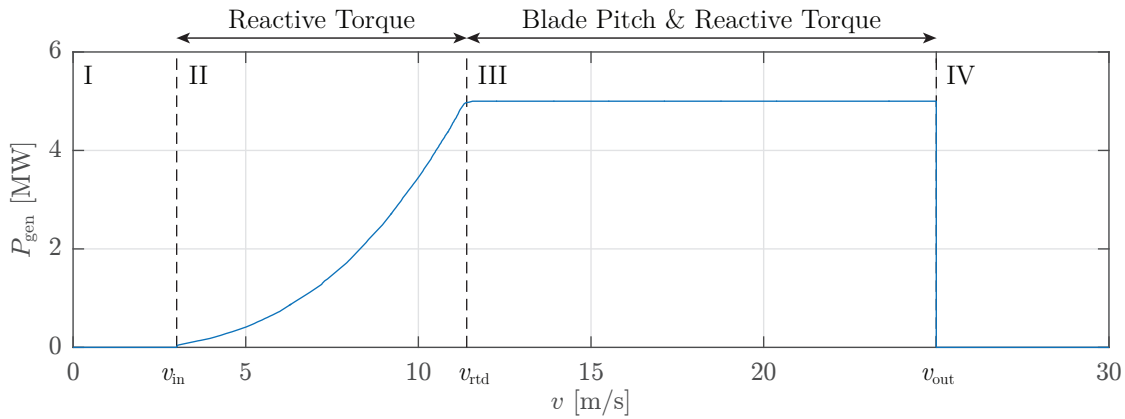
Fig. B.2: Generated power, P_{gen} as a function of wind speed, v, for the NREL 5.4 MW WT. Overlaid are the four different operations regions for the WT control strategy. Based on data in Jonkman et al. (2009).

is held constant at $\beta = 0°$ (see appendix B.2.2 for explanation) and, as such region II control is achieved solely by the turbine drivetrain without any involvement from the blade pitch system.

Region III: Above the rated wind speed and below the cut-out wind speed, v_{out}. The generator power is held constant. Thus for the DFPT based drivetrain, the DD pump torque must be held inversely proportional to the rotor speed. This is done by a combination of reactive torque and blade pitch control.

Region IV: Above the cut-out wind speed power extraction is ceased, and the rotor is brought to a halt to prevent damage to the turbine.

By only considering region II operation, the modelling task may be significantly simplified, since the blade pitch controller may be completely omitted. Furthermore, it may be surmised that if torque control is possible in region II, then it will also be possible in region III.

As described, the wind speed is exogenous and uncontrollable, as such it makes a poor control variable. Therefore figure B.2 may be transformed to rotor torque and speed instead of generated power and wind speed. This is done in appendix B.2.2, where control of the WT is considered. Addtional regions and control actions may also be added to the torque speed curve to reduce loading and aid in starting and stopping the WT.

This concludes the description of the NREL 5.4 MW reference WT. The mathematical modelling of the turbine will be presented next, where the governing equations are presented together with the specifications and region II control considerations.

B.2 WT Modelling

This sections presents the equations used for modelling the WT. The equations are in general valid, independent of the drivetrain topology and ability to pitch the rotor blades. The coefficient maps are, however, only valid for the NREL 5.4 MW turbine. Thus these maps will not be utilised for the 10 kW drivetrain as it is only formed as a development tool for forming a multirate MIMO model. It is however necessary to have a model describing the turbine as this will be utilised for controlling the 5.4 MW drivetrain.

Initially will the governing equations used for modelling the turbine be presented and these will be followed by an explanation of the WT operation regions considered for the NREL 5.4 MW turbine.

B.2.1 Governing Equations

Aerodynamics:
The WT functions by extracting power from the wind. Therefore the available power in the wind must be defined, and it is given by (Singh and Santoso 2011, p. 15):

$$P_{\text{wind}} = \frac{1}{2} A \rho_{\text{A}} v^3 \tag{B.1}$$

where A is the area acted upon by the wind, ρ_{A} is the air density and v is the wind speed. Note that equation B.1 bears a heavy resemblance to a combination of the regular power $(P = F v)$ and drag/lift $(F = 1/2 A C \rho v^2)$ equations.

The power that a WT is able to extract from the wind is governed by the power coefficient C_{p}, which is defined as the ratio between the wind power and mechanical rotor power, P_{r} (Singh and Santoso 2011, p. 17):

$$C_{\text{p}}(\lambda, \beta) = \frac{P_{\text{r}}}{P_{\text{wind}}} \qquad \text{where} \quad P_{\text{r}} = \tau_{\text{r}} \omega_{\text{r}} \tag{B.2}$$

τ_{r} is the aerodynamic torque applied to the rotor by the wind, and ω_{r} is the rotational speed of the rotor. Thus C_{p} is a measure of the rotor efficiency.

For a variable-speed variable-pitch turbine the power coefficient depends on both the pitch angle, as this heavily influences the torque generated by the lift and drag forces acting on the rotor, and the tip-speed ratio. The tip-speed ratio (TSR), λ, is defined as the ratio of the rotor tip-speed to the wind speed, thus it can be calculated by:

$$\lambda = \frac{\omega_{\text{r}} R_{\text{r}}}{v} \tag{B.3}$$

where R_{r} is the rotor radius. The TSR is then a measure of the fraction of power extracted from the wind by the turbine.

Torque and Power:

By combining equations B.1 and B.2 an expression for the mechanical rotor power may be derived:

$$P_r = \frac{1}{2} A_r \rho_A C_p(\lambda, \beta) v(t)^3 \tag{B.4}$$

where A_r is the rotor swept area. As noted, the power coefficient depends on both the TSR and the blade pitch angle, to illustrate this, figure B.3 shows a plot of the power coefficient as a function of the TSR and pitch angle.
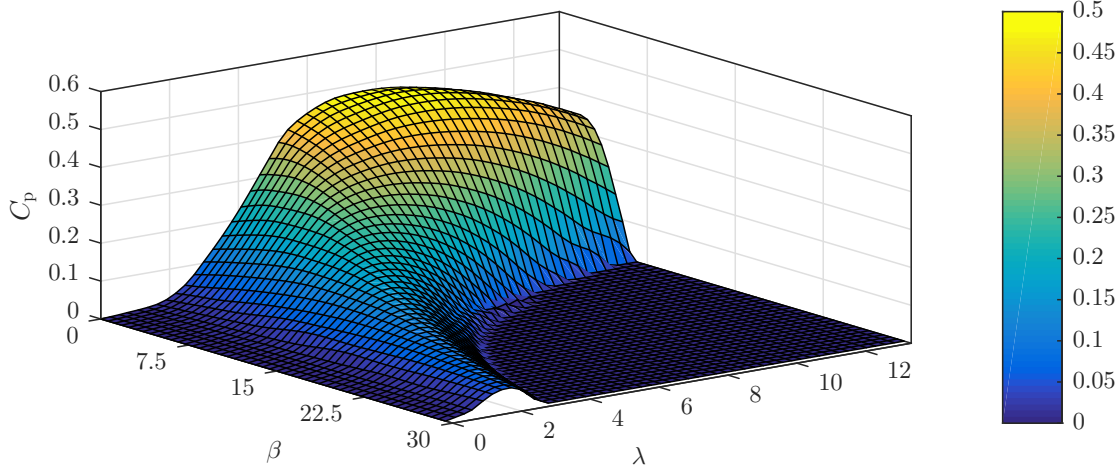
Fig. B.3: Power coefficient, $C_p(\lambda, \beta)$, as a function of tip-speed ratio, λ, and blade pitch-angle, β, for the NREL 5.4 MW turbine. The map is based on simulating the NREL 5.4 MW turbine for varying λ and β and tabulating the coefficient at steady state (Jonkman et al. 2009)

Here the power coefficient is limited to only being positive. It should, however, be noted that it may be negative in the case that grid power is utilised to rotate the rotor during possible start-up procedures, this is not considered in this project.

An expression for the rotor torque may be derived by dividing equation B.4 by the rotor speed, and then combining the result with equation B.3 to obtain:

$$\tau_r = \frac{1}{2} R_r A_r \rho_A C_q(\lambda, \beta) v(t)^2 \tag{B.5}$$

where $C_q(\lambda, \beta)$ is the torque coefficient, which is defined as:

$$C_q(\lambda, \beta) = \frac{C_p(\lambda, \beta)}{\lambda} \tag{B.6}$$

Similarly to the power coefficient, the torque coefficient is also a function both the TSR and pitch angle.

Figure B.4 shows a map of the torque coefficient.
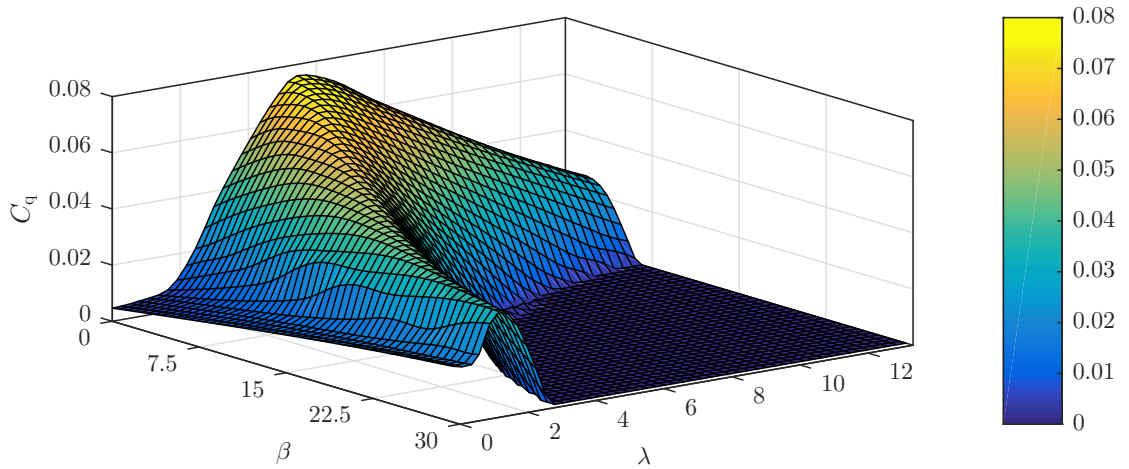
Fig. B.4: Torque coefficient, $C_q(\lambda, \beta)$, as a function of tip-speed ratio, λ, and blade pitch-angle, β, for the NREL 5.4 MW turbine. The map is based on simulating the NREL 5.4 MW turbine for varying λ and β and tabulating the coefficient at steady state (Jonkman et al. 2009).

Both the mechanical rotor power and torque depend on the operation of the WT, thus in the next section operation of the WT will be considered.

B.2.2 Region II Operation

The overall goal for operation of the WT is to maximise power production, while keeping component wear to a minimum. To maximise power production optimal values of reactive pump torque and rotor speed must be maintained. These may be found by reconsidering equation B.5 for the rotor torque. Solving for the wind speed in equation B.3 and together with equation B.6 inserting into equation B.5, an expression which defines an optimal reference for the reactive torque as a function of the rotor speed, such that an optimal TSR for power production is maintained, can be written as:

$$\tau_r^* = \frac{1}{2}\, R_r{}^3\, A_r\, \rho_A\, \frac{C_p(\lambda^*, \beta = 0°)}{\lambda^{*3}}\, \omega_r{}^2 = K_{II}\, \omega_r{}^2 \tag{B.7}$$

Plotting the optimal reference torque as a function of the rotor speed yields the red dashed curve in figure B.5.

Figure B.5 is seen from a rotor torque and speed reference frame where only the first three regions are shown. Additionally, the operating regions have been expanded with the modified regions I and II, regions $\tilde{I}$ and $\tilde{II}$, respectively. These modified regions serve as transitional regions, which serve to prevent step like changes in the torque command, where region $\tilde{I}$ also serves as a start-up region. Region II operation is now bounded by rotor speeds in the range of $1.3\,\omega_{r,in} \le \omega_r \le 0.99\,\omega_{r,rtd}$.

Only considering operation in region II is considered where the goal is to maximise power extraction from the wind, and this is done by maintaining an optimal TSR.
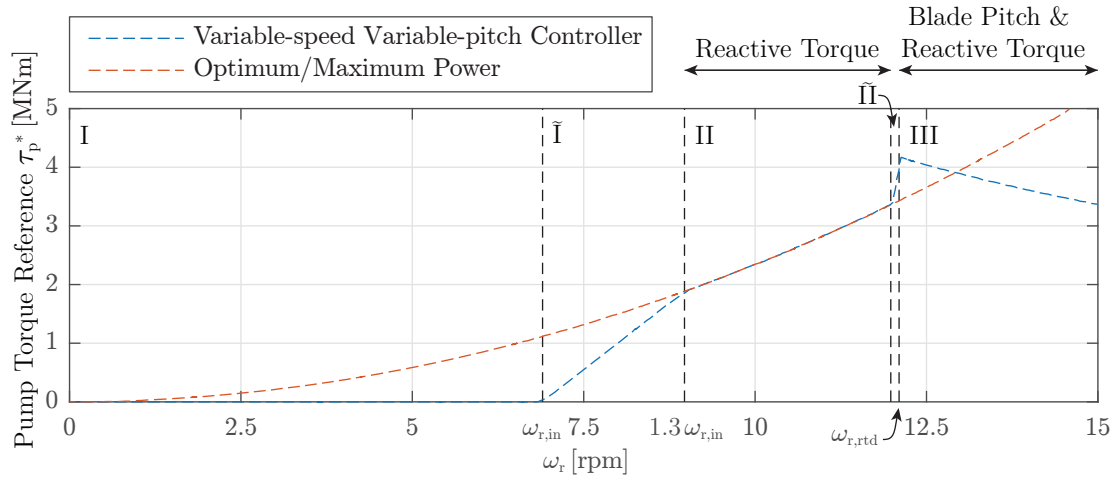
Fig. B.5: Reference reactive torque, τ_r^* and ideal torque for maximum power production as a function of rotor speed, ω_r^*, for the NREL 5.4 MW WT. Overlaid are the operating regions for the WT. For operation in region II, the variable-speed variable-pitch controller reduces to a variable-speed constant-pitch controller, since a constant pitch angle of $\beta = 0°$ is maintained for maximum power production. Based on data in Jonkman et al. (2009)

The purpose of the data presented in figure B.5 is then to act as a control reference for the reactive pump torque. Control based on equation B.7 requires only measurement of the rotor speed. The slow dynamics of the rotor speed will filter high frequency wind turbulence, and power production thus follows the average wind speed component more closely. Filtering of wind disturbance through the rotor dynamics also reduces excessive fluctuations in the reactive pump torque, but this comes at the cost of suboptimal tracking of the optimal TSR. It should be noted that curve obtained by plotting equation B.7 is only used for region II operation, since only region II seeks to maximise power production.

Figures B.3 and B.4 reveal that the blade pitch angle should be kept at a constant $\beta = 0°$ to maximise power and torque generation. Figure B.6 reiterates the maps of figures B.3 and B.4 for a constant $\beta = 0°$.

As seen in the figure, there exists optimal TSRs for maximising the power and torque. Since the objective in region II is to maximise the power production of the turbine, a constant TSR of $\lambda^* \approx 7.6$ should be maintained.

To be able to generate power using a WT wind is obviously necessary, the presented equations will generally be valid for the entire operating range of the WT, but since only region II operation is considered, the wind speed should be limited to prevent the WT from entering region III. In the following, appropriate wind data will briefly be considered.
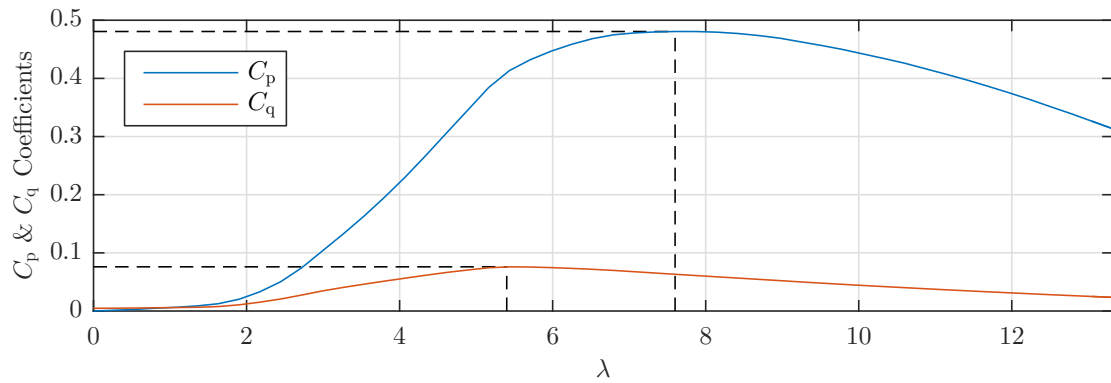
Fig. B.6: Power and torque coefficients, $C_p(\lambda, \beta)$ and $C_q(\lambda, \beta)$, as a function of tip-speed ratio, λ with $\beta = 0°$ for the NREL 5 MW turbine.

Turbulent Wind Model:

Wind is a varying phenomena, that is highly dependent on the surrounding environment. Accurate modelling of wind is thus a complex task, which requires consideration of many parameters that are specific to the location and WT. Since no specific location for the WT is considered, it is decided to simply model the wind with a time varying data series generated by the NREL program TurbSim.

TurbSim can generate 3D wind profiles for the complete NREL 5 MW simulation package FAST, but these may be simplified to 1D profiles aligned with the turbine rotor axis. Such a wind profile is illustrated in figure B.7, where the amplitude of the wind speed has been kept below the rated wind speed to maintain region II operation.
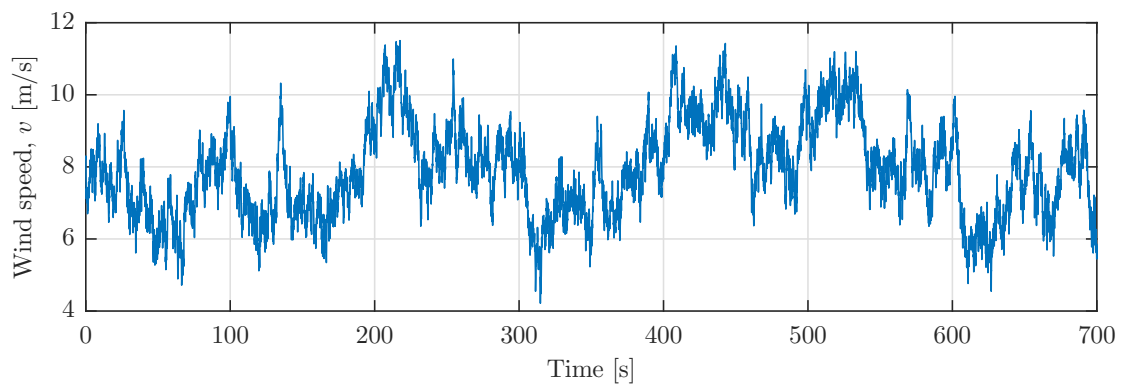
Fig. B.7: Time varying 1D wind speed data generated with the NREL program TurbSim.

Specifications:

The main specifications of the turbine are given in table B.1.

Description	Parameter	Value
Power rating	$P_{\mathrm{r,rtd}}$	5.4 MW
Torque rating	$\tau_{\mathrm{r,rtd}}$	4.25 MNm
Cut-in wind speed	v_{in}	3 m/s
Cut-in rotor speed	$\omega_{\mathrm{r,in}}$	6.9 rpm
Rated wind speed	v_{rtd}	11.4 m/s
Rated rotor speed	$\omega_{\mathrm{r,rtd}}$	12.1 rpm
Cut-out wind speed	v_{out}	25 m/s
Rotor radius	R_{r}	63 m
Rotor swept area	A_{r}	$\pi\,R_{\mathrm{r}}^2 \cos(2.5°) = 1.246 \times 10^4\,\mathrm{m}^2$
Rotor inertia	J_{r}	$3.88 \times 10^7\,\mathrm{kg\,m}^2$
Air density	$\rho_{\mathrm{A},@t=15°}$	$1.225\,\mathrm{kg/m}^3$
Region II constant	K_{II}	$2.086 \times 10^6\,\mathrm{Nm/rad/s}$

Tab. B.1: Main specifications of NREL offshore 5.4 MW baseline wind turbine (Jonkman et al. 2009, p. 2). The cosine term on the rotor swept area is included to compensate for the slight rotor tilt, which prevents the rotor blades striking the tower.

APPENDIX C

Digital Displacement Machine Designs

This appendix presents the general design structure of the DD pump and motor used in this projects 5.4 MW DFPT based drivetrain. It furthermore presents some elaborations upon the mathematical model of the 5.4 MW DDMs, including some explanatory geometric figures and a validation of utilised lookup tables. The appendix ends with a description of the calculation made to determine the chamber sizes for the DDMs used in the 5.4 MW and 10 kW DFPT models, respectively.

C.1 DD Pump Design Structure

To the authors knowledge there does not exist any commercial DD pumps in the multi-MW category, which makes the task of choosing a suitable DD pump design structure for the 5.4 MW DFPT challenging. The DD pump design could be chosen by taking a starting point in the relatively small DD pumps commercially available and then upscaling such a design to a 5.4 MW power rating. This could be a cumbersome process, and it might not be plausible that a DD pump, designed this way, would ever become part of a DFPT in the wind industry.

Instead an alternative approach is taken, where the design of the DD pump is based upon the state of the art technology available within digital hydraulics. This includes the study of the DFPT based drivetrain prototype developed for the 7 MW offshore WT by MHI and AIP. This approach is strongly inspired by the work done by Pedersen et al. (2016a), who has dimensioned a DD pump for a potential DFPT based drivetrain for the NREL 5.4 MW WT. The work done by Pedersen et al. (2016a) is based on the drawings by Kameda et al. (2014) and these are presented in figure C.1.

The pressure chambers depicted in the left of figure C.1 is controlled by an active LPV and a passive HPV. Each cylinder chamber is oriented radially at the circumference around the turbine rotor shaft. The displacement of each piston is done by a roller and the rotational movement of the cam ring. In this design the ring cam is directly connected to the turbine rotor shaft. External piping has been used for both the LPL and HPL, however, axial pipes along the rotor shaft have been utilised to connect the HPV to the HPL. The pump is build from four modules, where each module contain 32 cylinders actuated by a ring cam with 24 lobes. This constructing enables high fluid displacement for low speed rotational drive shafts while maintaining a good resolution as each pressure chamber does the number of lobes (24) cycles per revolution. However using 32 cylinders equally placed in the circumference around the rotor shaft, means that the cylinders will
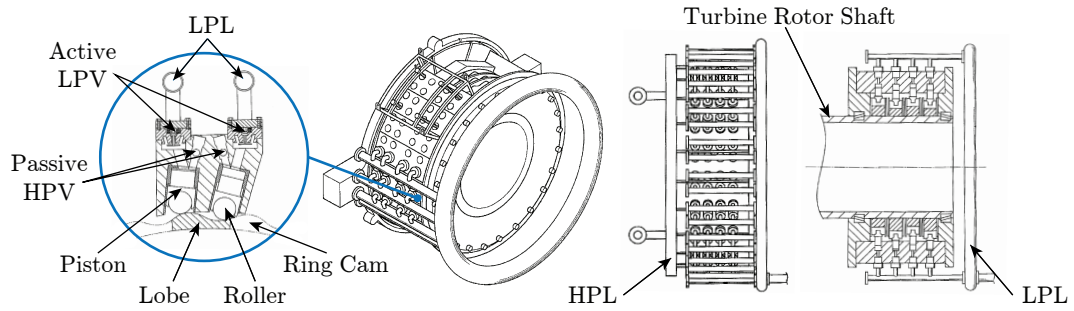
Fig. C.1: Variable DD pump design for the DFPT based drivetrain prototype for the SeaAngel
WT. To the left, sectional view of the individual pressure chambers. In the middle and to the
right, sectional views for the complete DD pump. Inspired by Kameda et al. (2014).

be actuated in parallel, which increases the size of the pressure ripples seen in the HPL.

The design depicted in figure C.1 has a power rating of 7.4 MW, and the design is thus
not considered directly applicable for a 5.4 MW DD pump

Hence work concerning the downsizing the DD pump design initially developed by MHI
and AIP is made. Similarly to the original design the downsized version contains 4
modules, however, each module now only includes 25 cylinders actuated by a cam ring
with 16 lobes. The design principle is seen in figure C.2.
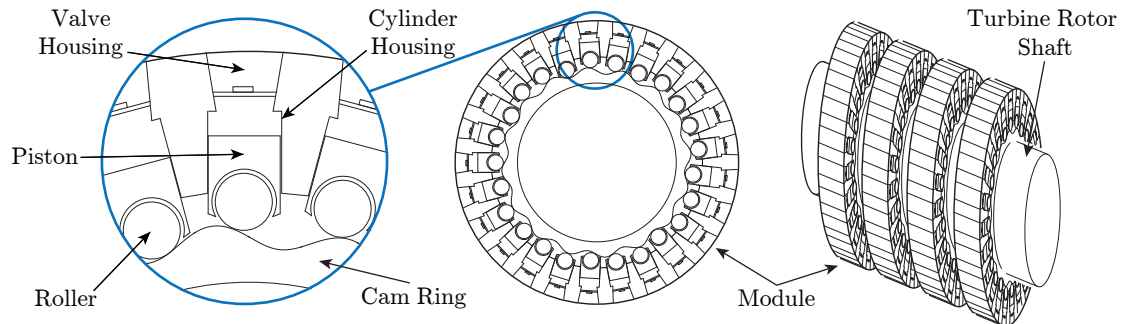
Fig. C.2: DD pump design used in this project's DFPT based drivetrain for a power rating of
5.4 MW. To the left sectional view of an individual pressure chamber. In the middle, a sectional
view of the entire cam ring and pressure chamber assembly. To the right four stacked modules
on a shared shaft. Drawing not to scale.

The parameters used to describe the pump presented in figure C.2 are listed in table 3.3.
The calculations used to derive these parameters can furthermore be found at the end of
this appendix, see appendix C.3.

C.2   DD Motor Design Structure

As for the DD pump there exists no commercially available DD motors in the multi-
megawatt category. It is thus necessary once again, to base the design structure of a
5.4 MW DD motor for the DFPT based drivetrain on preliminary designs developed

within the state of the art technology of DDMs.

MHI and AIP have developed a DD motor prototype for utilisation in the hydrostatic drivetrain for the SeaAngel WT. This drivetrain consists of two 3.5 MW DD motors, each connected to a separate synchronous generator (Sasaki et al. 2014). If this DD motor design should be used as basis for the DD motor used in this project's 5.4 MW DFPT based drivetrain some modifications have to be made. These modifications could consists of either downscaling the 3.5 MW DD motor to 2.5 MW and then utilise two of them, or alternatively upscaling the 3.5 MW DD motor to 5.4 MW. To simplify the mathematical modelling of the system it is chosen to utilise one DD motor with a power rating of 5.4 MW.

It is not only MHI and AIP that have presented work regarding DD machines, in recent years significant research has also addressed this topic. The PhD dissertation made by Johansen (2014) describes among other things, a partial design proposal for a 5.2 MW DD motor. The DD motor is composed of modules, where each module has a design similar to the Parker Calzoni radial piston motor. The motor construction of the 5.2 MW DD motor is depicted in figure C.3.
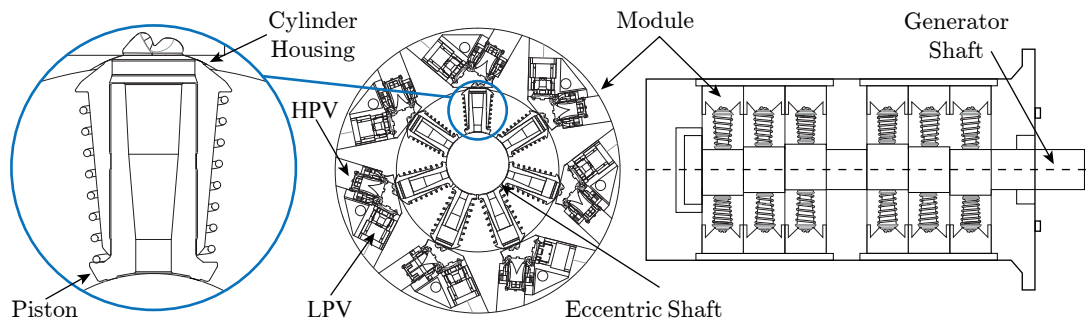
Fig. C.3: DD motor design structure used in this project's DFPT based drivetrain. To the left sectional view of an individual pressure chamber. In the middle, a sectional view of a single module. To the right six stacked modules on a shared shaft. Inspired by Johansen (2014).

Each module in the DD motor seen in figure C.3 consists of seven radially oriented cylinders. The piston of each cylinder is mounted on an eccentric shaft, which's rotation ensures each piston's displacement. The pressure chamber of each cylinder is connected to a LPV and a HPV, which are controlled according to the described motoring operation mode. For convenience the same valve characteristics will be used for LPV and HPV as for the valves in the presented DD pump. Johansen (2014) does not describe the specific locations of the LPL and HPL. However, the location of the LPV and HPV are placed in the outer circumference of the module, which suggests that the LPL and HPL could be comprised of external piping similarly to what is seen for the DD pump in figure C.1.

In the dissertation made by Johansen (2014) all relevant parameters for modelling the DD motor are presented. Furthermore with its power rating of 5.2 MW it is close to the desired power rating of 5.4 MW. Assuming that loses are present DD pump and HPL a power rating of 5.2 MW could be considered acceptable. Nevertheless for consistency the chamber dimensions are adjusted to accommodate a 5.4 MW power rating.

The parameters required for modelling the DD motor are presented in table 3.3. The calculations used to derive these parameters are furthermore elaborated upon at the end of this appendix, see appendix C.3.

C.3 Chamber Sizing of DFPT

This section has the purpose of presenting the calculations applied for determining the total displacement (including chamber dimensions) of the DDMs utilised in the 5.4 MW and 10 kW DFPT models. The design of the DD pumps and motors are presented in figures 3.3, 3.10, C.2 and C.3 respectively.

To complete this task a number of different known parameters will be utilised, these are presented in table C.1.

NREL 5.4 MW			DFPT Models (5.4 MW/10 kW)		
Description	**Variable**	**Value**	**Description**	**Pump/ Motor**	**Pump/ Motor**
Wind speed	$v_{r,rtd}$	11.4 m/s	HPL pressure	360 bar	360 bar
Rotor speed	$\omega_{r,rtd}$	1.2671 rad/s	LPL pressure	10 bar	10 bar
TSR	λ_{rtd}	7.0024 rad s	Num. of mod.	4/6	1/1
Torque coeff.	$C_{q,rtd}$	0.068	Cyl. per mod.	24/7	1/3
Rotor radius	R_r	63 m	Lobes per mod.	16/-	2/-
Air Density	ρ_{air}	1.225 kg/m^3			

Tab. C.1: The parameters utilised for calculating the displacements of the DDMs comprising the 5.4 MW and 10 kW DFPT drivetrains.

The calculations used to determine the displacement of the DDMs are close to identical, why only the sizing of the DD pump for the 5.4 MW will be presented in the following.

C.3.1 Power Rating of NREL WT

To determine the total displacement of the DD pump, the rated torque of the NREL rotor must first be determined. Knowing that the rated power is given to be 5.4 MW, the rated torque can be calculated using the rated rotor speed. However, for thoroughness it is chosen to calculate the rated torque using the rated wind speed. This is done using equation equation B.5, which for convenience is presented:

$$\tau_{r,rtd} = \frac{1}{2} R_r A_r \rho_{air} C_{q,rtd}(\lambda_{rtd}, \beta_{rtd}) v_{r,rtd}^2 \tag{C.1}$$

It should be noted that at rated wind speed the pitch angle, β_{rtd}, is equal to zero, thus the only unknown parameter in equation C.1 is the rotor swept area, A_r. The rotor swept area can according to Jonkman et al. (2009) be calculated as:

$$A_r = \frac{\pi}{4} \left(2 R_r \cos(2.5°)\right)^2 \tag{C.2}$$

Inserting equation C.2 into equation C.1 together with the parameters from table C.1 yields the rated rotor torque and power:

$$\tau_{r,rtd} = 4.24\,\text{MNm} \qquad\qquad P_{r,rtd} = \tau_{r,rtd}\,\omega_{r,rtd} = 5.38\,\text{MW} \qquad (\text{C.3})$$

C.3.2 Effective Displacement and Chamber Volume

Knowing the rated rotor torque the total effective displacement of the DD pump, $D_{p,total}$, and the effective displacement of a single pressure chamber, $D_{p,cylinder}$, can be determined by:

$$D_{p,total} = \frac{\tau_{r,rtd}}{p_H - p_L} = 761.9\,\text{L/rev} \qquad D_{p,chamber} = \frac{D_{p,total}}{4 \cdot 25 \cdot 16} = 0.476\,\text{L} \qquad (\text{C.4})$$

where the numbers $4 \cdot 25 \cdot 16$ represents the DD pump's number of modules, cylinders and lobes respectively.

When the volume of a single pressure chamber must be determined, the pumping operation must first be considered. Hence how the fluid inside the chamber initially is pressurised from p_L to p_H and next how the HPV is opened and displacement into the HPL is made. The only parameters known is the effective chamber displacement, which is insufficient for determining the chamber dimensions.

Thus some restriction regarding the relation between the piston stroke length, $x_{p,stroke}$, and the cylinder diameter, d_p, must be made. Inspecting the design of the 7 MW DD pump prototype developed by MHI and AIP, it is estimated that the piston diameter is the double length of the piston stroke, why it is chosen that two times the piston stroke length must equal the cylinder diameter. Furthermore must the dead volume, V_{p0}, of a chamber also be known. This is chosen to be equal to the stroke length times the cylinder cross sectional area $(\frac{1}{4}\,\pi\,d_p{}^2)$.

With the presented relations between the chamber dimensions it is however still challenging to find the exact solution of the stroke length (or chamber dimensions). This is because it will require the solution for the continuity equation, which is a non-linear partial differential equation. Thus instead a numerical approach is taken. It includes determining a static solution of the piston stroke length, and hereafter using the developed non-linear model of the DD pumps pressure chamber to create a numerical optimisation problem, where the calculated static stroke length is used as an initial guess.

Static Calculation of Chamber Dimensions::
The static calculation approuach utilises the presented relations between the chamber dimensions, and a static version of the continuity equation (transients and valve dynamics neglected) to create three equation with three unknowns. These are hereafter solved simultaneously, to calculate an qualified guess of $x_{p,stroke}$.

The first equation is based on a static version of the continuity equation and can with

some mathematical manipulation be written on the form:

$$\Delta V_{\text{chamber}} = -\Delta p \frac{V_{\text{chamber}}}{\beta}$$

$$\Delta x_{\text{p}} \tfrac{1}{4} \pi \, d_{\text{p}}^{\;2} = -(p_{\text{H}} - p_{\text{L}}) \frac{\tfrac{1}{4} \pi \, d_{\text{p}}^{\;2} \, x_{\text{p,stroke}} + V_{\text{p0}}}{\beta}$$

$$\Delta x_{\text{p}} = -(p_{\text{H}} - p_{\text{L}}) \frac{2 \, x_{\text{p,stroke}}}{\beta} \qquad (C.5)$$

Here Δx_{p} represents the distance which the piston must be moved to allow for a pressure increase form p_{L} to p_{H} and $V_{\text{p0}} = x_{\text{p,stroke}} \tfrac{1}{4} \pi \, d_{\text{p}}^{\;2}$.

The second equation describes the relation between $x_{\text{p,stroke}}$ and d_{p}:

$$2 \, x_{\text{p,stroke}} = d_{\text{p}} \qquad (C.6)$$

The third equation describes the relation between $x_{\text{p,stroke}}$, d_{p} and the effective chamber displacement $D_{\text{p,cylinder}}$:

$$D_{\text{p,cylinder}} = \tfrac{1}{4} \pi \, d_{\text{p}}^{\;2} \, (x_{\text{p,stroke}} + \Delta x_{\text{p}}) \qquad (C.7)$$

Equation equations C.5 to C.7 are hereafter solved simultaneously to achieve the solutions for the three unknowns $x_{\text{p,stroke}}$, d_{p} and Δx_{p}, which can be used to describe the initial cylinder dimension for the optimisation problem.

Optimisation of The Cylinder Chamber Dimensions:
The optimisation algorithm applied is very simple, since the need for a complex algorithm is not necessary due to the qualified initial chamber dimension guess. The algorithm uses a non-linear model of the DD pump's pressure chamber and evaluates the chamber's effective displacement at 10 different stroke lengths varying from 95% to 105% of the initial guess value. Afterwards the stroke length which results in the effective displacement closest to the displacement calculated by equation C.4 is chosen, and the process is repeated until a solution converges with an error $< 0.001 \, D_{\text{p,chamber}}$.

Comments on The Calculation Procedure:
The presented calculations applies for sizing the chamber values of all DDMs utilised in 5.4 MW and 10 kW model. It should be noted that the calculations made in equation C.1 have only been applied for the 5.4 MW DD pump, wheras the remaining DDMs rated torque is found using the right side of equation equation C.3. Furthermore should it be noted that for the DD motors the relation between the stroke length ,$x_{\text{m,stroke}}$, and the cylinder diameter, d_{m}, is 1.2 instead of 2. This choice is based on the design from Johansen (2014). The chamber dimensions the DD pumps and motors can be found in tables 3.3 and 3.4. This concludes the calculations made regarding the dimensioning of the DDMs.

Theoretical Proofs

This appendix contains some theoretical calculations and proofs relevant to the material presented in the thesis.

D.1 Lifted Vectors in a State-Space Form

Consider the situation depicted in figure D.1, where all the lifted system vectors are aligned in time.
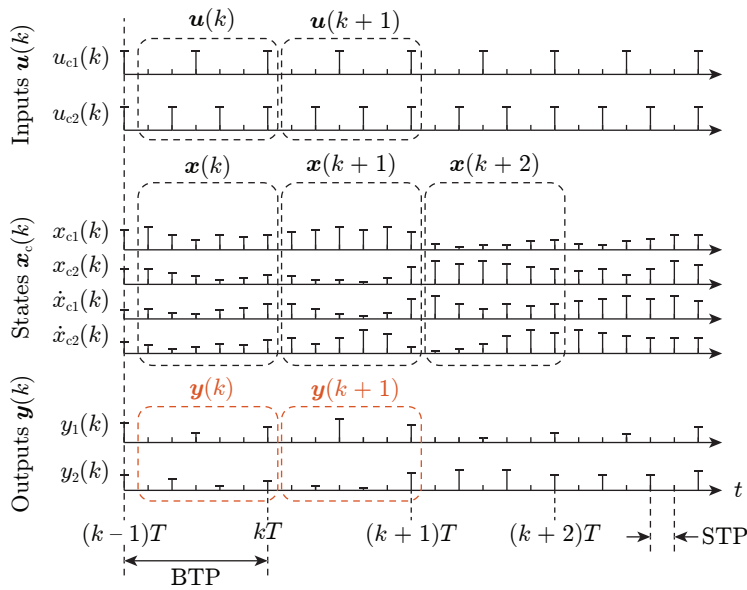
Fig. D.1: Multirate system with lifted vectors aligned.

Then to obtain the correct value for the first subvector in $\boldsymbol{x}(k+1)$, i.e. $\boldsymbol{x}_1(k+1)$, it would be possible to utilise a state equation of the form:

$$\boldsymbol{x}(k+1) = \boldsymbol{G}\boldsymbol{x}(k) + \boldsymbol{H}\boldsymbol{u}(k) \tag{D.1}$$

Consider now how to arrive at the correct value for the last subvector in $\boldsymbol{x}(k+1)$, i.e. $\boldsymbol{x}_6(k+1)$, then all inputs occurring during up till this point must be taken into account. Thus a possible state equation would be:

$$\boldsymbol{x}(k+1) = \boldsymbol{G}\boldsymbol{x}(k) + \boldsymbol{H_1}\boldsymbol{u}(k) + \boldsymbol{H_2}\boldsymbol{u}(k+1) \tag{D.2}$$

Since subsequent transitions will rely on the previous transitions it is essential that the correct final value is obtained in each block, why a state equation like the one just presented, must be used in the case that the blocks are chosen to be aligned. Thus the

model would be described by a state equation, which is not in the conventional form, why conventional control theory tools will most certainly not be directly applicable. Therefore the model structure presented in section 4.3 is used.

D.2 Linear Quadratic Regulator

In this section, the steady state gains for a discrete state feedback controller are derived using an optimisation based infinite horizon linear quadratic cost function. The presented equations are based on Lewis (2012) and expanded to show some additional steps in the derivation, which are not available in the original source material.

The is generally described by the state equation and with state feedback control law:

$$\boldsymbol{x}(k{+}1) = \boldsymbol{G}\boldsymbol{x}(k){+}\boldsymbol{H}\boldsymbol{u}(k) \qquad\qquad \boldsymbol{u}(k) = -\boldsymbol{K}\boldsymbol{x}(k) \qquad\qquad (\text{D.3})$$

Then an infinite horizon linear quadratic cost function of the form may be used to find the controller gains, which minimise the cost function:

$$J(k) = \sum_{i=k}^{\infty} \left[\boldsymbol{x}(i)^{\mathsf{T}}\boldsymbol{Q}\boldsymbol{x}(i){+}\boldsymbol{u}(i)^{\mathsf{T}}\boldsymbol{R}\boldsymbol{u}(i) \right] \qquad\qquad (\text{D.4})$$

where $\boldsymbol{Q}$ and $\boldsymbol{R}$ are real symmetric matrices, such that $\boldsymbol{Q}^{\mathsf{T}} = \boldsymbol{Q}$ and $\boldsymbol{R}^{\mathsf{T}} = \boldsymbol{R}$.

The cost function may be rewritten to a difference equation form, by shifting the summation from k to $k + 1$:

$$J(k) = \boldsymbol{x}(k)^{\mathsf{T}}\boldsymbol{Q}\boldsymbol{x}(k){+}\boldsymbol{u}(k)^{\mathsf{T}}\boldsymbol{R}\boldsymbol{u}(k){+}\sum_{i=k+1}^{\infty} \left[\boldsymbol{x}(i)^{\mathsf{T}}\boldsymbol{Q}\boldsymbol{x}(i){+}\boldsymbol{u}(i)^{\mathsf{T}}\boldsymbol{R}\boldsymbol{u}(i) \right] \qquad (\text{D.5})$$

$$= \boldsymbol{x}(k)^{\mathsf{T}}\boldsymbol{Q}\boldsymbol{x}(k){+}\boldsymbol{u}(k)^{\mathsf{T}}\boldsymbol{R}\boldsymbol{u}(k){+}J(k{+}1) \qquad\qquad (\text{D.6})$$

Assuming that the minimum cost may be written in a quadratic form:

$$\check{J}(k) = \boldsymbol{x}(k)^{\mathsf{T}}\boldsymbol{P}\boldsymbol{x}(k) \qquad\qquad (\text{D.7})$$

where $\boldsymbol{P}$ is also a real symmetric matrix such that

Then inserting the minimum cost into equation D.6 to obtain:

$$J(k){=}\boldsymbol{x}(k)^{\mathsf{T}}\boldsymbol{P}\boldsymbol{x}(k){=}\boldsymbol{x}(k)^{\mathsf{T}}\boldsymbol{Q}\boldsymbol{x}(k){+}\boldsymbol{u}(k)^{\mathsf{T}}\boldsymbol{R}\boldsymbol{u}(k){+}\boldsymbol{x}(k{+}1)^{\mathsf{T}}\boldsymbol{P}\boldsymbol{x}(k{+}1) \qquad (\text{D.8})$$

Inserting the state equation, and noting that since $\boldsymbol{P}$ is real symmetric then $\boldsymbol{H}^{\mathsf{T}}\boldsymbol{P}\boldsymbol{G} = \boldsymbol{G}^{\mathsf{T}}\boldsymbol{P}\boldsymbol{H}$, it is possible to write:

$$J(k){=}\boldsymbol{x}(k)^{\mathsf{T}}\boldsymbol{P}\boldsymbol{x}(k){=}\boldsymbol{x}(k)^{\mathsf{T}}\boldsymbol{Q}\boldsymbol{x}(k){+}\boldsymbol{u}(k)^{\mathsf{T}}\boldsymbol{R}\boldsymbol{u}(k){+}\boldsymbol{x}(k)^{\mathsf{T}}\boldsymbol{G}^{\mathsf{T}}\boldsymbol{P}\boldsymbol{G}\boldsymbol{x}(k){+}\boldsymbol{u}(k)^{\mathsf{T}}\boldsymbol{H}^{\mathsf{T}}\boldsymbol{P}\boldsymbol{H}\boldsymbol{u}(k){+}2\boldsymbol{u}(k)^{\mathsf{T}}\boldsymbol{H}^{\mathsf{T}}\boldsymbol{P}\boldsymbol{G}\boldsymbol{x}(k) \quad (\text{D.9})$$

By taking the derivative with respect to the control input vector $\boldsymbol{u}(k)$ the optimal control law may dervied:

$$\frac{\delta J(k)}{\delta \boldsymbol{u}(k)} = 2\boldsymbol{R}\boldsymbol{u}(k){+}2\boldsymbol{H}^{\mathsf{T}}\boldsymbol{P}\boldsymbol{H}\boldsymbol{u}(k){+}2\boldsymbol{H}^{\mathsf{T}}\boldsymbol{P}\boldsymbol{G}\boldsymbol{x}(k) \qquad\qquad (\text{D.10})$$

Setting $\delta J(k)/\delta \boldsymbol{u}(k) = 0$ and solving for $\boldsymbol{u}(k)$ gives the optimal control law as:

$$\boldsymbol{u}(k) = -\underbrace{\left(\boldsymbol{R} + \boldsymbol{H}^{\!\top}\boldsymbol{P}\boldsymbol{H}\right)^{-1}\boldsymbol{H}^{\!\top}\boldsymbol{P}\boldsymbol{G}}_{\boldsymbol{K}}\,\boldsymbol{x}(k) \tag{D.11}$$

The only task left is to determine the matrix $\boldsymbol{P}$. This may be done by deriving the discrete-time algebraic Riccati equation, which is done by substituting $\boldsymbol{u}(k)$ for the control law in equation D.9. By doing this, the equation may be rewritten to a quadratic form as a function of only $\boldsymbol{x}(k)$:

$$0 = \boldsymbol{x}(k)^{\!\top}\!\left[\boldsymbol{G}^{\!\top}\boldsymbol{P}\boldsymbol{G} - \boldsymbol{P} + \boldsymbol{Q} + \boldsymbol{K}^{\!\top}\boldsymbol{H}^{\!\top}\boldsymbol{P}\boldsymbol{H}\boldsymbol{K} - 2\boldsymbol{K}^{\!\top}\boldsymbol{H}^{\!\top}\boldsymbol{P}\boldsymbol{G} + \boldsymbol{K}^{\!\top}\boldsymbol{R}\boldsymbol{K}\right]\!\boldsymbol{x}(k) \tag{D.12}$$

This must be satisfied for every $\boldsymbol{x}(k)$, why it may be omitted and the following matrix equation is obtained:

$$0 = \boldsymbol{G}^{\!\top}\boldsymbol{P}\boldsymbol{G} - \boldsymbol{P} + \boldsymbol{Q} + \boldsymbol{K}^{\!\top}\boldsymbol{H}^{\!\top}\boldsymbol{P}\boldsymbol{H}\boldsymbol{K} - 2\boldsymbol{K}^{\!\top}\boldsymbol{H}^{\!\top}\boldsymbol{P}\boldsymbol{G} + \boldsymbol{K}^{\!\top}\boldsymbol{R}\boldsymbol{K} \tag{D.13}$$

$$0 = \boldsymbol{G}^{\!\top}\boldsymbol{P}\boldsymbol{G} - \boldsymbol{P} + \boldsymbol{Q} + \boldsymbol{K}^{\!\top}\!\left[\left(\boldsymbol{H}^{\!\top}\boldsymbol{P}\boldsymbol{H} + \boldsymbol{R}\right)\boldsymbol{K} - 2\boldsymbol{H}^{\!\top}\boldsymbol{P}\boldsymbol{G}\right] \tag{D.14}$$

Inserting the algebraic definition of the controller gain $\boldsymbol{K}$ to obtain:

$$0 = \boldsymbol{G}^{\!\top}\boldsymbol{P}\boldsymbol{G} - \boldsymbol{P} + \boldsymbol{Q} + \left[\left(\boldsymbol{R} + \boldsymbol{H}^{\!\top}\boldsymbol{P}\boldsymbol{H}\right)^{-1}\boldsymbol{H}^{\!\top}\boldsymbol{P}\boldsymbol{G}\right]^{\!\top}\!\left[\left(\boldsymbol{H}^{\!\top}\boldsymbol{P}\boldsymbol{H} + \boldsymbol{R}\right)\left(\boldsymbol{R} + \boldsymbol{H}^{\!\top}\boldsymbol{P}\boldsymbol{H}\right)^{-1}\boldsymbol{H}^{\!\top}\boldsymbol{P}\boldsymbol{G} - 2\boldsymbol{H}^{\!\top}\boldsymbol{P}\boldsymbol{G}\right] \tag{D.15}$$

The symmetric term $\boldsymbol{H}^{\!\top}\boldsymbol{P}\boldsymbol{G}$ may be factored out of the parenthesis to obtain:

$$0 = \boldsymbol{G}^{\!\top}\boldsymbol{P}\boldsymbol{G} - \boldsymbol{P} + \boldsymbol{Q} + \boldsymbol{G}^{\!\top}\boldsymbol{P}\boldsymbol{H}\left(\left(\boldsymbol{R} + \boldsymbol{H}^{\!\top}\boldsymbol{P}\boldsymbol{H}\right)^{-1}\right)^{\!\top}\!\left[\left(\boldsymbol{H}^{\!\top}\boldsymbol{P}\boldsymbol{H} + \boldsymbol{R}\right)\left(\boldsymbol{R} + \boldsymbol{H}^{\!\top}\boldsymbol{P}\boldsymbol{H}\right)^{-1} - 2\right]\boldsymbol{H}^{\!\top}\boldsymbol{P}\boldsymbol{G} \tag{D.16}$$

A matrix multiplied by its own inverse gives an identity matrix of appropriate size, simply resulting in a change of sign in the following equation. Furthermore, since both $\boldsymbol{R}$ and $\boldsymbol{H}^{\!\top}\boldsymbol{P}\boldsymbol{H}$ are real symmetric, the transpose may be omitted without consequence to obtain:

$$0 = \boldsymbol{G}^{\!\top}\boldsymbol{P}\boldsymbol{G} - \boldsymbol{P} + \boldsymbol{Q} - \boldsymbol{G}^{\!\top}\boldsymbol{P}\boldsymbol{H}\left(\boldsymbol{R} + \boldsymbol{H}^{\!\top}\boldsymbol{P}\boldsymbol{H}\right)^{-1}\boldsymbol{H}^{\!\top}\boldsymbol{P}\boldsymbol{G} \tag{D.17}$$

This is the discrete-time algebraic Riccati equation, which may be solved to obtain $\boldsymbol{P}$ using MATLAB's *dare* command, where after the controller state feedback gain $\boldsymbol{K}$ may simply be calculated.